Structural Performance of YSt-310 Cold-formed Steel Tubular Columns

A thesis submitted for the degree of

Doctor of Philosophy

By

Tekcham Gishan Singh

ꯇꯦꯀ꯭ꯆꯝ ꯒꯤꯁꯟ ꯁꯤꯡꯒ

B.Eng. NIT Karnataka, India

Department of Civil Engineering
Indian Institute of Technology Guwahati
Guwahati – 781039, India

This page is intentionally left blank.

to the Lord

to my dearest parents

Damu and Bina

This page is intentionally left blank.

Abstract

Construction industries in India are predominantly dominated by reinforced concrete structures, mainly because of their relatively long experiences and cheaper unskilled workforce. However in the last few decades, steel constructions in India, using cold-formed steel tubular/hollow sections, have become increasingly popular, as can be witnessed from many public and industrial structures. Among the various constructional steels available in India, the YSt-310 cold-formed steel tubular sections, conforming to IS 4923 (1997), is one of the most commonly preferred steel material for structural use. However, to the best of authors' knowledge, detailed and reliable material data including member test, for this particular steel are very limited or do not exist readily in the public domain. Moreover, the existing design equations, which were predominantly developed based on hot-rolled steels, relied on the elastic and perfectly plastic stress-strain material model, essentially ignoring the beneficial effect of strength enhancement from cold-forming. Consequently, the design practice results in overly conservative predictions, thus increasing the cost of construction. The primary objective of this study is then to setup a reliable material characteristics database for YSt-310 steel at various temperature levels, as well as to investigate the structural performance of both unperforated and perforated stub columns.

As a part of the study, material characteristics of YSt-310 cold-formed steel tubular sections have been studied at ambient temperature, elevated temperature and post-fire conditions. In the ambient temperature study, chemical compositions, metallographic examinations and mechanical properties have been estimated using standard test procedures. The investigations on the mechanical properties have further been

extended to elevated temperatures and post-fire conditions, and reduction factors of key material parameters have been estimated. Relationships between post-fire mechanical properties and microhardness values have also been established. Design reduction factors have been proposed for both elevated temperature and post-fire conditions, using the present and existing test results.

Structural performance of YSt-310 cold-formed steel tubular stub columns has been studied through experimental and numerical investigations. The extent of corner strength enhancement due to cold-forming has been studied using microhardness test. Additionally, geometric imperfections of stub columns have been measured by employing a non-contact 3D laser scanner. A total of 12 stub column have been tested, and the results been utilised to develop finite element models for parametric study, taking into account the geometric and material non-linearity. Using test and FE column capacities, the feasibility of current design guidelines for cold-formed tubular stub columns have been assessed and found to provide conservative predictions. An improved, modified design approach based on direct strength method (DSM) has been proposed which takes into account of strain-hardening behaviour of cold-formed steel tubular stub columns, observed at low slenderness ranges.

The study on the structural performance of YSt-310 cold-formed steel tubular stub columns has further been expanded by incorporating two opposite central circular perforations at mid-height of the column. The influence of perforations on the column capacities has been studied through experimental and validated FE models, covering a wide range of perforation sizes and cross-section slenderness. Additionally, imperfection amplitude models based on Dawson and Walker model have been proposed for both unperforated and perforated cold-formed steel stub columns using imperfection measurement results. The applicability of existing design equations for perforated columns has then been assessed using the columns capacities generated from test and FE results. A set of modified equations for the design of perforated cold-formed steel stub columns, for different perforation sizes, has been proposed based on DSM approach.

Declaration

I hereby declare that this thesis entitled **'Structural Performance of YSt-310 Cold-formed Steel Tubular Columns'** has been generated by me and purely represents my PhD work. Any material from unpublished or published work from others is referenced appropriately.

Date:

Place:

Mr Tekcham Gishan Singh

Reg. No: 146104036

This page is intentionally left blank.

Certificate

This is to certify that the thesis entitled '**Structural Performance of YSt-310 Cold-formed Steel Tubular Columns**' being submitted by **Mr Tekcham Gishan Singh** to the Indian Institute of Technology Guwahati, India for the award of degree of **Doctor of Philosophy** is a record of genuine research work carried out by him under my supervision.

The thesis work, in my opinion is worthy of considering for the award of degree of **Doctor of Philosophy** in accordance with the regulation of the institute.

Date:

Place:

Dr Konjengbam Darunkumar Singh
Professor
Department of Civil Engineering
Indian Institute of Technology Guwahati, India

This page is intentionally left blank.

Acknowledgements

Foremost, I would like to express my sincere gratitude and appreciation to my supervisor, **Prof. Konjengbam Darunkumar Singh**, for his constant encouragement, unconditional support, continued inspiration and guidance throughout my research work. I am so grateful to have him as my supervisor, who has moulded me to a new individual. To me, he is not only my supervisor but also a life-long mentor and a friend, from whom I have acquired a lot of priceless proficiency apart from academic.

I am thankful to the members of my doctoral committee: Prof. Sudip Talukdar (Chairman), Dr. Hrishikesh Sharma and Dr. Amit Shelke of the Department of Civil Engineering, Indian Institute of Technology Guwahati, who have generously offered their time and support to review my research work from time to time. Their suggessions, remarks and encouragements have been absolutely invaluable.

I would like to acknowledge the financial support, technical assistance, testing facilities etc., provided by the Department of Civil Engineering, Indian Institute of Technology Guwahati, to carry out this project.

The instrumental facilities, in particular, milling machine, 3D Laser scanner, CO2 laser cutting machine, Wire cut EDM, Optical microscope, Vickers Hardness tester, CO2 Laser Cut etc., provided by the Department of Mechanical Engineering, Indian Institute of Technology Guwahati is gratefully acknowledged. Also, the testing facility provided by Central Instrument Facility at Indian Institute of Technology

Guwahati is gratefully acknowledged. Also, I would like to highlight the technical support provided by Shimadzu New Delhi for Optical Emission Spectrometer (OES).

I would like to extend thanks to my caring senior PhD research scholars, in particular Dr. Sonu J.K., Dr. Khwairakpam Sachidananda and Mr PVR Narendra Babu, who have taught me the basic tools of Abaqus. My thanks also goes to Mr Sanasam Sunderlal Singh, PhD scholar of the Department of Mechanical Engineering, Indian Institute of Technology Guwahati, for his constant help and support to carryout metallographic examination.

It is my pleasure to thank my PhD colleagues, Mr G. R. Patil**,** Mr Ningthoukhongjam Sukumar Singh, Ms Sanasam Vipej Devi, Mr Ricky Lalthazuala, Mr Prasanta Kar, Mr Suman Kumar Mushahary, and Mr Jyotirmoy Haloi for their participation in discussion of experimental investigations, finite element modelling, design and other subjects.

I am also grateful to my friends and colleagues, in particular Ms Ngangkham Devarani, Ms Mayanglambam Bidyalakshmi Devi, Dr. Khwairakpam Shantakumar Singh, Mr Ningthoujam Somorjit Singh, Mr Chingtham Sanajaoba Singh, Mr Yaipharemba Meitei, Mr Konjengbam Anand Singh, Mr Loitongbam Gyanendro Singh, Mr Rajkumar Shufen, Mr Alex Kamson, Mr Moirangthem Krishnananda Singh, Thangjam Rishikesh Singh, Mr Mayanglambam Khogendrajit Singh, Mr Sabnam Gogoi who share my happiness and sadness and also help me, during the stay at IIT Guwahati Campus.

Finally but not the least, I would like to specially thank my parents and grandparents for their love, constant support and encouragement throughout the course of my research work. With all my love, I would like to dedicate this thesis to them.

Contents

ABSTRACT ..... **v**
DECLARATION ..... **vii**
CERTIFICATE ..... **ix**
ACKNOWLEDGEMENTS ..... **xi**
CONTENTS ..... **xiii**
LIST OF FIGURES ..... **xxi**
LIST OF TABLES ..... **xxxi**
NOTATIONS ..... **xxxv**

CHAPTER 1 INTRODUCTION **1**

1.1 BACKGROUND 1
1.1 POPULARITY OF TUBULAR STRUCTURES IN INDIA 2
1.2 PERFORATED TUBULAR MEMBERS 3
1.3 RESEARCH MOTIVATION 4
1.4 OBJECTIVES 5
1.5 OUTLINE OF THESIS 5

CHAPTER 2 LITERATURE REVIEW **11**

2.1 INTRODUCTION 11
2.2 MATERIAL PROPERTIES 12
2.2.1 Material properties at ambient temperature 12

2.2.2 Material properties at elevated temperature 13
2.2.3 Material properties after post-fire 15

2.3 STUB COLUMNS 16

2.3.1 Unperforated stub columns 17
2.3.1.1 Design rules 18
2.3.1.1.1 European Standard 18
2.3.1.1.2 American Standard 19
2.3.1.2 Design Methods 19
2.3.1.2.1 Effective Width Method 19
2.3.1.2.2 Direct Strength Method 20
2.3.1.2.3 Continuous Strength Method 21
2.3.2 PERFORATED STUB COLUMNS 22
2.3.2.1 Design rules 27
2.3.2.1.1 American Standard 27
2.3.2.1.2 Design formulae by Miller and Peköz (1994) 28

2.4 3D SCANNING AND EVALUATION OF LOCAL GEOMETRIC IMPERFECTIONS 28

2.5 SUMMARY 29

CHAPTER 3 MATERIAL CHARACTERISATION 33

3.1 INTRODUCTION 33

3.2 DETAILS OF MATERIAL SUPPLY 35

3.3 AMBIENT TEMPERATURE MATERIAL PROPERTIES 35

3.3.1 Chemical composition 36
3.3.2 Microstructure 36
3.3.3 Mechanical properties 38
3.3.3.1 Flat coupon tests 39
3.3.3.2 Corner coupon tests 39
3.3.3.3 Weld coupon tests 40
3.3.4 Test results and discussion 40

3.4 ELEVATED TEMPERATURES MECHANICAL PROPERTIES 42

3.4.1 General 42
3.4.2 Test specimens 42
3.4.3 Test apparatus 43
3.4.4 Test procedure 43
3.4.5 Test results and discussion 44
3.4.5.1 Stress-strain curves 45
3.4.5.2 Elastic modulus 45
3.4.5.3 Yield strength 46
3.4.5.4 Stresses at 0.5% and 1.5%, and 2.0% strains 46
3.4.5.5 Ultimate strength and strain 47
3.4.5.6 Fracture strain 47
3.4.6 Design reduction factors 47
3.4.7 Reliability analysis 48
3.4.8 Comparison of design reduction factors 49
3.4.8.1 Elastic modulus 49
3.4.8.2 Yield strength 51
3.4.8.3 Stress at 0.5% and 1.5% strain 52
3.4.8.4 Stress at 2.0% strain 53
3.4.8.5 Ultimate strength 55
3.4.8.6 Ultimate and fracture strains 56
3.5 POST-FIRE MECHANICAL PROPERTIES 58
3.5.1 General 58
3.5.2 Test specimens 58
3.5.3 Heat treatment 59
3.5.4 Tensile coupon test 60
3.5.5 Microhardness test 60
3.5.5.1 General 60
3.5.5.2 Hardness test 61
3.5.6 Experimental outcome 62
3.5.6.1 Tensile coupon test 62
3.5.6.1.1 Failure mechanism 62
3.5.6.1.2 Stress-strain relationships 62
3.5.6.1.3 Elastic modulus 63

3.5.6.1.4 Yield strength 64
3.5.6.1.5 Tensile strength 65
3.5.6.1.6 Ductility 65
3.5.6.2 Microhardness test 66
3.5.7 Comparison with previous investigations 66
3.5.7.1 Reduction factors 67
3.5.7.1.1 Elastic modulus 67
3.5.7.1.2 Yield strength 67
3.5.7.1.3 Tensile strength 68
3.5.7.1.4 Ductility 68
3.5.7.1.5 Evaluation of existing empirical formulae 68
3.5.8 Prediction formulae 69
3.5.8.1 Present test results 69
3.5.8.1.1 Reduction factors 69
3.5.8.1.2 Material strength and hardness 69
3.5.8.1.3 Stress-strain curve 70
3.5.8.2 Combined test results 71
3.5.9 Reliability analysis 71
3.6 SUMMARY 72
3.6.1 Ambient temperature material test 73
3.6.2 Elevated temperature material test 73
3.6.3 Post-fire material test 75

CHAPTER 4 STUB COLUMNS 133

4.1 INTRODUCTION 133
4.2 EXPERIMENTAL INVESTIGATION 135
4.2.1 Preparation of stub columns 135
4.2.2 Microhardness test 135
4.2.3 Local geometric imperfection 137
4.2.4 Stub column test 138
4.3 FINITE ELEMENT MODELLING 139
4.3.1 General 139
4.3.2 Finite element type 139

4.3.3 Flat and corner material properties 140
4.3.4 Weld material properties 140
4.3.5 Local geometric imperfection and residual stress 141
4.3.6 Loading and boundary conditions 142
4.3.7 Validation of FE procedure 142
4.3.8 Parametric study 144

4.4 CURRENT DESIGN CODE AND RULES 145

4.4.1 General 145
4.4.1.1 European code 145
4.4.1.2 Continuous strength method 147
4.4.1.3 Direct strength method 150
4.4.1.4 Modified DSM 151

4.5 RELIABILITY ANALYSIS 152

4.6 COMPARISION OF TEST AND FE STUB COLUMN STRENGTHS WITH DESIGN PREDICTIONS 153

4.6.1 General 153
4.6.2 Comparison with Eurocode 155
4.6.3 Comparison with CSM 156
4.6.4 Comparison with DSM 156
4.6.5 Comparison with modified DSM 157
4.6.6 Proposed modified DSM 158

4.7 SUMMARY 158

CHAPTER 5 PERFORATED STUB COLUMNS 183

5.1 INTRODUCTION 183

5.2 EXPERIMENTAL INVESTIGATION 184

5.2.1 General 184
5.2.2 Test material 184
5.2.3 Stub column preparation 185
5.2.4 Local Geometric imperfection 186

5.2.5 Strain measurement 186
5.2.6 Stub column tests 187
5.3 RESULTS AND DISCUSSION 187
5.3.1 Local geometric imperfection 187
5.3.1.1 Unperforated plate elements 188
5.3.1.2 Perforated plate elements 189
5.3.2 Compression test results 190
5.3.3 Effect of *d*/*w* on the capacity of stub columns 191
5.3.4 Strain distribution at perforations location 192
5.4 FINITE ELEMENT ANALYSIS 193
5.4.1 Finite element modelling 193
5.4.2 Validation of FE perforated model 194
5.4.3 Parametric study 194
5.4.4 Effect of perforation size ratio on the ultimate capacity of stub column using test and FE results 195
5.5 DESIGN METHODS FOR PERFORATED STEEL COLUMNS 196
5.5.1 Design equations by Shanmugam *et al*. (1999) 196
5.5.2 Design equations by Dhanalakshmi and Shanmugam (2001) 197
5.5.3 Design equations by Shanmugam and Dhanalakshmi (2001) 198
5.5.4 Design equations in AISI Standard 199
5.5.4.1 Determination of global buckling 199
5.5.4.2 Determination of local buckling 200
5.5.4.2.1 Determination of local buckling based on Effective Width Method (EWM) 200
5.5.4.2.2 Determination of local buckling based on Direct Strength Method (DSM) 201
5.5.4.2.3 Determination of local buckling stress based on Moen and Schafer (2009) 202
5.5.5 Design equation proposed by Miller and Peköz (1994) 203
5.5.5.1 Calculation of effective design width based on European, American and Australian standards 203
5.5.5.2 Calculation of effective design width based on British Standard 204

5.6 RELIABILITY ANALYSIS 204

5.7 DESIGN OF PERFORATED STEEL STUB COLUMNS 205

5.7.1 Assessment of current design methods for perforated steel members against test results 205

5.7.1.1 For perforation size ratio: $0.1 \leq d/w \leq 0.9$ 205

5.7.1.2 For perforation size ratio: $0.1 \leq d/w \leq 0.7$ 206

5.7.2 Assessment of current design methods for perforated steel members against test and FE results 207

5.7.2.1 For perforation size ratio: $0.1 \leq d/w \leq 0.9$ 207

5.7.2.2 For perforation size ratio: $0.1 \leq d/w \leq 0.7$ 208

5.7.3 Proposed design equation 209

5.8 CONCLUSIONS 210

CHAPTER 6 CONCLUSIONS 253

6.1 RESEARCH SUMMARY 253

6.1.1 Material characterisation 255

6.1.1.1 Ambient temperature tests 255

6.1.1.2 Elevated temperature material tests 256

6.1.1.3 Post-fire material tests 257

6.1.2 Unperforated stub column tests 258

6.1.3 Perforated stub column test 259

6.2 SUGESSIONS FOR FUTURE WORK 260

6.2.1 Extension to present research work 260

6.2.2 Other thoughts 261

REFERENCES 263

PUBLICATIONS 287

APPENDIX A 289

APPENDIX B 299

This page is intentionally left blank.

List of figures

Figure 1.1: Melbourne Star, Melbourne (Source: www.unsplash.com/photos/5-VkAlkUrI0) 8

Figure 1.2: Chennai Airport, India 8

Figure 1.3: CIDCO Exhibition and Convention Centre, India (Image by www.iniinfraengineering.com/upload_image/55.jpg) 9

Figure 1.4: Jawaharlal Nehru Stadium, India (Courtesy: Tata Structura Tubes Division, Kolkata) 9

Figure 1.5: Chhatrapati Shivaji International Airport, India (Courtesy: Tata Structura Tubes Division, Kolkata) 10

Figure 1.6: Perforation provided for electrical services 10

Figure 3.1: Definition of symbols and position of coupon specimens in (a) square and (b) rectangular hollow sections 76

Figure 3.2: Microstructure for 66 × 33 × 2.6 at (a) flat and (b) corner regions .. 76

Figure 3.3: Size of welds seen through optical microscope for (a) 60 × 40 × 2.9 and (b) 66 × 33 × 2.6 cross-sections 77

Figure 3.4: Typical microstructures: (a) HFIW seam for sample 66 × 33 × 2.6, (b) Widmanstätten, (c) partially-recrystallized zone and (d) parent material 78

Figure 3.5: Dimensions (mm) of: (a) flat, (b) corner and (c) weld coupon specimens 79

Figure 3.6: Ambient temperature tensile tests setup for (a) flat, (b) curve and (c) weld coupons 79

Figure 3.7: Stress-strain curves generated from the flat tensile coupon tests at ambient temperature 80

Figure 3.8: Stress-strain curves generated from the corner tensile coupon tests at ambient temperature 80

Figure 3.9: Stress-strain curves generated from the weld tensile coupon tests at ambient temperature 81

Figure 3.10: Definitions of mechanical parameters 81

Figure 3.11: Dimensions (mm) of coupon specimen for elevated temperature tensile coupon tests 82

Figure 3.12: Instrumental setup for elevated temperature tensile coupon tests 82

Figure 3.13: Stress-strain curves at different elevated temperatures for 50 × 50 × 2.9 cross-section..... 83

Figure 3.14: Stress-strain curves at different elevated temperatures for 60 × 60 × 2.6 cross-section..... 83

Figure 3.15: Stress-strain curves at different elevated temperatures for 80 × 40 × 2.6 cross-section..... 84

Figure 3.16: Measured moduli of elasticity at various elevated temperatures measured from tensile coupon tests. 84

Figure 3.17: Measured yield stress or 0.2% proof stresses from the tensile tests . 85

Figure 3.18: Measured values of stress corresponding to 0.5% strain at various elevated temperatures 85

Figure 3.19: Measured values of stress corresponding to 1.5% strain at different elevated temperatures 86

Figure 3.20: Measured values of stress corresponding to 2.0% strain at various elevated temperatures 86

Figure 3.21: Measured values of ultimate tensile strengths at different temperature levels 87

Figure 3.22: Measured values of strain (%) corresponding to ultimate strength .. 87

Figure 3.23: Measured fracture strains (%) from tensile coupon test under various temperatures 88

Figure 3.24: Comparison of elevated temperature Young's modulus reduction factors from present test data with current design standards and existing proposals 88

Figure 3.25: Comparison of elevated temperature Young's modulus reduction factors from all test data of cold-formed tubular sections with existing design standards and existing proposals 89

Figure 3.26: Comparison of elevated temperature yield stress reduction factors from present test data with current design standards and existing proposals 89

Figure 3.27: Comparison of elevated temperature yield strength reduction factors from all test data of cold-formed tubular sections with existing design; existing and current proposals 90

Figure 3.28: Comparison of elevated temperature reduction factors for stress at 0.5% strain from present test with those predicted by BS 5950 (2003) 90

Figure 3.29: Comparison of elevated temperature reduction factors for stress corresponding to 1.5% strain with those in BS 5950 (2003) and current proposal 91

Figure 3.30: Comparison of elevated temperature reduction factors for stress at 0.5% strain from all test data of cold-formed tubular sections with existing design standards and current proposal 91

Figure 3.31: Comparison of elevated temperature stress at 2.0% strain reduction factors from present test data with current design standards and existing proposals 92

Figure 3.32: Comparison of elevated temperature stress at 2.0% strain reduction factors for all test data of cold-formed tubular sections with design standards; existing and present proposals 92

Figure 3.33: Comparison of elevated temperature ultimate strength reduction factors from the present test result with predictions from design standards and existing proposals 93

Figure 3.34: Comparison of elevated temperature ultimate strength reduction factors from all test results with the predictions from design standards, existing proposals and current proposals 93

Figure 3.35: Comparison of elevated temperature reduction factors for strain corresponding to ultimate stress with the design curve by Chen and Young (2007) 94

Figure 3.36: Comparison of ultimate strain retention factor from current test and literature with the prediction curve proposed by Chen and Young (2007) 94

Figure 3.37: Comparison of elevated temperature fracture strain reduction factor from all test results with the prediction from existing and present proposed curves 95

Figure 3.38: Typical dimensions (in mm) of coupon specimen for post-fire tensile coupon test 95

Figure 3.39: A typical setup for electric furnace utilised for heating coupon specimens 96

Figure 3.40: A typical test setup of a tensile coupon specimen after being exposed to elevated temperatures 96

Figure 3.41: A typical sizes of an indent in the microhardness test 97

Figure 3.42: Typical failed specimens of 50 × 50 × 2.9 cross-section after tensile coupon tests under post-fire condition 97

Figure 3.43: Post-fire stress-strain curves for 50 × 50 × 2.9 cross-section 98

Figure 3.44: Post-fire stress-strain curves for 60 × 40 × 2.9 cross-section..... 98

Figure 3.45: Post-fire stress-strain curves for 63 × 33 × 2.6 cross-section..... 99

Figure 3.46: Post-fire elastic modulus reduction factors from present test and predictions 99

Figure 3.47: Post-fire yield strength reduction factors from present test and predictions 100

Figure 3.48: Post-fire tensile strength reduction factors from present test, existing and predictions..... 100

Figure 3.49: Post-fire ductility reduction factors from present test and current proposed prediction 101

Figure 3.50: Post-fire hardness reduction factors from present test and current proposed prediction 101

Figure 3.51: Post-fire elastic modulus reduction factors from test results and proposed design curve 102

Figure 3.52: Comparison of post-fire yield strength reduction factors from test and proposed curve..... 102

Figure 3.53: Comparison of post-fire tensile strength reduction factors from test results against the present proposed curve 103

Figure 3.54: Post-fire ductility reduction factors from test results and proposed curve 103

Figure 3.55: Relationship of hardness values and post-fire yield strengths..... 104

Figure 3.56: Relationship between hardness values and post-fire tensile strengths..... 104

Figure 3.57: Comparison of test and predicted post-fire stress-strain curves at different exposed temperatures for 50 × 50 × 2.9 cross-section..... 105

Figure 4.1: Convention used for numbering corner locations..... 161

Figure 4.2: A typical picture showing the creation of diamond indent..... 161

Figure 4.3: Hardness distributions across the cross-section length normalized by thickness for sample 66 × 33 × 2.6 162

Figure 4.4: Hardness distributions across the cross-section length normalized by thickness for sample 40 × 40 × 3.2 162

Figure 4.5: Hardness distributions across the cross-section length normalized by thickness for sample 60 × 40 × 2.9 163

Figure 4.6: Hardness value (H_v) distribution over normalized section length .. 163

Figure 4.7: 3D hardness distributions for 66 × 33 × 2.6-S2 164

Figure 4.8: Measurement of geometric imperfection: (a) extracting flat portion (b) measurement of geometric imperfection (c) a schematic longitudinal profile 164

Figure 4.9: Measured geometric imperfection for section 80 × 40 × 2.6 165

Figure 4.10: Stub columns compression test setup for 250 kN displacement control universal testing machine (UTM) 165

Figure 4.11: Stub columns compression test setup for 1000 kN load UTM 166

Figure 4.12: Typical local buckling failure mode for stub columns of (a) 50 × 50 × 2.9, (b) 60 × 40 × 2.9 and (c) 60 × 60 × 2.6 166

Figure 4.13: Load-end shortening curve for 50 × 50 × 2.9, 60 × 40 × 2.9 and 66 × 33 × 2.6 sections. 167

Figure 4.14: Load-end shortening curve for 40 × 40 × 3.2, 40 × 40 × 4.0, 80 × 40 × 2.6 and 60 × 60 × 2.6 sections 167

Figure 4.15: Comparison of experimental and numerical load-end shortening curves for sections including weld material property 168

Figure 4.16: Comparison of experimental and numerical load-end shortening curves (without weld) 168

Figure 4.17: Comparison of experimental and FE deformation for (a) 80 × 40 × 2.6-SC1 and (b) 66 × 33 × 2.6-SC1 169

Figure 4.18: Assessment of EC3: Part 1–1 (2005) Class–3 slenderness limit with the FE and test results 170

Figure 4.19: Assessment of EC3 effective width equation for internal flat element in compression. 170

Figure 4.20: Comparison of CSM base curve with test and FE data points 171

Figure 4.21: Assessment of CSM design prediction with test and results for non-slender cross-sections $\left(\bar{\lambda}_p \le 0.68\right)$ 171

Figure 4.22: Assessment of CSM design prediction with test and FE results for slender cross-sections $\left(\bar{\lambda}_p > 0.68\right)$ 172

Figure 4.23: Assessment of DSM with test and FE results 172

Figure 4.24: Assessment of modified DSM approach with test and FE results. 173

Figure 5.1: Section definitions of perforated stub column: (a) plan and (b) three dimensional views 212

Figure 5.2: Typical diagram showing measurement of local geometric imperfection for 80 × 40 × 2.6*d*/*w*0.7-1: (a) 3D wire frame scan image (b) perforated face and (c) surface profiles for four faces. 212

Figure 5.3: Location of Strain gauge for 60 × 40 × 2.9*d*/*w*0.7-02 stub column 213

Figure 5.4: Experimental setup of cold-formed tubular stub columns with circular perforation: (a) 60 × 40 × 2.6*d*/*w*0.9-2 compressing on 250 kN loading frame and (b) 60 × 60 × 2.6*d*/*w*0.3-1 on 1000 kN loading frame... 213

Figure 5.5: Inter-relationship between ω_d/t and $(f_y/f_{cr})^{0.5}$ for estimation of γ for unperforated columns 214

Figure 5.6: Inter-relationship between ω_d/t and $\left(f_y/f_{cr}\right)$ for estimation of β for unperforated columns 214

Figure 5.7: Typical representation for calculation of equivalent unstiffened plate element width, w_h at the location of hole..... 215

Figure 5.8: Interrelationship between ω_{dp}/t and $(f_y/f_{crl})^{0.5}$ for estimation of γ for perforated columns 215

Figure 5.9: Interrelationship between ω_{dp}/t and $\left(f_y/f_{crl}\right)$ for estimation of β for perforated columns 216

Figure 5.10: Load-end shortening curves for different (d/w) ratios of 50 × 50 × 2.9 cross-sections 216

Figure 5.11: Load-end shortening curves for different (d/w) ratios of 60 × 40 × 2.9 cross-sections 217

Figure 5.12: Load-end shortening curves for different (d/w) ratios of 60×60×2.6 cross-sections 217

Figure 5.13: Load-end shortening curves for different (d/w) ratios of 66×33×2.6 cross-sections 218

Figure 5.14: Load-end shortening curves for different (d/w) ratios of 80 × 40 × 2.6 cross-sections 218

Figure 5.15: Deformed shapes of 60 × 40 × 2.6 with different hole to width size (d/w) ratio ranging from 0.1–0.9 219

Figure 5.16: Deformed shapes of 80 × 40 × 2.6 with different hole to width size (d/w) ratio ranging from 0.1–0.9 219

Figure 5.17: Influence of opening size on column strength for three cross-sections: 60 × 60 × 2.6, 60 × 40 × 2.9 and 80 × 40 × 2.6 220

Figure 5.18: Axial strain distribution at perforation locations for stub column, 60 × 40 × 2.9d/w0.7-2 220

Figure 5.19: Axial strain distribution at perforation locations for stub column, 60 × 40 × 2.9d/w0.9-2 221

Figure 5.20: Load-end shortening curve and deformation at mid-height of 80 × 80 × 2.6d/w0.3-1 at various load levels: (A) before ultimate load (~ 280

kN), (B) at ultimate load (~ 290 kN) and (C) after ultimate load (~ 250 kN) 221

Figure 5.21: Comparison of Test and finite element (FE) load end-shortening curves for 50 × 50 × 2.9 cross-section 222

Figure 5.22: Comparison of Test and finite element (FE) load end-shortening curves for 60 × 40 × 2.9 cross-section 222

Figure 5.23: Comparison load end-shortening curves generated from experiment and FE of 60 × 60 ×2.6 cross-section stub column. 223

Figure 5.24: Comparison load end-shortening curves generated from experiment and FE of 66 × 33 ×2.6 cross-section stub column. 223

Figure 5.25: Comparison load end-shortening curves generated from experiment and FE of 80 × 40 ×2.6 cross-section stub column. 224

Figure 5.26: Comparison of post-ultimate deformed shapes – FE model and tested specimen for 60 × 60 × 2.6*d*/*w*0.9-1 224

Figure 5.27: Comparison of post-ultimate deformed shapes – FE model and tested specimen for 60 × 40 × 2.9*d*/*w*0.9-2 225

Figure 5.28: Comparison of post-ultimate deformed shapes – FE model and tested specimen for 80 × 40 × 2.6*d*/*w*0.1-1 225

Figure 5.29: Normalized ultimate load capacities for columns with different perforation (*d*/*w*) ratios. 226

Figure 5.30: Assessment of AISI S100 (2016) DSM prediction with test results 226

Figure 5.31: Assessment of AISI DSM (2016) prediction using critical elastic buckling stress by Moen and Schafer (2009) with test results. 227

Figure 5.32: Assessment of DSM in AISI S100 (2016) and DSM with critical elastic buckling stress by Moen and Schafer (2009) predictions against the test results 227

Figure 5.33: Assessment of AISI DSM (2016) prediction with test and FE column capacities 228

Figure 5.34: Relationship between K_1 and K_2 coefficients against perforation size ratio, d/w 228

Figure 5.35: Relationship between K_3 and perforation size ratio, d/w 229

Figure 5.36: Relationship between K_4 and perforation size ratio, d/w 229

Figure 5.37: Assessment of unperforated design curve against the ultimate capacities of cold-formed steel stub columns having perforations with size ratio, d/w up to 0.2 230

Figure 5.38: Assessment of proposed design curve for perforated cold-formed steel stub columns having perforations d/w up to 0.3 230

Figure 5.39: Assessment of proposed design curve for perforated cold-formed steel stub columns having perforations d/w up to 0.5 231

Figure 5.40: Assessment of proposed design curve for perforated cold-formed steel stub columns having perforations d/w up to 0.7 231

Figure 5.41: Assessment of proposed design curve for perforated cold-formed steel stub columns having perforations d/w up to 0.9 232

Figure 5.42: Comparison of test and numerical perforated column capacities with design predictions for $\lambda_l \leq 0.776$ 232

Figure 5.43: Comparison of test and numerical perforated column capacities with design predictions for $\lambda_l > 0.776$ 233

Figure 5.44: Assessment of DSM in AISI S100 (2016) prediction using critical elastic buckling stress by Moen and Schafer (2009) and proposed modified DSM prediction against the test and FE result 233

List of tables

Table 2.1: Summary of available elevated temperature mechanical properties of cold-formed steel tubular sections 31

Table 2.2: Summary of available post-fire mechanical properties of cold-formed steel tubular sections 31

Table 3.1: Nominal cross-sectional dimensions of YSt-310 cold-formed steel hollow sections 106

Table 3.2: Chemical composition and mechanical strength of YSt-310 as per mill certificate 106

Table 3.3: Optical Emission Spectrometer analysis results 106

Table 3.4: Summary of flat coupon tensile tests 107

Table 3.5: Summary of corner coupon tensile tests 107

Table 3.6: Summary of weld coupon tensile tests 108

Table 3.7: Key material properties recorded from tensile coupon test at various elevated temperatures 109

Table 3.8: Reduction factors of key material parameters at elevated temperature 111

Table 3.9: Data collected from previous literature. 113

Table 3.10: Comparison of elevated temperature reduction factors with present test results with predictions from design standards and literature .. 114

Table 3.11: Comparison of elevated temperature reduction factors with all test results with design predictions 116

Table 3.12: Proposed elevated temperature reduction factors for 0.2% proof strength; stress at 0.5%, 1.5%, 2.0% strains and ultimate strength. 118

Table 3.13: Summary of post-fire mechanical properties of YSt-310 cold-formed steel hollow sections 119

Table 3.14: Comparisons of reduction factors obtained from the present test results and design predictions proposed in this Chapter 121

Table 3.15: Proposed post-fire reduction factor predictive equations for YSt-310 cold-formed steel. 123

Table 3.16: Stress-strain material models for post-fire mechanical properties of YSt-310 cold-formed steels tubular sections 124

Table 3.17: Proposed post-fire reduction factor predictive equations for cold-formed steels 126

Table 3.18: Comparisons of post-fire reduction factors of cold-formed steel tubular sections 127

Table 4.1: Measured section dimensions, geometric imperfection and results of stub columns 174

Table 4.2: Validation of FE models against the test results considering either with weld or without weld material in the FE models 174

Table 4.3: Generated stub column capacities and corresponding displacements from FE models 175

Table 4.4: Assessment of design predictions from current design equations as well as proposed equations against the test results 179

Table 4.5: Assessment of design predictions from current design equations as well as proposed equations against FE 180

Table 4.6: Comparison of FE and test results with design predictions for non-slender/ stocky cross-sections 180

Table 4.7: Comparison of FE and test results with design predictions for slender cross-sections 180

Table 4.8: Comparison of all FE and test results with design predictions..... 181

Table 4.9: Comparison of all FE and test results with design predictions for resistance factor of $\phi = 0.85$ 181

Table 5.1: Section dimensions of stub columns 234

Table 5.2: Summary of measured local geometric imperfection for unperforated stub columns 236

Table 5.3: Summary of measured local geometric imperfection for perforated stub columns 237

Table 5.4: Summary of measured local geometric imperfection for perforated stub columns 238

Table 5.5: Comparison of ultimate load (P_{FE-P}) and corresponding displacements (δ_{FE-P}) generated FE against the test results. 239

Table 5.6: Comparison of test and FE perforated column capacities with design predictions proposed in this chapter. 240

Table 5.7: Summary of compression test of perforated cold-formed stub columns and comparison with design prediction for perforation size ratio, $d/w \leq 0.9$ 247

Table 5.8: Summary of compression test of perforated cold-formed stub columns and comparison with design prediction for perforation size ratio, $d/w \leq 0.7$ 249

Table 5.9: Summary of comparison of stub column ultimate capacities from test and FE with design prediction for $d/w \leq 0.9$ 251

Table 5.10: Summary of comparison of stub column ultimate capacities from test and FE with design prediction for $d/w \leq 0.7$ 251

Table 5.11: Coefficient for design of perforated cold-formed steel tubular sections with circular perforation 252

This page is intentionally left blank.

Notations

A_0	Total surface area of perforations
A_c	Cross-sectional area of tensile coupon specimen
A_{cr}	Corner cross-sectional area
A_{eff}	Effective cross-sectional area
A_g	Gross cross-sectional area
A_{net}	Cross-sectional area perforated column at the location of perforation
A_p	Gross cross-sectional area of plated (flat) elements
A_s	Total surface area of the member
B	Nominal width of cross-section
b	Effective width
b_{cl}	Web centreline width
$b_{eq,\,flat}$	Equivalent flat element for RHS
$b_{eq,cl}$	Web equivalent width
$b_{eq,cl}$	Web equivalent width
b_{flat}	Web flat width
b_{DW}	Effective design width
C_1, C_2 , C_3 and C_4	CSM Material coefficients
CHS	Circular hollow section
COV	Coefficient of variance
CSM	Continuous Strength Method
C_p	Correction factor

c	Flat element width
D	Nominal depth of cross-section of specimen
DSM	Direct Strength Method
DSM_{ARR}	Modified DSM by Arrayago *et al*. (2017)
DSM_{RR}	Modified DSM by Rossi and Rasmussen (2013)
d	Diameter of perforation
E	Young's modulus at ambient temperature
E_{csm}	CSM strain hardening slope
E_T	Young's modulus at elevated temperature T ºC
E_T^*	Post-fire Young's modulus at ambient temperature after being exposed to elevated temperature T ºC
E_{sh}	CSM strain hardening slope
F_m	Mean value of fabrication factor
F_{cre}	Elastic global buckling stress
F_n	Nominal compressive stress
f_{csm}	CSM design stress
f_u	Tensile stress
$f_{u,T}$	Tensile stress at elevated temperature T ºC
f_y	Yield stress/strength (0.2% proof stress)
H_V	Microhardness value at ambient temperature
$H_{V,T}^*$	Microhardness value at ambient temperature after being exposed to elevated temperature T ºC
I_{gx}	Gross area second moment of area about the major axis
I_{gy}	Gross area second moment of area about the minor axis
$I_{gx,net}$	Net area second moment of area about the major axis
$I_{gy,net}$	Net area second moment of area about the major axis
K	Effective length factor
K_1,K_2 , K_3 and K_4	Coefficients of proposed modified DSM equation
k	Buckling factor/coefficient

k^{*}_{Expt}	Post-fire reduction factor generated from the test
$k^{*}_{\Pr ed}$	Predicted post-fire reduction factor
k_T	Reduction factor for material parameter at elevated temperature T ºC
k^{*}_T	Post-fire reduction factor for key material parameter at ambient temperature after being exposed to elevated temperature T ºC
$k_{E,T}$	Elevated temperature Young's modulus reduction factor
$k^{*}_{E,T}$	Post-fire Young's modulus reduction factor at ambient temperature after being exposed to elevated temperature T ºC
k_1, k_2 and k_3	Sets of coefficients for perorated plates/member developed by Shanmugam and his co-workers (1999, 2001)
$k_{0.2,T}$	Elevated temperature 0.2% proof stress reduction factor
$k^{*}_{0.2,T}$	Post-fire 0.2% proof stress reduction factor at ambient temperature after being exposed to elevated temperature T ºC
$k_{0.5,T}$	Elevated temperature reduction factor for stress at 0.5% strain
$k^{*}_{0.5,T}$	Post-fire reduction factor for stress at 0.5% strain
$k_{1.5,T}$	Elevated temperature reduction factor for stress at 1.5% strain
$k^{*}_{1.5,T}$	Post-fire reduction factor for stress at 1.5% strain at ambient temperature after being exposed to elevated temperature T ºC
$k_{2.0,T}$	Elevated temperature reduction factor for stress at 2.0% strain
$k^{*}_{2.0,T}$	Post-fire reduction factor for stress at 2.0% strain at ambient temperature after being exposed to elevated temperature T ºC
$k_{u,T}$	Elevated temperature ultimate stress reduction factor
$k^{*}_{u,T}$	Post-fire reduction factor for ultimate stress at ambient after being exposed to elevated temperature, T ºC
$k_{\varepsilon_u,T}$	Elevated temperature ultimate strain reduction factor at temperature, T ºC

$k^*_{\varepsilon_u,T}$	Post-fire reduction factor for ultimate strain at ambient temperature after being exposed to elevated temperature T ºC
$k_{\varepsilon_f,T}$	Reduction factor for fracture strain at elevated temperature T ºC
$k^*_{\varepsilon_f,T}$	Post-fire reduction factor for fracture strain at ambient temperature after being exposed to elevated temperature, T ºC
L	Overall length of stub column
l_e	Effective length of stub column
M_m	Mean value of material factor
m	Plate slenderness ratio
N	Number of observation
n	Strain hardening exponent or Ramberg-Osgood parameter
n_T	Strain hardening exponent at elevated temperatures, T ºC
n^*_T	Strain hardening exponent at ambient temperature after being exposed to elevated temperature, T ºC
P_{csm}	Un-factored design strength based on Continuous Strength Method
P_{crl}	Critical elastic buckling load
P_{DS}	Un-factored design strength based on Dhanalakshmi and Shanmugam (2001)
P_{DSM}	Un-factored design strength based on Direct Strength Method detailed in AISI S100-16 (2016)
P_{DSM-RR}	Un-factored design strength based on modified Direct Strength Method proposed by Rossi and Rasmussen (2013)
$P_{DSM-ARR}$	Un-factored design strength based on modified Direct Strength Method proposed by Arrayago *et al.* (2017)
P^*_{DSM}	Un-factored design strength based on proposed modified Direct Strength Method (DSM)
P_{EC3}	Un-factored design strength based on Eurocode

P_{FE}	Ultimate strength recorded from finite element analysis (unperforated)
$P_{FE–P}$	Ultimate strength recorded from finite element analysis (perforated)
P_m	Mean value of ultimate column capacity to predicted load ratio
$P_{MP–EC3}$	Column capacity proposed by Miller and Peköz (1994) simplified formula detailed in EC3-1-5 (2006)
$P_{MP–BS}$	Column capacity proposed by Miller and Peköz (1994) simplified formula detailed in BS 5950-5 (1998)
P_{ne}	Nominal axial strength for distortional buckling
P_{ne}	Nominal axial strength for yielding, and global (flexural, torsional or flexural-torsional) buckling
P_{nl}	Nominal axial strength of column undergoing local buckling
$P_{nl–ARR}$	Nominal axial strength proposed by Arrayago *et al.* (2017)
$P_{nl–DSM}$	Nominal axial strength for local buckling based on DSM
$P_{nl–DSM}$	Nominal axial strength for local buckling based on DSM considering elastic buckling stress proposed by Moen and
$P_{nl–EWM–MS}$	Nominal axial strength for local buckling based on EWM
$P_{nl–RR}$	Nominal axial strength proposed by Rossi and Rasmussen (2013)
P_{Test}	Ultimate strength of stub column (unperforated)
$P_{Test–P}$	Ultimate strength of stub column (perforated)
P_{SD}	Un-factored design strength based on Shanmugam and Dhanalakshmi (2001)
P_{STT}	Un-factored design strength based on Shanmugam *et al.* (2001)
$P_{STT–C}$	Un-factored axial strength for corner area in design strength based on Shanmugam *et al.* (2001)
$P_{STT–P}$	Un-factored axial strength for perforated plate in design strength based on Shanmugam *et al.* (2001)
$P_{STT–UP}$	Un-factored axial strength for unperforated plate in design strength based on Shanmugam *et al.* (2001)
P_m	Mean value

P_{sq}	Squash load
P_u	Ultimate capacity of stub column (unperforated)
P_{u-P}	Ultimate capacity of stub column (perforated)
P_y	Yield load
(V_p)	Coefficient of variances
RHS	Rectangular hollow section
r_g	Radius of gyration
r_i	Inner corner radius of specimen
r_o	Outer corner radius of specimen
SHS	Square hollow section
T	Temperature in ºC
t	Thickness of specimen
V_F	Coefficient of variation of fabrication factor
V_m	Coefficient of variation of material factor
V_p	Coefficient of variation
W_p	Perforation width
w	Flat element width
β	Reliability index or imperfection amplitude coefficient in Dawson and Walker (1972) model
δ_u	End-shortening value or deformation at ultimate strength of column for unperforated stub column
δ_{u-P}	End-shortening value or deformation at ultimate strength of column for perforated stub column
ε_{csm}	Maximum attainable strain
ε_f	Percentage elongation at fracture at ambient temperature
$\varepsilon_{f,T}$	Percentage elongation at fracture at elevated temperature, T ºC

$\varepsilon^*_{f,T}$	Fracture strain at ambient temperature after being exposed to elevated temperature, T ºC
ε_{lb}	Local buckling strain
ε_u	Strain corresponding to ultimate stress at ambient temperature or predicted tensile strain in the case of CSM
$\varepsilon_{u,T}$	Strain corresponding to ultimate stress at elevated temperature, T ºC
$\varepsilon^*_{u,T}$	Strain corresponding to ultimate stress at ambient temperature after being exposed to elevated temperature, T ºC
ε_y	Yield strain
γ	Imperfection amplitude coefficient in Dawson and Walker (1972) model
λ_l	Slenderness factor for local buckling of column
λ_c	Slenderness factor
$\bar{\lambda}_p$	Cross-sectional slenderness
υ	Poisson's ratio of steel
ρ	Reduction factor parameter
ω_d	Measured local geometric imperfection for unperforated stub columns
ω_{dp}	Measured local geometric imperfection for perforated stub columns
ω_0	Local geometric imperfection amplitude proposed by Gardner and Nethercot (2004b)
ϕ	Resistance factor
$\sigma_{0.05}$	Ambient temperature 0.05% proof stress
$\sigma_{0.2}$	Ambient temperature 0.2% proof stress
$\sigma_{0.2,T}$	0.2% proof stress at elevated temperature, T ºC

$\sigma^{*}_{0.2,T}$	0.2% proof stress at ambient temperature after being exposed to elevated temperature, T ºC
$\sigma_{0.5}$	0.05% proof stress at ambient temperature
$\sigma_{0.5,T}$	0.05% proof stress at elevated temperature, T ºC
$\sigma^{*}_{0.5,T}$	0.05% proof stress at ambient temperature after being exposed to elevated temperature, T ºC
$\sigma_{1.0}$	1.0% proof stress at ambient temperature
$\sigma_{1.5}$	1.5% proof stress at ambient temperature
$\sigma_{1.5,T}$	1.5% proof stress at elevated temperature, T ºC
$\sigma^{*}_{1.5,T}$	1.5% proof stress at ambient temperature after being exposed to elevated temperature, T ºC
$\sigma_{2.0}$	2.0% proof stress at ambient temperature
$\sigma_{2.0,T}$	2.0% proof stress at elevated temperature, T ºC
$\sigma^{*}_{2.0,T}$	2.0% proof stress at ambient temperature after being exposed to elevated temperature, T ºC
σ_{cr}	Elastic critical buckling stress
$\sigma_{cr,cs}$	Full cross-section elastic critical buckling stress
σ_{u}	Ultimate stress at ambient temperature
$\sigma_{u,T}$	Ultimate stress at elevated temperature, T ºC
$\sigma^{*}_{u,T}$	Ultimate stress at ambient temperature after being exposed to elevated temperature, T ºC
ψ	Stress ratio

Chapter 1

Introduction

1.1 BACKGROUND

Tubular steel sections have several advantages over open sections, such as high compression, bending and torsional resistances in addition to their inherent aesthetically appealing nature; ease in speedy production and prefabrication etc. Hence, they are widely employed in many industrial, commercial and residential buildings, as well as bridges etc. Figure 1.1 shows an example of a landmark structure which has been constructed using tubular (circular) sections. Based on the production route chosen at the time of manufacturing process, tubular steel sections can be classified mainly into two groups: hot-rolled and cold-formed tubular sections. Hot-rolled tubular steel sections are produced or finished at temperatures above their recrystallization temperature; whereas, in the case of cold-formed steel tubular sections, they are manufactured at ambient temperature by gradually forming an uncoiled metal sheet firstly into circular tubes using a series of automated rollers, with the sides being welded continuously through various welding techniques (e.g. high-frequency induction, submerged arc welding). The circular hollow section (CHS) is further passed into a series of automated rollers until the desired cross-section (such

square or rectangular hollow sections, RHS) is fulfilled (see e.g. Davison and Birkemoe, 1983; Rossi *et al.*, 2013). During cold-forming process, stress-strain behaviour of the virgin sheet (parent) material (identified with clearly defined and generally distinct yield point, followed by plateau region) has been observed to change to a rounded stress-strain material behaviour with a certain amount of strain hardening (see in Ringle, 1969; Afshan *et al.*, 2013). However, most of the contemporary international design codes do not incorporate the strength enhancement due to cold-forming and rely principally on the elastic-perfectly plastic stress-strain material model, which is usually applicable for hot-rolled steel section.

Further, unlike conventional hot-rolled sections, cold-formed tubular sections are usually thinner, possess excellent surface finish, associated with speedy production process and are generally accompanied with high strength and stiffness to weight ratios, as a result of forming process at ambient temperature (see Guo *et al.*, 2007; Cai *et al.*, 2019). With the advancement of cold-forming techniques, thicker steel sections up to 25 mm are now being manufactured, see Guo *et al.* (2007). In the steel market, besides the traditional cold-formed square, rectangular and circular hollow sections, interesting newer tubular sections such as **flat-oval** (Zhu and Young, 2012; Sachidananda and Singh, 2017); **elliptical** (e.g., Gardner and Chan, 2007; Chan and Gardner, 2008; Theofanous *et al.*, 2009b; Narendra and Singh, 2016); **semi-elliptical** (Silvestre *et al.*, 2013; Singh and Singh, 2019); **semi-oval** (Chen and Young, 2017, 2018b, 2018a) etc., have now been introduced.

1.1 POPULARITY OF TUBULAR STRUCTURES IN INDIA

In India, the construction industry has mainly been dominated by reinforced concrete structures, with limited steel structures. However, of late, a visible increase in the adoption of steel structures (especially cold-formed steel sections) has been observed, such as airport, shopping malls, stadia, railway platform sheds, skywalks, industrial buildings etc. Some examples are shown in Figures 1.2–1.5. Amongst the various constructional steels available in India (such as YSt-210, YSt-240, YSt-355 etc.), the YSt-310 cold-formed steel, conforming to IS 4923 (1997) with a nominal yield

strength of 310 MPa, a tensile strength of 450 MPa and minimum percentage elongation at failure of 10%, is one of the most widely used tubular structural steel. However, to the best of author's knowledge, detailed and reliable investigations on its material characteristics are found to be very limited (e.g. Arivalagan and Kandasamy, 2010) and not readily available, for ambient, elevated and post-fire temperatures. In addition, the structural performance of YSt-310 cold-formed steel tubular sections has not been reported so far, and no test data are available to assess the applicability of the currently available international design standards in the literature. It may be noted that, although, Tata Structura YSt-355, with nominal yield and tensile strengths of 355 and 490 MPa respectively, has been introduced recently by Tata Structura Tubes Division (2019); however it has not been readily available in the local market yet.

1.2 PERFORATED TUBULAR MEMBERS

In steel construction, perforations (or cut-outs or holes or openings) are provided on the structural members (beams and columns) to incorporate various modifications or needs such as hidden electrical and signal wirings, heating and cooling air-circulations, inspection and maintenance work (especially for bridges and towers), fresh and waste water plumbing; connection to other members; aesthetic appearance; material optimisation etc., (see details in Shanmugam, 1997; Shanmugam *et al.*, 1999; Shanmugam and Dhanalakshmi, 2001; Moen and Schafer, 2009; Pellegrino *et al.*, 2009; Moen and Schafer, 2011; Yao and Rasmussen, 2012; Ghazijahani *et al.*, 2014; Kulatunga *et al.*, 2014; Feng and Young, 2015; Feng *et al.*, 2016; Yao *et al.*, 2016 ; Sonu and Singh, 2017a etc.). However, the introduction of perforation in a tubular structural member can influence the load transfer mechanism. Due to this, redistribution of stresses can occur, thereby causing stress concentration and localised failure at the vicinity of the perforation (as detailed in Feng and Young, 2015; Yao *et al.*, 2016). A typical example of perforation made for providing electrical services is shown in Figure 1.6.

1.3 RESEARCH MOTIVATION

Based on the literature review (provided in **Chapter 2**), it has been observed that detailed and reliable investigations on the material characteristics of YSt-310 cold-formed steel tubular sections are very limited (e.g. Arivalagan and Kandasamy, 2010) and not readily available for ambient temperature. In addition, the structural performance of YSt-310 cold-formed steel tubular sections, at ambient temperature has not been studied so far and no test data are available.

The change in the properties of structural steel when exposed to elevated temperature is well documented in the literature, e.g., Outinen and Mäkeläinen (2004); Gunalan and Mahendran (2014); McCann *et al.* (2015); Chen *et al.* (2016); Liu *et al.* (2017a); Li and Young (2017a); Li and Young (2018) etc. However, for cold-formed steel tubular sections having nominal yield stress less than 460 MPa as per EC3-1-12 (2007), limited literature are available (Outinen *et al.*, 2001; Balarupan, 2015; McCann *et al.*, 2015; Imran *et al.*, 2018). Moreover, since the reduction factors proposed by past researchers are based on individual test results (and hence valid for specific campaign), the applicability of the previously proposed equations to YSt-310 cold-formed steel needs to be assessed; and thus the need for investigating the elevated temperature mechanical properties of this steel material is imperative.

In recent years, limited, but increasing research interests have been witnessed on the investigation of the residual post-fire mechanical properties of steel through tensile coupon tests. These studies were mainly focussed on deterioration of mechanical properties of different types of cold-formed steel (see e.g. Outinen and Mäkeläinen, 2004; Outinen, 2007; Gunalan and Mahendran, 2014; Wang *et al.*, 2014; Lu *et al.*, 2016; Huang and Young, 2017; Li and Young, 2018 etc.). From the literature review, it is found that limited post-fire studies were conducted on cold-formed steel tubular sections. It has also been observed that post-fire properties are depended on steel types (or grades). Moreover, it is seen that the predictive equations to determine the mechanical properties of steel structure after a fire event, proposed by previous

researchers are based on limited test data and hence there is a need to enrich the test database, so as to assess their suitability.

Further, it has been noted that an extensive research work has been reported from the late1950's, on steel plates (e.g. Ritchie and Rhodes, 1975; Shakerley and Brown, 1996; Shanmugam *et al.*, 1999; Cheng *et al.*, 2013); beams (e.g. Yu and Davis, 1973; Narayanan and Rockey, 1981; Sivakumaran and Zielonka, 1989; Shan *et al.*, 1994; Shan *et al.*, 1996; Moen, 2008; Chen and Cao, 2010; Feng *et al.*, 2017 and Sonu and Singh, 2017 etc.); and columns (e.g., Marshall and Nurick, 1970; Shanmugam *et al.*, 1999; Dhanalakshmi and Shanmugam, 2001; Moen, 2008; Moen and Schafer, 2011) demonstrating the reduction on member strength capacity due to presence of perforation. However, it has been evident that most of the published experimental and numerical studies focussed mainly on plates and open cold-formed steel sections, and an apparent lack of a systematic study on perforated rectangular tubular (closed) steel sections subjected to axial compression, can be seen.

1.4 OBJECTIVES

Based on the literature review (**Chapter 2**), three key objectives have been identified for the current research work. The primary objective of this thesis is to investigate the fundamental material characteristics of YSt-310 cold-formed steel so that it can contribute to the pool of experimental data for cold-formed steel tubular sections, and thus making them readily available to researchers and design engineers. The second objective is to investigate the structural performances of unperforated and perforated short columns through experimental and numerical (finite element) studies. The third objective is to assess the applicability of existing design standards and proposed equations, based on the test and finite element results.

1.5 OUTLINE OF THESIS

This chapter (**Chapter 1**) outlines a brief introduction on the overview of cold-formed steel tubular sections and their applications as a structural member in the construction

industry. Then, the popularity of tubular steel construction and presently available cold-formed steel material for structural application in India is presented. Further, the importance and the effect of perforations on the structural member are briefly presented. Finally, the research objective and outline of this thesis is described at the end of this chapter.

Chapter 2 describes a brief review of the literature that is relevant to the present research work. The motive of this chapter is to provide an overview of the important topics followed by possible gap areas, supported with appropriate literature, discussed at the relevant stages of this thesis work.

In **Chapter 3**, the ambient temperature material characteristics of YSt-310 cold-formed steel rectangular and square hollow sections such as elemental composition, metallographic structure, and mechanical properties have been investigated through various standard test methods. Key stress-strain parameters *viz*., Young's Modulus, proof stress, ultimate strength, percentage elongation, strain hardening exponent etc. have been computed from the stress-strain curves generated from tensile coupon tests. Elevated temperature mechanical properties of YSt-310 cold-formed steel have been studied through steady-state elevated temperature tensile coupon tests (**Chapter 3)**. A total of 31 tensile coupon tests have been performed at temperatures ranging from approximately ambient to 800 °C and the reduction factors of key material parameters have been estimated. Additionally, in **Chapter 3**, the post-fire mechanical properties of YSt-310 cold-formed steel tubular section have been studied through standard tensile coupon and microhardness tests at ambient temperature. Stress-strain curves, key material parameters and microhardness values, generated from the tests, have been analysed.

In **Chapter 4**, the structural performance of YSt-310 cold-formed steel tubular stub columns has been investigated through experimental and numerical programme. The extent of strength enhancement in the corner region due to cold-forming has been investigated using microhardness tests. A total of 12 stub column tests have been performed to investigate the cross-sectional capacity of YSt-310 cold-formed square

(SHS) and rectangular hollow section (RHS) stub columns. Using validated FE models (considering 3D laser scanner measured local geometric imperfections), a parametric study has been performed to study the performance of stub columns covering a wide range of cross-sectional slenderness. The column capacities generated from the test and FE models have been utilised to assess the accurateness of the current international guidelines for the design of cold-formed steel columns, such as European Standard, EC3-1-1 (2005); American standard, AISI S100-16 (2016) and design methods such as Continuous Strength Method (CSM); and modified Direct Strength Method (DSM) by Rossi and Rasmussen (2013) and Arrayago *et al.* (2017).

Chapter 5 presents an extension of the work highlighted in **Chapter 4**, by taking into account two opposite central circular perforations (of equal diameter) at mid-height of the column. A parametric study has been performed covering a wide range of cross-sectional slenderness and perforation diameters to width ratios, to study the effect of perforation sizes on the ultimate capacity of columns.

The final chapter (**Chapter 6**) presents a summary of the important findings from the research project as well as possible research areas that could be conducted in the future.

Figure 1.1: Melbourne Star, Melbourne (Source: www.unsplash.com/photos/5-VkAlkUrI0)

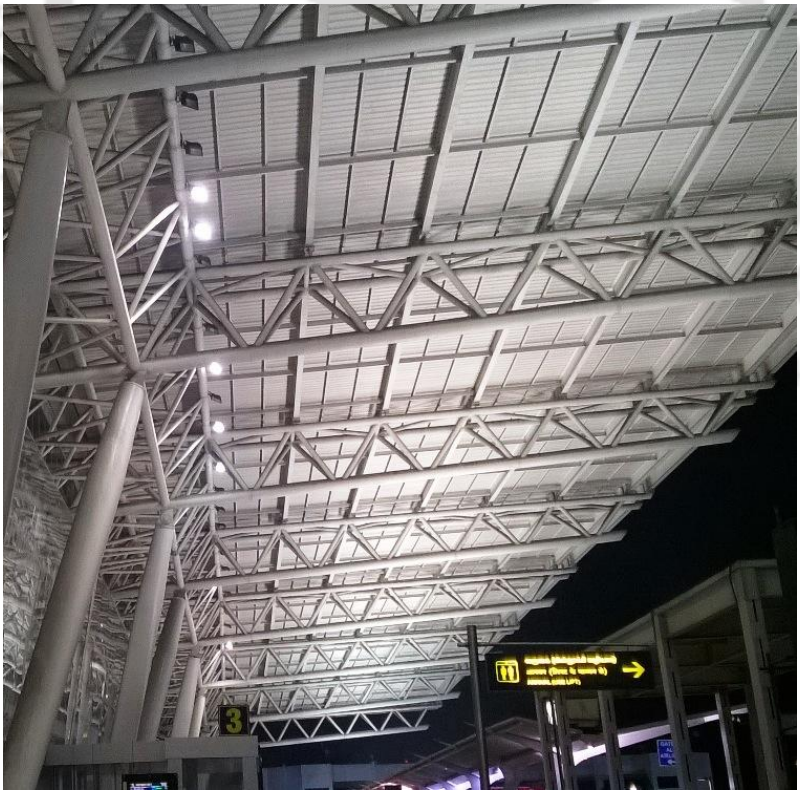

Figure 1.2: Chennai Airport, India

Figure 1.3: CIDCO Exhibition and Convention Centre, India (Image by www.iniinfraengineering.com/upload_image/55.jpg)

Figure 1.4: Jawaharlal Nehru Stadium, India (Courtesy: Tata Structura Tubes Division, Kolkata)

Figure 1.5: Chhatrapati Shivaji International Airport, India (Courtesy: Tata Structura Tubes Division, Kolkata)

Figure 1.6: Perforation provided for electrical services

Chapter 2

Literature review

2.1 INTRODUCTION

This chapter has been divided into three major broad subject areas and presents an outline on the previous research works conducted on the performance analysis and design aspects of cold-formed steel tubular sections, by providing concise literature review for each subject area, pertinent to this thesis. Firstly, earlier research works on the mechanical properties of YSt-310 cold-formed steel tubular section are briefly reviewed. Secondly, a summary of the previous research works on the investigation of the cross-sectional capacity of YSt-310 cold-formed steel tubular stub columns has been presented, including test and numerical programs, codified design expressions and design proposals recommended in the literature. This is followed by a brief review on the structural performance of perforated cold-formed steel tubular stub columns conducted previously (both experimental and numerical investigations) and relevant design approaches, recommended in the literature. Based on the literature review, research gaps are then identified in the analysis and design of cold-formed steel tubular sections.

2.2 MATERIAL PROPERTIES

For the analysis and design of structural steel members, mechanical characteristics and key material design parameters, *viz*., Young's Modulus, yield stress, tensile stress, elongation at fracture etc. need to be ascertained (both at ambient and elevated temperatures, as well as at ambient temperature after being exposed to elevated temperature i.e. post-fire stage). These important material design parameters are generally estimated *via* relevant standard tensile coupon tests (e.g., Key *et al.*, 1988; Gardner *et al.*, 2010; Afshan *et al.*, 2013; Becque and Wilkinson, 2017). In this section, a brief review of the previous work on the estimation of mechanical properties of cold-formed steel tubular sections at various temperatures, *viz*., ambient temperature, elevated temperature and post-fire conditions are presented.

2.2.1 Material properties at ambient temperature

Extensive researches on the ambient temperature mechanical properties of various grades of cold-formed steels – Low strength steel, i.e., having yield stress, f_y < 460 MPa (e.g. **Q235** by Liu *et al.*, 2017a; **S235** by Gardner *et al.*, 2010; **SM490** by Kim *et al.*, 2014; **S355** by Zhang *et al.*, 2016; **C450** by Becque and Wilkinson, 2017 etc.); high-strength steel, 460 MPa < f_y < 690 MPa (e.g. **G500** and **G550** by Rogers and Hancock, 1997; **S650** by Tran *et al.*, 2016; **Q690** by Qing and Bin, 2013 etc.); and ultra-high strength steel, f_y > 690 MPa (e.g., **HSA800** by Kim *et al.*, 2014; **S900** by Li and Young, 2017b; **S960** by Li *et al.*, 2019, **S1100** by Ma, 2016, **VHS1350** by Zhao, 2000 etc.) have been conducted as part of estimation of member performances, previously. However, to the best of author's knowledge, detailed and reliable investigations on the material characteristics of YSt-310 cold-formed steel are found to be very limited (e.g. Arivalagan and Kandasamy, 2010) and not readily available in the public domain, particularly for researchers and designers. Arivalagan and Kandasamy (2010) reported the tensile test results of 'three' coupons extracted from the flat regions of SHS having nominal cross-sectional dimensions of 72.0 × 72.0 × 3.2; however details of important material parameters such as elastic modulus, Ramberg–Osgood parameter or strain hardening exponent etc., have not been

reported. Therefore, a systematic study, on the mechanical property of YSt-310 cold-formed steel tubular sections, is necessary to develop a reliable material database.

2.2.2 Material properties at elevated temperature

The change in the properties of structural steel when exposed to elevated temperature is well documented in the literature, e.g., Outinen and Mäkeläinen (2004); Chen *et al.* (2006); Outinen (2007); Chen and Young (2007); Kankanamge and Mahendran (2011); Ye and Chen (2012); Huang and Young (2014a); Wang *et al.* (2014); Gunalan and Mahendran (2014); McCann *et al.* (2015); Chen *et al.* (2016); Liu *et al.* (2017a); Winful *et al.* (2017); Li and Young (2017a); Imran *et al.* (2018); Li and Young (2018); Liang *et al.* (2019) etc. Since, the focus of present study is to evaluate the elevated temperature mechanical properties of low strength steel such as YSt-310, a brief review on past works pertinent to the current study, particularly low strength steel, (i.e. having nominal yield stress less than 460 MPa as per EC3-1-12, 2007), has been presented herein.

Outinen *et al.* (2001) studied the mechanical properties of structural steel S355J2H at elevated temperature, through steady state tensile coupon tests extracted from three dissimilar (SHSs. Details of test setup and results were presented in this research report. Based on the test results, the enhancement in the yield strength due to cold-forming was found to retain for elevated temperatures up to 600 °C whilst the effect vanished thereafter.

Elevated temperature mechanical properties of four different SHSs made of grade 450 were estimated by Balarupan (2015). Based on the study, strength and stiffness reduction factors were proposed, as the predictions of European code, EC3-1-2 (2005), American Specification, AISC 360 (2010) and Australian Standards, AS 4100 (1998) as well as those proposed by Chen and Young (2007); and Kankanamge and Mahendran (2011) were found to be unsuitable.

McCann *et al.* (2015) conducted material tests on three cold-formed steel sections, namely circular (CHS), square (SHS) and rectangular (RHS) hollow sections of S355J2H steel grade at both steady and transient state fire conditions. It was reported that the reduction factors provided in the European Standard, EC3-1-2 (2005) and Australian Standard, AS 4100 (1998) which are based on hot-finished material were found to be still suitable for cold-formed steel tubular sections.

Imran *et al.* (2018) studied the elevated temperature mechanical properties of cold-formed steel SHS, RHS and CHS of grade 350 *via* tensile coupon tests. It was reported that the reduction factors predicted by design codes AS 4100 (1998); BS 5950 (2003); EC3-1-2 (2005); and AISC 360 (2010) as well as existing proposal from the literature Chen and Young (2007); Kankanamge and Mahendran (2011); and Balarupan (2015) were either unsafe or overly-conservative for cold-formed steel tubular sections. Further, a set of design equations for yield strength; stress at 2.0% strain; elastic modulus and ultimate strength reduction factors was proposed.

From the above brief literature review, it is seen that limited studies on elevated temperature mechanical properties of cold-formed steel tubular sections have been reported (see summary in Table 2.1). Additionally, it may be noted that the conclusion made by McCann *et al.* (2015) on the applicability of reduction factors of hot-rolled sections to cold-formed sections, based on comparison of test reduction factors with existing fire design codes was found to be contradictory to those made by Balarupan (2015) and Imran *et al.* (2018). This may be due to the difference in manufacturing processes of these sections, although the coupons were cut from similar cross-sectional geometry; and unavailability of extensive test data for assessment. Moreover, since the reduction factors proposed by past researchers are based on individual test results (and hence valid for specific campaign), the applicability of the previously proposed equations to YSt-310 cold-formed steel needs to be assessed.

2.2.3 Material properties after post-fire

Now, as post-fire properties of structural members become more important to rehabilitation structural engineers, increased focussed attentions have been drawn towards post-fire researches (e.g., Qiang *et al.*, 2012b; Qiang *et al.*, 2013; Wang *et al.*, 2014; Gunalan and Mahendran, 2014; Wang *et al.*, 2015; Chen *et al.*, 2016; Lu *et al.*, 2016; Lu *et al.*, 2017a; Huang and Young, 2017; Liu *et al.*, 2017b; Li and Young, 2018; Azhari *et al.*, 2018; Kesawan and Mahendran, 2018 etc.). In the recent years, limited, but increasing research interests have been witnessed on the investigation of the residual post-fire mechanical properties of steel through tensile coupon tests. These studies were mainly focussed on deterioration of mechanical properties of different types of steel e.g. cold-formed steel (e.g. Outinen and Mäkeläinen, 2004; Outinen, 2007; Gunalan and Mahendran, 2014; Wang *et al.*, 2014; Lu *et al.*, 2016; Huang and Young, 2017; Li and Young, 2018 etc.); hot-rolled steel (e.g., Smith *et al.*, 1981; Kirby *et al.*, 1986; Ding *et al.*, 2006; Zhang *et al.*, 2009; Chen and Cao, 2010; Qiang *et al.*, 2012b; Lee *et al.*, 2012; Qiang *et al.*, 2013; Wang *et al.*, 2015; Lu *et al.*, 2016; Liu *et al.*, 2017b; Tao *et al.*, 2018; Gao *et al.*, 2018 etc.); cast steel (e.g. Lu *et al.*, 2017b); reinforcing steel (e.g., Dias 1992; Neves *et al.*, 1996; Nikolaou and Papadimitriou, 2004; Felicetti *et al.*, 2009; Tao *et al.*, 2012 etc.) and pre-stressing wire (e.g., Lu *et al.*, 2017a) with different grades of steel and cooling methods or rates after being heated to predetermined elevated temperature. In this section, a brief overview of previous studies on post-fire material properties of cold-formed steel is presented.

Outinen and Mäkeläinen (2004) and Outinen (2007) investigated the residual mechanical properties of S355 cold-formed steel at room temperature extracted from sub columns tested at high temperature. The post-fire yield strength was found to be more than the nominal yield strength, although significant reduction in the yield strength was observed as compared to that of room temperature yield strength value, after being exposed to elevated temperature. The elastic modulus was found to be fluctuating as the exposed temperature increases.

Lu *et al.* (2016) conducted an experimental investigation to study the post-fire mechanical behaviour of cold-formed (Q235) steel after being heated to pre-determined elevated temperatures. Additionally, the effect of multiple heating-cooling cycles (three cycles through air cooling method) on the mechanical properties of steel was also studied. The test results revealed that cold-formed steels were more sensitive to heating and cooling processes than hot-rolled steels. Cold-formed steels were able to regain 65% and 85 % of parent (unheated) yield strength and tensile strength respectively, after being exposed to 800 °C. The effect of cyclic heating and cooling methods on the mechanical strength of hot-rolled steel was observed to be insignificant.

Kesawan and Mahendran (2018) undertook a study on the post-fire mechanical properties of cold-formed steel of grade G350 and G450. Based on the tensile coupon test results, it was observed that the reduction in the post fire yield and tensile strength was found to remain unaffected when the exposed temperature was below 300 °C, whereas, for elastic modulus it was 500 °C. These steel were able to regain about 60% and 65% of their ambient temperature yield and tensile strengths respectively, after being exposed up to 800 °C.

From the brief literature review presented above, it can be seen that limited post-fire studies were conducted on cold-formed steel tubular sections (summarised in Table 2.2). It has also been observed that, post-fire properties are depended on steel types (or grades). Moreover, it is also seen that the predictive equations to determine the mechanical properties of steel structure after a fire event, proposed by previous researchers are based on limited test data and hence there is a need to enrich the test database, so as to assess their suitability.

2.3 STUB COLUMNS

Stub column is a compression member, that are made in such a way that the member is long enough to retain the representative distribution of residual stresses and local geometric imperfection, but short enough to avoid global buckling before the yield

load is reached (see in Yu and Tall, 1969; Rasmussen and Hancock, 1995; Yang and Hancock, 2004; Theofanous and Gardner, 2009; Gardner *et al.*, 2010; Saliba and Gardner 2013; Wang *et al.*, 2017 etc). Stub column tests are generally performed for various reasons, e.g., i) to estimate the average stress-strain curve of the complete cross-section which takes into account the effect of residual stresses and strength enhancements (both in the corner and flat regions due to cold-forming), ii) to establish a relationship between cross-sectional slenderness and ultimate column capacity of steel cross-sections, iii) to study local buckling behaviour of compression members etc. (see Yu and Tall, 1969; Hancock and Zhao, 1992; Chan and Gardner, 2008; Huang and Young, 2012; Wang *et al.*, 2017 etc.). The following sections reviews the literature related to unperforated and perforated stub columns (subjected to pure compression). Further, in each of the sections, reviews of some of the available pertinent design rules and methods are also summerised.

2.3.1 Unperforated stub columns

The main idea behind cross-sectional classification of members under pure compression is to estimate the extent of cross-sectional resistance, before which the member is failed by local buckling, in the elastic range. Cross-sections are considered to be in the Class 1–3, if their ultimate load is able to attain the yield load (squash load) before failure, whereas those failed to attain the yield load due to local buckling are considered to be in the Class–4 cross-section (see in Chan and Gardner 2008; Wang *et al.*, 2017). Extensive experimental and numerical studies have been performed previously for various tubular cross-sections such as **square/rectangular** (e.g., Theofanous and Gardner 2009; Hu *et al.* 2011; Ma *et al.*, 2016 etc.), **circular** (e.g., Zhao (2000); Ma *et al.*, 2016 etc.), **elliptical** (e.g., Chan and Gardner, 2008; Zhao and Packer, 2009; Chan *et al.*, 2010; Cai *et al.*, 2019; Chen and Young, 2019 etc.), **flat-oval** (Zhu and Young, 2011; Sachidananda and Singh, 2015), **semi-oval** (Chen and Young, 2018c; Chen and Young, 2018a), **welded/fabricated box sections** (Yang and Hancock, 2004; Kim *et al.*, 2014; Shi *et al.*, 2015; Li *et al.*, 2019), **polygonal cross-sections** (e.g., Aoki *et al.*, 1991; Godat *et al.*, 2012) etc., to establish the cross-sectional slenderness limit, considering various steel materials such as **low**

strength steel (Chen and Young 2019), **high strength steel** (Rasmussen and Hancock 1992; Ma *et al.*, 2016), **ultra-high strength steel** (Zhao *et al.*, 2004; Shi *et al.*, 2015), **austenitic grade EN 1.4301** (SHS, RHS and CHS) by Gardner (2002) etc. As of now, to the best of author's knowledge, no experimental investigations on the structural performance of YSt-310 cold-formed steel tubular stub column have been reported and also the applicability of the cross-sectional classification presented in design codes (e.g., EC3-1-1, 2005) has not been assessed yet.

2.3.1.1 Design rules

Country specific design standards/codes are established by various nations (such as European, American, Chinese, Canadian, Japanese, Australian, Indian etc.) for safe and reliable design of various constructional materials, *viz*., wood, reinforced concrete, steel, steel concrete composite etc. In this section, a short introduction of globally excepted and widely used steel design codes (such as European, American standards) for cross-sectional classification and also for member capacity of stub columns are presented.

2.3.1.1.1 European Standard

The European Standard, EC3-1-1 (2005) or EN 1993-1-1 (2005), was published in 2005, by the European Committee for Standardisation (CEN), superseding the previous standard DD ENV 1993-1-1 (1992), introduced in 1992. EC3-1-1 (2005) forms the Part 1.1 of Eurocode 3: Design of Steel Structures – General Rules and Rules for Buildings. Currently, EC3-1-1 (2005) has been revised and superseded by EN 1993-1-1:2005/A1 (2014), published in 2014 (amendment only). In the newly amended design standard, i.e., EN 1993-1-1:2005/A1 (2014), the cross-section classification limits (e.g., '33' for Class–1, '38' for Class–2, '42' for Class–3 etc.) are not changed.

In addition, the European Standard, EC3-1-5 (2006) or EN 1993-1-5 (2006) covers guidelines for calculation of effective widths for Class 4 cross-sections. EC3-1-5 (2006) forms the Part 1.5 of Eurocode 3: Design of Steel Structures – Plated Structural

Elements. The design standard has been further amended in 2017 and entitled as EN 1993-1-5:2006/A1 (2017). The newly amended design standard, EN 1993-1-5:2006/A1 (2017) has made certain modification in the Subclause 4.4, where local slenderness calculation formula (presented in Equation 4.2) has been changed to a generalised equation considering the effect of stress ratio, ψ. However, the equation for calculation of reduction factor of internal compression elements remains the same (i.e. unchanged) with the expression detailed in EC3-1-5 (2006).

2.3.1.1.2 American Standard

The first American Iron and Steel Institute (AISI) specification for design cold-formed steel members was introduced in 1946, mainly based on the work done led by Professor George Winter in 1939-1946. The AISI standard, AISI S100-16 (2016), entitled 'North American Specification for the Design of Cold-Formed Steel Structural Member'; published in 2016 serves as the latest design standard superseding all design specifications previously published. This design provision supports various design philosophies, namely Limit State Design (LSD) and Load and Resistance Factor Design (LRFD); and Allowable Stress Design (ASD) by providing appropriate resistance and safety factors respectively. In this latest design specification, Direct Strength Method (DSM), which was previously included in Appendix 1 of the 2012 Edition, is now incorporated in Chapter E of this specification, allowing users to estimate design strength of axially compressive members (undergoing local buckling) either through Effective Width Method (EWM) or Direct Strength Method (DSM), which are discussed in Section 2.3.1.2 below.

2.3.1.2 Design Methods

2.3.1.2.1 Effective Width Method

The concept of 'Effective Width or Unified Effective Width' is the fundamental notion behind Effective Width Method (EWM) and it was introduced for the first time by Karman *et al.* (1932), to estimate the ultimate load-carrying capacity of long square thin plates loaded with compressive stress on the two opposite edges of the plate.

Based on this concept, the stress distribution across the entire width is assumed to be carried by two strips (total of the two strip widths being the 'effective width') and the stress is considered to be uniformly distributed in the effective width of the plate. However, experimental results showed that the theoretical effective width formula derived by Karman *et al.* (1932) was found to be suitable for thin plates, but over-estimated for thick (stockier) plates. Therefore, the formulae have been modified by various researchers such as Frankland (1940); Winter (1947); Dwight (1969); Lind *et al.* (1971); Faulkner (1975); Vilnay and Rockey (1981); and Hansen *et al.* (2010) etc. Of the various modified expressions, the proposal made by Winter (1947) is the most widely used equation. Presently, the modified version of Winter (1947), which takes into account of stress gradient in both stiffened and unstiffened plates (e.g., Kalyanaraman *et al.*, 1972; Kalyanaraman and Pekoz, 1978; Desmond *et al.*, 1978; Desmond *et al.*, 1981b; Desmond *et al.*, 1981a etc.), geometric imperfection and residual stress (e.g., Liew *et al.*, 1989) as well as plates with perforations (e.g. Yu and Davis, 1973; Ortiz-Colberg, 1981; Miller and Peköz, 1994 etc.), has been adopted in many design standards such as European, American and Australian standards.

2.3.1.2.2 Direct Strength Method

Direct Strength Method (DSM) was developed by Schafer and Peköz (1998b) to eliminate the limitations in finding the cross-sectional area using Effective Width Method (EWM) which are being utilised in the traditional design codes (as mentioned in Section 2.3.1.2.1). The DSM is straight forward and capable of designing complex cross-sections which may be difficult or not possible for EWM. DSM has been included in AISI S100-16 (2016) for design of cold-formed carbon or low alloy steel structural members. DSM relies on the estimation of elastic local, global and distortional buckling stress using numerical tools such as finite strip method software, CUFSM (see in Schafer and Ádány, 2006) or finite element method (FEM) (e.g. using Abaqus (2010). The estimated stresses are combined with the yield stress to estimate a non-dimension parameter called cross-section slenderness (λ) and the strength curve is developed to predict the capacity of a member. DSM predicts the member capacity based on its full cross-section slenderness unlike effective width method which

predicts section capacity based on the most slender constituent element. The DSM has also been extended cold-formed stainless steel sections, based on the research work conducted by many researchers (e.g., Lecce, 2006; Lecce and Rasmussen, 2006; Becque *et al.*, 2008; Rossi *et al.*, 2009).

DSM provision implemented in AISI S100-16 (2016) and its earlier editions does not account for the strain hardening effects in the design of short/stocky cross-sections. Design predictions using DSM for short (stocky) columns show a great degree of conservativeness. To improve the column capacity prediction at low slenderness range (i.e. for stocky cross-sections), Rossi and Rasmussen (2013) replaced the classical horizontal yield limit by a linear expression relating cross-section slenderness, ultimate stress and proof stress, for stainless steel sections. Further, Arrayago *et al.* (2017) proposed a full-range DSM curve based on carbon steel strength curve with few modifications but following a similar procedure proposed by Rossi and Rasmussen (2013). The applicability of such proposed modified equations needs to be assessed for cold-formed carbon steel tubular sections.

2.3.1.2.3 Continuous Strength Method

Continuous Strength Method (CSM) is a deformation-based design approach, introduced by Gardner (2002, 2008) and his co-workers. CSM allows material strain hardening (generally observed for stocky/non-sender stainless-steel cross-sections, i.e., Class–1, 2 and 3 sections) benefits to be rationally exploited. The design method relies on bilinear stress-strain material model, approximating the rounded material characteristic seen in cold-formed and stainless sections. On the other hand, the present design standards for cold-formed carbon steel do not account for strain hardening behaviour, instead followed the idealised linear-perfectly plastic material model, thereby resulting in overly conservative and scattered predictions for compressive cross-section, at lower cross-section slenderness range (see Zhao *et al.*, 2017). In CSM, the cross-sectional classification to handle local buckling has been replaced by a 'base curve', derived from stub column and beam tests data of carbon steel, stainless steel, aluminium sections, to set a continuous relationship between

cross-section slenderness and deformation capacity. Over the last decade, the applicability of CSM, which was originally developed for the design of non-slender stainless steel plated sections (e.g., Gardner, 2002; Afshan and Gardner, 2013) has been refined and extended to wider cross-sections (e.g., Ahmed *et al.*, 2016; Zhao *et al.*, 2017), structural loading conditions (e.g., Afshan and Gardner, 2013; Liew and Gardner, 2015; Zhao *et al.*, 2015b; Arrayago and Real, 2015; Zhao *et al.*, 2015a etc.) as well as various constructional materials such as cold-formed steel (e.g., Zhao *et al.*, 2017; Yun and Gardner, 2018), high-strength steel (e.g., Zhao *et al.*, 2017), aluminium (see Su *et al.*, 2014; Su *et al.*, 2016), composite (such as Gardner *et al.*, 2017; Yang *et al.*, 2018) etc. However, it is seen that, the applicability of CSM for cold-formed carbon low-yield steel (such as YSt-310) hollow sections have not been reported, so far.

2.3.2 PERFORATED STUB COLUMNS

Perforations (or cut-outs or holes or openings) are provided on the structural members (beams and columns) to incorporate various modifications or needs such as hidden electrical and signal wirings, heating and cooling air-circulations, inspection and maintenance work (especially for bridges and towers), fresh and waste water plumbing, connection to other members; aesthetic appearance; and material optimisation (see Shanmugam, 1997; Shanmugam *et al.*, 1999; Shanmugam and Dhanalakshmi, 2001; Moen and Schafer, 2009; Pellegrino *et al.*, 2009; Moen and Schafer, 2011; Yao and Rasmussen, 2012; Ghazijahani *et al.*, 2014; Kulatunga *et al.*, 2014; Feng and Young, 2015; Feng *et al.*, 2016; Yao *et al.*, 2016; Sonu and Singh, 2017a etc.). However, introduction of perforation in a tubular structural member can influence the load transfer mechanism. Due to this, redistribution of stresses can occur, thereby causing stress concentration and localised failure at the vicinity of the perforation (see Feng and Young, 2015; Yao *et al.*, 2016).

Extensive research work on the effects of perforation, have been reported since the late1950's, on steel plates (e.g., Kumai, 1951; Schlack, 1964; Vann, 1971; Ritchie and Rhodes, 1975; Narayanan and Chow, 1984; Larsson, 1987; Shakerley and Brown,

1996; Ko, 1998; Shanmugam *et al.*, 1999; Kim *et al.*, 2009; Cheng *et al.*, 2013; Saad-Eldeen *et al.*, 2016 etc.) and beams (e.g., Yu and Davis, 1973; Narayanan and Rockey, 1981; Sivakumaran and Zielonka, 1989; Schuster, 1992; Shan *et al.*, 1994b; Shan *et al.*, 1994a; Shan *et al.*, 1996; Liu and Chung, 2003; Moen, 2008; Lagaros *et al.*, 2008; Zhou and Young, 2010; Uzzaman *et al.*, 2012; Lian *et al.*, 2017; Wang and Young, 2017; Feng *et al.*, 2017; Sonu and Singh, 2017a etc.), and columns (e.g., Marshall and Nurick, 1970; Shanmugam *et al.*, 1999; Pu *et al.*, 1999; Shanmugam and Dhanalakshmi, 2001; Dhanalakshmi and Shanmugam, 2001; Moen and Schafer, 2008; Shariati and Rokhi, 2008; Moen and Schafer, 2011; Yao and Rasmussen, 2012; Umbarkar *et al.*, 2013; Feng and Young, 2015; Yao and Rasmussen, 2016; Feng *et al.*, 2016; Yao *et al.*, 2016 etc.), demonstrating the reduction on member strength capacity due to presence of perforations.

Marshall and Nurick (1970) studied the symmetric progressive buckling load of thin-walled mild steel square tubes (seam welded) with circular perforations. Two opposite central circular perforations having different diameters (perforation diameter to flat-width ratios ranges from 0.35 to 0.83) were drilled on the specimens. The perforated tubes were tested under quasi-static load with a displacement rate of 5.08mm/min and the ultimate loads were estimated. Based on the test results, a linear decrease in the ultimate buckling load as the perforation diameter increases was reported.

Yu and Davis (1973) studied the buckling and post-buckling behaviour of cold-formed steel members having square and circular perforations for stiffened and circular perforations for unstiffened elements, through experimental and analytical investigations. For a member with stiffened elements, the reduction in buckling load of elements having square perforations was found to be more affected as compared with those with circular perforations, although they have approximately the same post-buckling loads for similar perforation widths. Further, an equation to estimate effective design width for stiffened elements (based on Winter and Pian, 1946) and a separate set of equations for critical buckling stress for perforated unstiffened compression elements were also proposed (based on AISI, 1968).

Ortiz-Colberg (1981) conducted a series of compression test on cold-formed steel perforated intermediate and long stub channel columns (having cross-section slenderness ratio ≤ 70.0 and perforation size ratio ≤ 0.5). It was observed that, the increase in diameter of circular perforation based on the depth of web decreased the ultimate column capacity. However, the effect of single circular perforation at mid-height of intermediate and long columns on the ultimate capacities was found to be insignificant. Further, a modified effective width formulae (in the format proposed by Winter, 1947) was developed based on the test results, and has now been incorporated in AISI Specifications (e.g., AISI S100-16, 2016) for the design of cold-formed steel structural members.

Pu *et al.* (1999) studied the local buckling behaviour of symmetrically perforated lipped-channel columns through experimental and analytical investigation. The study comprised of an extensive stub column tests made from lipped-channel sections and the influence of size, position and aspect ratio of rectangular perforations on the ultimate strength of columns were explored. Based on the experimental results, it was observed that the strength of a thin channel column could be severely reduced for perforations located in the effective area; however, for perforations located in the ineffective area, the strength was found to be hardly affected. In addition, it was also observed that the effect of aspect ratio of rectangular perforation on the ultimate capacity is ineffective.

A numerical investigation on the post-buckling behaviour and ultimate capacity of the centrally perforated square plate was performed by Shanmugam *et al.* (1999). The study covered various key parameters such as plate slenderness, perforation shape and size, boundary condition to the perforated plate and nature of loading. Based on the finite element (FE) analysis results, parameters such as perforation size and plate slenderness ratio were found to have a significant effect on the ultimate capacity of perforated plates. Moreover, the ultimate capacities of plates with circular perforations were observed to be higher than those with square perforations. Finally, based on best-fit regression analysis on the numerical data, a simplified design

formula to predict the ultimate load capacity of perforated plates, as a function of plate slenderness and opening size, was established.

Ultimate load capacity of perforated equal-angle stub columns, having both single and multiple perforations of flat-oval shape, were determined experimentally and numerically by Dhanalakshmi and Shanmugam (2001). Test results have shown that the reduction in ultimate capacities was ~ 50% for 60% perforation size ratio, whereas the effect was found to be negligible for 20% perforation size ratio. Further, using validated FE models; parametric study was performed covering wider range of cross-sectional slenderness ratio and perforation sizes. Finally, a design equation was proposed, using two non-dimentional parameters: *viz*., plate slenderness and opening size ratio, to compute the load capacity for perforated equal-angle stub columns (irrespective of perforation shape) based on the test and FE results.

Shanmugam and Dhanalakshmi (2001) conducted a numerical study on the ultimate column capacities of perforated cold-formed steel channel stub columns. Validated FE models were employed for parametric study covering important parameters such as cross-section slenderness (slenderness ratio ranges from 29.3 to 133.7), perforation size (perforation size ratio ranging from 0.0 to 0.6), perforation shapes (square, circular and manufacturer's precut shapes), as well as stub columns having single or multiple perforations. Using the FE results, a design equation was developed in a similar form as those proposed by authors previously (Dhanalakshmi and Shanmugam, 2001) for perforated channel stub columns.

Moen and Schafer (2008) demonstrated the reduction in post-peak ductility, and observed that the influence on ultimate strength due to the introduction of slotted perforations in lipped channel stub columns was found to be minimal. Using 78 test and 213 FE column strength data, Moen and Schafer (2011) modified the DSM given in North American Specification (AISI S100-07, 2007), for perforated cold-formed steel columns into six different options. Among the six design options, the Design Option 4 (wherein the local buckling capacity was limited to net area based yield capacity) was later adopted in North American Specification (AISI S100-16, 2016).

Yao and Rasmussen (2012) studied inelastic stress distributions, load transfers and failure modes on perforated plates and C-section columns in compression by considering parameters such as perforation shapes, sizes and spacing using isoparametric spline finite strip method (ISFSM). Based on the ISFSM analysis results, it was concluded that perforation shape has marginal influence on the ultimate capacity of columns.

Feng and Young (2015) conducted a series of tests on high strength aluminium alloy SHS stub columns with central circular perforations. Based on the comparison of perforated cold-formed carbon steel column design predictions (e.g. Miller and Peköz, 1994; Shanmugam *et al.*, 1999; Dhanalakshmi and Shanmugam, 2001; AISI S100-16, 2016) with test results, and it was concluded that the design equations was found to be inappropriate for the design of aluminium alloy stub columns with central circular perforations.

Feng *et al.* (2016) investigated the effect of perforation size and number of perforations on the ultimate strength of aluminium alloy CHS columns. The appropriateness of available design equations for aluminium (such as Aluminum Design Manual, 2005; GB 50429, 2007; EC9-1-1, 2007 and perforated steel structural members, (e.g., Shanmugam *et al.*, 1999; Shanmugam and Dhanalakshmi, 2001; Dhanalakshmi and Shanmugam, 2001; AISI S100-16 2016 etc.), were examined based on perforated aluminium circular column test data. It was observed that Chinese aluminium code GB 50429 (2007) and effective area method (in which the effective area is calculated by deducting the perforated area from the gross area of CHS) of cold-formed steel design rules in AISI S100-16 (2016) for perforated structural members was found to be more suitable for the design of perforated aluminium alloy CHS columns.

Yao *et al.* (2016) conducted a comprehensive parametric study to assess the effects of perforation parameters such as perforation sizes and spacings, on the load capacities of open cross-sections (e.g., channel, rack, hat sections etc.). Further, the accurateness of design formulae of DSM detailed in AS/NZS 4600 (2005), Design Option 4

proposed by Moen and Schafer (2011) and 2 out of 19 design options proposed by Yao and Rasmussen (2014) based on the column strength data from Yao *et al.* (2016) were evaluated in the companion paper (Yao and Rasmussen, 2016) and concluded that the Proposed Method 2 (which is a modification to DSM available in AS/NZS 4600, 2005) by Yao and Rasmussen (2014) is found be the best method.

It has been noticed that, although comprehensive researches have been reported on the reduction of load capacity due to the presence of perforation, considering various key parameters such as perforation sizes, shapes, locations etc., and developed design equations to predict member capacity of perforated structural steel columns, most of the published experimental and numerical studies have been found to focus mainly on plates and open cold-formed steel sections. It may be noted that the perforation diameter to flat width ratio, in publicly available design standard such as AISI S100-16 (2016) for cold-formed carbon steel is limited to 0.5. However, up to best of author's knowledge, there is an apparent lack of a systematic study on perforated rectangular tubular (closed) steel sections subjected to axial compression.

2.3.2.1 Design rules

2.3.2.1.1 American Standard

Design formulae are provided in North American Specification (NAS), AISI S100-16 (2016) to estimate the column capacity of cold-formed steel structural members with circular perforations, which are based on EWM and DSM. The effective width formulae for uniformly compressed stiffened elements with circular perforation, detailed in Appendix 1 of AISI S100-16 (2016), is based on the research work conducted by Ortiz-Colberg (1981); whereas, the modified direct strength method for estimation of nominal axial strength for local and distortional buckling of perforated (holes) member in compression (presented in Chapter E of AISI S100-16, 2016) is based on work of Moen and Schafer (2011). Although, a brief description of the development of design equation for perforated steel members in recent years has been presented above, more details to estimate the member capacity of perforated stub columns are covered and assessed in **Chapter 5** of this thesis.

2.3.2.1.2 Design formulae by Miller and Peköz (1994)

A simplified design approach for the treatment of perforations in plates was presented by Miller and Peköz (1994), based on the experimental and analytical investigations of local buckling behaviour of cold-formed steel lipped-channel sections with rectangular perforation in the web. Based on this approach, the effective width of a perforated web is estimated based on the effective design width of unperforated web and size of perforation. In particular, if the size of perforation is smaller than the uneffective portion of web, the effect of perforation is ignored. However, if the perforation size is extended towards the effective design width region of unperforated web, then the effective width of the perforated web is estimated by subtracting the perforation size from the unstiffened plate element width. In Chapter 5, a detailed description and comprehensive evaluation of this approach is presented.

2.4 3D SCANNING AND EVALUATION OF LOCAL GEOMETRIC IMPERFECTIONS

It is well known that, the resistance of a structural member is greatly influenced by the amplitude and distribution of geometric imperfection (see Cruise and Gardner, 2006; Zhao *et al.*, 2015d; Zhao *et al.*, 2015c; Jia-Lin *et al.*, 2016; Arrayago *et al.*, 2017 etc.). Geometric imperfections are introduced right from the manufacturing process due to their thin-walled nature although they were produced within specified tolerance limit (provided in various national guidelines). The tubular sections are transported, stored and then fabricated at the construction site or workshops. During these stages, geometric imperfections in the form of undulations or bends are introduced on the surface or member as a whole. Measurement of local geometric imperfection were performed as a part of experimental programme by various researchers, e.g., Schafer and Peköz (1998a); Young and Lui (2005); Theofanous and Gardner (2010); Huang and Young (2012); Zhao *et al.* (2015c) etc. Ellobody and Young (2005a) and Young and Lui (2005) etc., measured local imperfection amplitude using coordinate measuring machine having accuracy of 0.001 mm. Additionally, researchers such as Schafer and Peköz (1998a); Theofanous and Gardner (2010); Zhao *et al.* (2015c); Ma

et al. (2016); Wang *et al.* (2017) etc., used linear variable displacement transducers (LVDTs) which were attached to the head of a milling machine to measure initial geometric imperfection at centreline along the length of untested specimen which was firmly fasten on a flat bed. Besides, Cruise and Gardner (2006) used an array of displacement transducers fixed on a carriage which can be driven on a vertical guiding and measured imperfection amplitudes of a specimen which was hung adjacent to the guide rail. Furthermore, Huang and Young (2012) used a dial gauge of accuracy 0.001 mm to measure imperfection amplitude at mid-length of the specimen, considering zero imperfection at the corners. It is worth mentioning that most of the methods detailed above utilised single or multipoint descrite contact-measurement techniques, which may be applicable to relatively flat surfaces; however, the technicques are generally time consuming and involve tedious measurement process; and may also generate limited data points. In the last few years, some researchers, e.g., Zhao *et al.* (2015d); Tran *et al.* (2016); Wang *et al.* (2017) etc., have started using non-contact laser scanner and transducer to extract imperfection information based on full three dimensional (3D) profile of the specimen. As compared to conventional imperfection measurement techniques, the 3D laser scanning methods are quick, easy to empliment and can generate accurate full geometry of the member.

2.5 SUMMARY

This chapter has briefly described an overview of the subject areas carried out within this thesis, in particular, material characterization at various temperatures as well as performance analysis and design of cold-formed steel tubular columns (both unperforated and perforated columns). Based on the literature review, it has been witnessed that the ambient temperature material characteristics of YSt-310 cold-formed tubular sections are limited and not readily available in the public domain for both researchers and designers. In addition, the elevated temperature and post-fire mechanical properties of YSt-310 cold-formed steel has not been reported so far and also, the mechanical property database of all cold-formed steels available in the literature (for both elevated temperatures and post-fire) are found to be limited. Furthermore, the investigation on the structural performance of YSt-310 cold-formed

steel tubular stub columns, for both unperforated and perforated, has not been studied previously. Therefore, in this research project, an attempt has been made to setup an accurate material characteristics as well as column performance database for YSt-310 cold-formed steel square and rectangular hollow sections. The test results are then utilised to assess the applicability of design guidelines which are developed based on hot-rolled steel materials and recommend efficient practical design guidelines for cold-formed steel tubular sections.

Table 2.1: Summary of available elevated temperature mechanical properties of cold-formed steel tubular sections

Authors	Steel grade	Cross-sections	Test mode/state	Temperature, *T* (ºC)
Outinen *et al.* (2001)	S355J2H	SHS	Transient	20–1000
Balarupan (2015)	Grade 450	SHS	Steady	20–700
McCann *et al.* (2015)	S355J2H	SHS, RHS, CHS	Both steady and transient	20–1000
Imran *et al.* (2018)	Grade 350	SHS, RHS, CHS	Steady	20–800

Table 2.2: Summary of available post-fire mechanical properties of cold-formed steel tubular sections

Authors	Grade of steel	Cross-sections	*T* (°C)
Outinen and Mäkeläinen (2004, 2007)	S355	SHS	334–710
Lu *et al.* (2016)	Q235	SHS	300–800
Kesawan and Mahendran (2018)	G350 and G450	SHS, RHS	100–800

This page is intentionally left blank.

Chapter 3

Material characterisation

3.1 INTRODUCTION

Accurate estimation of basic mechanical properties is the foremost and fundamental step in the analysis and establishing of design equations for structural members. In this chapter, a comprehensive experimental programme to characterise the material characteristics of Tata Structura YSt-310 cold-formed steel SHSs and RHSs are studied at three different temperature conditions, namely ambient temperature, elevated temperature and post-fire conditions. A detailed description of test material, testing procedure, equipment used, test results and discussion are reported in this chapter.

In Section 3.2 of this chapter, a detailed description of the steel material considered for this project is described.

In Section 3.3 of this chapter, chemical composition, metallography and mechanical properties of YSt-310 cold-formed steel tubular sections have been investigated at ambient temperature using standard test procedures. Chemical compositions recorded

from the test are compared with those provided in the mill certificate of the steel manufacturer. Microstructures of flat, corner and weld regions of the hollow sections are studied. Tensile coupon specimens extracted from the flat, corner and weld regions of each cross-section of YSt-310 material considered in this research work have been tested using standard tensile coupon tests. A detailed description of the experimental program, including extraction of the tensile specimens, laboratory tensile coupon tests to generate full stress-strain curves as well as estimation of key material parameters viz., Young's modulus, proof stress, tensile stress, ductility and Romberg–Osgood material parameter (*n*) are reported in this section.

In Section 3.4 of this chapter, the elevated temperature mechanical properties of the cold-formed steel have been evaluated using steady-state test approach. In this test method, tensile coupon specimens extracted from the flat regions of SHSs and RHSs have been first heated to predetermined elevated temperatures ranging from 100 to 800 ºC and then standard tensile coupon tests have been performed to generate the full stress-strain curves. The retention factors obtained from the current experimental programme have been compared with predictions based on current fire design standards as well as those reported in the literature for cold-formed steel at elevated temperatures. A new set of fire design retention factors have then been proposed for cold-formed steels tubular sections based on lower bound values, considering both the current and previously reported experimental data.

In Section 3.5 of this chapter, an experimental programme to study the residual mechanical properties of YSt-310 cold-formed steel tubular sections after being exposed to elevated temperatures is described. First, the coupon specimens extracted from the flat regions have been exposed to the pre-determined elevated temperatures in the range ~ 300–800° C, and then the residual mechanical properties and hardness value have been estimated through standard tensile coupon and microhardness test at ambient temperature after natural air cooling. Two sets empirical equations are proposed separately to predict the residual post-fire reduction factors based on the i) current experimental results of Tata Structura YSt-310 cold-formed steel, and ii) cold-formed steel of various grades presently available in the literature.

3.2 DETAILS OF MATERIAL SUPPLY

The steel material considered in the research work is commercially available YSt-310 cold-formed steel, conforming to IS 4923 (1997) with a nominal yield strength of 310 MPa, a tensile strength of 450 MPa and minimum percentage elongation at failure of 10%. The tubular sections are available in the market under the brand name as Tata Structura YSt-310 manufactured by Tata Steel India (Tata Steel, 2013). Tata Steel uses high-frequency induction welding (HFIW) technique to produce a continuous longitudinal seam-welded square and rectangular hollow sections. A total of seven dissimilar cross-sections, namely four SHSs and three RHSs have been chosen based on the limitation of testing facilities presently available at the laboratory. The tubular sections have been supplied in uncut lengths of 6000 mm lengths by SM Corporation Ltd. (an authorised Tata Steel India distributor located at Guwahati, India). The nominal cross-sectional dimensions are listed in Table 3.1, where B, D, t, r_i, r_o and A_g are the width, depth, thickness, inner corner radius, outer corner radius and gross cross-sectional area of the sections as detailed in Figure 3.1. The notation to represent the nominal cross-sectional dimensions throughout this thesis is $B \times D \times t$, and hence $50.0 \times 50.0 \times 2.9$ denotes a rectangular hollow section with width, depth and thickness of 50.0 mm, 50.0 mm and 2.9 mm respectively.

3.3 AMBIENT TEMPERATURE MATERIAL PROPERTIES

In this section, the ambient temperature material characteristics of YSt-310 cold-formed steel SHS and RHS are investigated experimentally. The test programme comprises of estimation of chemical compositions, metallographic examination and evaluation of mechanical property. The detailed explaination of the step by step test procedure, instrument utilised, test results and discussion on the test results are reported in the following sections.

3.3.1 Chemical composition

The manufacturer's laboratory test results for chemical composition and tensile coupon test, extracted from a RHS – 50 × 50 × 2.9, as given in the mill certificate are shown in Table 3.2. The metal chemical components of YSt-310 cold-formed tubular sections have been determined on three specimens extracted from three cross-sections, namely 66 × 33 × 2.6, 60 × 40 × 2.9 and 40 × 40 × 3.2. Optical Emission Spectrometer (OES) has been used to investigate elemental composition of the material considered. The percentage of elemental compositions (e.g. C, Si, Mn, S, Fe etc.) found in the above three specimens are shown in Table 3.3. It can be observed from examining Tables 3.2 and 3.3 that the quantity of Carbon and Phosphorus content resulted from the present test are slightly higher than that of mill certificate; however Manganese and Sulfur content are quite matching. Element such as Silicon, Copper, Nickel, Titanium, Aluminium, Niobium and Nitrogen are also found to be present based on the present test results. It may be noted that mill certificate does not specify the method followed to measure chemical composition.

3.3.2 Microstructure

Metallographic examination for YSt-310 steel has been conducted on three samples - 66 × 33 × 2.6, 60 × 40 × 2.9 and 40 × 40 × 3.2 to investigate the characteristics of microstructure for the flat, corner and weld portions using an optical microscope. Three transverse cross-sections from 66 × 33 × 2.6, 60 × 40 × 2.9 and 40 × 40 × 3.2 have been cut using a rotary hacksaw and milled flat using a lathe machine. The metallographic study has been carried out at Material Science Laboratory of Department of Mechanical Engineering, Indian Institute of Technology Guwahati. The surfaces have been ground on a series of silicon carbide paper under continuous flushing of water and polished using 50 nm aluminium oxide abrasive, to remove any scratch formed during cutting. Finally, the sample has been etched using a solution of 5% nitric acid and ethanol.

Typical microstructure seen under optical microscope of flat and curved portions are shown in Figure 3.2 (a) and (b) respectively, where the white areas are primary ferrite and the grey areas are pearlite (a mixture of ferrite and cementite). A difference in the morphology of flat and corner grains has been observed: the grains in the flat region are found to be relatively larger, see Figure 3.2 (a) in comparison to those of corner regions wherein the grains are smaller and elongated (see Figure 3.2 (b)). The elongated grains in the corner region may due to the mechanical pressure applied during cold-forming process. This could be the primary reason for enhanced material strength seen in curved coupon specimens as compared to flat coupon specimens (further discussion in Section 3.3.3). From the microstructure of weld region, the size of weld line has been determined for two cross-sections: 60 × 40 × 2.9 and 66 × 33 × 2.6 as shown in Figure 3.3 (a) and (b) respectively. The sizes of weld are further used to decide the size of weld coupon in Section 3.3.3. Different zones of a typical weld region (welded using high frequency induction welder, HFIW) of 66 × 66 × 2.6 cross-section at higher resolution are shown in Figure 3.4 (a). The welded seam is composed of three zones namely weld zone (or fusion zone), heat affected zone (HAZ) and parent (or base) material (e.g., Kavousi Sisi and Mirsalehi, 2016). The weld junction consists of white ferrite grains due to decarburization during welding. HAZ further consists of three layers: overheated, recrystallised and partially-recrystallised area. Widmanstätten pattern have been observed in the overheated area (see Figure 3.4 (b)) and smaller (as compared to parent material) grains of ferrite and pearlite layer have been observed in the recrystallised area (see Figure 3.4 (c)). The formation of coarser grain and Widmanstätten pattern in the overheated area as well as finer ferrite and pearlite grain in the recrystallised area would be the main reason for higher mechanical strength and hardness value observed in weld coupon tests and microhardness tests respectively which will be further discussed in later part of this chapter (similar results were also reported by researchers, e.g., Hu *et al.*, 2011; Kavousi Sisi and Mirsalehi, 2016). However, it may be mentioned that post-weld heat treatment process can reduce and homogenize higher hardness value in the HAZ (e.g. Kavousi Sisi and Mirsalehi, 2016).

3.3.3 Mechanical properties

The fundamental stress-strain properties of the YSt-310 structural tubular steel have been investigated through standard tensile coupon test. Flat, curved and weld coupon specimens have been extracted from each of the flat, corner and weld portion of each steel sections in the direction parallel to the direction of rolling process (see Figure 3.1). All the 21 coupon specimens have been tested at ambient temperature (~ 23 ºC) using a 250 kN capacity universal testing machine (UTM), manufactured by Bangalore Integrated System Solutions (BISS) India located at Central Instrument Facility (CIF) of Indian Institute of Technology Guwahati. The tensile test has been conducted using displacement control method with a displacement rates of 0.05 mm/min up to strain corresponding to proof stress (≤ ~0.2% strain) and 0.4 mm/min (> ~0.2% strain) as recommended by Huang and Young (2014c). The experimental investigations measured the basic material properties including the Young's modulus, 0.05% proof stress, 0.2% proof stress, 1.0% proof stress, ultimate strength and percentage elongation at fracture point considering standard gauge length of $5.65\sqrt{A_c}$ where A_c is the cross-sectional area of the coupon specimen. As recommended by researchers such as Rasmussen and Hancock (1993); Mirambell and Real (2000); Arrayago *et al.* (2013); Real *et al.* (2014); Arrayago *et al.* (2015) etc., the Ramberg–Osgood parameter or strain hardening exponent, *n* calculated by using the expression given in Equation 3.1 is reported in this thesis, where $\sigma_{0.2}$ and $\sigma_{0.05}$ are the 0.2% and 0.05% proof stress respectively.

$$n = \frac{\ln(4)}{\ln\left(\frac{\sigma_{0.2}}{\sigma_{0.05}}\right)} \tag{3.1}$$

It may be noted that attempts have been made in the literature (e.g., Young and Lui, 2005; Young, 2008; Huang and Young, 2012; Afshan *et al.*, 2013; Somodi and Kövesdi, 2017) to measure residual stress *via* measurement of residual strain and then converting to residual stress. However, researchers such as Ellobody and Young

(2005b); Huang and Young (2014b); Anwar-us-saadat *et al.* (2016); Ma *et al.* (2016) etc., reported that both the ultimate load capacity and load-end shortening behaviour are not significantly affected by consideration of residual stress, in their finite element analyses. Therefore the measurement of residual stress is not included in the present study.

3.3.3.1 Flat coupon tests

Flat coupon specimens having dimensions of 12.5 mm wide and 50 mm gauge length, conforming to ASTM E8 / E8M (2015) has been extracted from the central portion of the face opposite to the welded face for each section as shown in Figure 3.1. The dimensions of flat coupon specimens reported by Huang and Young (2014c) have been adopted in the current study provided see Figure 3.5 (a). The coupon specimens have been cut using a wire-cutting EDM (Electrical discharge machining). The thickness and width of the flat coupon specimens have been measured to determine the actual cross-sectional area using a digital Vernier calliper prior to the tensile test. The longitudinal strain has been measured with an extensometer of gauge length 50 mm directly mounted on the coupon specimen using two contact points as shown in Figure 3.6 (a).

3.3.3.2 Corner coupon tests

Corner coupon specimens have been extracted from the corner portion (see Figure 3.1) with a nominal size of 6 mm wide and 25 mm gauge length. The overall dimensions of the coupon specimen are shown in Figure 3.5 (b). It may be noted that similar coupon dimensions were used in Huang and Young (2014a). The cross-sectional area of the extracted curved coupon specimens has been measured using AutoCAD method as recommended by Huang and Young (2014c) prior to testing. A pair of v-shaped hydraulic clamps have been used to grip the curved coupon specimens. The gap between the inner curved portion of the coupon and v-shaped clamped has been filled with a steel rod to firmly grip the curved coupon as shown in Figure 3.6 (b). Similar gripping technique for curved coupon test was also used by other researchers such as Afshan *et al.* (2013). Using a 25 mm gauge length

extensometer, the longitudinal strain has been measured by directly mounting on the curved coupon specimen.

3.3.3.3 Weld coupon tests

In the literature, very rarely, results of tensile coupon extracted from the weld portion of cold-formed tubular section have been reported (e.g. Zhu *et al.*, 2016). In this study, tensile tests of weld coupons have also been carried out, to assess variation of material strengths at various locations of the cold-formed section (see Figure.3.1). The size of the weld has been determined by using an optical microscope for 60 × 40 × 2.9 and 66 × 33 × 2.6 rectangular sections as discussed in Section 3.3.2. The average weld size of 60 × 40 × 2.9 and 66 × 33 × 2.6 are found to be ~1237.86 µm and ~1548.15 µm respectively. Weld coupons having a maximum size of 4 mm, which is approximately two times the size of the weld as seen in the two sections, have been considered. The width of the weld coupon for tensile testing has been considered in such a way that the heat affected zone (HAZ) / weld is within the coupon width, and material portion outside the HAZ is minimal. Similar coupon dimensions with a gauge length of 25 mm as employed in Huang and Young (2014c), are considered in this study as shown in Figure 3.5 (c). Weld coupon tensile tests have been carried out with the intention of estimating the strength of the weld. The width and thickness have been recorded using a digital Vernier calliper prior to the tensile test. Similar to curved coupon test, the longitudinal strain gauge has been measured using a 25 mm gauge length extensometer as shown in Figure 3.6 (c).

3.3.4 Test results and discussion

Stress-strain curves generated from the tensile coupon tests are plotted in Figures 3.7–3.9 respectively for flat, corner and weld coupons. The fundamental material parameters such as Young's modulus (E), 0.05% proof stress ($\sigma_{0.05}$), 0.2% proof stress ($\sigma_{0.2}$), 1.0% proof stress ($\sigma_{1.0}$), ultimate strength (σ_u), percentage elongation at fracture point (ε_f) and strain hardening exponent (n) extracted from the recorded

stress-strain curve are summarised in Tables 3.4–3.6 for flat, curved and weld coupons respectively. The definitions of mechanical parameters are described in Figure 3.10. The initial Young's Modulus has been evaluated from the initial linear portion of the stress-strain curve as per ASTM E8 / E8M (2015) and correspondingly 0.05%, 0.2% and 1.0% proof stress have then been estimated. The ultimate stress, σ_u and percentage elongation at fracture, ε_f (%) have been noted from the stress-strain curve. Strain hardening exponent, *n* is estimated based on the Equation 3.1 described above. The mean value of Young's modulus of flat, curved and weld coupon tests are computed to be 198372.0, 184414.0 and 180237.0 MPa respectively. It is observed, the mean values of Young's modulus of flat and curved are similar but slightly lesser than those of flat coupons. Similar findings have also been observed in high strength steel by Wang *et al.* (2017). As reported in the literature (e.g. Chajes *et al.*, 1963; Karren and Winter, 1965; Karren, 1967; Ashraf *et al.*, 2005; Ellobody and Young, 2005a; Young and Lui, 2005; Huang and Young, 2012; Ma *et al.*, 2015; Ma *et al.*, 2016; Wang *et al.*, 2017 etc.), cold-forming induced significant strength enhancement in the corner region of various cold-formed steels sections. In the present study, similar observations have also been seen for YSt-310 cold-formed steel where average 0.2% proof stress and ultimate stress of the curved coupon are respectively 26% and 34% more than those of flat coupons. However, it has been seen that the ductility (or strain at fracture, ε_f) of corner coupon has been reduced by ~ 53.13% on average as compared to those of flat coupons (provided in Tables 3.4 and 3.5). The tensile test results of weld coupon are found to be similar to those of curved coupon specimens.

3.4 ELEVATED TEMPERATURES MECHANICAL PROPERTIES

3.4.1 General

Evaluating the mechanical properties of steel at elevated temperature is normally conducted by either of the two approaches, namely steady-state (isothermal) or transient-state (an-isothermal) tests. In the steady-state tests, the coupon specimens are first heated to a predetermined temperature and then tensile test is performed whilst keeping the temperature constant throughout the test process, whereas, in the case of transient-state, the coupons are loaded initially at a predetermined stress level whilst the temperature of the specimen is allowed to increase until fracture. The steady-state approach is generally appropriate for generating the full stress-strain material model whereas the transient-state is generally utilised to understand the material creep (time-dependent deformation) performance in both increasing and decreasing temperatures (detailed in Qiang *et al.*, 2012a; Hu *et al.*, 2018 etc.). However, since the current test programme is focused on generating the stress-strain material properties and the reduction factors, only the steady-state test method has been adopted in this experimental study. In the following subsections, description of the experimental programme is discussed, in which the tensile coupons extracted from two SHSs and a RHS are tested at elevated temperatures.

3.4.2 Test specimens

Elevated temperature mechanical properties of YSt-310 cold-formed steel tubular sections have been performed on three cross-sections, namely – 50 × 50 × 2.9, 60 × 60 × 2.6 and 80 × 40 ×2.6. A total of 31 tensile coupon specimens have been cut from flat portions (except the face containing weld region) in the direction parallel to the rolling direction. It may be mentioned that the yield and tensile strengths of coupons cut from the corner and weld regions have been found to be higher than those cut from flat regions (see Section 3.3.4), only the tensile coupons from the flat regions have been considered in the present study, to provide nominal material properties. The

tensile specimens have been cut using wire cut EDM and the dimensions of the coupon are shown in Figure 3.11. The dimensions of tensile coupon are of similar to those utilised in the literature (e.g., Huang and Young, 2014a; Li and Young, 2017a) and provided in ASTM E21 (2009). A central line has been marked along the length of coupon specimen to provide a guideline for aligning the coupon specimens.

3.4.3 Test apparatus

The load frame (which has been used in the Section 3.3.3 for ambient temperature coupon tests) has been utilised to carry out the tensile coupon tests at elevated temperatures. An electric furnace, capable of generating high temperature up to 1400 ^{o}C has been employed. A typical instrumental setup for the tensile test at elevated temperature is shown in Figure 3.12. The furnace has two independent heating zones, each facilitated with two heating elements. The air temperature in the heating chamber is regulated by a control unit. The temperature of the two heating zone is measured by using two internal thermocouples fitted inside the chamber. The air temperature inside the furnace has been cross-verified with an external thermocouple. A calibrated, 25 mm gauge length with maximum travel range of ± 2.5 mm, ceramic rod type high temperature extensometer has been used to measure the strain during the high temperature tensile tests. For the ambient temperature tensile coupon tests, a calibrated ambient temperature 25 mm gauge length extensometer has been used. It is to be noted that for specimens with large elongation, the actuator displacement has been utilised to generate the complete strain-strain curve. The top and bottom ends of the furnace have been covered with glass-wool to avoid any loss of heat during the tensile coupon tests. The load, strain and temperature generated during the test process have been recorded using a data acquisition system manufactured by BISS.

3.4.4 Test procedure

The specimen width and thickness have been measured initially within the gauge length at three different points using a digital Vernier calliper having an accuracy of 0.01 mm and the average value of three cross-sectional areas has been further utilised

in stress calculation. Ambient temperature (~ 23 °C) tensile coupon tests have been first performed following the procedure detailed in Section 3.3.3. For elevated temperature coupon tests, the upper end of the coupon specimen has been gripped using a pair of flat surface hydraulic clamps, whilst the lower end has been free allowing expansion during the heating process. The extensometer rod has been aligned and connected perpendicularly to the tensile coupon. Sufficient pressure has been given to avoid any slip between the ceramic rod and coupon surface. The specimens have been first heated to the target temperatures of ranging from ~ 100 to 800 °C and then allowed to keep constant for about 20 minutes conforming to the minimum holding time as per ASTM E21 (2009), to ensure uniform heat distribution throughout the specimen inside the furnace chamber. The specimen temperature has been also validated using a laser heat gun. The tensile sample has been loaded using the displacement control mode at a constant displacement rate of 0.3 mm/min until fracture of the coupon, similar to the rate adopted by Li and Young (2017a). It is to be noted that, since the specimens expanded during the heating process, the amount of expansion has been added to the initial gauge length (25 mm) so as to include the increased gauge length of the extensometer. The test has been continued until fracture or the attainment of ~ 30-50% of the ultimate load at the post-peak.

3.4.5 Test results and discussion

In this section, the results from the tensile coupon tests cut from the three cross-sections (50 × 50 × 2.9, 60 × 60 × 2.6 and 80 × 40 ×2.6) are analysed and discussed. The notations for the basic material properties such as elastic modulus; yield stress (0.2% proof stress); stresses at 0.5%, 1.5% and 2.0% strains; tensile strength and corresponding strains (%) and fracture strains (%) are respectively represented by E, $\sigma_{0.2}$, $\sigma_{0.5}$, $\sigma_{1.5}$, $\sigma_{2.0}$, σ_u, ε_u and ε_f for ambient temperature (as detailed in Figure 3.10). The Ramberg–Osgood parameter or strain hardening exponent, n is calculated based on Equation 3.1. A suffix T is added to represent material properties at elevated temperature. For example, the $\sigma_{0.2,T}$ represents 0.2% proof stress at elevated temperature, T.

3.4.5.1 Stress-strain curves

The engineering stress-strain curves generated from the tensile coupon tests at different elevated temperatures approximately between 20 and 800 °C are shown in Figures 3.13–3.15 respectively for 50 × 50 × 2.9, 60 × 60 × 2.6 and 80 × 40 ×2.6. It is observed from the figures that all the three cross-sections show similar rounded (i.e. pronounced non-linear) stress-strain curves, with reduced stiffness and strength as the temperature increases; with no definite yield strength at both ambient and elevated temperatures. The ductility of coupon specimens exposed to the temperatures between 100 to 400 °C is found to be relatively low as compared to ambient as well as high temperatures above 500 °C; similar to those test results in the literature (such as Balarupan, 2015; McCann *et al.*, 2015; Imran *et al.*, 2018 etc.,). It is to be mentioned that, although, not necessary for the present scope of study, a pause of around 1 min of the actuator displacement, can lead to stress drop (i.e. 'static drop' as detailed in Chen and Young, 2007), which can result in a smooth and continuous transition in stress-strain curve, once resumed, as shown Figure. 3.10.

3.4.5.2 Elastic modulus

Elastic modulus represents an important design parameter influencing the stiffness of steel structures. The elastic modulus corresponding to a target elevated temperature, E_T is estimated as the slope of the initial linear portion of the stress-strain curve according to the method detailed in ASTM E21 (2009). The estimated Young's modulus values are presented in Table 3.7 and are also plotted against the elevated temperatures in Figure 3.16. As expected, the test results show a decreasing trend of modulus of elasticity as the exposed temperature increases from ambient to 800 °C, although some slight scatter in the test values are noticed. The scattering of modulus values may be related to the sensitiveness of measurement procedure and equipment used as reported by other researchers such as Kodur *et al.* (2010); Ye and Chen (2012); McCann *et al.* (2015); Liang *et al.* (2019) etc. The Young's modulus is found to be unaffected up to 200 °C but rapidly reduced beyond 200 °C.

3.4.5.3 Yield strength

Yield strength is generally referred for defining the grade of steel material and also represents an important parameter after elastic modulus for the design of steel structures. As depicted in the isothermal material curves (as shown in Figures 3.13–3.15) of both ambient and elevated temperatures, no well-defined yield points have been observed (similar to those of stainless steel) and therefore, 0.2% proof stress is taken as the yield strength of the material considered. The estimated yield strength values are presented in Table 3.7 and shown in Figure 3.17. From Figure 3.17, a gradual reduction in the yield stress has been observed (except 50 × 50 × 2.9, for which no reduction is observed) and appears somewhat stabilised; further, the yield stresses values are seen to be in a band of 390–543 MPa, for the three cross sections. The initial differences in the yield stress values at T < ~ 300 °C may be related to difference in the level of cold-working during forming process. However, the differences in yield stress vanishes (or converges), for $T \geq$ ~ 300 °C. While for $T \geq$ ~ 300 °C, a rapid drop in the values of yield stress can be seen, attaining a value of ~ 25 MPa at 800 °C.

3.4.5.4 Stresses at 0.5% and 1.5%, and 2.0% strains

Fire design standards such as BS 5950 (2003), EC3-1-2 (2005) specify reduction factors for stresses at different strain levels for various design applications and therefore, stresses corresponding to 0.5% strain ($\sigma_{0.5,T}$), 1.5% strain ($\sigma_{1.5,T}$) and 2.0% strain ($\sigma_{2.0,T}$) have been computed from the elevated temperature stress-strain curves. The derived stresses at 0.5%, 1.5% and 2.0% strain levels are presented in Table 3.7 and are also plotted with increasing temperatures in Figures 3.18–3.20 respectively. In general, the pattern of variation for all the three stresses (i.e., $\sigma_{0.5,T}$, $\sigma_{1.5,T}$ and $\sigma_{2.0,T}$) are similar to that of yield stress ($\sigma_{0.2,T}$). However, at ~ 800 °C, the reduced stress values are found to be 34.28 MPa, 36.16 MPa and 36.75 MPa for stresses at 0.5%, 1.5% and 2.0% strains, respectively; which is slightly higher than the corresponding yield stress value (see Figure 3.17).

3.4.5.5 Ultimate strength and strain

The ultimate strength of a coupon specimen exposed to a particular elevated temperature represented by $\sigma_{u,T}$ is the maximum stress which the coupon specimen takes before failure. The measured values of ultimate strengths from the present steady state tensile test programme are reported in Table 3.7 and shown against temperatures in Figure 3.21, whilst the corresponding strains $\varepsilon_{u,T}$ are also presented in Table 3.7 and shown in Figure 3.22. It may be observed that, on average of the three cross-sections, ~ 86% of ambient temperature ultimate strength is retained for temperature up to 400 °C and then decreased rapidly beyond 400 °C. Similar observations were reported by McCann *et al.* (2015). It may also be seen from Figure 3.22 that, whilst there is some scatter, the ultimate strain (i.e. strain corresponding to ultimate strength) followed a decreasing trend as the temperature increases till 600 °C. In other words, the ultimate stress reached sooner but formation of necking is delayed as the temperature increases. Similar observations have also been reported by earlier researchers such as McCann *et al.* (2015), Imran *et al.* (2018) etc.

3.4.5.6 Fracture strain

The percentage elongation at fracture or fracture strain, $\varepsilon_{f,T}$ (in %) is the maximum strain at failure of a coupon specimen. Table 3.7 presents the fracture strain (%) recorded from the present test programme and they are also plotted in Figure 3.23. It can be observed that, the fracture strains are lower than that of ambient temperature up to 400 °C. However, overall an increasing trend may be observed as the temperature ranges from 100 to 800 °C. Similar trends have been reported by Liang *et al.* (2019) on cold-formed and hot-rolled stainless steel at elevated temperature.

3.4.6 Design reduction factors

Reduction factors represent the relative decrease in mechanical properties of a material as temperature rises and are defined as the ratio of the material property

(Young's modulus; yield stress; stress corresponding to 0.5%, 1.5% and 2.0% strain; tensile strength and corresponding strains; fracture strains) being considered at a particular elevated temperature to that of ambient temperature value. In this section, reduction factors of key material properties derived from the present experimental programme (provided in Table 3.8) are compared with those detailed in fire design standards (AS 4100, 1998; BS 5950, 2003; EC3-1-2, 2005; IS 800, 2007; AISC 360, 2010) as well as those proposed by previous researchers on cold-formed steel tubular sections (Balarupan, 2015; McCann *et al.*, 2015; Imran *et al.*, 2018). It is to be noted that the reduction factors for elastic modulus and yield strength detailed in IS 800 (2007) are similar to those mentioned in AS 4100 (1998), therefore, the comparisons made in the further part of this Chapter are referred only to AS 4100 (1998). The reduction factors derived from both steady and transient state elevated temperature test results from various cold-formed steel cross-sections, such as RHS, SHS and CHS, conducted by Outinen *et al.* (2001), Balarupan (2015), McCann *et al.* (2015) and Imran *et al.* (2018), are also compared with the current test results as well as design predictions. Based on the comparison, suitable design reduction factors are recommended in the following sections. A summary of the data collected from the past test results are presented in Table 3.9.

3.4.7 Reliability analysis

Statistical analysis has been performed to check the reliability of the design predictions based on current design standards: AS 4100 (1998); BS 5950 (2003); EC3-1-2 (2005); IS 800 (2007); and AISC 360 (2010) and literature: Balarupan (2015); McCann *et al.* (2015); and Imran *et al.* (2018). The reliability analysis is based on procedure detailed in the commentary on NAS specification AISI S100-16C (2016) for design of cold-formed steel structural member. The mean values, P_m and coefficient of variances, V_p (COV) of the ratios of reduction factors (test to predicted values given in Tables 3.10 and 3.11) have been utilised to determine the resistance factors (ϕ) of design rules using Equation C–B3.2.2–15 of AISI S100-16C (2016) to achieve a target reliability index (β) of 2.5 and above. The design prediction is considered to be reliable if the calculated reliability index is greater than or equal to

the target value of 2.5. As recommended in AISI S100-16C (2016), dead (DL) to live (LL) load ratio of 0.2 has been assumed. A load combination of 1.2DL+1.6LL has been utilised in the analysis for direct comparison (see e.g. Huang and Young, 2014a). The statistical parameters representing the mean and coefficient of variances values for material properties and fabrication factor, *viz.* $M_m = 1.10$, $F_m = 1.00$, $V_M = 0.10$ and $V_F = 0.05$ have been adopted for all key parameters except ultimate strength for which $V_M = 0.05$ as detailed in ASCE (2002). A correction factor has been applied to account for the effect of the number of observation (*N*) considered in estimating the resistance factor as per AISI S100-16 (2016). The estimated resistance factors and reliability indexes are reported in Tables 3.10 and 3.11.

3.4.8 Comparison of design reduction factors

3.4.8.1 Elastic modulus

The elastic modulus reduction factor, $k_{E,T}$ determined as the ratio of elastic modulus at elevated temperature, E_T to that of ambient temperature, *E* from the current tests, are presented in Table 3.8. Comparison of reduction factors with current design standards such as EC3-1-2 (2005), AISC 360 (2010) and AS 4100 (1998) as well as design curves proposed by Balarupan (2015) and Imran *et al.* (2018) has been made (as shown in Figure 3.24). It may be observed from Figure 3.24 that, for temperatures range 200 < *T* < 600 °C, the values of $k_{E,T}$ obtained from the present test results are slightly scattered, but clearly a decreasing trend can be seen as temperature increases. The reduction factors in this temperature range are found to be lower than the codal values: AS 4100 (1998); EC3-1-2 (2005); and AISC 360 (2010) and those proposed by Balarupan (2015) and Imran *et al.* (2018). It also appears that the design reduction factor given in AS 4100 (1998) as well as design curves proposed by Balarupan (2015) and Imran *et al.* (2018) are slightly over predicted for temperature above 200 °C. Overall, the design values in EC3-1-2 (2005) and AISC 360 (2010) agree well with the present test results. A summary of the statistical comparison of present test results

with predicted design values in terms of mean, coefficient of variance (COV), recommended resistance factor and target reliability index are presented in Table 3.10.

The elastic modulus reduction factors generated from the present tests are compared with those reported in Outinen *et al.* (2001); Balarupan (2015); McCann *et al.* (2015); and Imran *et al.* (2018) (see Figure 3.25). It can be observed that the present test results follow similar reduction trend with those reported in Outinen *et al.* (2001); Balarupan (2015); McCann *et al.* (2015); and Imran *et al.* (2018). In addition, comparison have also been made with the $k_{E,T}$ from all test results (both present and past experimental results) with current fire design predictions AS 4100 (1998); EC3-1-2 (2005); AISC 360 (2010) and design curve proposed by Balarupan (2015); Imran *et al.* (2018) as shown in Figure 3.25. It can be seen that, for temperatures up to 400 °C, the design $k_{E,T}$ values given by AS 4100 predict well with the test results, whilst for temperatures above 400 °C, the test results are below the codal predictions. The design curves proposed by Balarupan (2015) and Imran *et al.* (2018) seem to be slightly higher for temperatures, 200 < T < 700 °C. A comparison of all test results and those design elastic modulus reduction factors provided in design provisions and literature are summarised in Table 3.11. It is to be noted that a best fit (using least square method) design curve has been attempted to the combined test results, however since the test data are highly scattered, a conservative prediction with mean ~ 1.00 and COV ~ 0.25 values is obtained, similar to those resulted using EC3-1-2 (2005) and AISC 360 (2010), indicating that best fit design curve could not improve the prediction further. Overall, the values predicted by EC3-1-2 (2005) and AISC 360 AISC 360 (2010) seem to agree well with all test results and offer conservative prediction ($P_m \geq 1.0$). Therefore, the design elastic modulus reduction factors detailed in EC3-1-2 (2005) and AISC 360 (2010) are recommended for cold-formed steel tubular sections. Reliability analysis has been conducted and the resistance factors (ϕ) have been estimated to offer a target reliability index, $\beta \geq 2.5$ (see in Table 3.11).

3.4.8.2 Yield strength

The yield strength reduction factors, $k_{0.2,T}$ has been estimated as the ratio of yield (0.2% proof) stress at elevated temperature, $\sigma_{0.2,T}$ to that of ambient temperature yield stress, $\sigma_{0.2}$ and are reported in Table 3.8. The test results are also plotted in Figure 3.26 and compared with those detailed in EC3-1-2 (2005), AISC 360 (2010) and AS 4100 (1998) as well as design curve proposed by Balarupan (2015) and Imran *et al.* (2018). It is to be noted that EC3-1-2 (2005) design provision provides a set of separate yield strength reduction factors for stocky (Class 1–3) and slender (Class 4) cross-sections in Table 3.1 and Table E.1 of EC3-1-2 (2005), based on the stress at 2.0% strain and 0.2% proof stress respectively. For analysis purpose, the stress corresponding to Table 3.1 and Table E.1 of EC3-1-2 (2005) are respectively represented as EC3-1-2 (2005) and EC3-1-2 (2005)–Class 4. American standard, AISC 360 (2010) provides yield strength reduction factor based on stress at 2.0% strain, whilst the $k_{0.2,T}$ prediction value provided in Australian standard, AS 4100 (1998) and design curve by Balarupan (2015) and Imran *et al.* (2018) are based on 0.2% proof stress. It can be observed from Figure 3.26, that the $k_{0.2,T}$ prediction value presented in Table 3.1 of EC3-1-2 (2005) and AISC 360 (2010) are unconservative to the present test results. For temperatures above 500 °C, the AS 4100 (1998) overpredicts reduction factors. The $k_{0.2,T}$ prediction values detailed in Table E.1 of EC3-1-2 (2005) for Class 4 cross-section generally provide lower bound values. The reduction factors proposed by Balarupan (2015) (for temperatures up to 700 °C) and Imran *et al.* (2018) agree well with the current test results. Table 3.10 shows a summary of the statistical comparison of the present test results with design provisions and proposal in literature. Based on the reliability analysis, recommended resistance factors are presented (in Table 3.10) to achieve the specified target reliability index.

The yield strength reduction factors reported in literature: Outinen *et al.* (2001); Balarupan (2015); McCann *et al.* (2015) and Imran *et al.* (2018) has also been compared with present results as well as design predictions in AS 4100 (1998); EC3-

1-2 (2005); AISC 360 (2010); Balarupan (2015) and Imran *et al.* (2018) as shown in Figure 3.27. It can be seen from Figure 3.27 that the present test results agree well with yield strength reduction factors reported previously by Outinen *et al.* (2001); Balarupan (2015); McCann *et al.* (2015) and Imran *et al.* (2018). The predictions made by EC3-1-2 (2005) for stocky sections (Class 1–3) and AISC 360 (2010) are generally above the test values for temperatures below 800 °C (see Figure 3.27). It has also been observed, the $k_{0.2,T}$ from the test results are below the prediction curve presented in AS 4100 (1998) for temperatures above 500 °C. Overall, the reduction factors predicted by EC3-1-2 (2005) for slender sections (Class–4) provide a lower bound values to the test results for the temperature range considered. The yield strength reduction factor proposed by Balarupan (2015) and Imran *et al.* (2018) predicts well with the test results. The comparison of $k_{0.2,T}$ values predicted by AS 4100 (1998); EC3-1-2 (2005); AISC 360 (2010); Balarupan (2015) and Imran *et al.* (2018) against the test results (both from present and literature) are summarised in Table 3.11. It seems that the predictions provided in EC3-1-2 (2005) (Class 1–3), AISC 360 (2010) and Balarupan (2015) are unconservative, whilst those values set out in EC3-1-2 (2005)–Class 4, AS 4100 (1998) and design curve proposed by Imran *et al.* (2018) predict conservative value. However, the design $k_{0.2,T}$ provided by EC3-1-2 (2005)–Class 4 are slightly overpredicts in the temperatures range 200 °C < T < 500 °C; whilst AS 4100 (1998) underpredicts in the temperatures range 500 °C < T < 900 °C. In addition, the design $k_{0.2,T}$ provided Imran *et al.* (2018) is found to be applicable up to 800 °C. Therefore, a set of $k_{0.2,T}$ values (see Table 3.12) which are slightly conservative (~ 10%) but still give identical COV (~ 0.30) has been proposed based on the lower bound values. To achieve target reliability index $\beta \geq 2.50$, resistance factors are recommended as presented in Table 3.11.

3.4.8.3 Stress at 0.5% and 1.5% strain

The British Fire design standard BS 5950 (2003) provides a separate reduction factor of the strength of cold-formed steel corresponding to stresses at 0.5% and 1.5% strain

for elevated temperatures up to 600 °C. The reduction factor for stress at 0.5% strain, $k_{0.5,T} = \left(\sigma_{0.5,T} / \sigma_{0.5}\right)$ and 1.5% strain, $k_{1.5,T} = \left(\sigma_{1.5,T} / \sigma_{1.5}\right)$ generated from the present tests programme are reported in Table 3.8. The predictions provided in BS 5950 (2003) for stresses at 0.5% and 1.5% strain are compared with present test results in Figures 3.28 and 3.29, respectively. Overall, the BS 5950 (2003) predictions agree well with the test results (elevated temperatures up to 600 °C) for 0.5% strain with a mean value of 1.09 and COV of 0.13, whilst for 1.5% strain, the prediction has been found to be unconservative with mean value of 0.96 and COV of 0.07 as given in Table 3.10. Reliability index of 2.50 can be achieved by utilising resistance factor of 0.95 and 0.90 for 0.5% and 1.5% strains respectively.

The reduction factor for stress at 0.5% strain from the present test results are compared with those reported by Outinen *et al.* (2001) (see Figure 3.30). As it can be observed that the present and past test results are in good agreement. It is to be noted that, since the reduction factors in BS 5950 (2003) are applicable only up to 600 °C, a design prediction for stress at 0.5% strain is proposed (see Table 3.12) for elevated temperatures up to 1000 °C, based on the experimental test results. The proposed reduction factors provide conservative prediction with the mean value of 1.02 and COV of 0.12. Resistance factor (ϕ) of 0.85 is recommended to offer a target reliability index $\beta \geq 2.50$ (as given in Table 3.11). Besides, since the reduction factors for stress at 1.5% strain is only available for temperatures up to 600 °C, a set of design prediction value are proposed based on the present test data for temperatures up to 800 °C as plotted in Figure 3.29 and presented in Table 3.12. The proposed reduction factors for stress at 1.5% strain are found to be conservative offering the mean value of 1.02 and COV of 0.14. The target reliability index can be achieved by adopting a resistance factor of 0.85.

3.4.8.4 Stress at 2.0% strain

As mentioned in Section 3.4.3.3, the fire design provision, EC3-1-2 (2005) allows the use of material strength at 2.0% strain for stocky (Class 1–3) cross-sections as deformation is of less concern in case of a fire event. The reduction factor for stress

at 2.0% strain, $k_{2.0,T}$ calculated as the ratio of stress at 2.0% strain at elevated temperature, $\sigma_{2.0,T}$ to that of ambient temperature value, $\sigma_{2.0}$ are shown in Table 3.8. The $k_{2.0,T}$ generated from the current test programme have been compared with those values given in EC3-1-2 (2005) and AISC 360 (2010), stress at 2.0% strain in BS 5950 (2003), Balarupan (2015) and Imran *et al.* (2018) as shown in Figure 3.31. As can be observed that, for temperatures 100 to 300 °C, the $k_{2.0,T}$ from the current test results are slightly below to those predicted by BS 5950 (2003) and Imran *et al.* (2018) curves, whilst for temperatures higher than 300 °C, the test result reduction factors agree well with the predicted values. The reduction factors from EC3-1-2 (2005) and AISC 360 (2010) are generally on the higher side (i.e. overpredicted) for all temperatures range. The design predictions proposed by Balarupan (2015) are in good agreement with the present test results. Statistical comparison of $k_{2.0,T}$ from current test results against the design predictions in BS 5950 (2003); EN1993-1-2. (2005); AISC 360 (2010); Balarupan (2015) and Imran *et al.* (2018) are presented in Table 3.10. It has been observed that the presently available reduction factors for stress at 2.0% strain in BS 5950 (2003); EN1993-1-2. (2005); AISC 360 (2010) and Imran *et al.* (2018) are not suitable for YSt-310 cold-formed steel tubular sections. The $k_{2.0,T}$ values provided by Balarupan (2015) are conservative with the mean value of 1.03 and COV of 0.16. However, the predictions are applicable up to 700 °C. Recommended resistance factors are provided in Table 3.10 to achieve the target reliability index.

The reduction factors for stress at 2.0% strain reported by previous researchers on cold-formed steel tubular section, namely Outinen *et al.* (2001); Balarupan (2015); McCann *et al.* (2015) and Imran *et al.* (2018) are also compared with the current test results and plotted against corresponding temperature in Figure 3.32. In addition, $k_{2.0,T}$ determined from the test are also compared with those predicted by EC3-1-2 (2005), AISC 360 (2010), BS 5950 (2003), Balarupan (2015) and Imran *et al.* (2018) as shown in Figure 3.32. The $k_{2.0,T}$ values generated from the current test are found to be

consistent with the test results reported in the literature, except some scatters have been observed in the temperatures range 200 to 400 °C. Table 3.11 presents the summary of the comparison of reduction factors obtained from the present test and literature with those provided in fire design provisions BS 5950 (2003); EN1993-1-2. (2005) and AISC 360 (2010) and proposals Balarupan (2015) and Imran *et al.* (2018). The $k_{2.0,T}$ values provided by EC3-1-2 (2005) and AISC 360 (2010) are generally non-conservative, especially for temperatures ranging from 400 to 800°C. The reduction factors provided by BS 5950 (2003) and Imran *et al.* (2018) are slightly overpredicted for temperatures, $100 < T < 300$ °C, whilst the predicted values for temperatures beyond 300 °C agree closely to the experimental values. It is to be mentioned that the reduction factors presented by BS 5950 (2003) and Balarupan (2015) are applicable up to 600 °C. Therefore, a set of design $k_{2.0,T}$ values considering lower bound test values, for various temperatures range up to 1000 °C is proposed herein (as presented in Table 3.12). It is shown that the proposed $k_{2.0,T}$ values are generally conservative (~ 10%) with COV value of ~ 0.31. Table 3.11 provides the recommended resistance factors to obtain reliability index of 2.5 and above.

3.4.8.5 Ultimate strength

The reduction factor for ultimate strength (i.e. $k_{u,T} = \sigma_{u,T} / \sigma_u$) determined from the current test programme are presented in Table 3.8 and compared these values with those provided in EC3-1-2 (2005), AISC 360 (2010) and Imran *et al.* (2018) as shown in Figure 3.33. As can be seen from the comparison that EC3-1-2 (2005) and Imran *et al.* (2018) predict slightly higher ultimate strength reduction factors for temperatures up to 400 °C, whilst for higher temperatures, the test results agree well with the design values. The design curve for $k_{u,T}$, presented in AISC 360 (2010) appears to be on the higher side for the temperatures range considered. Overall the statistical analysis reveals that the reduction factors provided in EC3-1-2 (2005), AISC 360 (2010) and Imran *et al.* (2018) are unconservative as detailed in Table 3.10. Resistance factors to achieve the target reliability index of 2.5 and above are also presented in Table 3.10.

The $k_{u,T}$ values calculated from the present tests as well as those reported in Balarupan (2015), McCann *et al.* (2015) and Imran *et al.* (2018) have been also compared with the design reduction factors in EC3-1-2 (2005), AISC 360 (2010) and Imran *et al.* (2018) as shown in Figure 3.34 and Table 3.11. The reduction factors predicted by EC3-1-2 (2005) compared with the combined test results and observed to generate conservative prediction with the mean value of 1.13, but high COV of 0.88. The $k_{u,T}$ curve proposed by Imran *et al.* (2018) seems to provide slightly upper bound values for temperatures up to 400 °C. However, for higher temperature, the proposed curve provides lower bound predictions to the test results (see Figure 3.34). The AISC 360 (2010) design provision predicts unconservative prediction with mean and COV of ~ 0.89 and 0.30, respectively. Overall, the present design provisions are found to be unsuitable, and therefore, design values for ultimate strength reduction factor are proposed as presented in Table 3.12. The design curve is able to provide a conservative prediction with the mean value of 1.19 and a lower COV of 0.34. Resistance factors are recommended for reliability indices of EC3-1-2 (2005), AISC 360 (2010), Imran *et al.* (2018) and proposed design values, which offers reliability index greater than 2.5.

3.4.8.6 Ultimate and fracture strains

The ultimate or tensile strain $\varepsilon_{u,T}$ is defined as the percentage strain corresponding to tensile strength. Reduction factor of tensile strain, $k_{\varepsilon_u,T}$ at various temperature ranges, obtained as the ratio of ultimate strain at elevated temperature, $\varepsilon_{u,T}$ to that at ambient temperature, ε_u recorded from the present test are reported in Table 3.8 and plotted in Figure 3.35. Since there is no prediction formula for ultimate strain in current design codes, design curve proposed by Chen and Young (2007), which was developed based on the experimental results of cold-formed steel (brake-pressed) has been utilised to compare the present test data (see Figure 3.35 and Table 3.10). As can be seen that the current ultimate strain reduction factors agreed well with the prediction formula, although there exists a significant scatter in the test data has been observed. The $k_{\varepsilon_u,T}$

generated from the test results from McCann *et al.* (2015) and Imran *et al.* (2018) as well as present test are also compared with the proposed curves by Chen and Young (2007) as shown in Figure 3.36 and summarised in Table 3.11. It can be seen that, although there is significant scatter of the test results, the design curve provides conservative prediction having mean of 2.75 and COV of 1.40. Resistance factor of 0.10 is recommended to achieve the target reliability index of 2.5 and above, which then resulted in $\beta = 2.66$. Hence, the design curve proposed by Chen and Young (2007) is recommended for reduction factor for strain corresponding to ultimate stress.

Currently no fire design provision provides reduction factor for ductility/elongation at fracture/fracture strain, $k_{\varepsilon_f,T}(=\varepsilon_{f,T}/\varepsilon_f)$. Therefore, the reduction factor formula for the fracture strain proposed by McCann *et al.* (2015) has been compared with the present test results as well as the combined test results (present and those reported by McCann *et al.* (2015)) shown in Figure 3.37. It can be seen from the figure that the curve slightly overpredicts the test results for temperatures up to 400 °C, whilst for higher temperatures the curve agrees well with the all test results. Hence, a modified design curve has been proposed herein (following McCann *et al.*, 2015, considering a polynomial expression of degree one) based on the lower bound values of combined test data as shown in Equations 3.2 and 3.3. Tables 3.10 and 3.11 present the summary statistical analysis. It is observed that the proposed design curve is able to provide improved conservative prediction with mean value of 2.20 and COV of 0.60. Resistance factor of 0.70 is recommended to offer a reliability index of 2.5 and above.

For $T \leq 200$ °C $\quad k_{\varepsilon_f,T} = \dfrac{\varepsilon_{f,T}}{\varepsilon_f} = 1 - 0.0046(T - 20°C)$ (3.2)

For $T > 200$ °C $\quad k_{\varepsilon_f,T} = \dfrac{\varepsilon_{f,T}}{\varepsilon_f} = -0.1082 + 0.0017(T - 20°C)$ (3.3)

3.5 POST-FIRE MECHANICAL PROPERTIES

3.5.1 General

The residual mechanical strength of Tata Structura YSt-310 cold-formed steel tubular sections after being exposed to elevated temperatures is presented in this section. First, the coupon specimens extracted from the flat regions have been exposed to predetermined elevated temperatures in the range ~ 300–800° C, and then the residual mechanical properties and hardness value have been estimated at ambient temperature after natural air cooling. The results from the experimental programme are reported in the form of post-fire stress-strain curves and associated basic material properties (e.g. elastic modulus, proof stresses, tensile strength, percentage elongation at fracture, Ramberg–Osgood material parameters etc.) as well as surface hardness values. The detailed descriptions of the test method such as high-temperature treatment, tensile coupon tests and microhardness measurements are described in the following sections.

3.5.2 Test specimens

The post-fire mechanical strength of YSt-310 cold-formed steel tubular sections has been studied using an SHS and two RHSs, *viz*., 50 × 50 × 2.9, 66 × 33 × 2.6 and 60 × 40 × 2.9. Flat coupon specimens of 6 mm width and 25 mm gauge lengths, have been extracted from the central flat portions of the faces perpendicular to the face containing weld line. The dimensions of coupon specimen conform to ASTM E21 (2009), AS 2291 (2007) and ISO 6892-2 (2011) and recent work on post-fire mechanical property (e.g. Huang and Young, 2017; Li and Young, 2018). Typical dimensions (in millimetres) of coupon specimen are detailed in Figure 3.38. As observed in Section 3.3.4, the yield and tensile strengths of coupons cut from the corner and weld regions have been found to be higher than those cut from flat regions, only the tensile coupons from the flat regions have been considered in the present study, to provide nominal material properties. The tensile coupon specimens have been cut in the longitudinal direction using a wire cut EDM.

3.5.3 Heat treatment

The tensile coupons have been exposed to different predetermined elevated temperatures using an electric furnace in the range of ~ 300–800 °C. In this test programme, the predetermined temperatures include 300 °C, 400 °C, 500 °C, 550 °C, 600 °C, 650 °C, 700 °C, 750 °C and 800 °C. However, temperatures at 100 °C and 200 °C are excluded as the post-fire mechanical performance of steel were reported to be unaffected, by earlier researchers such as Outinen and Mäkeläinen (2004); Qiang *et al.* (2012b); Lu *et al.* (2016) etc. The electric furnace, which has been utilised for investigating elevated temperature mechanical properties in Section 3.4.3, has been employed for preheating the coupon specimens. The coupon specimen has been placed at the middle of the heating chamber using a threaded pin *via* a hole provided in the coupon specimen during the heating and cooling process, and the lower end has been allowed to expand freely. A typical setup for heating the coupon specimen is shown in Figure 3.39. Three coupons, one from each cross-section, have been heated at the same time. During the heating process, glass wool has been used to seal any possible gaps to prevent any heat lost from the chamber. The coupon specimens have been heated at the rate of 20 °C/min until the attainment of the predetermined temperature. To ensure uniform temperature distribution over the tensile coupon specimen, the predetermined temperature is generally maintained for some time, (i.e. soak time). Earlier work have reported the use of soak times ranging from 20 to 40 minutes (e.g. Wang *et al.*, 2014; Huang and Young, 2017 etc.), however, it has been shown to have minimum/limited effect on the stress-strain curves for tensile coupon specimens. In the present study, the predetermined temperature has been maintained for 20 minutes, which is specified as the minimum holding time as per ASTM E21 (2009). The furnace has been stopped manually after the soak time has reached, and the specimen has been then allowed to cool down in the chamber. For further cooling down to room temperature (23 °C), the specimen has been taken out from the heating chamber once the furnace temperature reached below 100 °C. No artificial cooling techniques have been utilised to enhance the cooling process. The average value of

the temperatures recorded by the two internal thermocouples in each zone is used throughout the chapter to simplify the study.

3.5.4 Tensile coupon test

The basic stress-strain mechanical properties of cold-formed steel for both ambient and post-elevated temperature have been determined through tensile coupon test. A total of 27 coupon specimens have been tested at ambient temperature (~ 23 °C) after the heating and cooling process. The tensile test procedure detailed in Section 3.3.3 for the material test at ambient test has been followed here. The tensile test has been conducted on the 250 kN capacity loading frame, through the displacement control method with a displacement rate of 0.05 mm/min in the elastic range and 0.4 mm/min (beyond the elastic range) until failure as recommended by Huang and Young (2014c). The longitudinal strains have been recorded using the 25 mm gauge length extensometer. The test has been continued till the fracture point of the specimen so as to record the total percentage elongation. The test setup for tensile coupon test is shown in Figure 3.40.

3.5.5 Microhardness test

3.5.5.1 General

As mention in Chapter 2 above, tensile coupon test is a destructive process to evaluate the post-fire mechanical properties of steel and may not be the choice in the case where extraction of coupon specimens is impossible or difficult. In such an unavoidable situation, microhardness test could be utilised to evaluate the material strength after a fire event non-destructively by establishing reliable relationship/calibration between material strength and hardness value, H_v. The evaluation of material strength after a fire event can then be accomplished on-site using a portable hardness tester. In the present study, Vickers microhardness test has been performed to measure the post-fire hardness value, H_v^* from all coupons which

have been exposed to different predefined elevated temperature, *T* and the same has been utilised to develop a relationship with material strength.

3.5.5.2 Hardness test

Vickers microhardness tester has been employed to measure the surface hardness of coupon specimens after being exposed to different elevated temperatures. The hardness test has been performed after the tensile coupon test. The microhardness values have been measured, by carefully choosing surfaces, near the grip portions (but unaffected by hydraulic grips) of the coupon. The chosen surface has been then grounded on a rotating disk (water lubricated) equipped with silicon carbide paper, until a smooth and shiny metal surface has been achieved. The surface flakes have been removed during this process. Diamond shaped indents (see Figure 3.41) have been created on the surface of the sample with the help of a pyramidal indenter. The indent has been made at different locations with a separation of about 2–5 mm. A striking force of 500gf has been utilised to create the indent. The diagonal lengths of the indent have been recorded manually with measuring button and the hardness value, H_v has been automatically generated from the microhardness testing machine. The basic principle to calculate the hardness value is integrated with the testing machine which relied on Equation 3.4 (as given in Cruise, 2007),

$$H_v = k\frac{F}{A} = 0.102\left(\frac{2f\sin\left(\frac{\alpha}{2}\right)}{d_{av}^{\ 2}}\right) \tag{3.4}$$

where *A* is the area of indent formed on the surface of the specimen, *F* is the force applied (500gf), d_{av} is the average length of the two diagonal lengths and α is the internal angle of the indenter. Three hardness values have been measured randomly from different locations of the coupons and the average of the three hardness values reported in Table 3.13.

3.5.6 Experimental outcome

3.5.6.1 Tensile coupon test

In this section, the results from the tensile coupon test are discussed, and reduction factors $\left(k_{Expt}^{*}\right)$ are evaluated from the test results to estimate the deterioration in material strength due to elevated temperature. It is to be noted that the evaluated reduction factors and their corresponding reduction factors and predictive equations (presented in the later sections) from the previous research work, as well as proposed equations, are also plotted in the same figure, to avoid repetition.

3.5.6.1.1 Failure mechanism

All tensile coupons have been tested until fracture at ambient temperature after the coupons have been exposed to elevated temperatures. Typical failure modes of the coupons for 50 × 50 × 2.9 cross-section is shown in Figure 3.42, including the coupon specimen which has not been exposed to elevated temperature, for comparison purpose. It has been observed that all the coupon specimens failed, essentially in ductile mode, as identified by necking formation (i.e. brittle failure has not been seen) irrespective of the exposed temperature.

3.5.6.1.2 Stress-strain relationships

The stress-strain curves recorded from the tensile coupon tests are shown in Figures 3.43, 3.44 and 3.45 for 50 × 50 × 2.9, 60 × 40 × 2.9 and 63 × 33 × 2.6 cross-sections respectively. The temperatures in the legends indicate the maximum air temperature to which the specimens have been exposed inside the furnace. The post-fire stress-strain curves differ greatly from that of ambient temperature coupons (i.e. without heat treatment). It is observed that the stress-strain curves generated from the experimental programme exhibit a rounded curve followed by a moderate degree of strain hardening (due to cold-forming process) for specimens tested at ambient temperature (detailed in Section 3.3.4). However, for specimens tested after cooling down from being heated to a specified temperature above ~ 300 ºC, a clearly defined

yield point, yield plateau region and subsequently prominent strain hardening have been observed. The basic material parameters of tensile coupons exposed to temperature *T*, such as elastic modulus $\left(E_T^*\right)$, yield strength/0.2% proof stress $\left(\sigma_{0.2,T}^*\right)$, stress at 0.5% strain $\left(\sigma_{0.5,T}^*\right)$, stress at 1.5% strain $\left(\sigma_{1.5,T}^*\right)$, stress at 2.0% strain $\left(\sigma_{2.0,T}^*\right)$, tensile strength $\left(\sigma_{u,T}^*\right)$, percentage strain at tensile strength $\left(\varepsilon_{u,T}^*\right)$, percentage strain at fracture $\left(\varepsilon_{f,T}^*\right)$ and Ramberg–Osgood parameter $\left(n_T^*\right)$ have been determined from the stress-strain curves and summarised in Table 3.13 for all coupon specimens. The Ramberg–Osgood parameter $\left(n_T^*\right)$ at temperature *T* is calculated based on Equation 3.1, i.e., $n_T^* = \ln(4)/\sigma_{0.2,T}^*/\sigma_{0.05,T}^*$ where $\sigma_{0.2,T}^*$ and $\sigma_{0.05,T}^*$ are the stresses corresponding to the point of intersection of the stress-strain curve and proportional lines offset at 0.2% and 0.05% strains, respectively. A typical representation for the determination of key material properties is shown in Figure 3.10.

3.5.6.1.3 Elastic modulus

The post fire elastic modulus, E_T^* has been estimated as the slope of the initial linear portion of the stress-strain curves (similar to those followed in Qiang *et al.*, 2012b; Wang *et al.*, 2015; Lu *et al.*, 2016; and Kesawan and Mahendran, 2018) as shown in Figure 3.10. To illustrate the deterioration in the stiffness of the material after fire, the post-fire elastic modulus reduction factor is defined as ratio of elastic modulus of coupon, E_T^* tested at ambient temperature after cooling down from elevated temperature, *T* to that of ambient temperature coupon without fire exposure, *E*. The summary of the reduction factor of elastic modulus of the coupon specimens extracted from the three cross-sections is detailed in Table 3.14. Elastic modulus residual factor, $k_E^* = E_T^*/E$ of all coupon specimens are also plotted as a function of exposure temperature in Figure 3.46. It is observed from the figure that the elastic modulus reduction factor is scattered and not significantly affected by elevated/exposed temperature (up to ~800 °C). This is similar to the observations found in previous research work Kesawan and Mahendran (2018). On an average, the percentage

reduction factor of elastic modulus is ~ 6.99%. Thus, it can be concluded that YSt-310 cold-formed steel can regain closure to its ambient temperature stiffness after being exposed to elevated temperature up to 802 °C and hence favourable for reuse after cooling, as far as the stiffness values are concerned.

3.5.6.1.4 Yield strength

Yield strength constitutes an important material parameter used to define the grade of steel material and also as a key design parameter. Earlier research work on the post-fire mechanical properties of steel considered either 0.2% proof stress (e.g., Lu *et al.*, 2017a; Huang and Young, 2017) or stress corresponding yield plateau (e.g., Kesawan and Mahendran, 2018) as yield strength. The stress-strain curves generated from the present study are, (i) rounded without yield plateau for coupon specimens without heat treatment and (ii) distinctly defined yield stress followed by yield plateau for post-fire coupon specimens. However, the yield plateau in the stress-strain curves of most of the tensile test results of post-fire coupon specimens does not have a sufficiently flat portion to determine yield strength. Therefore, the 0.2% proof stress has been considered as the yield strength for all coupon specimen tested in the present study. The yield strength of all coupon specimens obtained from this experimental investigation is summarised in Table 3.13. The post-fire yield strength reduction factors, $k^{*}_{0.2,T}$ is defined as the ratio of yield strength of tensile coupons, $\sigma^{*}_{0.2,T}$ after cooling down from elevated temperature, T (heated up to 802 ºC) to the yield strength of unheated or parent coupon at ambient temperature $\sigma_{0.2}$ (i.e. without being exposed to fire). The yield strength reduction factors of the cross-sections considered are summarised in Tables 3.14. The reduction factors are also plotted as a function of different exposed temperatures in Figure 3.47. As seen in Figure 3.47, the post-fire yield strength of 50 × 50 × 2.9 and 66 × 66 × 2.6 cross-section is unaffected till 411.5 °C, however for 60 × 40 × 2.9; the yield strength is slightly reduced by ~ 5%. The average yield strength reduction factor for the three cross-sections at 411.5 °C is found to be 1.00, which signifies that the effect of heating up to 411.5°C is negligible on yield strength. However, when the temperature is above 411.5 °C, a significant

reduction in the yield strength has been observed. On an average, the reduction in the yield strength by ~ 13%, 30% and 41% have been found when the exposed the temperature are at 516.5 °C, 713 °C and 802 °C, respectively. In another word, cold-formed YSt-310 steel tubular sections are able to regain their ambient temperature yield strength up to ~ 87%, 70% and 59% after cooling down from being heated up to 516.5 °C, 713 °C and 802 °C, respectively.

3.5.6.1.5 Tensile strength

The tensile strength reduction factor, $k_{u,T}^{*}$ is defined as the ratio of the tensile strength of coupon after cooling down from elevated temperatures *T*, $\sigma_{u,T}^{*}$ to that of ambient temperature without exposed to fire, σ_u . Figure 3.48 describes the ultimate strength reduction factors plotted as a function of different exposed temperatures. It has been observed that the amount of yield strength reduction (in post-fire condition) is more prominent than that of tensile strength when the exposed temperature exceeds ~ 400 °C. Similar findings were reported by Lu *et al.* (2016). The deterioration in the residual tensile strength is found to be unaffected below 411.5 °C, however as the exposed temperature increases beyond 411.5 °C, a gradual decrease in tensile strength has been observed. The reduction in tensile strengths are found to be ~ 84% and 77% when the exposed temperatures are at 713 °C and 802 °C, respectively. Therefore, it may be concluded that YSt-310 cold-formed steel can regain its ambient temperature tensile strength ~ 75% after being exposed to elevated temperature up to 802 °C and hence favourable for reuse after post-fire.

3.5.6.1.6 Ductility

The ductility of steel denotes the level of plastic deformation that the material can undergo before fracture and is defined as the ratio of gauge length at fracture to the initial gauge length of the tensile coupon. The effect of exposed temperature on the post-fire mechanical strength is examined by comparing the percentage elongation at fracture of coupons exposed at different levels of elevated temperature. The post-fire

ductility reduction factor, $k^*_{\varepsilon_f,T}$ is defined as the ratio of percentage elongation at fracture, $\varepsilon^*_{f,T}$ of coupon after cooling down from elevated temperatures, T to that of ambient temperature without exposed to fire, ε_f. The ductility reduction factors at different levels of exposed temperatures are summarised in Table 3.14 and also plotted in Figure 3.49. It has been observed that, on an average, the ductility reduction factor is decreased by ~ 30% of unheated coupon at the exposed temperature of 411.5 °C and then gradually increased by ~ 45 % at 802 °C. Overall, all the coupon specimens are able to retain the nominal elongation/ductility levels specified in IS 4923 (1997) after cooling down from temperature as high as 802 °C and hence favourable for reuse at the post-fire condition.

3.5.6.2 Microhardness test

The hardness value reduction factors $k^*_{H_V,T}$ are calculated as the ratio of microhardness values of post-fire coupons after experiencing heat treatment, $H^*_{v,T}$ to that of non-heated parent material coupons, H_v and are summarised for all three cross-sections in Table 3.14. The hardness value reduction factors are plotted against the preselected exposed temperature in Figure 3.50. It has been seen from the figure that a similar trend as that of yield and ultimate strength reduction factors have been observed. The hardness values of coupon specimens heated up to 411.5 °C are found to be similar to that of original parent material surface hardness. Reduction in the surface hardness is observed to be gradually decreasing when the exposed temperature reaches above 411.5 °C, and the minimum value is about ~ 75% of parent hardness value at 802 °C. Therefore it can be concluded that ~ 75% of original material surface hardness can be regained after cooling from being exposed to a maximum temperature of 802 °C.

3.5.7 Comparison with previous investigations

In this section, the post-fire mechanical property reduction factors from existing literature of various cold-formed steel grades, *viz.*, S355 by Outinen and Mäkeläinen

(2004), and Outinen (2007); Q235 by Lu *et al.* (2016); and G450 and G350 by Kesawan and Mahendran (2018) are compared with the present test results (see Figures 3.51–3.54. Further, the reduction factor based on predictive equations proposed by earlier researchers: Gunalan and Mahendran (2014); Lu *et al.* (2016); Kesawan and Mahendran (2018), are assessed to the present test results of YSt-310 steels and then their suitability has been checked (see Figures 3.46–3.48). The discussion covers only the results of material extracted from the flat regions of the cold-formed tubular steel section.

3.5.7.1 Reduction factors

3.5.7.1.1 Elastic modulus

The comparison of post-fire elastic modulus reduction factors of existing cold-formed steel results with the present test results is presented in Figure 3.51. As discussed in Section 3.5.6.4, the elastic modulus reduction factors of YSt-310 are scattered and no significant reduction has been observed similar to that of G450 and G350 reported by Kesawan and Mahendran (2018) and S355 by Outinen and Mäkeläinen (2004). Overall, about 55.79% of the data points are below the parent ambient temperature elastic modulus for T > 300 °C. It may be concluded that residual elastic modulus of all steel grades is scattered within ± 20 GPa which is similar to the case of ambient temperature (unheated) tensile coupon test results. Thus considering such scatters, it can be said that elastic modulus reduction factor is unaffected by the post-fire condition.

3.5.7.1.2 Yield strength

Figure 3.52 shows the comparison of post-elevated yield strength reduction factors from the present study with those of previously reported cold-formed steel tubular sections. The reduction in the yield strength for YSt-310 steel (yield stress = 310 MPa) with increasing exposed temperature is found to be similar for all steel grades previously studied: Outinen and Mäkeläinen (2004); Outinen (2007); Lu *et al.* (2016) and Kesawan and Mahendran (2018), for temperature above 300 °C. On an average,

the maximum percentage reduction at ~ 800 °C is found to be ~ 50%, which signifies that 50% of ambient temperature yield strength can be regained after being exposed to ~ 800 °C.

3.5.7.1.3 Tensile strength

The tensile strength reduction factors derived from the present test results are compared with those previously studied by researchers (such as Lu *et al.*, 2016; Kesawan and Mahendran, 2018) and is shown in Figure 3.53. A similar trend in the tensile strength reduction factor as that of yield strength reduction factor has been observed, however the reduction in tensile strength (~ 66% at ~ 800 °C) is found to be lower than that of yield strength (~ 50% at ~ 800 °C) for all cold-formed steels considered.

3.5.7.1.4 Ductility

The reduction factors for percentage elongation at fracture or ductility, determined from the present test results are compared with those reported by Lu *et al.* (2016) and is presented in Figure 3.54. It can be observed that the ductility reduction factors reported by Lu *et al.* (2016) shows slightly higher values as compared present test data. This may be associated with lower grade of steel used in Lu *et al.* (2016) as compared to the present test steel grade. A similar observation was reported by Gunalan and Mahendran (2014) based on the test results of cold-formed steel sheets.

3.5.7.1.5 Evaluation of existing empirical formulae

The prediction formulae proposed by previous researchers (Gunalan and Mahendran, 2014; Lu *et al.*, 2016; Kesawan and Mahendran, 2018) based on the post-fire reduction factors of various cold-formed steels have been checked against the present test results to assess the applicability on YSt-310 steel material, as shown in Figures 3.46–3.48. It is shown that the formulae proposed by Kesawan and Mahendran (2018) for yield strength and tensile strength reduction factors are able to provide conservative predictions of 8% and 11% respectively when compared to present test results.

However, reduction factors predicted by the other formulae proposed by researchers such as Gunalan and Mahendran (2014); Lu *et al*. (2016), based on earlier work on post-fire mechanical properties of cold-formed steel are found to be unsuitable. Therefore, accurate design equations have been developed to predict the post-fire mechanical property reduction factors based on the present test data as well as a combination of previous and present test results separately. A new set of equations to predict post-fire yield strength and ultimate strength based on the microhardness values (H_v) have also been proposed based on the present microhardness test results, in the following sections.

3.5.8 Prediction formulae

3.5.8.1 Present test results

3.5.8.1.1 Reduction factors

A set of design prediction formulae to determine the post-fire reduction factor, $\left(k^*_{\mathrm{Pred}}\right)$ for elastic modulus, yield strength, tensile strength, percentage elongation at fracture and microhardness value as a function of predetermined elevated temperature, *T* for YSt-310 cold-formed steel has been developed based on the present test results and are summarised in Table 3.15. The lower bound values of the reduction factors corresponding to the exposed temperature have been utilised to develop the predictive equations. The comparison of the residual reductions factors predicted by proposed equations with those obtained from present study are shown in Figures 3.46–3.50. The applicability of the predictive equations proposed herein is accessed through reliability analysis in Section 3.5.9.

3.5.8.1.2 Material strength and hardness

As mentioned in Section 3.5.5, microhardness test is a quick and easier way to evaluate the post-fire material strength as the amount of material required is very less as compare to tensile coupon test. Based on the present test results, two formulae to

establish a relationship between the post-fire yield strength and tensile strength as a function of microhardness values have been developed. The correlation between yield strength and tensile strength against hardness value are plotted in Figures 3.55 and 3.56 and then generate a linear relationship using least square regression method. The resulting relationships are given in Equations 3.5 and 3.6, and the corresponding R^2 values are 0.7742 and 0.7732 for yield strength and tensile strength, respectively.

$$\sigma_{0.2}^{*} = 3.3154 H_{v}^{*} - 144.15 \tag{3.5}$$

$$\sigma_{u}^{*} = 2.4363 H_{v}^{*} 74.476 \tag{3.6}$$

3.5.8.1.3 Stress-strain curve

With the growing use of advanced numerical tools in structural engineering, the need of accurate material models has been increasing. In this section, the suitability of presently available material models are accessed with the post-fire stress-strain curves of YSt-310 cold-formed steel. As described in Section 3.5.6.3, the stress-strain profile of YSt-310 cold-formed steel follows a rounded non-linear curve for specimens without heat treatment whereas for specimen tested at ambient temperature after being exposed to elevated temperature (~ 300–800 °C) exhibits definite yield point followed by yield plateau. It is recommended that the two-stage stress-strain model proposed by Mirambell and Real (2000) using the first (*n*) and second (*m*) strain hardening exponent proposed by Arrayago *et al.* (2015) for specimen at ambient temperature as expressed in Equation 3.7 of Table 3.16. It is to be noted that, for the post-fire stress-strain characteristics, the material model proposed by Tao *et al.* (2012) which has been originally developed by Mander (1983), as given in Equation 3.8 of Table 3.16 is recommended. However, the expressions for $\varepsilon_{p,T}^{*}$ and $E_{p,T}^{*}$ is modified based on the present test results using least square regression analysis. The comparison of test and predicted stress-strain curves for 50 × 50 × 2.9 cross-section at different level of exposed elevated temperatures are shown in Figure 3.57.

3.5.8.2 Combined test results

A separate set of design prediction formulae considering all grade of steels previously studied and present test results has been developed to predict the post-fire reduction factors for elastic modulus, yield strength, tensile strength and percentage elongation at fracture. The test results from earlier research work: Outinen and Mäkeläinen (2004); Outinen (2007); Lu *et al.* (2016); and Kesawan and Mahendran (2018) have been taken into account to developed the predictive model. The proposed design equations for elastic modulus, yield strength, ultimate strength and percentage elongation at fracture reduction factors are presented in Figures 3.51–3.54 respectively and also summarised in Table 3.17. The compatibility of the developed post-fire reduction factor formulae are discussed in Section 3.5.9 by using reliability analysis.

3.5.9 Reliability analysis

In this section, the applicability of the proposed formulae has been assessed by comparing its predicted values with the experimental data of the post-fire mechanical properties of YSt-310 and combined test results for cold-formed steel reported by research including the present test results using reliability analysis, similar to those detailed in Section 3.4.7 of this thesis. The comparison of the test results against the design predictions are given in Tables 3.14 and 3.18 separately for present test data of YSt-310 steel and consolidated test data from various steel grades from Outinen and Mäkeläinen (2004); Outinen (2007); Lu *et al.* (2016); and Kesawan and Mahendran (2018) with current experimental results. The mean and coefficient of variance from the comparisons have been estimated. The resistance factors (ϕ) of 0.9, recommended by Huang and Young (2017) for elastic modulus, yield strength and ultimate strength reduction factor for ferritic stainless steel has been considered. However, resistance factors (ϕ) of 0.85 and 0.9 respectively, have been adopted for elongation at fracture and microhardness reduction factor to determine the target reliability index.

Based on the present test results presented in Table 3.14, the mean values of the reduction factor of post-fire elastic modulus, yield strength, tensile strength, percentage elongation at fracture and micro-hardness are 1.09, 1.09, 1.06, 1.17 and 1.05 and their corresponding coefficient of variances are 0.09, 0.08, 0.05, 0.21 and 0.05 respectively. The calculated reliability indexes of all reduction factors are found to be greater than 2.5, and hence the proposed equations for YSt-310 cold-formed steel are reliable.

Similarly, the mean values from the comparison of post-fire mechanical property reduction factors from the present study as well as the results from existing test results of different steel grades reported by the authors: Outinen and Mäkeläinen (2004); Outinen (2007); Lu *et al.* (2016); and Kesawan and Mahendran (2018), against the reduction factors from the predicted equations are 1.11, 1.11, 1.08 and 1.22 for elastic modulus, yield strength, tensile strength and percentage elongation at fracture and the corresponding coefficient of variances are 0.12, 0.09, 0.07 and 0.24 respectively. The details of the comparison is presented in Table 3.18. The proposed design equations considering the cold-formed steel test results from existing literature and present experimental results, for the prediction of post-fire reduction factors of elastic modulus, yield strength, tensile strength and percentage elongation at fracture are reliable as the calculated reliability indexes are greater than 2.5.

3.6 SUMMARY

In this chapter, a systematic and extensive investigation on the material characteristics of one of the most widely used structural steel: YSt-310 cold-formed steel tubular section, manufactured by Tata Structura Tubes Division (2019) is presented. The tests have been conducted in three different temperatures: ambient temperature, elevated temperature and post-fire conditions. Key concluding remarks drawn from the study, based on the temperature considered, are presented in the following subsections.

3.6.1 Ambient temperature material test

A comprehensive experimental programme to investigate material characteristics of YSt-310 cold-formed SHS and RHS under ambient temperature condition has been conducted. Results from elemental analysis *via* from optical emission spectrometer (OES) investigation, metallographic examination using optical microscope and mechanical properties through tensile coupon test have been presented. A total of 21 coupon specimens have been tested at ambient temperature (~ 21 ºC) and key stress-strain parameters *viz*., Young's modulus, proof stresses, ultimate strength, percentage elongation, strain hardening exponent etc., have been generated from based on flat, corner and weld coupon tests data. Based on the ambient temperature test results following conclusions are made:

a) Based on the metallographic examination, a difference in the morphology of flat and corner grains has been observed: the grains in the flat region are found to be relatively larger in comparison to those of corner regions wherein the grains are smaller and elongated.

b) From the tensile coupon test results, it has been observed that the mean values of Young's modulus of curved and weld coupons are similar but slightly lesser than those of flat coupons, whilst average the 0.2% proof stress and ultimate stress of the curved coupon are respectively 26% and 34% more than those of flat coupons. The tensile test results of weld coupon are found to be similar to those of curved coupon specimens.

3.6.2 Elevated temperature material test

An experimental programme to determine the mechanical properties of YSt-310 cold-formed steel tubular sections under steady-state elevated temperatures has been presented. A total of 31 tensile coupon specimens, extracted from two squares and rectangular tubular sections, have been tested at various temperature levels ranging from ambient to 800 °C approximately. Key material properties such as Young's

modulus; yield stress; stresses corresponding to 0.5%, 1.5% and 2.0% strains; ultimate strength and corresponding strains (%); fracture strains (%) and Ramberg–Osgood parameter estimated from the elevated temperature stress-stain curves have been reported. The reduction factors of the material parameters from the current test programme have been computed and compared with those provided in current design provisions such as European, EC3-1-2 (2005); Australian, AS 4100 (1998); American, AISC 360 (2010); British Standards, BS 5950 (2003); and Indian Standard IS 800 (2007), as well as those reported by earlier researchers such as Outinen *et al.* (2001); Chen and Young (2007); Balarupan (2015); McCann *et al.* (2015); and Imran *et al.* (2018). Based on the comparison, the following conclusions are made:

a) The reduction factors of the material properties reported in the past for cold-formed steel tubular sections are in close agreement (within a scatter band) with the present test results, although the scatter is relatively higher for the case of elastic modulus reduction factor.

b) Reduction factors (except for elastic modulus) presented in most of the current design standards (based on hot-rolled steels) are found to be not suitable for cold-formed steel tubular sections.

c) The elastic modulus and yield strength reduction factors provided in Indian Standard, IS 800 (2007) are not suitable for YSt-310 cold-formed steel tubular sections.

d) The ultimate strain reduction factor curve proposed by Chen and Young (2007) based on the brake-pressed cold-formed steel is found to be suitable for cold-formed steel tubular sections.

e) Reduction factors for 0.2% proof stress; stresses corresponding to 0.5%, 1.5% and 2.0% strains; ultimate stress and fracture strain (%) are proposed based on both present and literature test results, and found to offer improved mean (conservative) reliable predictions. Hence it is therefore recommended for inclusion in the future revision of fire design codes.

3.6.3 Post-fire material test

An experimental investigation to study the post-fire mechanical properties of YSt-310 cold-formed steel has been presented. The flat coupon specimens extracted from the flat regions of YSt-310 cold-formed steel sections have been exposed to nine pre-selected elevated temperatures ranging from ~ 300–800 °C and maintained for a soak time of 20 minutes. The coupon specimens have been then cooled down to ambient temperature through natural air cooling method inside the furnace chamber. The post-fire mechanical properties determined from the stress-strain curves generated through tensile coupon test as well as microhardness values using Vickers's hardness test have been documented in this chapter. Based on the test results following points are made:

a) The post-fire elastic modulus of YSt-310 cold-formed steel are scattered but no significant reduction with exposed temperature have been observed.

b) The post-fire yield strength and tensile strength are able to retain at its parent material ambient temperature material strength when the exposed temperature is below ~ 400 °C, but significantly reduced to ~ 59% and 77% respectively when exposed to ~ 800 °C.

c) The surface hardness of YSt-310 steel is found to retain its parent material till 400 °C, but reduced by ~ 25% when the exposed temperature is at ~ 800 °C.

d) Two correlations between yield and tensile strengths against hardness value have been developed to provide an alternative for determining material strengths, without actually performing tensile coupon test.

e) Two sets empirical equations are proposed separately to predict the residual post-fire reduction factors based on the i) current experimental results of Tata Structura YSt-310 cold-formed steel, and ii) cold-formed steel of various grades presently available in the literature. The applicability of the proposed design formulae has been checked through reliability analysis and found to provide excellent agreement when compared with the test results.

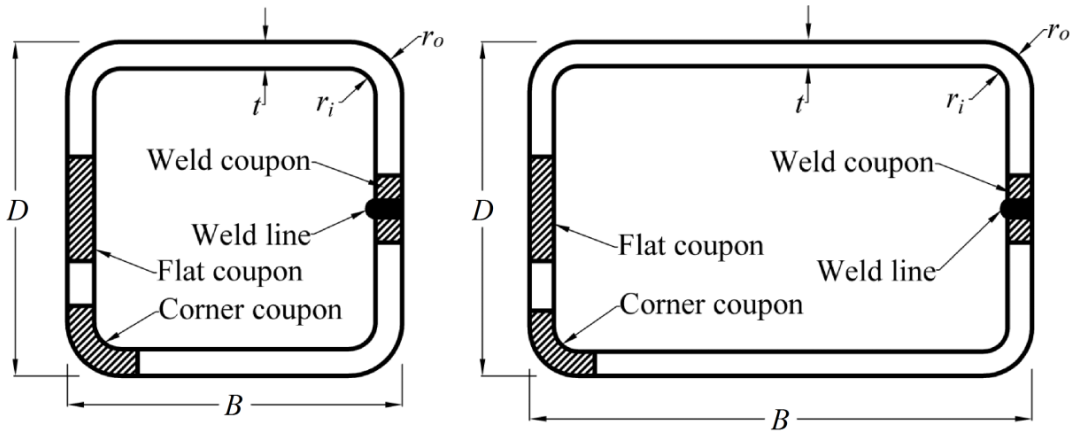

(a) (b)

Figure 3.1: Definition of symbols and position of coupon specimens in (a) square and (b) rectangular hollow sections

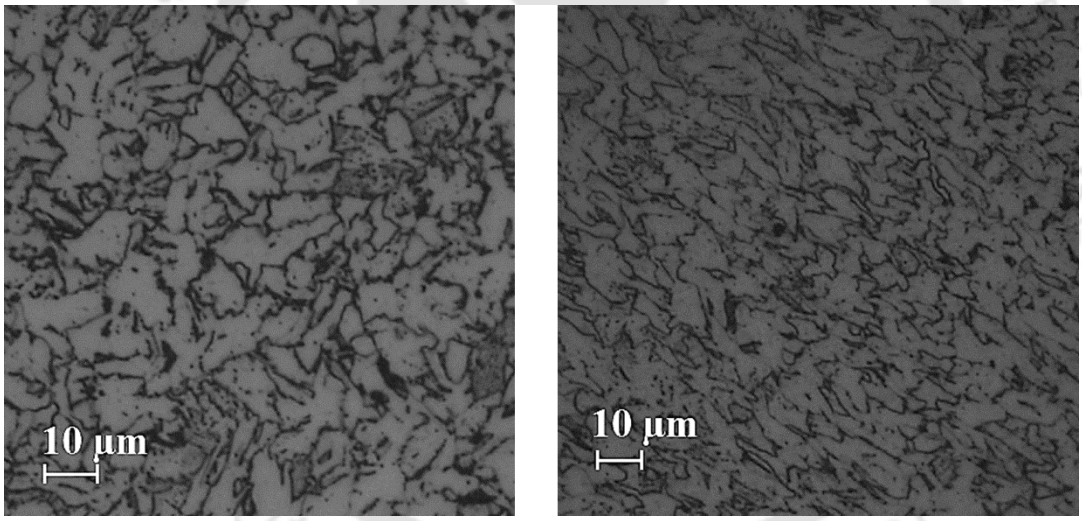

(a) (b)

Figure 3.2: Microstructure for 66 × 33 × 2.6 at (a) flat and (b) corner regions

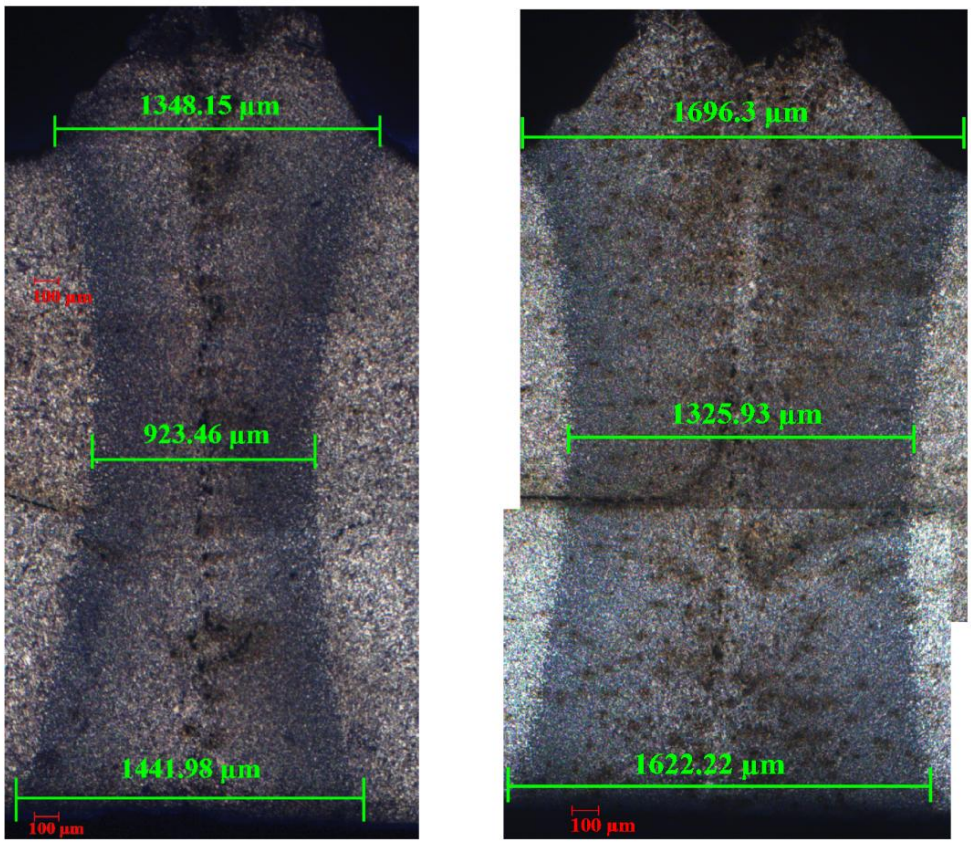

(a) (b)

Figure 3.3: Size of welds seen through optical microscope for (a) 60 × 40 × 2.9 and (b) 66 × 33 × 2.6 cross-sections

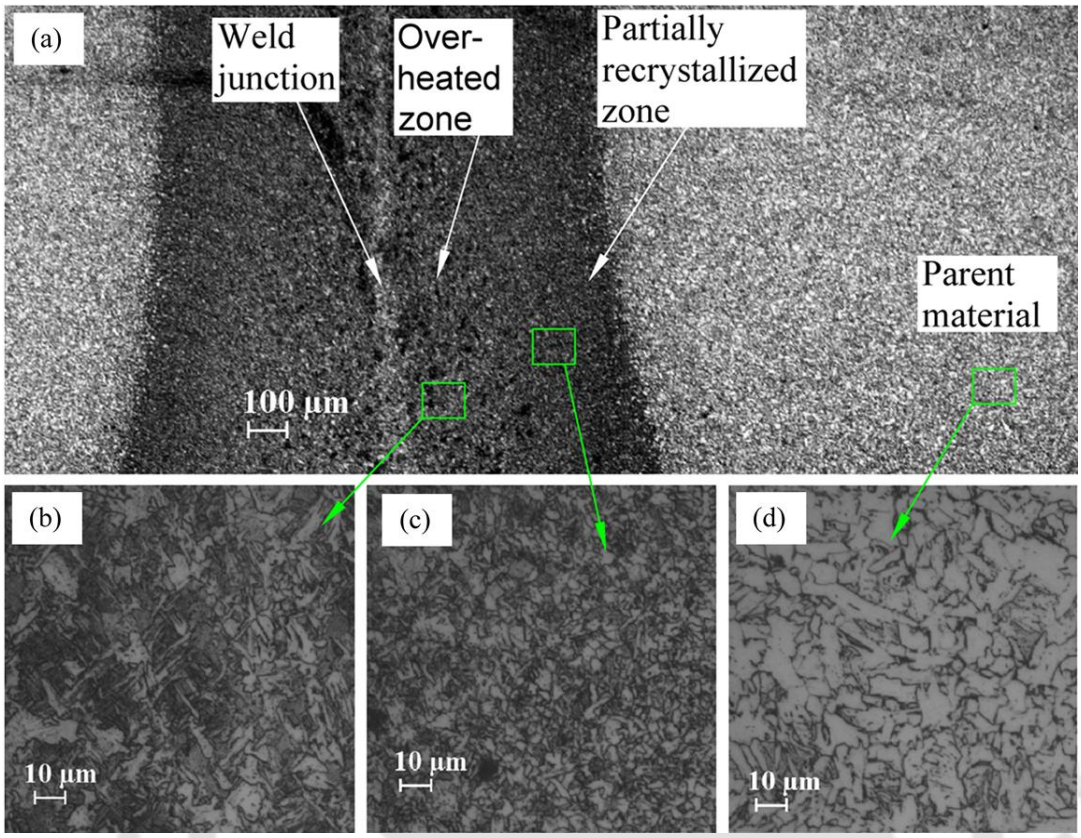

Figure 3.4: Typical microstructures: (a) HFIW seam for sample 66 × 33 × 2.6, (b) Widmanstätten, (c) partially-recrystallized zone and (d) parent material

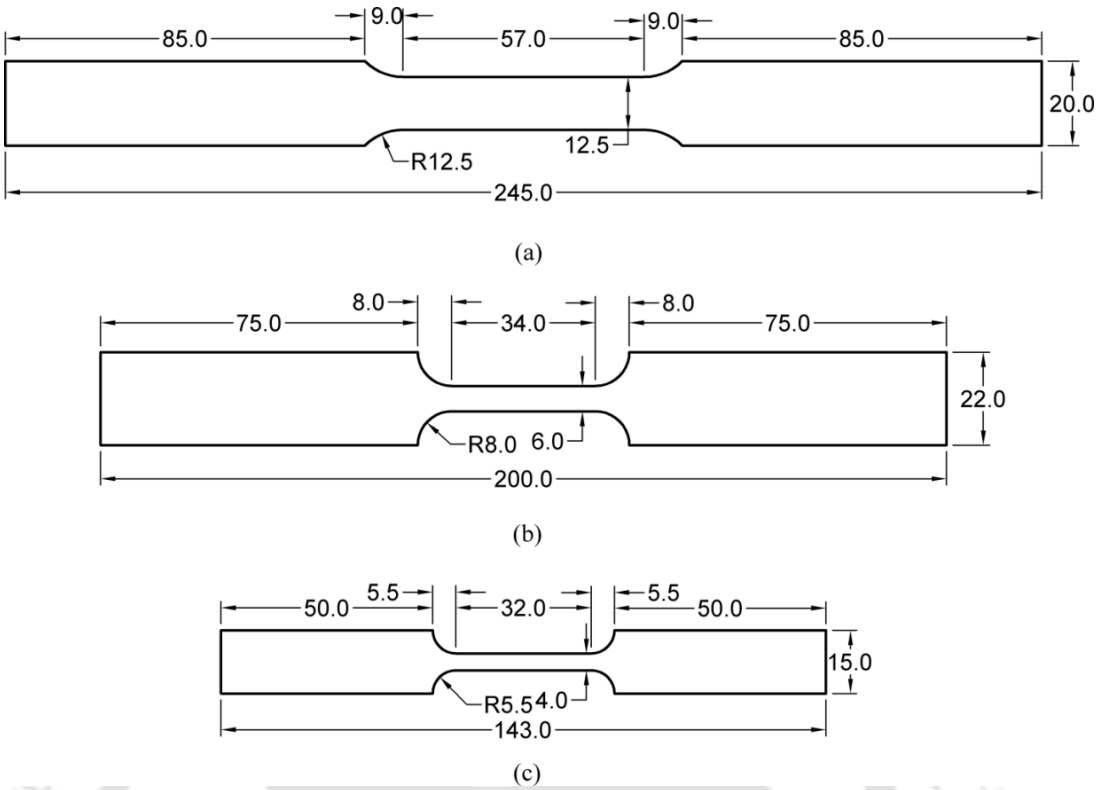

Figure 3.5: Dimensions (mm) of: (a) flat, (b) corner and (c) weld coupon specimens

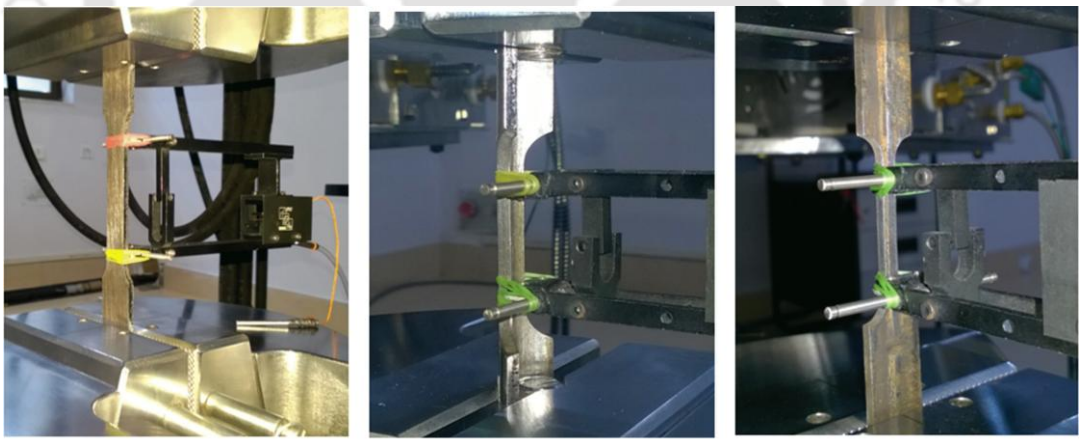

(a) (b) (c)

Figure 3.6: Ambient temperature tensile tests setup for (a) flat, (b) curve and (c) weld coupons

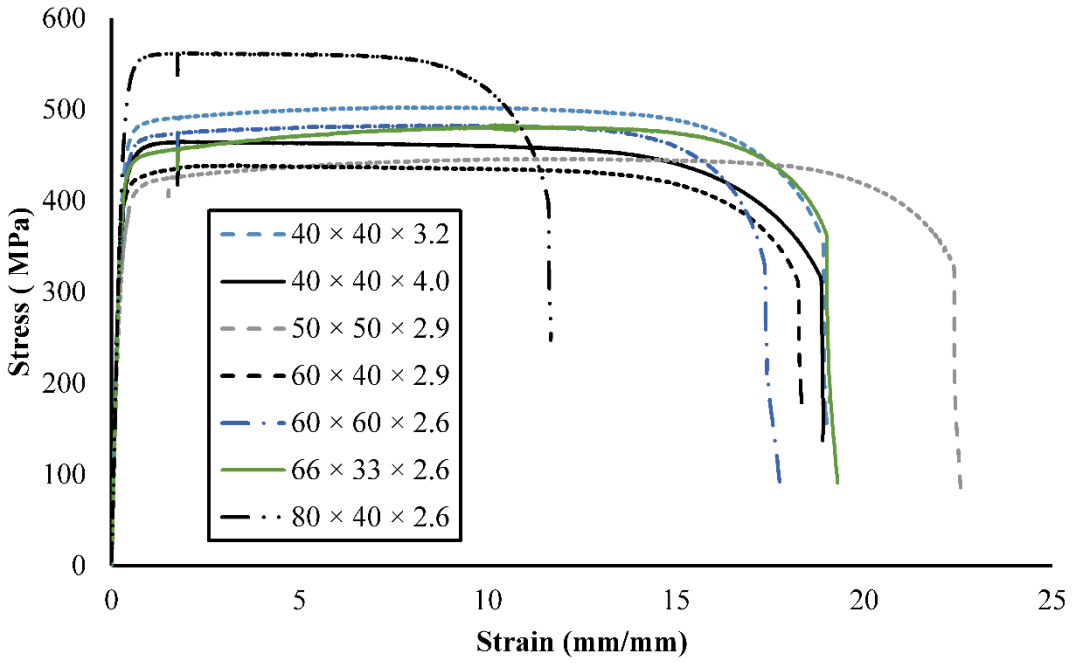

Figure 3.7: Stress-strain curves generated from the flat tensile coupon tests at ambient temperature

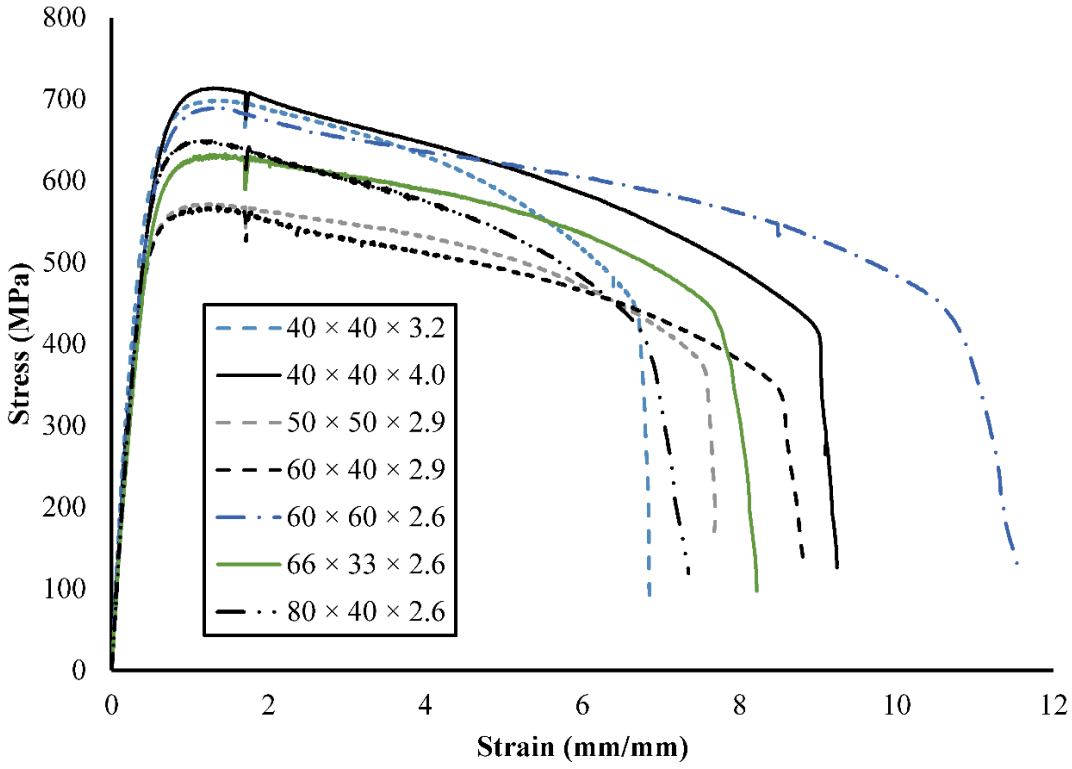

Figure 3.8: Stress-strain curves generated from the corner tensile coupon tests at ambient temperature

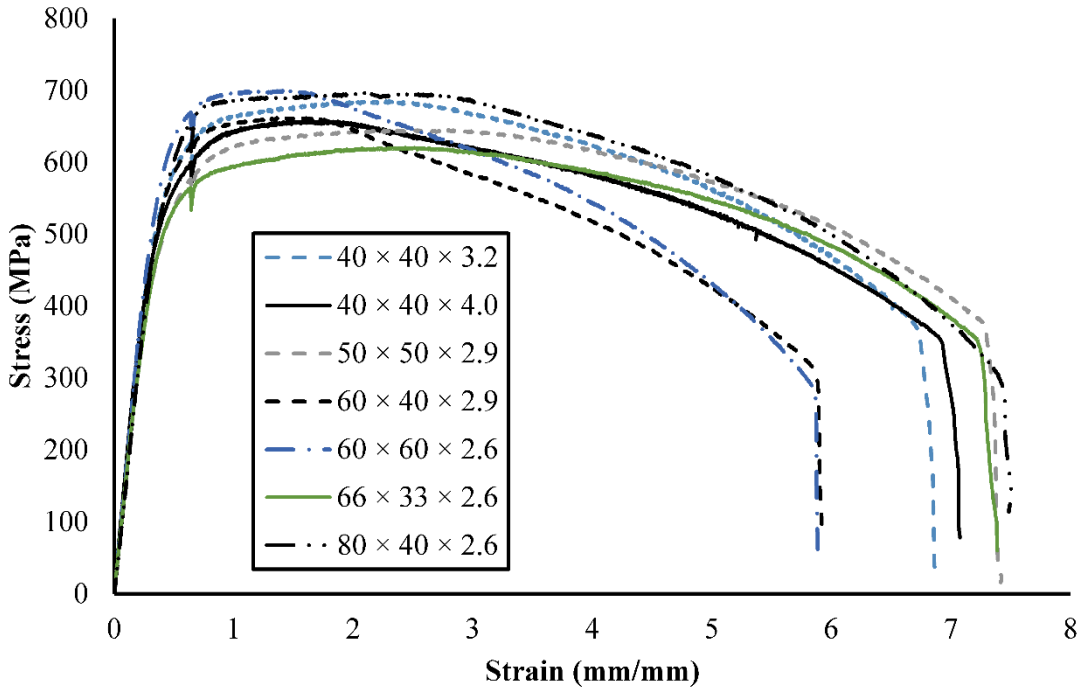

Figure 3.9: Stress-strain curves generated from the weld tensile coupon tests at ambient temperature

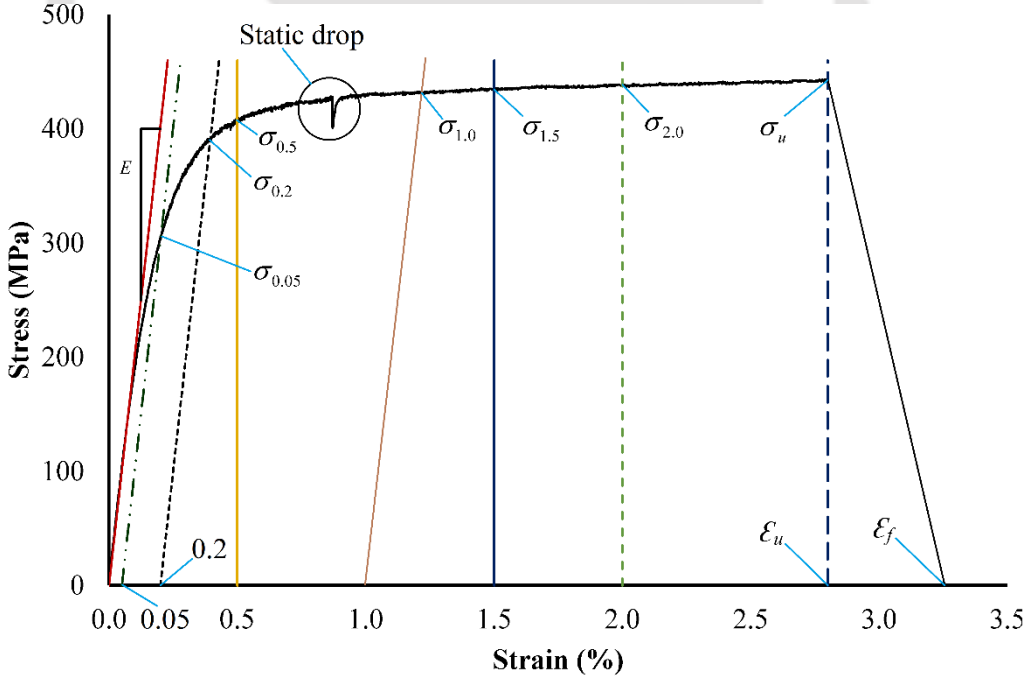

Figure 3.10: Definitions of mechanical parameters

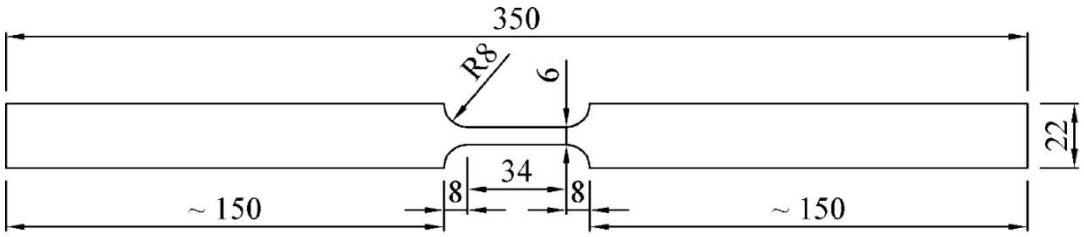

Figure 3.11: Dimensions (mm) of coupon specimen for elevated temperature tensile coupon tests

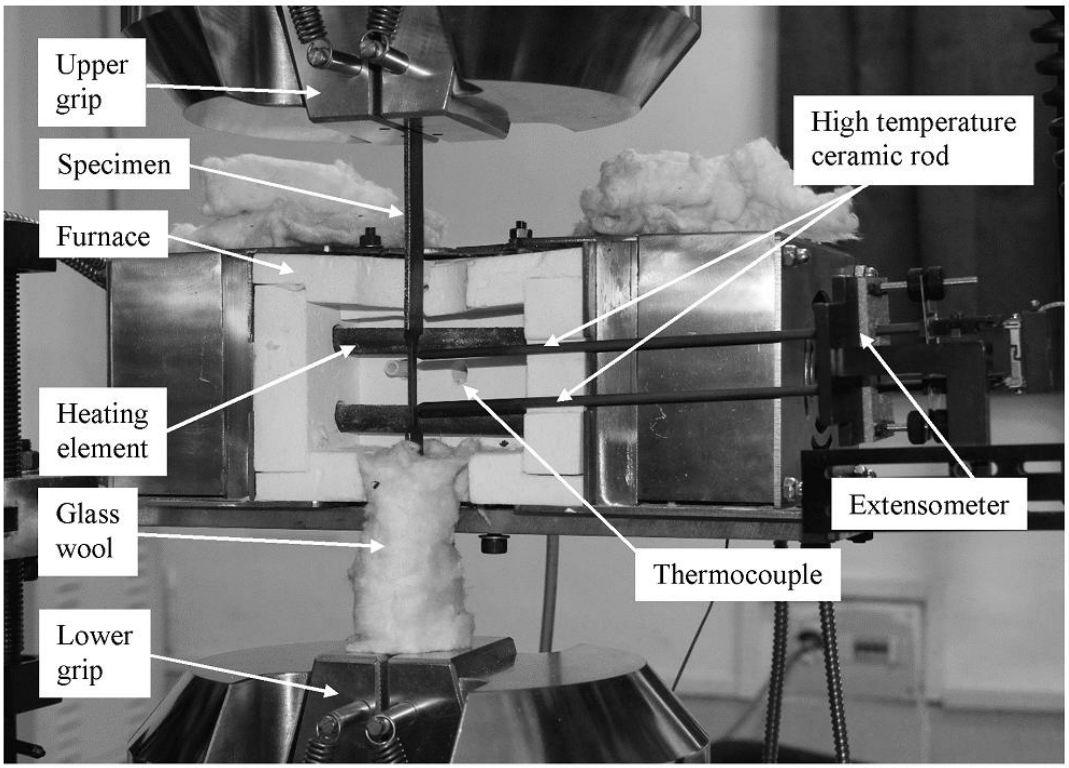

Figure 3.12: Instrumental setup for elevated temperature tensile coupon tests

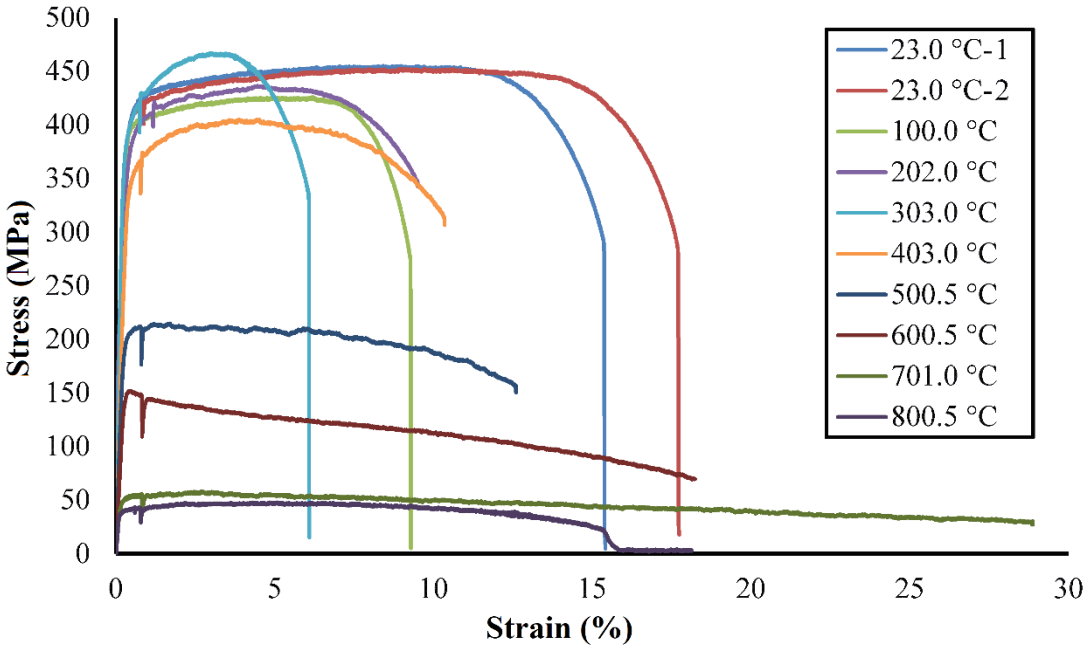

Figure 3.13: Stress-strain curves at different elevated temperatures for 50 × 50 × 2.9 cross-section

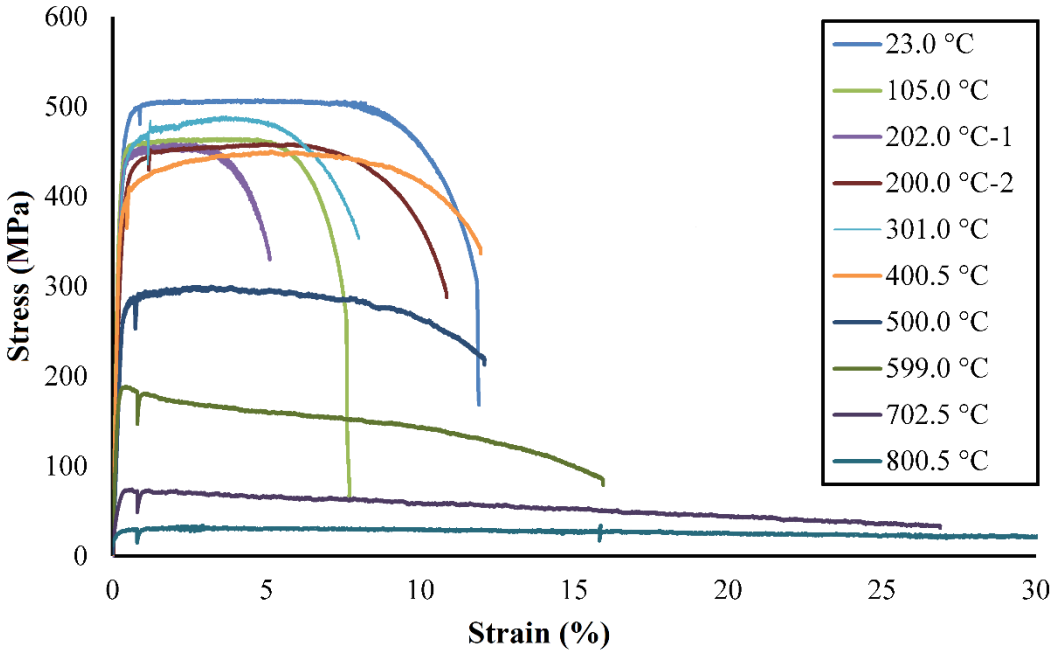

Figure 3.14: Stress-strain curves at different elevated temperatures for 60 × 60 × 2.6 cross-section

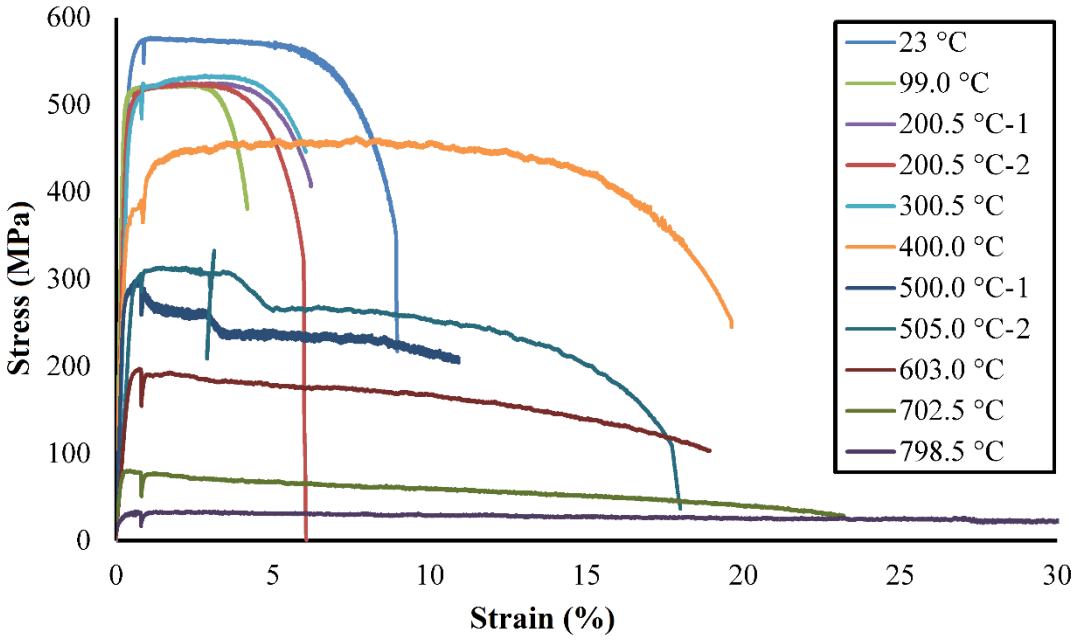

Figure 3.15: Stress-strain curves at different elevated temperatures for 80 × 40 × 2.6 cross-section

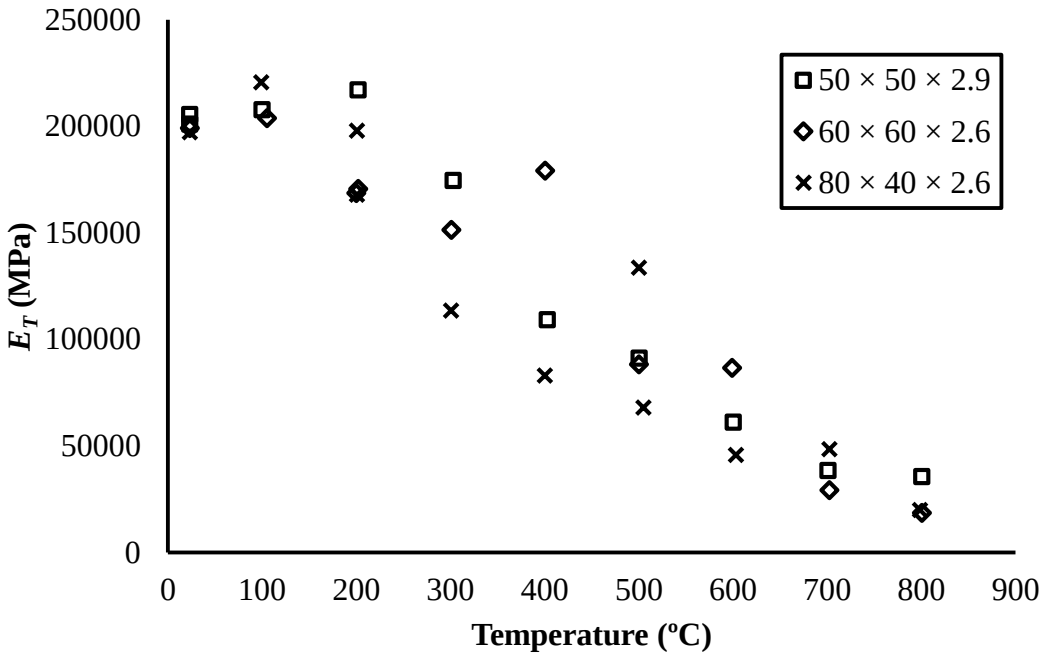

Figure 3.16: Measured moduli of elasticity at various elevated temperatures measured from tensile coupon tests.

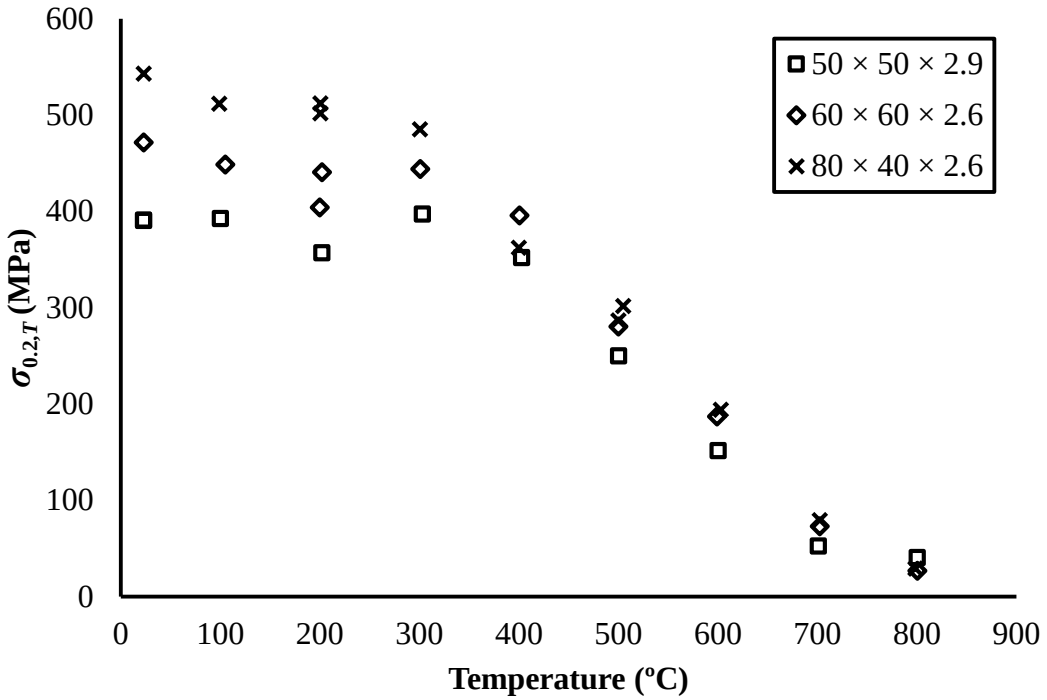

Figure 3.17: Measured yield stress or 0.2% proof stresses from the tensile tests

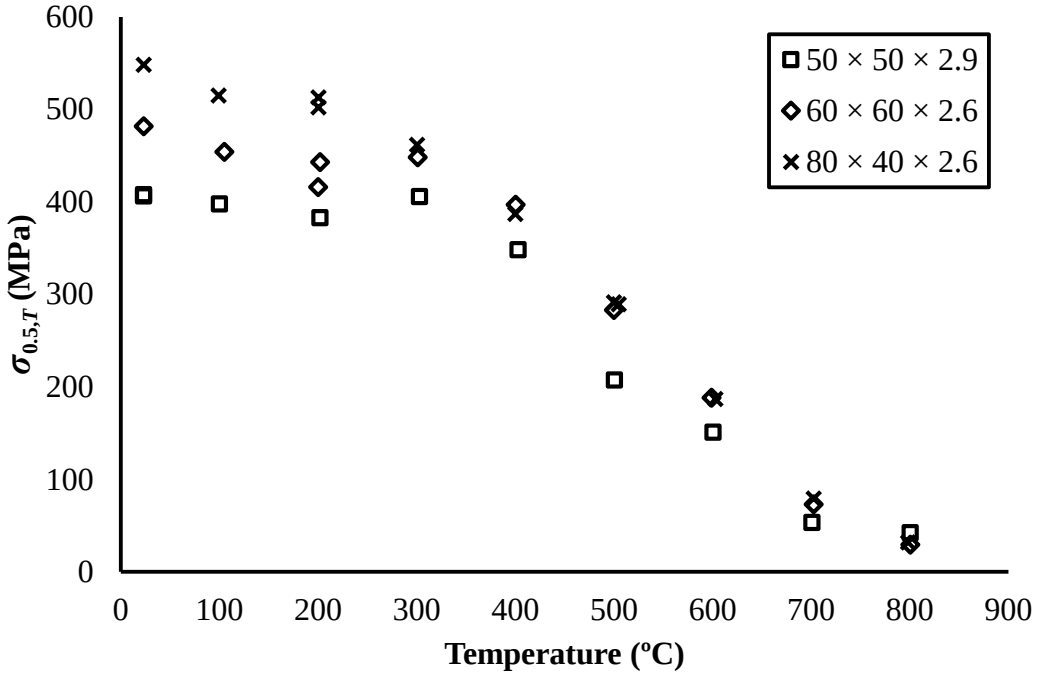

Figure 3.18: Measured values of stress corresponding to 0.5% strain at various elevated temperatures

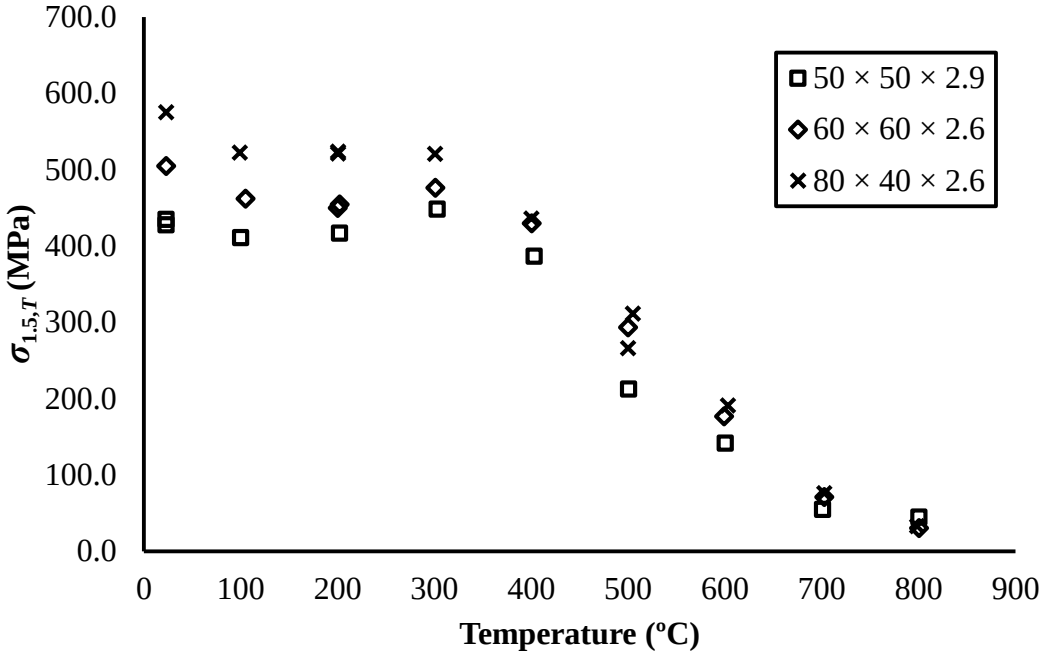

Figure 3.19: Measured values of stress corresponding to 1.5% strain at different elevated temperatures

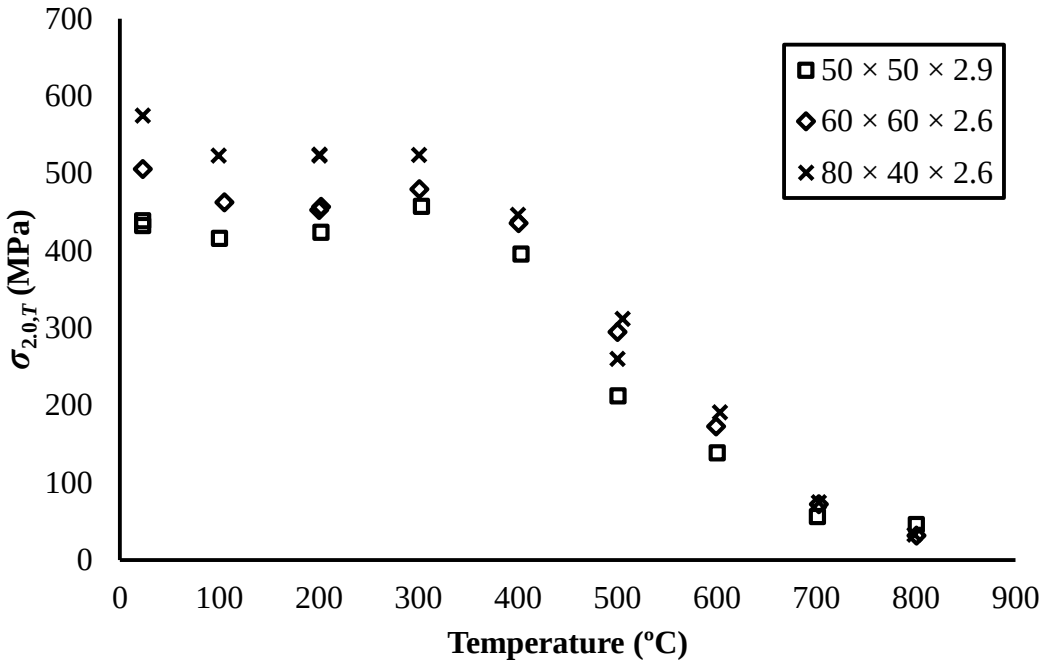

Figure 3.20: Measured values of stress corresponding to 2.0% strain at various elevated temperatures

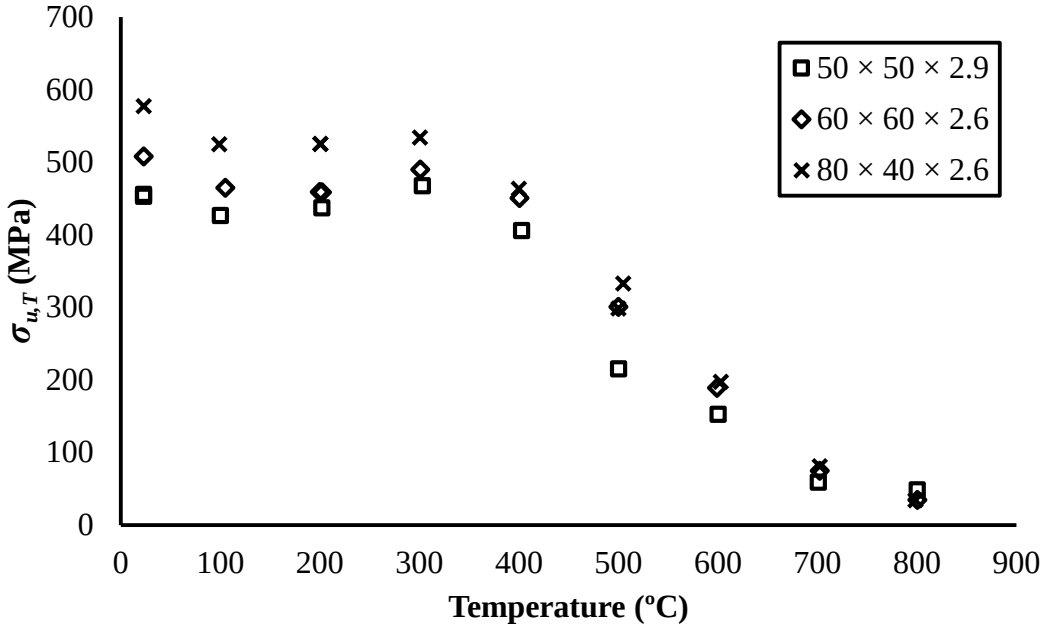

Figure 3.21: Measured values of ultimate tensile strengths at different temperature levels

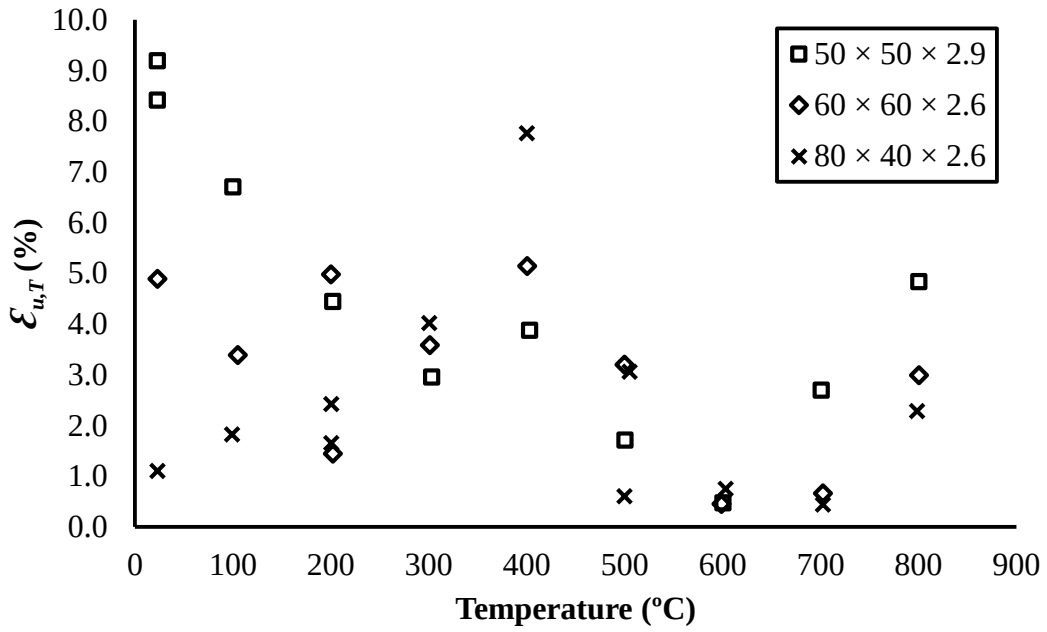

Figure 3.22: Measured values of strain (%) corresponding to ultimate strength

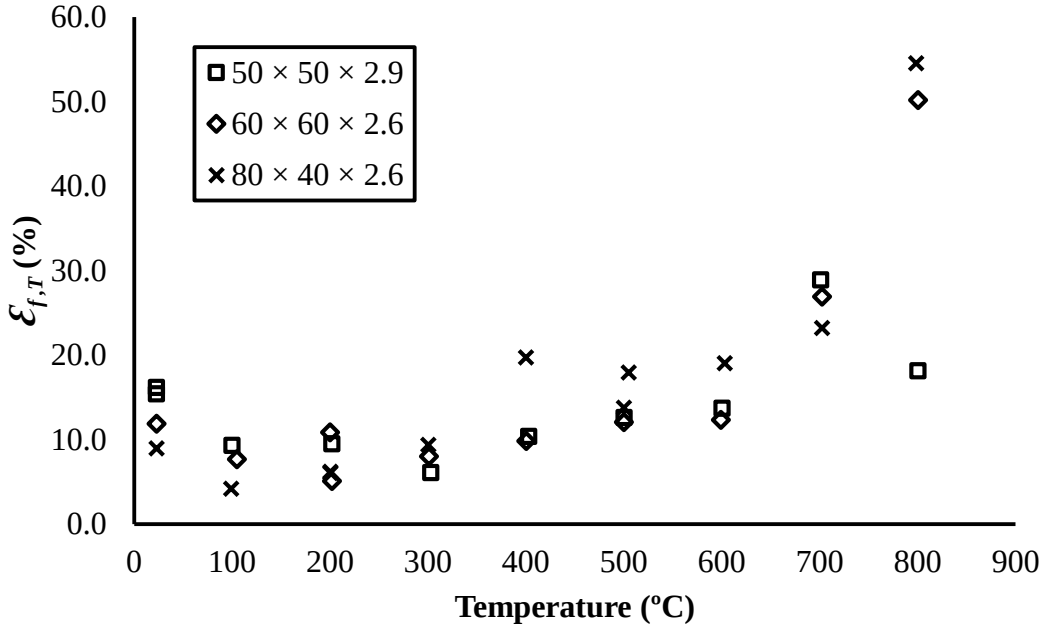

Figure 3.23: Measured fracture strains (%) from tensile coupon test under various temperatures

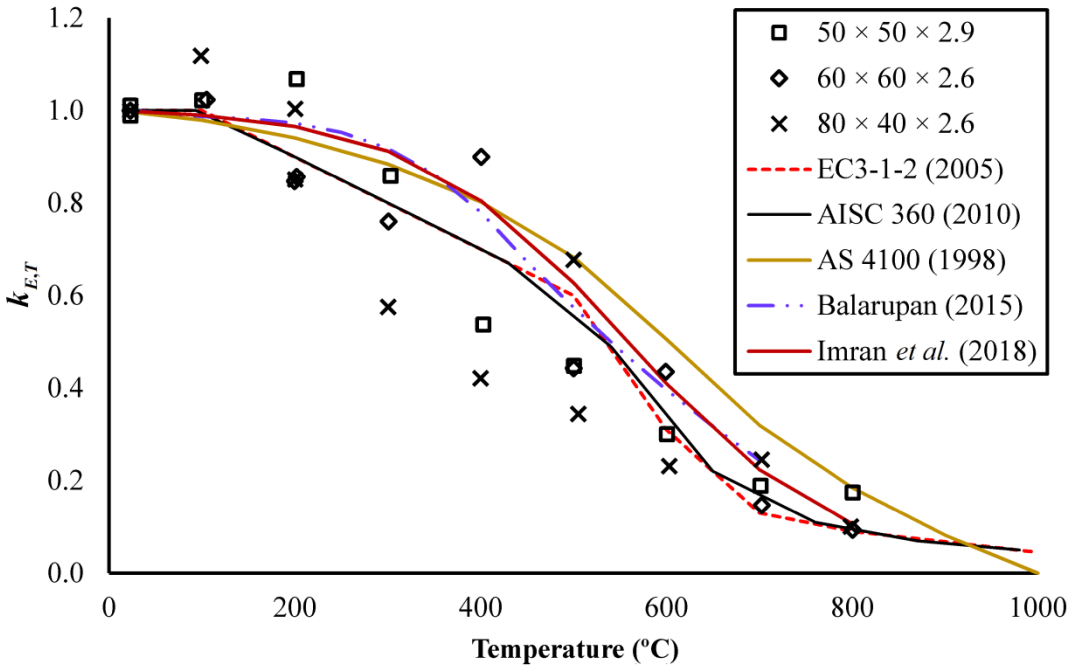

Figure 3.24: Comparison of elevated temperature Young's modulus reduction factors from present test data with current design standards and existing proposals

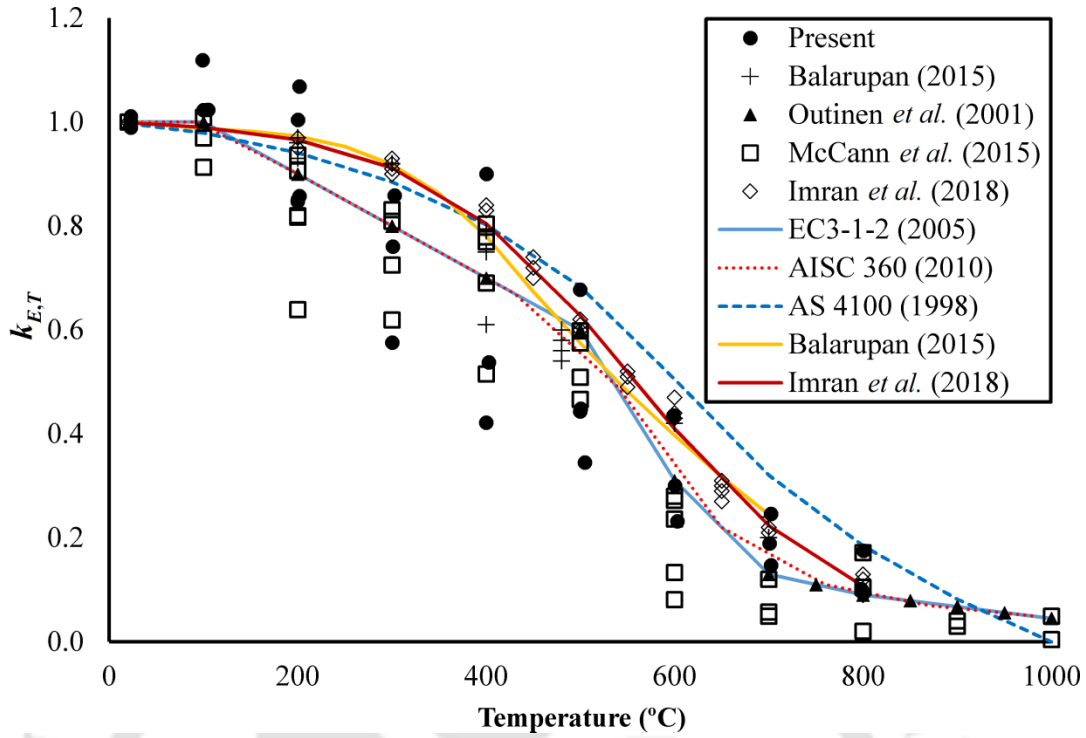

Figure 3.25: Comparison of elevated temperature Young's modulus reduction factors from all test data of cold-formed tubular sections with existing design standards and existing proposals

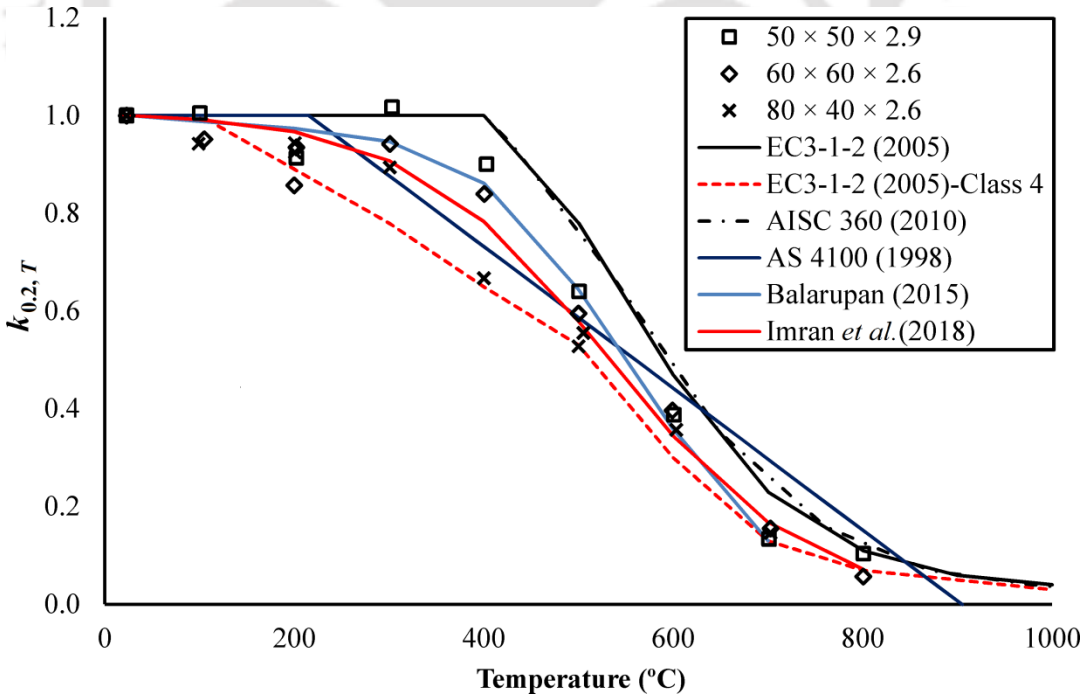

Figure 3.26: Comparison of elevated temperature yield stress reduction factors from present test data with current design standards and existing proposals

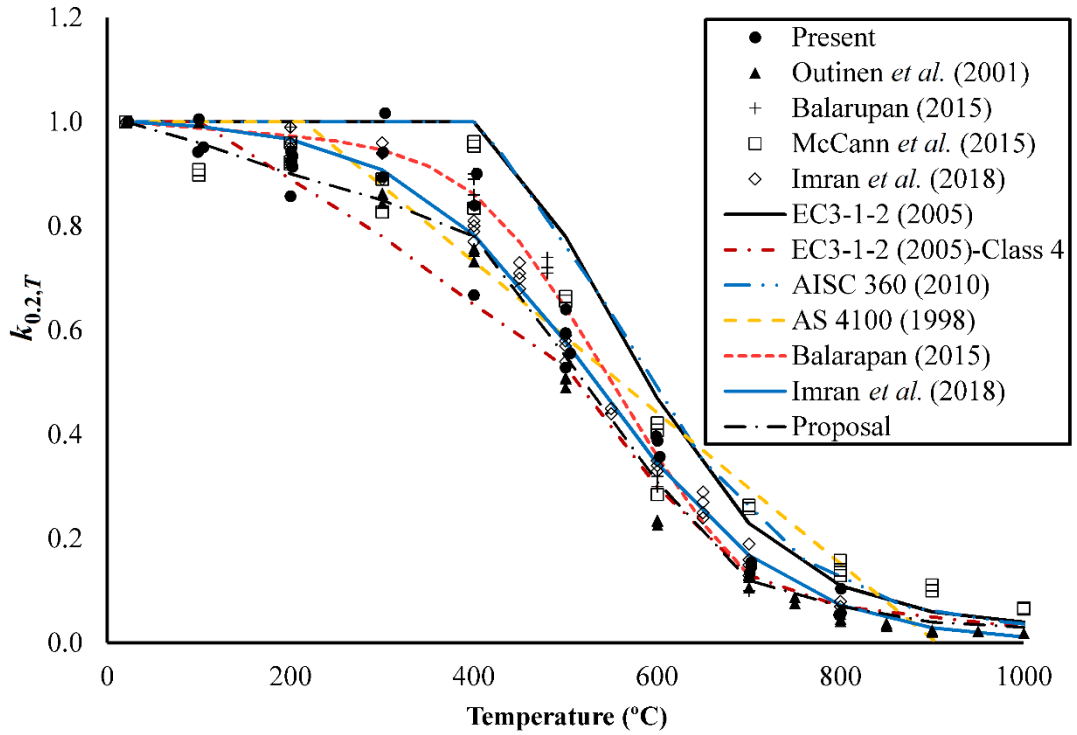

Figure 3.27: Comparison of elevated temperature yield strength reduction factors from all test data of cold-formed tubular sections with existing design; existing and current proposals

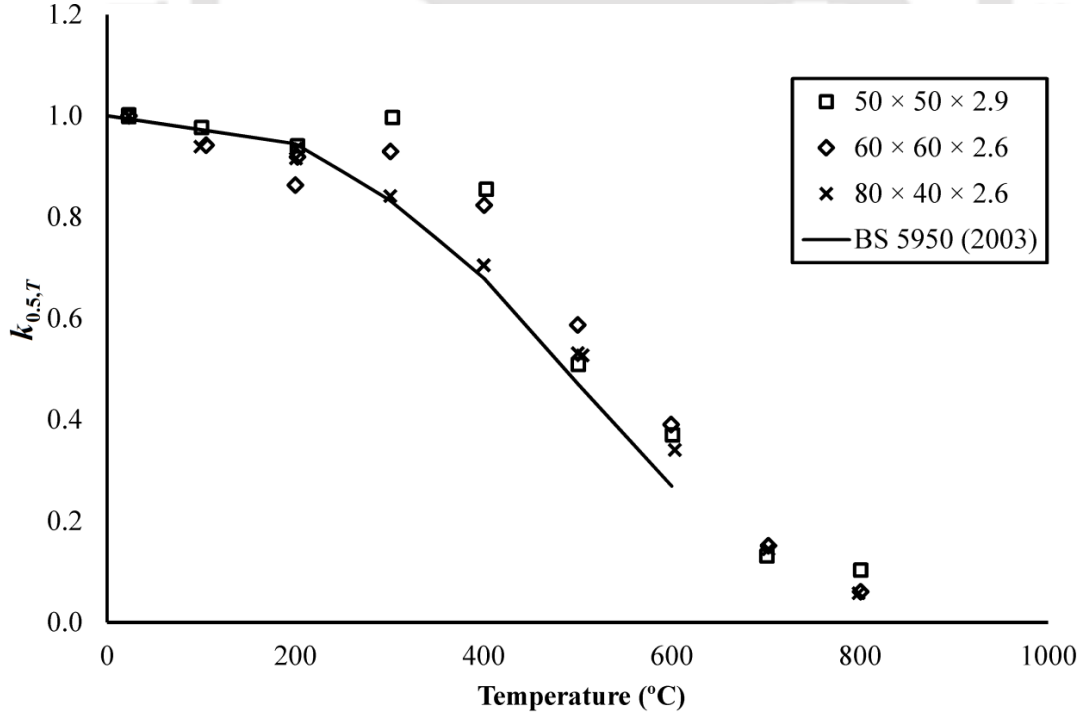

Figure 3.28: Comparison of elevated temperature reduction factors for stress at 0.5% strain from present test with those predicted by BS 5950 (2003)

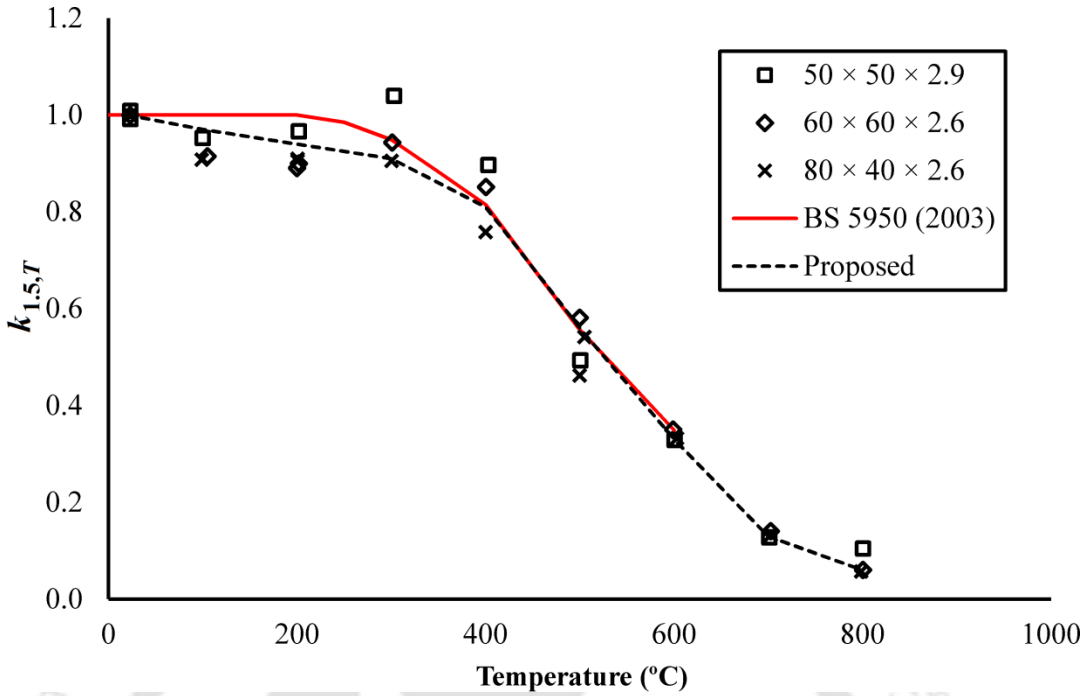

Figure 3.29: Comparison of elevated temperature reduction factors for stress corresponding to 1.5% strain with those in BS 5950 (2003) and current proposal

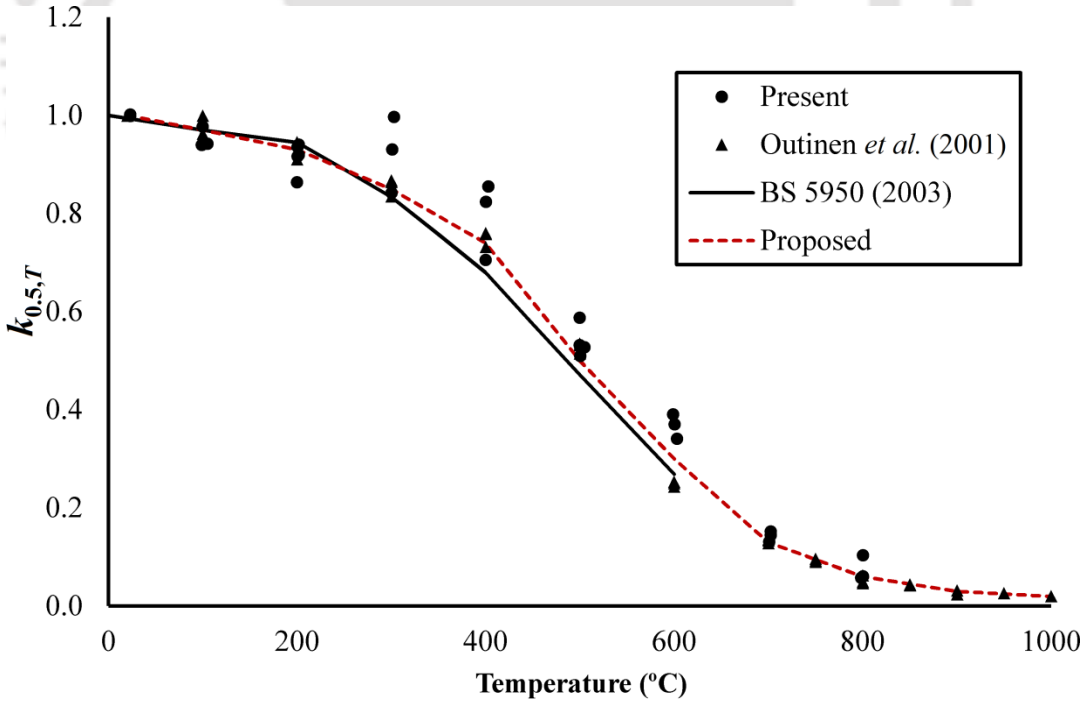

Figure 3.30: Comparison of elevated temperature reduction factors for stress at 0.5% strain from all test data of cold-formed tubular sections with existing design standards and current proposal

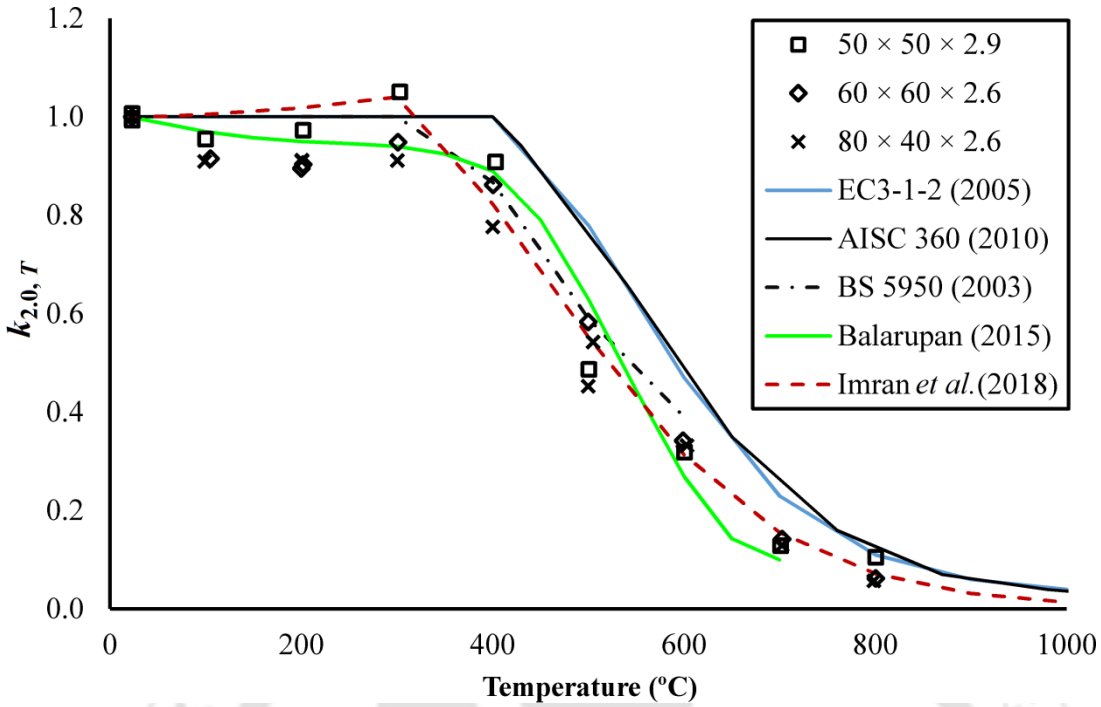

Figure 3.31: Comparison of elevated temperature stress at 2.0% strain reduction factors from present test data with current design standards and existing proposals

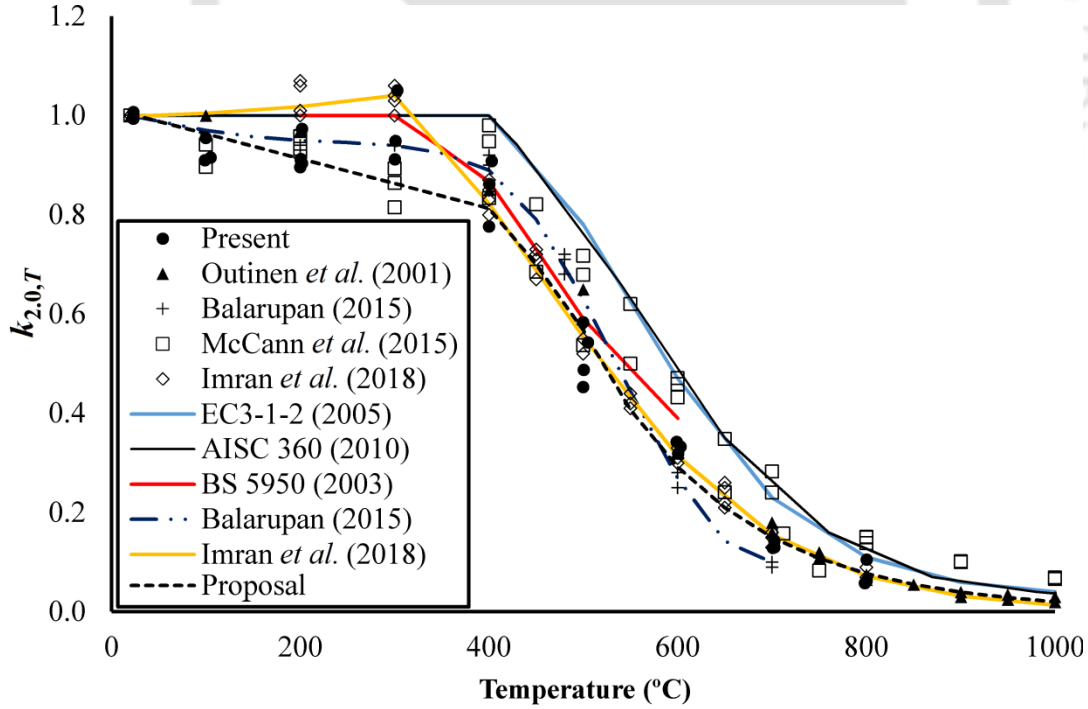

Figure 3.32: Comparison of elevated temperature stress at 2.0% strain reduction factors for all test data of cold-formed tubular sections with design standards; existing and present proposals

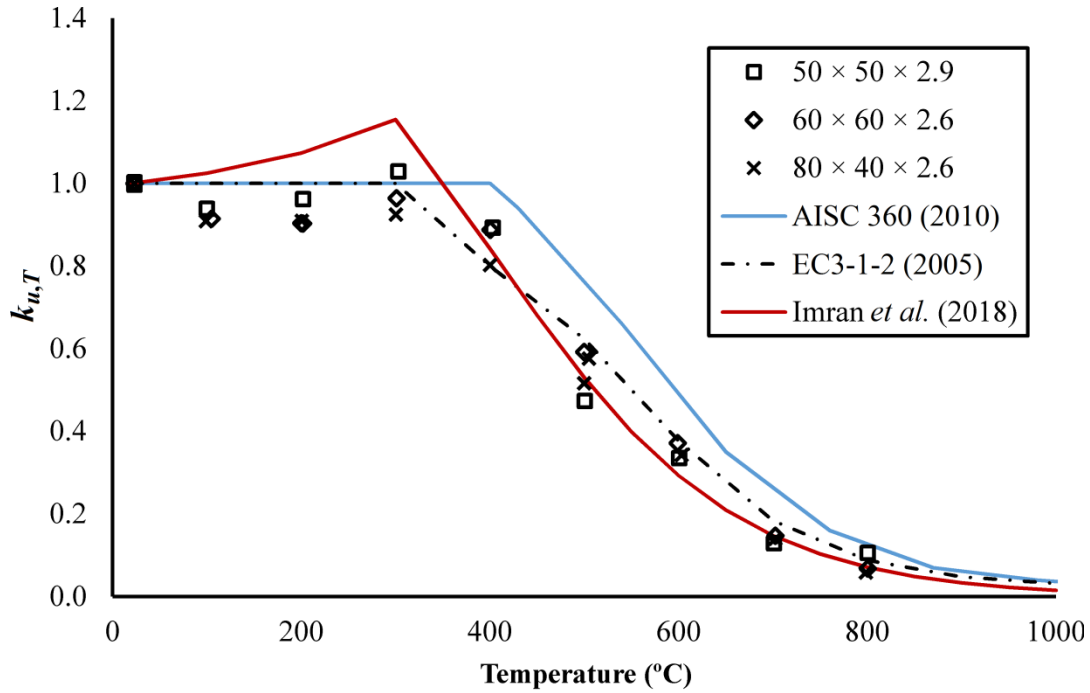

Figure 3.33: Comparison of elevated temperature ultimate strength reduction factors from the present test result with predictions from design standards and existing proposals

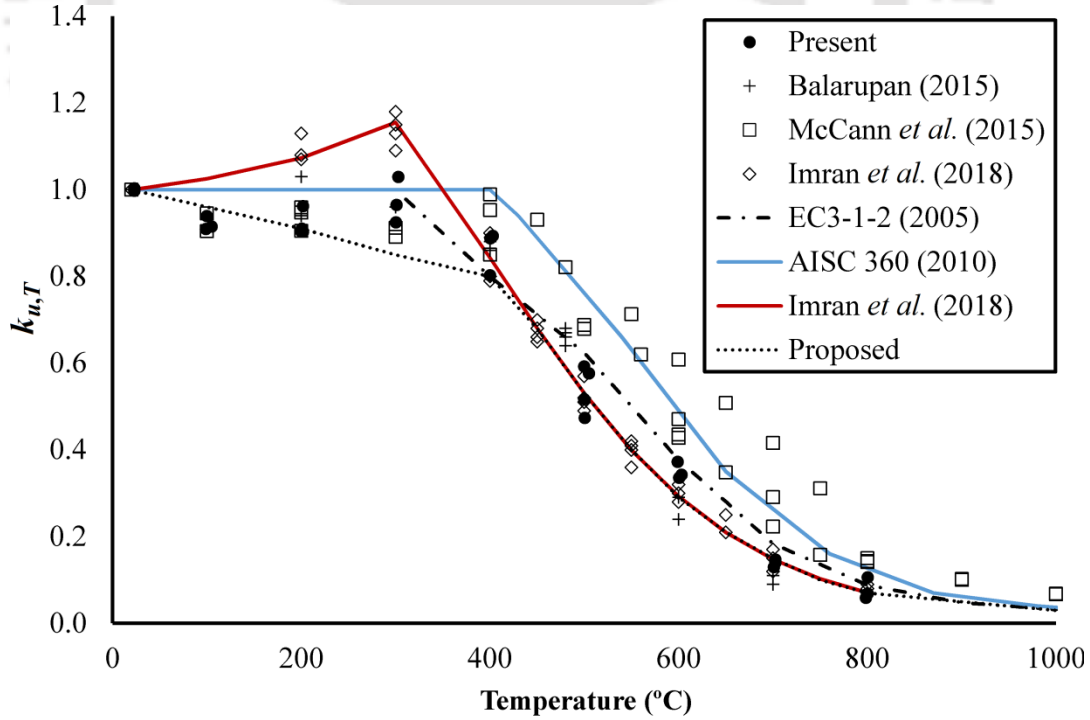

Figure 3.34: Comparison of elevated temperature ultimate strength reduction factors from all test results with the predictions from design standards, existing proposals and current proposals

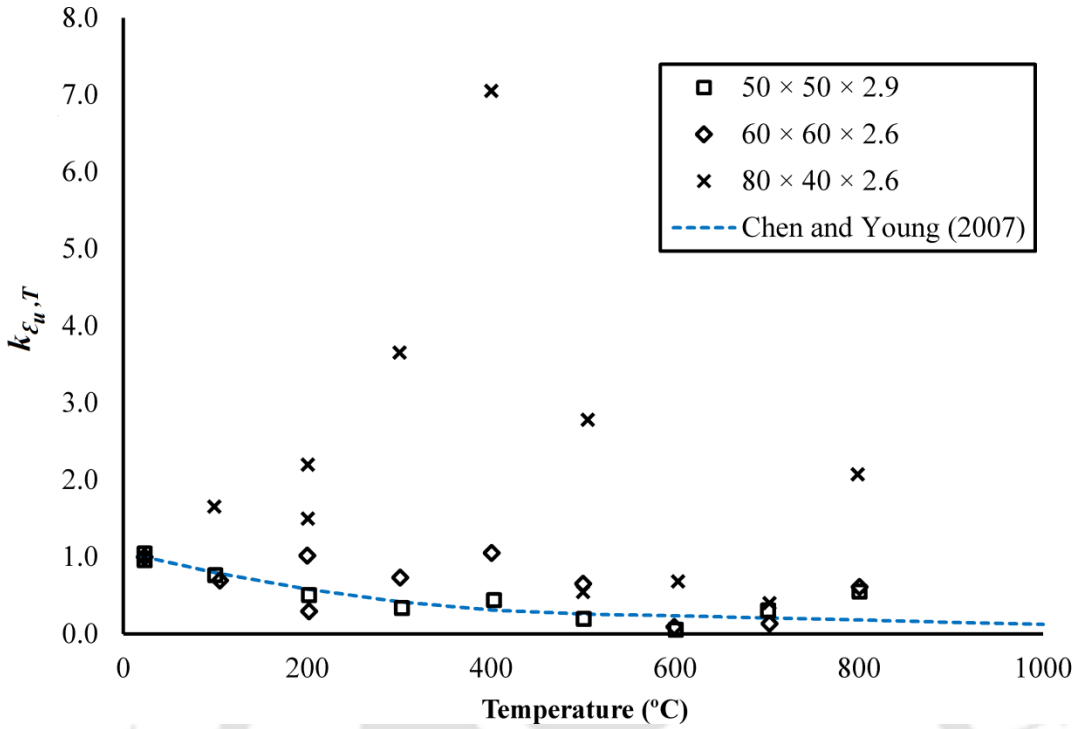

Figure 3.35: Comparison of elevated temperature reduction factors for strain corresponding to ultimate stress with the design curve by Chen and Young (2007)

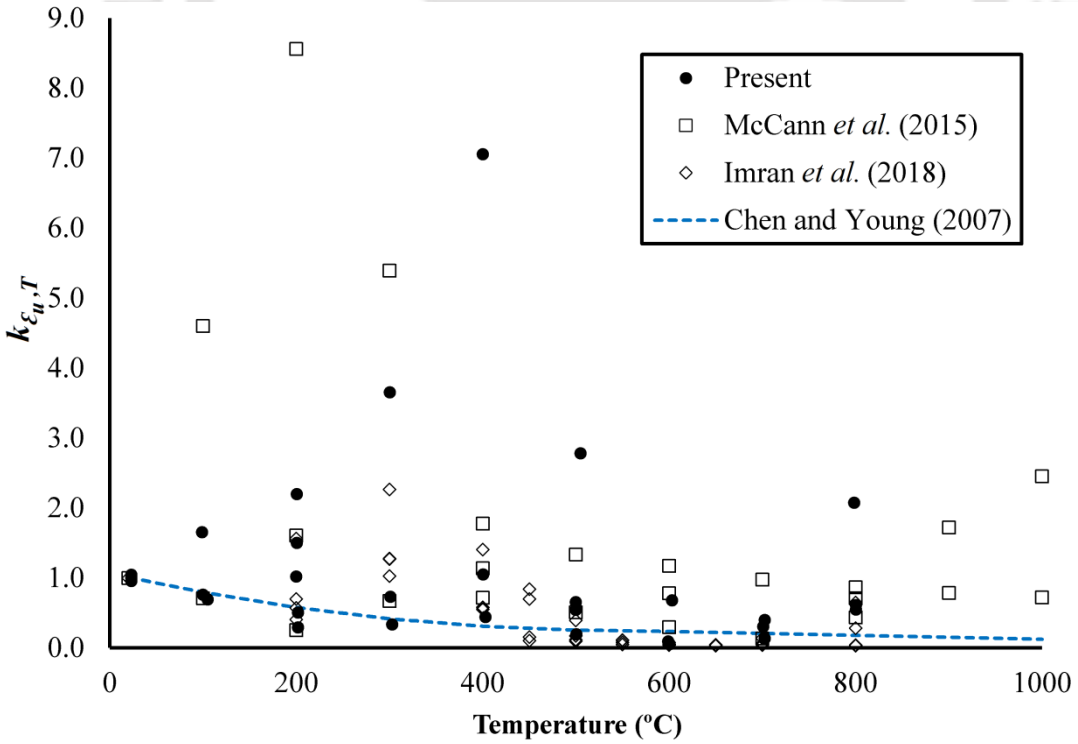

Figure 3.36: Comparison of ultimate strain retention factor from current test and literature with the prediction curve proposed by Chen and Young (2007)

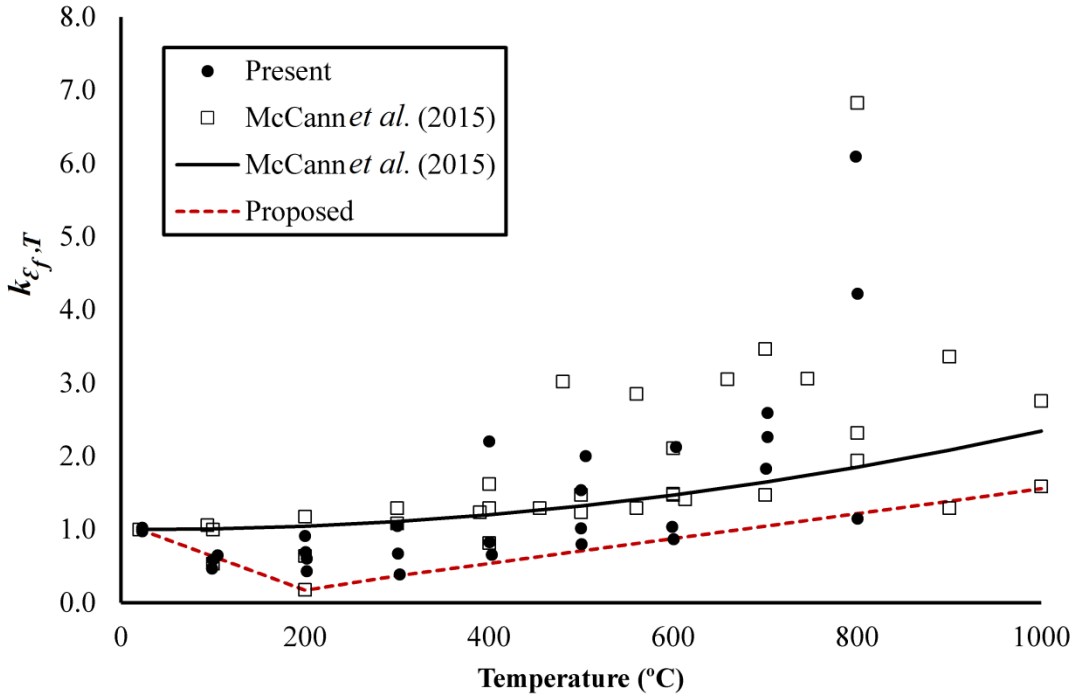

Figure 3.37: Comparison of elevated temperature fracture strain reduction factor from all test results with the prediction from existing and present proposed curves

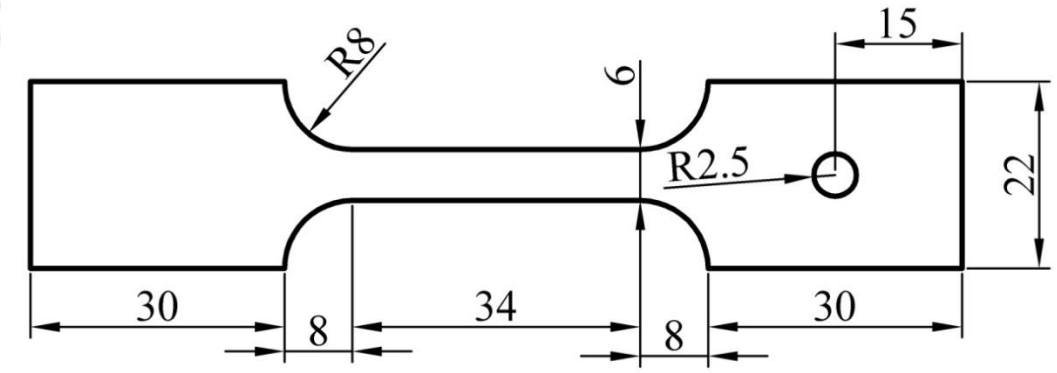

Figure 3.38: Typical dimensions (in mm) of coupon specimen for post-fire tensile coupon test

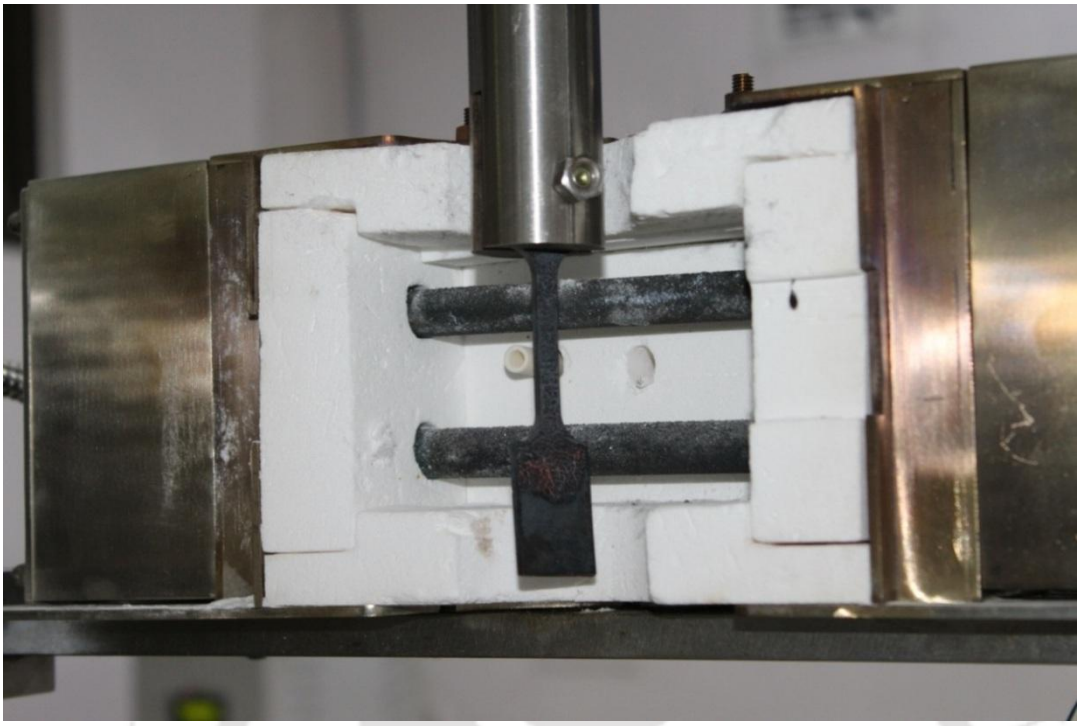

Figure 3.39: A typical setup for electric furnace utilised for heating coupon specimens

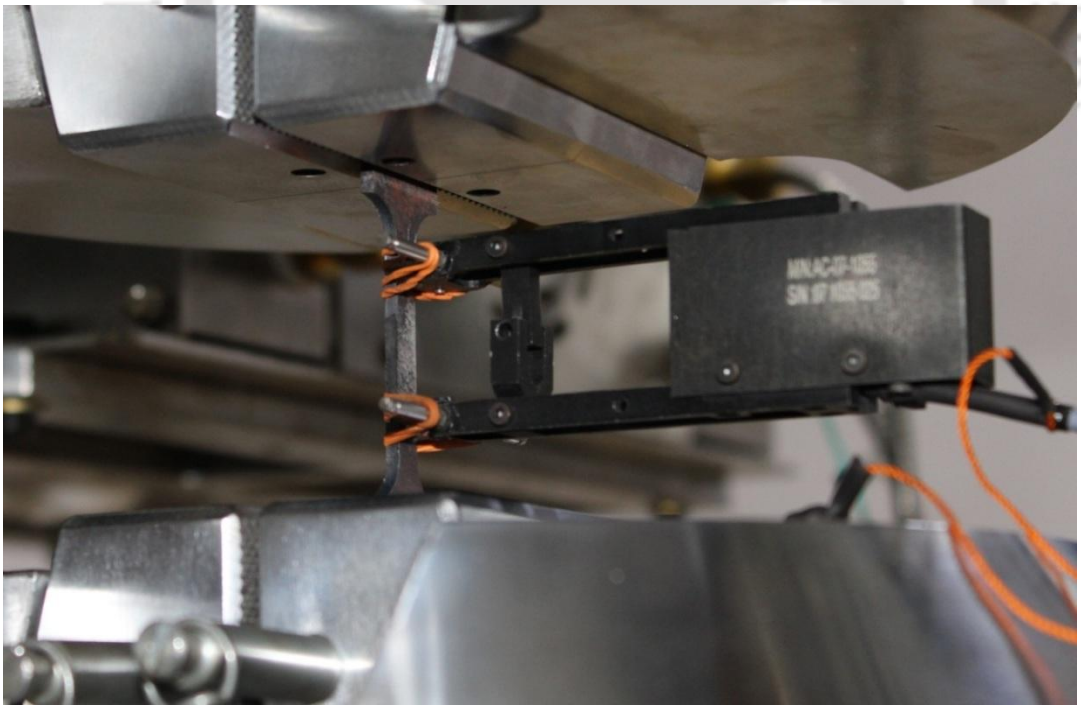

Figure 3.40: A typical test setup of a tensile coupon specimen after being exposed to elevated temperatures

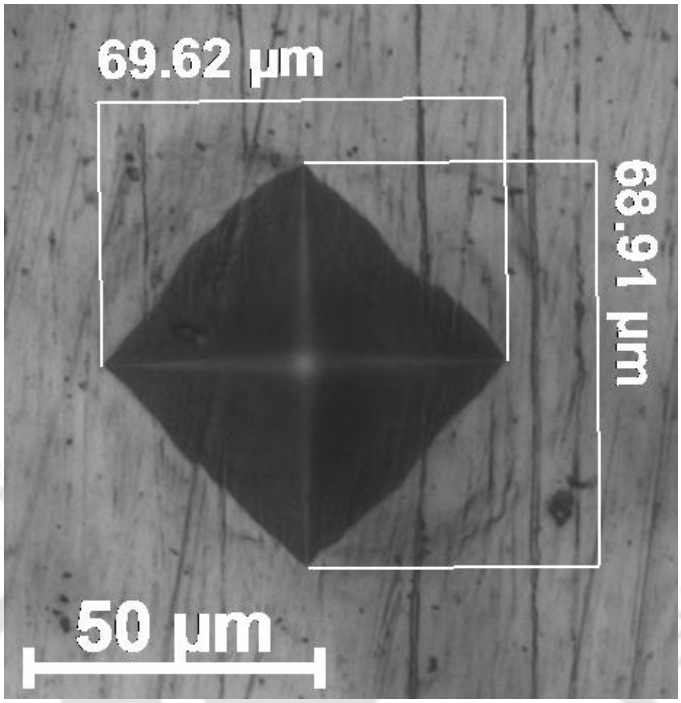

Figure 3.41: A typical sizes of an indent in the microhardness test

Figure 3.42: Typical failed specimens of 50 × 50 × 2.9 cross-section after tensile coupon tests under post-fire condition

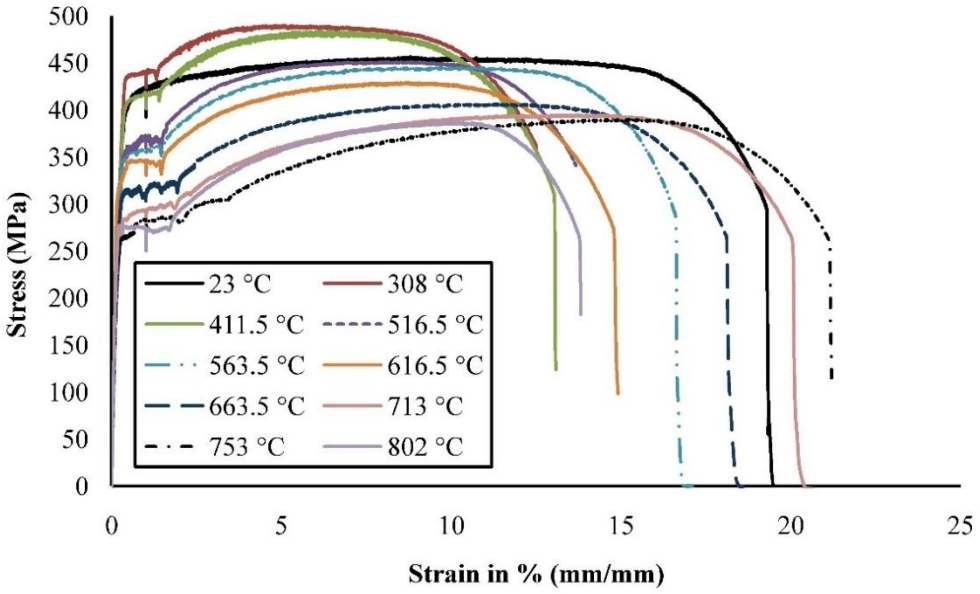

Figure 3.43: Post-fire stress-strain curves for 50 × 50 × 2.9 cross-section

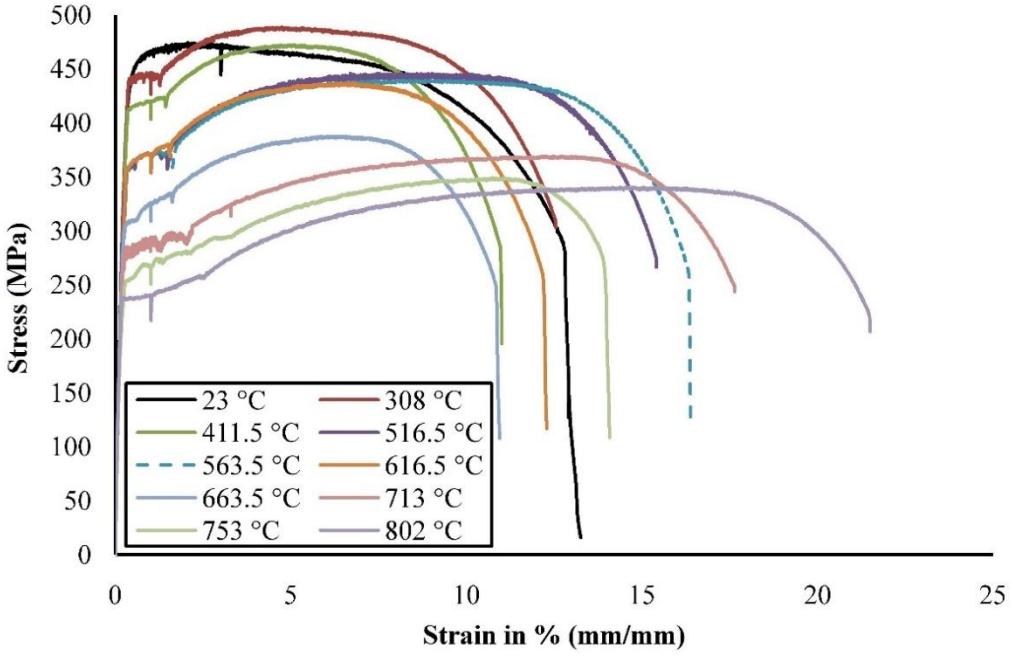

Figure 3.44: Post-fire stress-strain curves for 60 × 40 × 2.9 cross-section

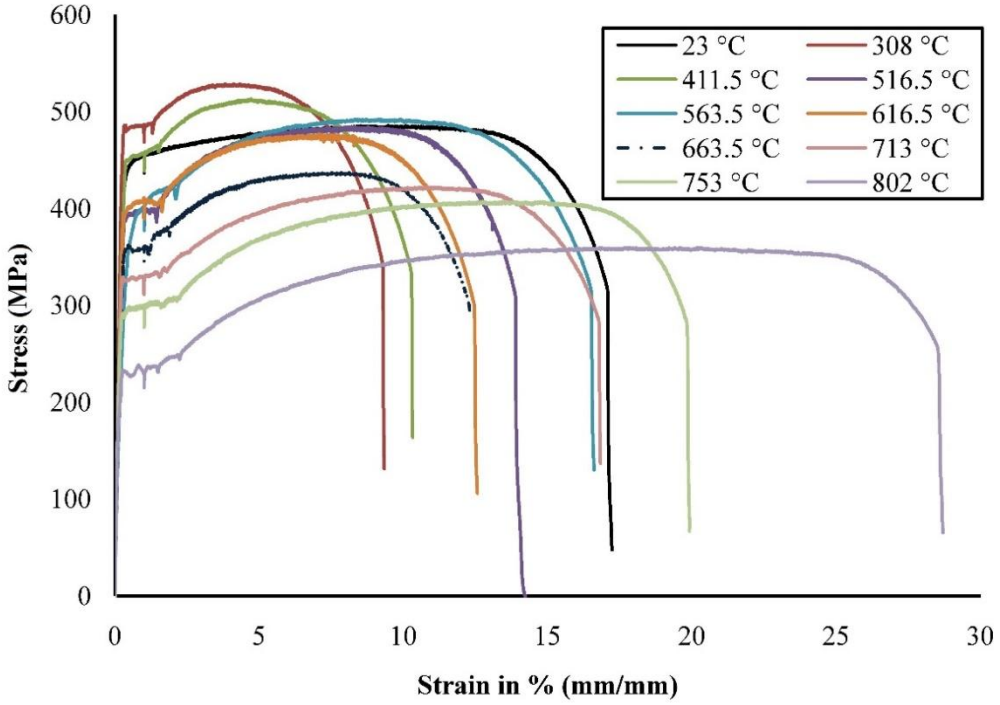

Figure 3.45: Post-fire stress-strain curves for 63 × 33 × 2.6 cross-section

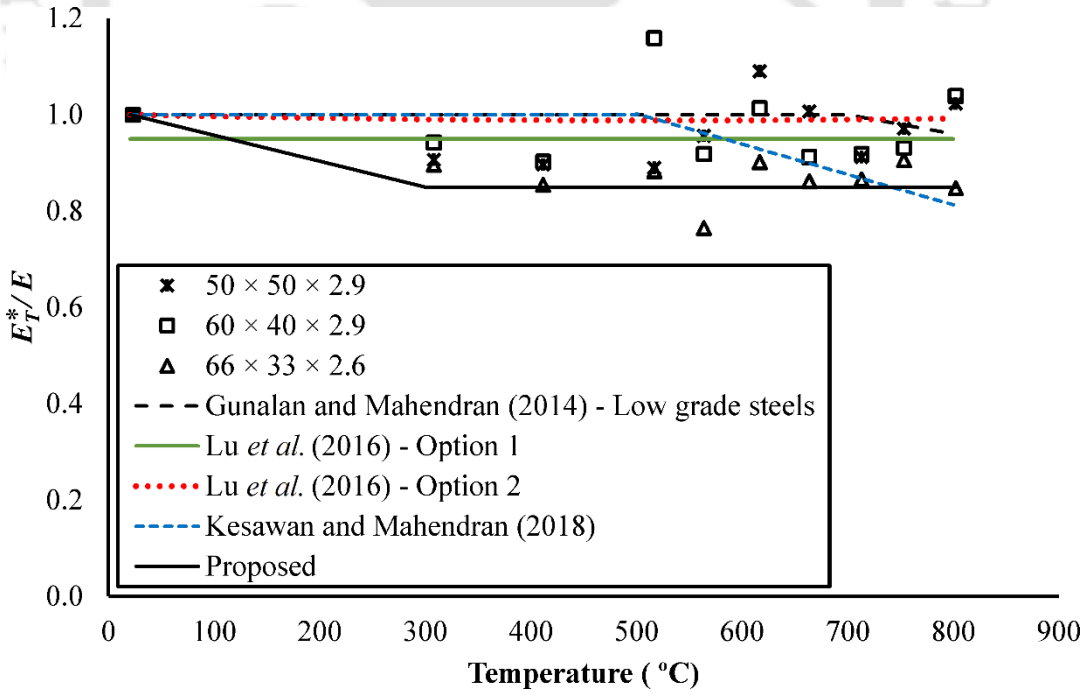

Figure 3.46: Post-fire elastic modulus reduction factors from present test and predictions

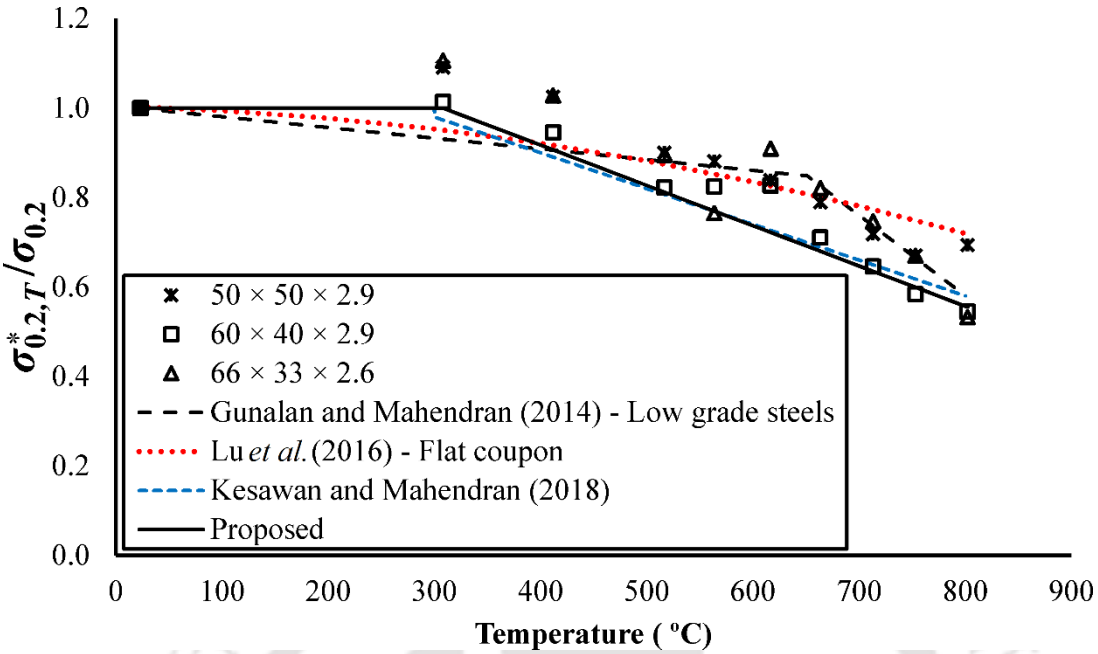

Figure 3.47: Post-fire yield strength reduction factors from present test and predictions

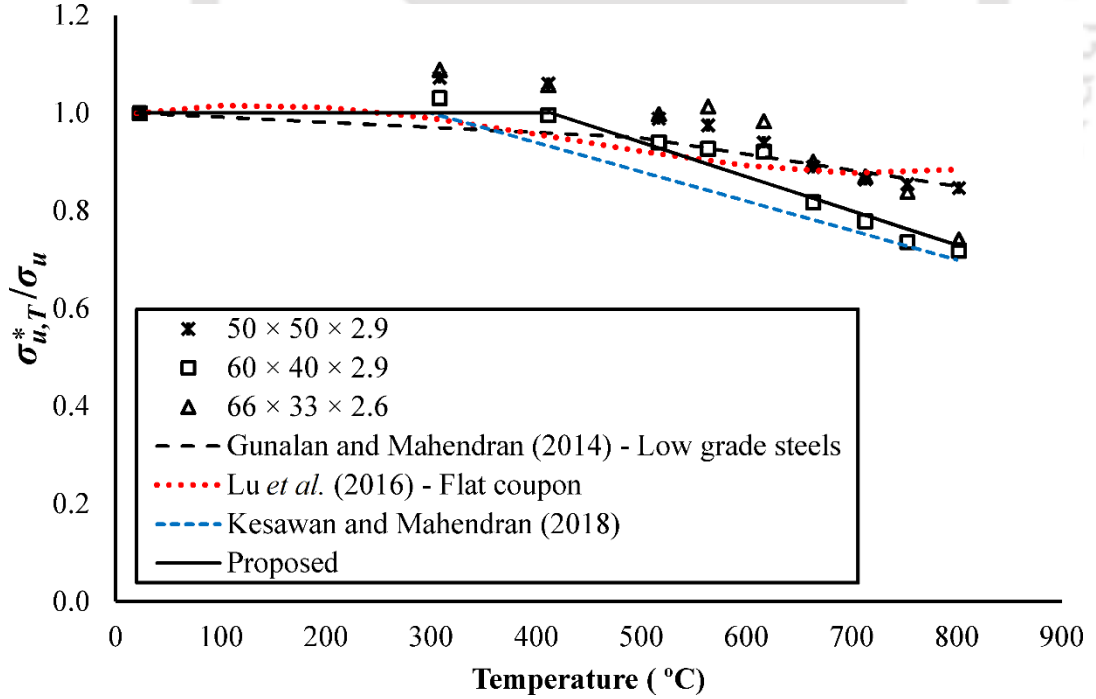

Figure 3.48: Post-fire tensile strength reduction factors from present test, existing and predictions

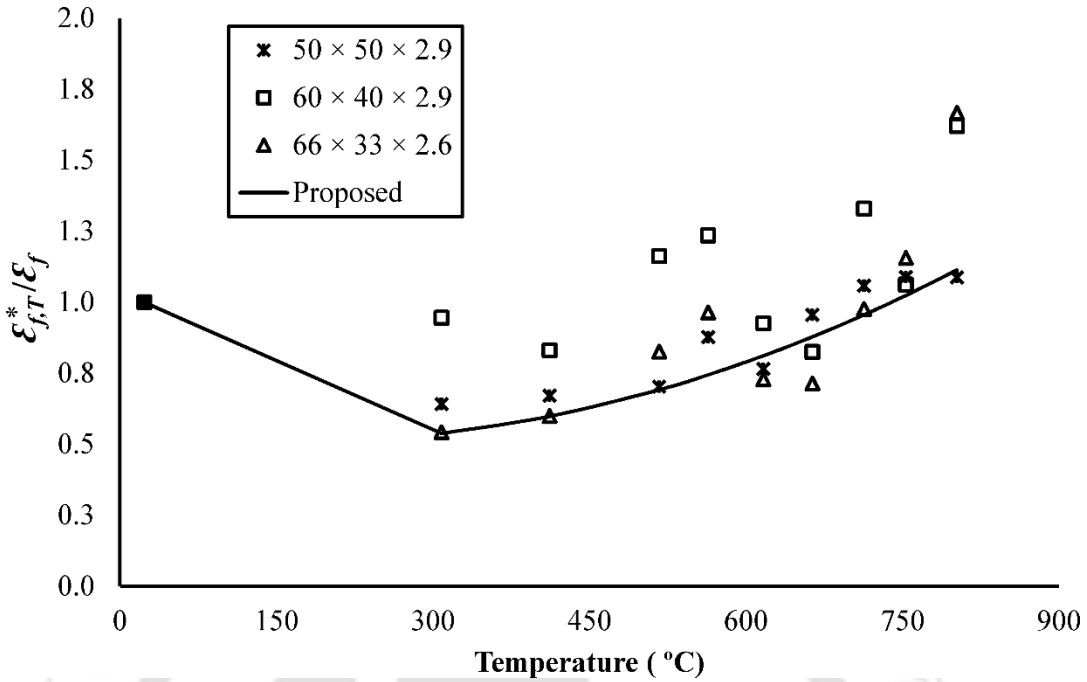

Figure 3.49: Post-fire ductility reduction factors from present test and current proposed prediction

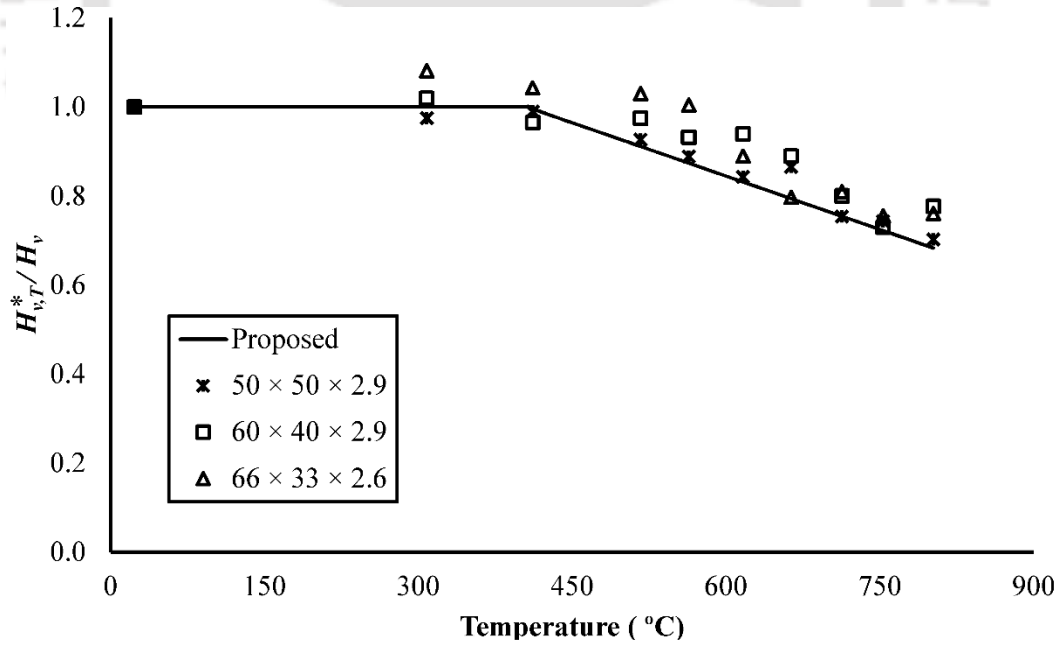

Figure 3.50: Post-fire hardness reduction factors from present test and current proposed prediction

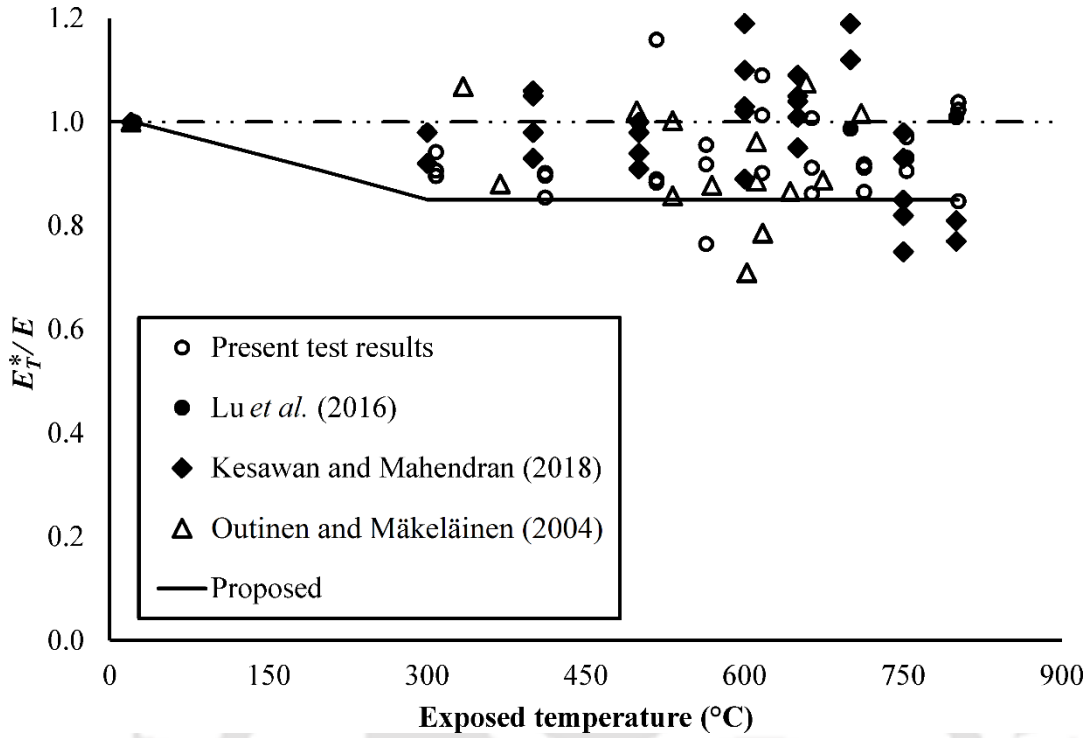

Figure 3.51: Post-fire elastic modulus reduction factors from test results and proposed design curve

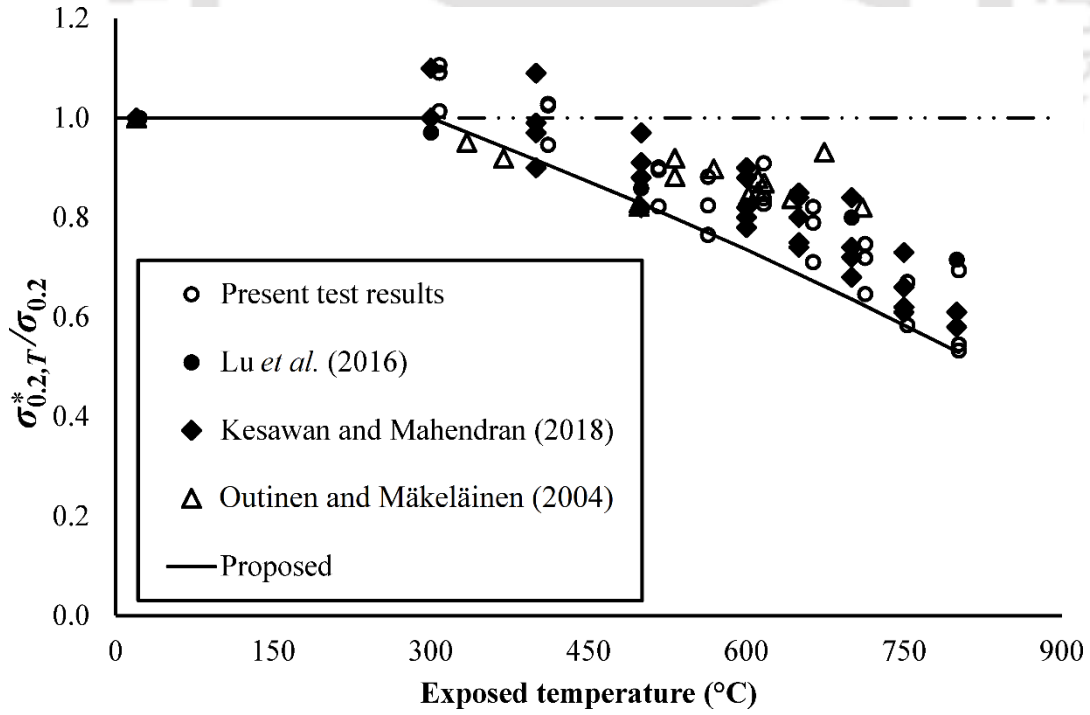

Figure 3.52: Comparison of post-fire yield strength reduction factors from test and proposed curve

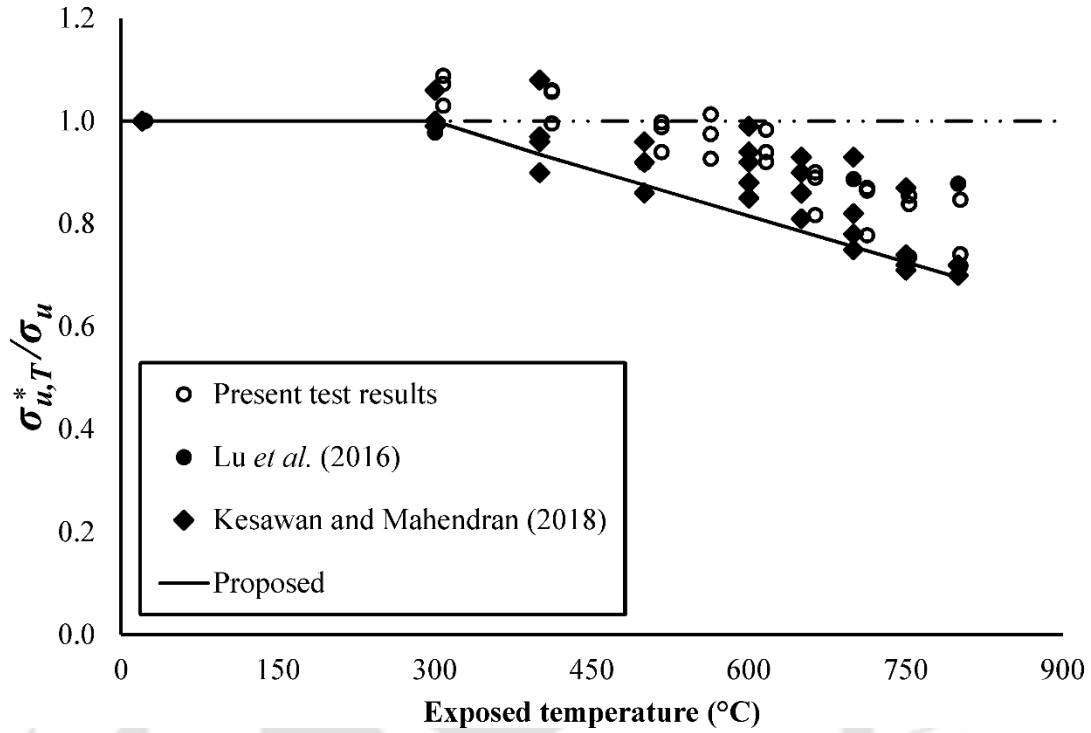

Figure 3.53: Comparison of post-fire tensile strength reduction factors from test results against the present proposed curve

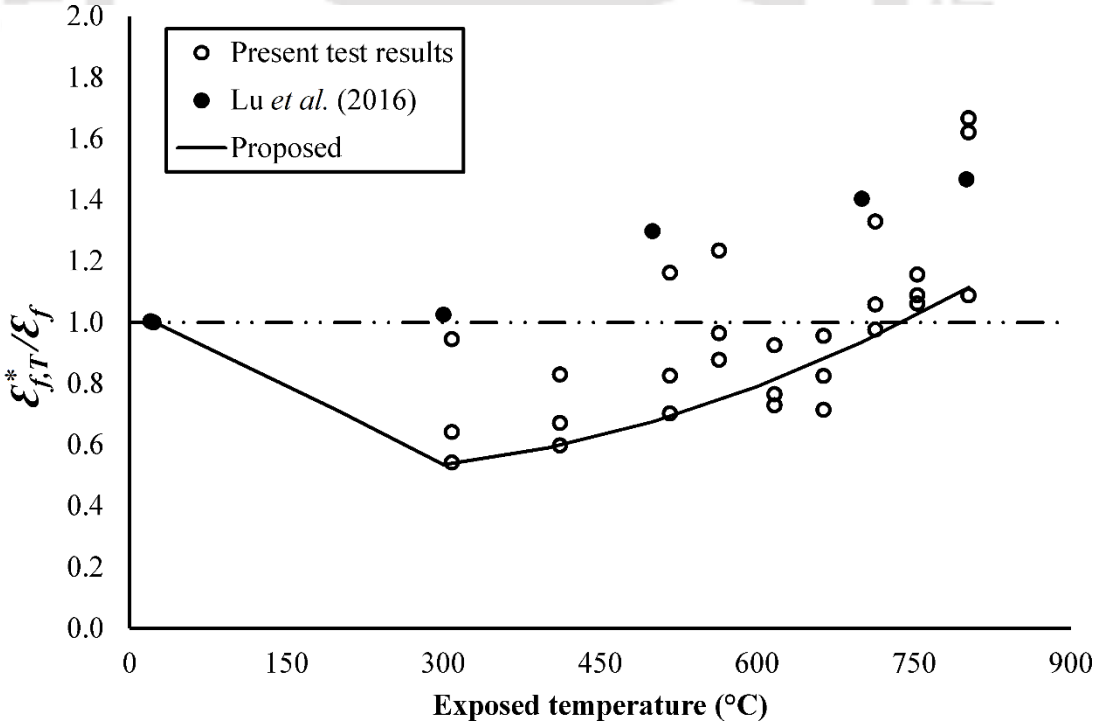

Figure 3.54: Post-fire ductility reduction factors from test results and proposed curve

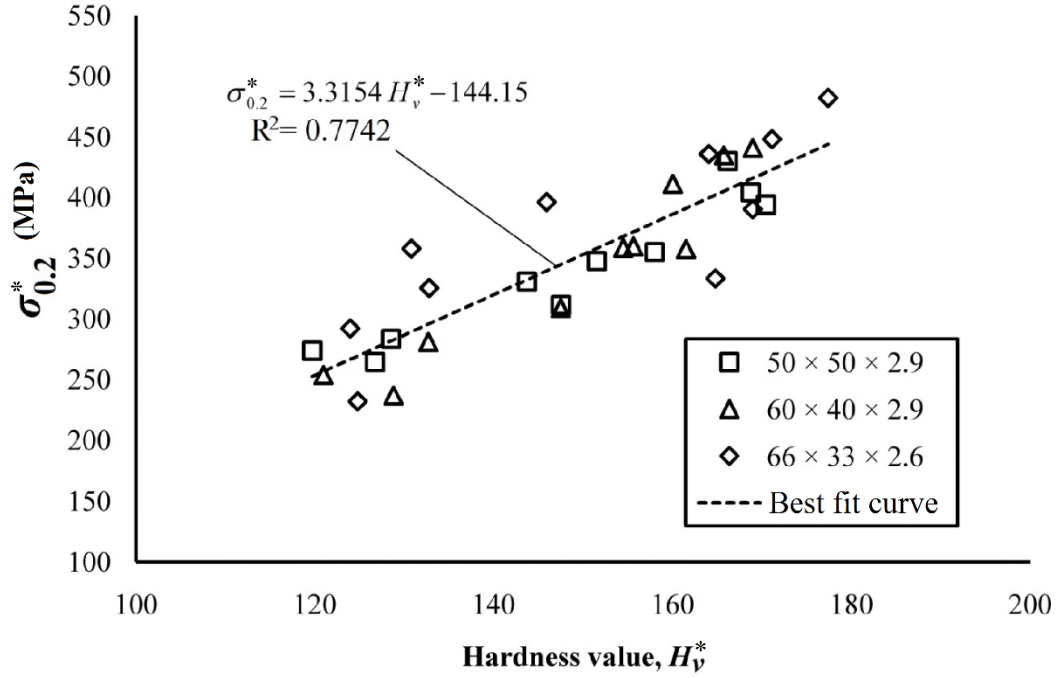

Figure 3.55: Relationship of hardness values and post-fire yield strengths

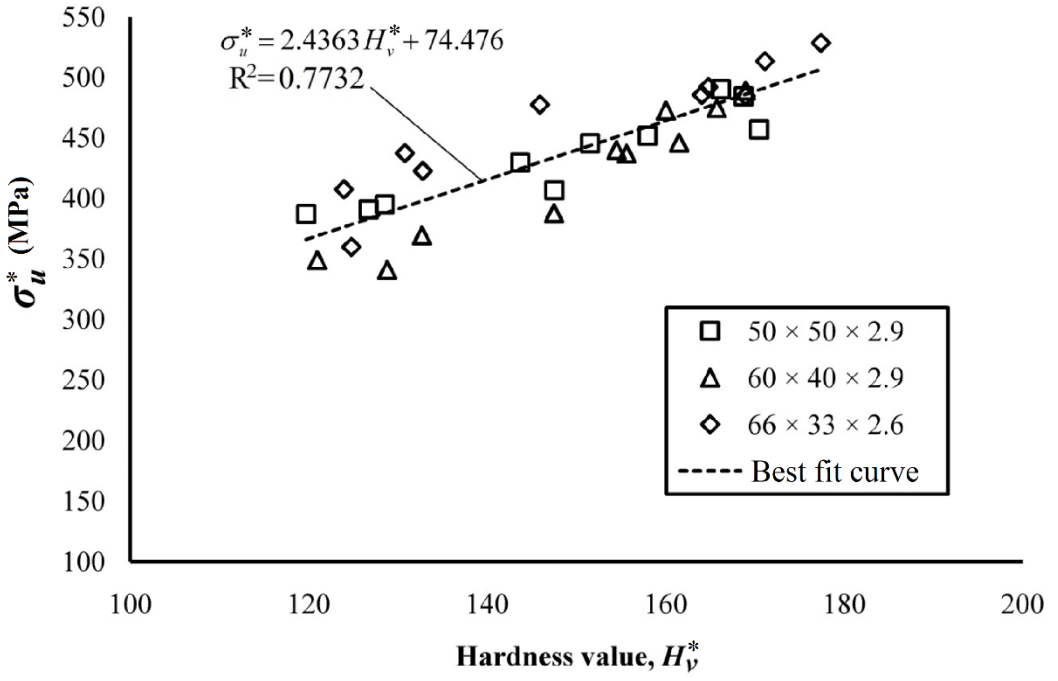

Figure 3.56: Relationship between hardness values and post-fire tensile strengths

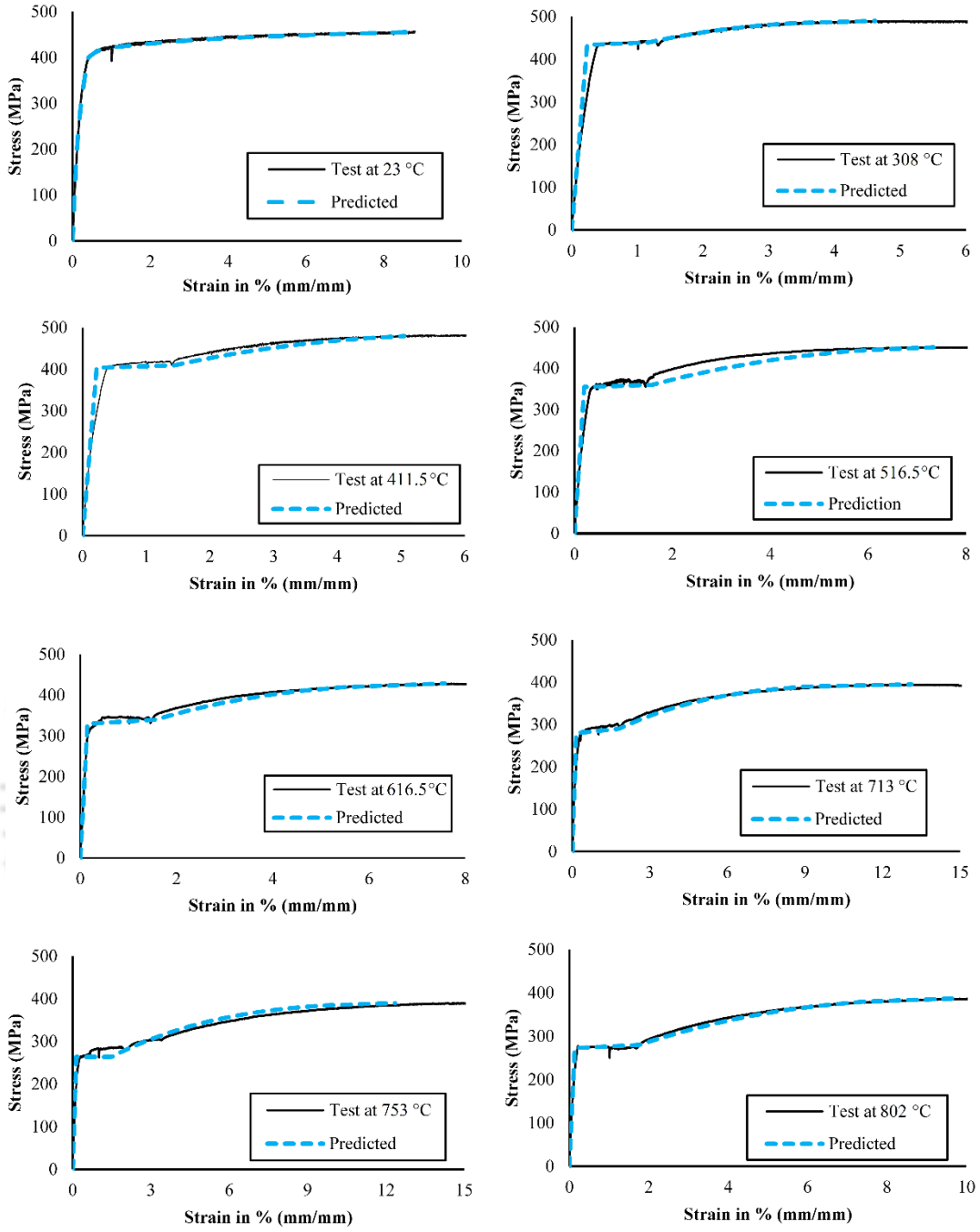

Figure 3.57: Comparison of test and predicted post-fire stress-strain curves at different exposed temperatures for 50 × 50 × 2.9 cross-section

Table 3.1: Nominal cross-sectional dimensions of YSt-310 cold-formed steel hollow sections

B (mm)	D (mm)	t (mm)	r_i (mm)	r_o (mm)	A_g (mm^2)
40.0	40.0	3.2	3.2	6.4	445.0
40.0	40.0	4.0	4.0	8.0	535.0
50.0	50.0	2.9	2.9	5.8	525.0
60.0	60.0	2.6	2.6	5.2	580.0
60.0	40.0	2.9	2.9	5.8	525.0
66.0	33.0	2.6	2.6	5.2	470.0
80.0	40.0	2.6	2.6	5.2	580.0

Table 3.2: Chemical composition and mechanical strength of YSt-310 as per mill certificate

Chemical composition (%)						Mechanical strength		
Section	C	Mn	S	P	Fe	Yield strength (MPa)	Tensile strength (MPa)	Elongation at failure (%)
50 × 50 × 2.9	0.049	0.768	0.007	0.011	Bal.	435.00	475.00	28.00

Table 3.3: Optical Emission Spectrometer analysis results

Cross-section	Summary of chemical composition (%)											
	C	Si	Mn	P	S	Cu	Ni	Ti	Al	Nb	N	Fe
40 × 40 × 3.2	0.110	0.055	0.82	0.031	0.007	0.014	0.034	0.001	0.047	0.002	0.013	Bal.
60 × 40 × 2.9	0.067	0.021	0.62	0.027	0.007	0.013	0.029	0.001	0.038	0.003	0.013	Bal.
66 × 33 × 2.6	0.095	0.010	0.88	0.033	0.008	0.013	0.031	0.001	0.050	0.003	0.014	Bal.

Table 3.4: Summary of flat coupon tensile tests

Cross-section	E (MPa)	$\sigma_{0.05}$ (MPa)	$\sigma_{0.2}$ (MPa)	$\sigma_{1.0}$ (MPa)	σ_u (MPa)	ε_f (%)	n
40 × 40 × 3.2	202000	357	457	489	503.16	18.99	5.6
40 × 40 × 4.0	200000	312	419	462	465.22	18.92	4.7
50 × 50 × 2.9	190024	265	370	422	446.48	22.56	4.2
60 × 40 × 2.9	201845	320	408	432	439.35	18.33	5.7
60 × 60 × 2.6	204082	307	431	471	483.24	17.76	4.1
66 × 33 × 2.6	190653	343	428	454	483.30	19.29	6.3
80 × 40 × 2.6	200000	397	520	560	562.89	11.68	5.1
Mean (P_m)	198372	329	433	470	483.40	18.20	5.1
COV (V_p)	0.03	0.13	0.11	0.10	0.09	0.18	0.16

Table 3.5: Summary of corner coupon tensile tests

Cross-section	E (MPa)	$\sigma_{0.05}$ (MPa)	$\sigma_{0.2}$ (MPa)	$\sigma_{1.0}$ (MPa)	σ_u (MPa)	ε_f (%)	n
40 × 40 × 3.2	193424	400	599	698	700.00	6.85	3.4
40 × 40 × 4.0	184211	288	574	712	714.30	9.24	2.0
50 × 50 × 2.9	176191	300	506	570	571.53	7.69	2.7
60 × 40 × 2.9	187050	366	502	565	569.90	8.80	3.5
60 × 60 × 2.6	192308	317	556	688	689.31	11.53	2.5
66 × 33 × 2.6	177305	266	520	630	633.23	8.22	2.1
80 × 40 × 2.6	180412	315	570	645	649.19	7.35	2.3
Mean (P_m)	184414	322	547	644	647	8.53	2.6
COV (V_p)	0.04	0.14	0.07	0.09	0.09	0.18	0.23

Table 3.6: Summary of weld coupon tensile tests

Cross-section	E (MPa)	$\sigma_{0.05}$ (MPa)	$\sigma_{0.2}$ (MPa)	$\sigma_{1.0}$ (MPa)	σ_u (MPa)	ε_f (%)	n
40 × 40 × 3.2	184502	463	593	672	685.49	6.86	5.6
40 × 40 × 4.0	187500	432	558	653	657.75	7.06	5.4
50 × 50 × 2.9	176289	386	535	632	645.69	7.42	4.3
60 × 40 × 2.9	182292	430	589	660	662.27	5.92	4.4
60 × 60 × 2.6	186567	517	645	698	700.14	5.88	6.3
66 × 33 × 2.6	173077	401	534	602	620.44	7.39	4.8
80 × 40 × 2.6	171429	465	627	690	696.60	7.50	4.6
Mean	180237	442	583	658	667	6.90	5.1
COV	0.04	0.10	0.07	0.05	0.04	0.10	0.15

Table 3.7: Key material properties recorded from tensile coupon test at various elevated temperatures

Cross-sections	T (°C)	E_T (MPa)	$\sigma_{0.2,T}$ (MPa)	$\sigma_{0.5,T}$ (MPa)	$\sigma_{1.5,T}$ (MPa)	$\sigma_{2.0,T}$ (MPa)	$\sigma_{u,T}$ (MPa)	$\varepsilon_{u,T}$ (%)	$\varepsilon_{f,T}$ (%)	n_T
50 × 50 × 2.9	23.0-1	200959	390.89	407.72	434.85	438.47	455.26	8.41	15.41	5.59
	23.0-2	205382	390.44	406.39	427.49	432.44	452.57	9.19	16.16	5.15
	100.0	207751	392.65	397.66	410.82	415.77	426.13	6.70	9.29	4.43
	202.0	216962	356.88	382.81	416.64	423.61	436.59	4.44	9.50	4.51
	303.0	174431	397.32	405.67	448.17	457.41	467.25	2.95	6.09	13.57
	403.0	109163	351.81	348.03	386.64	395.42	405.35	3.87	10.35	11.33
	500.5	91045	250.00	207.37	212.62	212.09	214.90	1.71	12.60	4.44
	600.5	61050	151.55	150.79	141.66	138.57	152.24	0.47	13.70	16.95
	701.0	38351	52.32	53.35	54.97	56.08	58.60	2.69	28.87	10.30
	800.5	35474	40.62	42.01	44.98	45.80	48.17	4.83	18.11	19.93
60 × 60 × 2.6	23.0	199107	471.54	481.82	504.92	505.48	507.74	4.89	11.89	6.42
	105.0	203735	448.58	454.01	461.94	462.44	464.59	3.39	7.69	10.52
	202.0-1	170642	440.60	442.91	454.50	456.68	458.46	1.44	5.10	11.99
	200.0-2	168698	404.18	416.10	449.80	452.66	458.91	4.98	10.84	4.54
	301.0	151296	444.05	448.15	476.44	479.45	489.63	3.58	8.00	17.44
	400.5	179159	395.92	396.93	429.86	435.49	450.64	5.14	9.84	14.81
	500.0	88228	280.50	282.96	293.41	294.86	300.51	3.20	12.08	22.74
	599.0	86664	187.08	188.25	176.86	172.82	188.83	0.45	12.32	26.54
	702.5	29262	73.19	73.10	71.09	71.96	74.67	0.66	26.93	6.28
	800.5	18609	26.99	29.22	30.59	31.47	34.55	2.99	50.17	5.65

Table 3.7: (Continued) Key material properties recorded from tensile coupon test at various elevated temperatures

Cross-sections	T (°C)	E_T (MPa)	$\sigma_{0.2,T}$ (MPa)	$\sigma_{0.5,T}$ (MPa)	$\sigma_{1.5,T}$ (MPa)	$\sigma_{2.0,T}$ (MPa)	$\sigma_{u,T}$ (MPa)	$\varepsilon_{u,T}$ (%)	$\varepsilon_{f,T}$ (%)	n_T
80 × 40 × 2.6	23.0	197209	543.00	548.15	575.31	574.92	577.15	1.10	8.95	5.30
	99.0	220592	511.71	514.95	522.36	523.03	524.58	1.82	4.17	41.55
	200.5-1	197935	512.30	512.94	523.56	524.33	524.99	1.65	6.20	27.82
	200.5-2	167860	502.06	502.14	521.07	523.08	524.93	2.42	6.06	16.55
	300.5	113465	485.30	461.68	520.82	523.87	533.70	4.02	9.39	13.65
	400.0	83054	362.36	386.71	436.21	446.31	463.11	7.76	19.72	–
	500.0-1	133562	286.81	291.43	266.05	260.27	298.11	0.60	13.76	21.24
	505.0-2	67956	301.66	289.21	311.63	311.81	332.67	3.06	17.92	22.43
	603.0	45683	194.03	186.76	191.28	191.05	197.52	0.75	19.03	15.30
	702.5	48436	79.41	79.19	76.37	74.63	80.65	0.44	23.21	8.98
	798.5	19844	29.31	31.60	32.91	32.98	33.91	2.28	54.52	5.67

Table 3.8: Reduction factors of key material parameters at elevated temperature

Cross-sections	T (°C)	$\frac{E_T}{E}$	$\frac{\sigma_{0.2,T}}{\sigma_{0.2}}$	$\frac{\sigma_{0.5,T}}{\sigma_{0.5}}$	$\frac{\sigma_{1.5,T}}{\sigma_{1.5}}$	$\frac{\sigma_{2.0,T}}{\sigma_{2.0}}$	$\frac{\sigma_{u,T}}{\sigma_{u}}$	$\frac{\varepsilon_{u,T}}{\varepsilon_{u}}$	$\frac{\varepsilon_{f,T}}{\varepsilon_{f}}$
		$k_{E,T}$	$k_{0.2,T}$	$k_{0.5,T}$	$k_{1.5,T}$	$k_{2.0,T}$	$k_{u,T}$	$k_{\varepsilon_u,T}$	$k_{\varepsilon_f,T}$
50 × 50 × 2.9	23.0-1	0.99	1.00	1.00	1.01	1.01	1.00	0.96	0.98
	23.0-2	1.01	1.00	1.00	0.99	0.99	1.00	1.04	1.02
	100.0	1.02	1.01	0.98	0.95	0.95	0.94	0.76	0.59
	202.0	1.07	0.91	0.94	0.97	0.97	0.96	0.50	0.60
	303.0	0.86	1.02	1.00	1.04	1.05	1.03	0.34	0.39
	403.0	0.54	0.90	0.85	0.90	0.91	0.89	0.44	0.66
	500.5	0.45	0.64	0.51	0.49	0.49	0.47	0.19	0.80
	600.5	0.30	0.39	0.37	0.33	0.32	0.34	0.05	0.87
	701.0	0.19	0.13	0.13	0.13	0.13	0.13	0.31	1.83
	800.5	0.17	0.10	0.10	0.10	0.11	0.11	0.55	1.15
60 × 60 × 2.6	23.0	1.00	1.00	1.00	1.00	1.00	1.00	1.00	1.00
	105.0	1.02	0.95	0.94	0.91	0.91	0.92	0.69	0.65
	202.0-1	0.86	0.93	0.92	0.90	0.90	0.90	0.29	0.43
	200.0-2	0.85	0.86	0.86	0.89	0.90	0.90	1.02	0.91
	301.0	0.76	0.94	0.93	0.94	0.95	0.96	0.73	0.67
	400.5	0.90	0.84	0.82	0.85	0.86	0.89	1.05	0.83
	500.0	0.44	0.59	0.59	0.58	0.58	0.59	0.65	1.02
	599.0	0.44	0.40	0.39	0.35	0.34	0.37	0.09	1.04
	702.5	0.15	0.16	0.15	0.14	0.14	0.15	0.13	2.26
	800.5	0.09	0.06	0.06	0.06	0.06	0.07	0.61	4.22

Table 3.8 (Continued) Reduction factors of key material parameters at elevated temperature

Cross-sections	T (°C)	$\frac{E_T}{E}$	$\frac{\sigma_{0.2,T}}{\sigma_{0.2}}$	$\frac{\sigma_{0.5,T}}{\sigma_{0.5}}$	$\frac{\sigma_{1.5,T}}{\sigma_{1.5}}$	$\frac{\sigma_{2.0,T}}{\sigma_{2.0}}$	$\frac{\sigma_{u,T}}{\sigma_{u}}$	$\frac{\varepsilon_{u,T}}{\varepsilon_{u}}$	$\frac{\varepsilon_{f,T}}{\varepsilon_{f}}$
		$k_{E,T}$	$k_{0.2,T}$	$k_{0.5,T}$	$k_{1.5,T}$	$k_{2.0,T}$	$k_{u,T}$	$k_{\varepsilon_u,T}$	$k_{\varepsilon_f,T}$
80 × 40 × 2.6	23.0	1.00	1.00	1.00	1.00	1.00	1.00	1.00	1.00
	99.0	1.12	0.94	0.94	0.91	0.91	0.91	1.65	0.47
	200.5-1	1.00	0.94	0.94	0.91	0.91	0.91	1.50	0.69
	200.5-2	0.85	0.92	0.92	0.91	0.91	0.91	2.20	0.68
	300.5	0.58	0.89	0.84	0.91	0.91	0.92	3.65	1.05
	400.0	0.42	0.67	0.71	0.76	0.78	0.80	7.05	2.20
	500.0-1	0.68	0.53	0.53	0.46	0.45	0.52	0.55	1.54
	505.0-2	0.34	0.56	0.53	0.54	0.54	0.58	2.78	2.00
	603.0	0.23	0.36	0.34	0.33	0.33	0.34	0.68	2.13
	702.5	0.25	0.15	0.14	0.13	0.13	0.14	0.40	2.59
	798.5	0.10	0.05	0.06	0.06	0.06	0.06	2.07	6.09

Table 3.9: Data collected from previous literature.

Source	Cross–sections (mm)	Test method	No. of data collected						
			$k_{E,T}$	$k_{0.2,T}$	$k_{0.5,T}$	$k_{2.0,T}$	$k_{u,T}$	$k_{\varepsilon_u,T}$	$k_{\varepsilon_f,T}$
Outinen *et al.*(2001)	SHS 50 × 50 × 3	Transient	14	14	14	14	–	–	–
	SHS 80 × 80 × 3	Transient	14	12	12	14	–	–	–
	SHS 100 × 100 × 3	Transient	14	12	12	14	–	–	–
Balarupan (2015)	SHS 65 × 65 × 3	Steady	2	2	–	2	2	–	–
	SHS 65 × 65 × 6	Steady	7	7	–	7	7	–	–
	SHS 100 × 100 × 2	Steady	6	6	–	6	6	–	–
	SHS 100 × 100 × 6	Steady	4	4	–	4	4	–	–
McCann *et al.* (2015)	CHS 193.7 × 8	Steady	11	11	–	11	11	11	10
	RHS 250 × 150 × 10	Steady	11	11	–	11	11	11	11
	SHS 150 × 150 × 8	Steady	5	5	–	5	5	5	5
	RHS 250 × 150 × 10	Transient	8	–	–	7	7	–	7
	SHS 150 × 150 × 8	Transient	6	–	–	5	5	–	5
Imran *et al.* (2018)	SHS 100 × 100 × 2	Steady	11	11	–	11	11	11	–
	SHS 100 × 100 × 3	Steady	11	11	–	11	11	11	–
	RHS 100 × 50 × 2	Steady	11	11	–	11	11	11	–
	CHS 114 × 3.5	Steady	11	11	–	11	11	11	–
Total			146	128	38	144	102	71	38

Table 3.10: Comparison of elevated temperature reduction factors with present test results with predictions from design standards and literature

Design standards/ proposals	Reduction factors																			
	$k_{E,T}$					$k_{0.2,T}$					$k_{0.5,T}$									
	P_m	V_p	N	ϕ	β	P_m	V_p	N	ϕ	β	P_m	V_p	N	ϕ	β	P_m	V_p	N	ϕ	β
EC3-1-2 (2005)	1.07	0.28	31	0.70	2.56	0.84	0.18	31	0.65	2.66	–	–	–	–	–	–	–	–	–	–
EC3-1-2 (2005)–Class 4	–	–	–	–	–	1.10	0.15	31	0.90	2.65	–	–	–	–	–	–	–	–	–	–
BS 5950 (2003)	–	–	–	–	–	–	–	–	–	–	1.09	0.13	25	0.95	2.52	0.96	0.07	25	0.90	2.50
AS 4100 (1998)	0.82	0.27	31	0.55	2.55	0.89	0.25	31	0.60	2.66	–	–	–	–	–	–	–	–	–	–
AISC 360 (2010)	1.01	0.24	31	0.70	2.64	0.82	0.21	31	0.60	2.66	–	–	–	–	–	–	–	–	–	–
Balarupan (2015)	0.89	0.21	28	0.65	2.66	0.99	0.09	28	0.90	2.55	–	–	–	–	–	–	–	–	–	–
McCann *et al*. (2015)	–	–	–	–	–	–	–	–	–	–	–	–	–	–	–	–	–	–	–	–
Imran *et al*. (2018)	0.91	0.25	31	0.60	2.72	1.00	0.13	31	0.85	2.62	–	–	–	–	–	–	–	–	–	–

Table 3.10: (Continued) Comparison of elevated temperature reduction factors with present test results with predictions from design standards and literature

Design standards/ proposals	Reduction factors																			
	$k_{2.0,T}$					$k_{u,T}$					$k_{\varepsilon_u,T}$					$k_{\varepsilon_f,T}$				
	P_m	V_p	N	ϕ	β	P_m	V_p	N	ϕ	β	P_m	V_p	N	ϕ	β	P_m	V_p	N	ϕ	β
EC3-1-2 (2005)	0.82	0.20	31	0.60	2.72	0.93	0.12	31	0.80	2.65	–	–	–	–	–	–	–	–	–	–
EC3-1-2 (2005)–Class 4	–	–	–	–	–	–	–	–	–	–	–	–	–	–	–	–	–	–	–	–
BS 5950 (2003)	0.93	0.08	24	0.85	2.57	–	–	–	–	–	–	–	–	–	–	–	–	–	–	–
AS 4100 (1998)	–	–	–	–	–	–	–	–	–	–	–	–	–	–	–	–	–	–	–	–
AISC 360 (2010)	0.80	0.23	31	0.55	2.72	0.82	0.21	31	0.60	2.68	–	–	–	–	–	–	–	–	–	–
Chen and Young (2007)	–	–	–	–	–	–	–	–	–	–	3.15	1.46	31	0.10	2.56	–	–	–	–	–
Balarupan (2015)	1.03	0.16	28	0.85	2.55	–	–	–	–	–	–	–	–	–	–	–	–	–	–	–
McCann *et al*. (2015)	–	–	–	–	–	–	–	–	–	–	–	–	–	–	–	0.99	0.62	31	0.25	2.75
Imran *et al.* (2018)	0.97	0.14	31	0.80	2.68	0.98	0.15	31	0.80	2.68	–	–	–	–	–	–	–	–	–	–

Table 3.11: Comparison of elevated temperature reduction factors with all test results with design predictions

Design standards/ proposals	Reduction factors																			
	$k_{E,T}$					$k_{0.2,T}$					$k_{0.5,T}$					$k_{1.5,T}$				
	P_m	V_p	N	ϕ	β	P_m	V_p	N	ϕ	β	P_m	V_p	N	ϕ	β	P_m	V_p	N	ϕ	β
EC3-1-2 (2005)	1.04	0.25	177	0.70	2.65	0.83	0.29	159	0.50	2.72	–	–	–	–	–	–	–	–	–	–
EC3-1-2 (2005)–Class 4	–	–	–	–	–	1.12	0.28	159	0.70	2.68	–	–	–	–	–	–	–	–	–	–
BS 5950 (2003)	–	–	–	–	–	–	–	–	–	–	1.06	0.11	46	0.90	2.59	0.96	0.07	25	0.90	2.50
AS 4100 (1998)	0.87	0.85	172	0.16	2.50	1.09	1.46	157	0.04	2.56	–	–	–	–	–	–	–	–	–	–
AISC 360 (2010)	1.00	0.23	177	0.70	2.65	0.81	0.31	159	0.50	2.54	–	–	–	–	–	–	–	–	–	–
Balarupan (2015)	0.91	0.21	146	0.65	2.66	0.99	0.17	131	0.75	2.72	–	–	–	–	–	–	–	–	–	–
McCann *et al*. (2015)	–	–	–	–	–	–	–	–	–	–	–	–	–	–	–	–	–	–	–	–
Imran *et al*. (2018)	0.90	0.22	160	0.65	2.58	1.00	0.20	147	0.75	2.58	–	–	–	–	–	–	–	–	–	–
Proposed	–	–	–	–	–	1.10	0.30	159	0.70	2.52	1.02	0.12	69	0.85	2.62	1.02	0.14	31	0.85	2.51

Table 3.11: (Continued) Comparison of elevated temperature reduction factors with all test results with design predictions

Design standards/ proposals	Reduction factors																			
	$k_{2.0,T}$					$k_{u,T}$					$k_{\varepsilon_u,T}$					$k_{\varepsilon_f,T}$				
	P_m	V_p	N	ϕ	β	P_m	V_p	N	ϕ	β	P_m	V_p	N	ϕ	β	P_m	V_p	N	ϕ	β
EC3-1-2 (2005)	0.85	0.26	175	0.55	2.69	1.13	0.88	133	0.15	2.76	–	–	–	–	–	–	–	–	–	–
EC3-1-2 (2005)–Class 4	–	–	–	–	–	–	–	–	–	–	–	–	–	–	–	–	–	–	–	–
BS 5950 (2003)	0.97	0.10	120	0.85	2.52	–	–	–	–	–	–	–	–	–	–	–	–	–	–	–
AS 4100 (1998)	–	–	–	–	–	–	–	–	–	–	–	–	–	–	–	–	–	–	–	–
AISC 360 (2010)	0.83	0.27	175	0.55	2.57	0.89	0.30	133	0.55	2.66	–	–	–	–	–	–	–	–	–	–
Chen and Young (2007)	–	–	–	–	–	–	–	–	–	–	2.75	1.40	102	0.10	2.66	–	–	–	–	–
Balarupan (2015)	1.11	0.28	141	0.70	2.65	–	–	–	–	–	–	–	–	–	–	–	–	–	–	–
McCann *et al*. (2015)	–	–	–	–	–	–	–	–	–	–	–	–	–	–	–	1.10	0.56	69	0.35	2.71
Imran *et at*. (2018)	1.04	0.21	159	0.75	2.65	1.12	0.34	129	0.65	2.60	–	–	–	–	–	–	–	–	–	–
Proposed	1.10	0.31	175	0.65	2.66	1.19	0.34	133	0.70	2.56	–	–	–	–	–	2.20	0.60	69	0.70	2.55

Table 3.12: Proposed elevated temperature reduction factors for 0.2% proof strength; stress at 0.5%, 1.5%, 2.0% strains and ultimate strength.

Temperature (°C)	Reduction factors at temperature, T relative to ambient temperature value				
	$k_{0.2,T}$	$k_{0.5,T}$	$k_{1.5,T}$	$k_{2.0,T}$	$k_{u,T}$
20	1.00	1.00	1.00	1.00	1.00
100	0.96	0.97	0.97	0.96	0.96
200	0.90	0.93	0.94	0.91	0.91
300	0.85	0.85	0.91	0.86	0.85
400	0.78	0.74	0.81	0.81	0.80
500	0.55	0.50	0.56	0.57	0.53
600	0.31	0.30	0.33	0.29	0.29
700	0.12	0.13	0.13	0.15	0.15
800	0.07	0.06	0.06	0.08	0.07
900	0.04	0.03	–	0.04	0.05
1000	0.03	0.02	–	0.02	0.03

#Note: Linear interpolation may be used for reduction factors in the intermediate temperature

Table 3.13: Summary of post-fire mechanical properties of YSt-310 cold-formed steel hollow sections

Cross-sections	Temp. (ºC)	E_T^* (MPa)	$\sigma_{0.2,T}^*$ (MPa)	$\sigma_{0.5,T}^*$ (MPa)	$\sigma_{1.5,T}^*$ (MPa)	$\sigma_{2.0,T}^*$ (MPa)	$\sigma_{u,T}^*$ (MPa)	$\varepsilon_{u,T}^*$ (%)	$\varepsilon_{f,T}^*$ (%)	n_T^*	$H_{v,T}^*$
50 × 50 × 2.9	23.00	205184	394.26	408.52	429.71	433.35	456.92	8.79	19.47	3.71	170.43
	308.0	186000	430.10	436.59	450.30	464.50	490.14	5.04	12.50	2.67	166.17
	411.5	184000	404.24	410.05	424.65	441.51	484.39	6.51	13.08	3.80	168.73
	516.5	182513	355.12	357.66	370.87	398.62	451.74	8.12	13.68	3.67	157.97
	563.5	196154	347.57	352.90	350.98	383.57	445.54	10.09	17.09	3.20	151.50
	616.5	223684	330.77	344.24	337.65	368.26	429.48	8.72	14.91	22.19	143.70
	663.5	206667	311.40	314.40	315.24	323.98	406.60	11.65	18.61	4.72	147.50
	713.0	187200	283.47	286.30	296.98	304.72	395.00	13.74	20.62	4.66	128.50
	753.0	199200	264.40	266.76	286.74	281.17	390.68	15.29	21.20	6.34	126.70
	802.0	210000	273.74	246.11	273.92	292.21	387.06	10.01	21.19	13.02	119.70

Table 3.13: (Continued.) Summary of post-fire mechanical properties of YSt-310 cold-formed steel

Cross-sections	Temp. (°C)	E_T^* (MPa)	$\sigma_{0.2,T}^*$ (MPa)	$\sigma_{0.5,T}^*$ (MPa)	$\sigma_{1.5,T}^*$ (MPa)	$\sigma_{2.0,T}^*$ (MPa)	$\sigma_{u,T}^*$ (MPa)	$\varepsilon_{u,T}^*$ (%)	$\varepsilon_{f,T}^*$ (%)	n_T^*	$H_{v,T}^*$
60 × 40 × 2.9	23.00	197339	434.70	447.17	469.03	471.26	474.58	2.06	13.26	3.99	165.70
	308.0	185878	440.71	438.60	451.55	465.29	489.03	4.74	12.54	4.16	168.93
	411.5	178011	411.14	412.15	423.33	440.96	472.44	9.21	11.01	5.27	160.00
	516.5	228703	357.53	362.18	358.08	391.43	446.06	6.70	15.41	4.76	161.47
	563.5	181250	358.36	364.18	372.90	387.90	439.94	9.49	16.38	4.05	154.47
	616.5	200000	359.66	364.86	380.04	394.20	436.94	6.77	12.28	3.53	155.60
	663.5	180000	308.92	310.12	332.87	346.23	387.83	6.12	10.94	10.11	147.47
	713.0	181250	280.95	287.37	295.60	292.15	369.30	12.24	17.63	8.97	132.67
	753.0	183750	253.79	256.27	275.77	279.83	349.15	10.74	14.08	5.62	120.93
	802.0	205000	237.03	237.63	245.76	252.85	340.87	14.59	21.49	13.58	128.77
66 × 33 × 2.6	23.00	220000	435.96	444.28	458.22	463.11	485.50	9.46	17.22	6.64	164.03
	308.0	197143	482.29	483.63	494.94	508.27	528.46	3.82	09.34	20.20	177.37
	411.5	188000	448.20	449.83	449.46	482.04	513.31	4.71	10.31	6.00	171.10
	516.5	194286	390.47	394.96	398.61	421.87	484.55	8.21	14.22	6.33	168.93
	563.5	168235	333.44	362.26	416.80	421.50	491.97	9.23	16.61	2.65	164.77
	616.5	198333	396.33	400.48	405.37	423.39	477.41	7.08	12.56	6.31	145.90
	663.5	189643	358.03	360.54	357.10	383.72	437.31	8.12	12.30	4.99	130.77
	713.0	190357	325.55	325.55	333.32	344.18	422.52	10.83	16.82	16.47	132.77
	753.0	199286	292.26	297.96	301.64	304.81	407.38	12.74	19.91	10.19	123.93
	802.0	186500	232.26	227.84	233.88	246.42	359.82	17.80	28.70	7.06	124.77

Table 3.14: Comparisons of reduction factors obtained from the present test results and design predictions proposed in this Chapter

Cross-sections	Temp. (ºC)	k^*_{Expt}					k^*_{Pred}					k^*_{Expt}/k^*_{Pred}				
		E^*_T	$\sigma^*_{0.2,T}$	$\sigma^*_{u,T}$	ε^*_T	$H^*_{v,T}$	E^*_T	$\sigma^*_{0.2,T}$	$\sigma^*_{u,T}$	ε^*_T	$H^*_{v,T}$	E^*_T	$\sigma^*_{0.2,T}$	$\sigma^*_{u,T}$	ε^*_T	$H^*_{v,T}$
50 × 50 × 2.9	23.0	1.00	1.00	1.00	1.00	1.00	1.00	1.00	1.00	1.00	1.00	1.00	1.00	1.00	1.00	1.00
	308.0	0.91	1.09	1.07	0.64	0.97	0.85	1.00	1.00	0.54	1.00	1.07	1.09	1.07	1.19	0.97
	411.5	0.90	1.03	1.06	0.67	0.99	0.85	0.91	1.00	0.60	1.00	1.06	1.14	1.06	1.12	0.99
	516.5	0.89	0.90	0.99	0.70	0.93	0.85	0.81	0.93	0.69	0.91	1.05	1.11	1.07	1.01	1.02
	563.5	0.96	0.88	0.98	0.88	0.89	0.85	0.77	0.90	0.74	0.87	1.13	1.14	1.09	1.18	1.02
	616.5	1.09	0.84	0.94	0.77	0.84	0.85	0.72	0.86	0.81	0.83	1.28	1.16	1.09	0.95	1.01
	663.5	1.01	0.79	0.89	0.96	0.87	0.85	0.68	0.83	0.88	0.79	1.19	1.16	1.08	1.09	1.09
	713.0	0.91	0.72	0.86	1.06	0.75	0.85	0.64	0.79	0.96	0.75	1.07	1.13	1.09	1.11	1.00
	753.0	0.97	0.67	0.86	1.09	0.74	0.85	0.60	0.76	1.02	0.72	1.14	1.12	1.13	1.06	1.03
	802.0	1.02	0.69	0.85	1.09	0.70	0.85	0.56	0.73	1.11	0.68	1.20	1.24	1.17	0.98	1.03
60 × 40 × 2.9	23.0	1.00	1.00	1.00	1.00	1.00	1.00	1.00	1.00	1.00	1.00	1.00	1.00	1.00	1.00	1.00
	308.0	0.94	1.01	1.03	0.95	1.02	0.85	1.00	1.00	0.54	1.00	1.11	1.01	1.03	1.76	1.02
	411.5	0.90	0.95	1.00	0.83	0.97	0.85	0.91	1.00	0.60	1.00	1.06	1.05	1.00	1.39	0.97
	516.5	1.16	0.82	0.94	1.16	0.97	0.85	0.81	0.93	0.69	0.91	1.36	1.01	1.01	1.68	1.07
	563.5	0.92	0.82	0.93	1.24	0.93	0.85	0.77	0.90	0.74	0.87	1.08	1.07	1.04	1.67	1.07
	616.5	1.01	0.83	0.92	0.93	0.94	0.85	0.72	0.86	0.81	0.83	1.19	1.15	1.07	1.15	1.13
	663.5	0.91	0.71	0.82	0.83	0.89	0.85	0.68	0.83	0.88	0.79	1.07	1.04	0.99	0.94	1.12
	713.0	0.92	0.65	0.78	1.33	0.80	0.85	0.64	0.79	0.96	0.75	1.08	1.02	0.99	1.39	1.06
	753.0	0.93	0.58	0.74	1.06	0.73	0.85	0.60	0.76	1.02	0.72	1.09	0.97	0.97	1.04	1.01
	802.0	1.04	0.55	0.72	1.62	0.78	0.85	0.56	0.73	1.11	0.68	1.22	0.99	0.99	1.45	1.14

Table 3.14: (Continued.) Comparisons of reduction factors obtained from the present test results and design predictions proposed in this Chapter

Cross-sections	Temp. (ºC)	k^*_{Expt}					k^*_{Pred}					k^*_{Expt}/k^*_{Pred}				
		E^*_T	$\sigma^*_{0.2,T}$	$\sigma^*_{u,T}$	ε^*_T	$H^*_{v,T}$	E^*_T	$\sigma^*_{0.2,T}$	$\sigma^*_{u,T}$	ε^*_T	$H^*_{v,T}$	E^*_T	$\sigma^*_{0.2,T}$	$\sigma^*_{u,T}$	ε^*_T	$H^*_{v,T}$
66 × 33 × 2.6	23.0	1.00	1.00	1.00	1.00	1.00	1.00	1.00	1.00	1.00	1.00	1.00	1.00	1.00	1.00	1.00
	308.0	0.90	1.11	1.09	0.54	1.08	0.85	1.00	1.00	0.54	1.00	1.06	1.11	1.09	1.00	1.08
	411.5	0.85	1.03	1.06	0.60	1.04	0.85	0.91	1.00	0.60	1.00	1.00	1.14	1.06	1.00	1.05
	516.5	0.88	0.90	1.00	0.83	1.03	0.85	0.81	0.93	0.69	0.91	1.04	1.11	1.08	1.20	1.13
	563.5	0.76	0.76	1.01	0.96	1.00	0.85	0.77	0.90	0.74	0.87	0.89	0.99	1.13	1.29	1.15
	616.5	0.90	0.91	0.98	0.73	0.89	0.85	0.72	0.86	0.81	0.83	1.06	1.26	1.14	0.90	1.07
	663.5	0.86	0.82	0.90	0.71	0.80	0.85	0.68	0.83	0.88	0.79	1.01	1.21	1.09	0.81	1.00
	713.0	0.87	0.75	0.87	0.98	0.81	0.85	0.64	0.79	0.96	0.75	1.02	1.18	1.10	1.03	1.07
	753.0	0.91	0.67	0.84	1.16	0.76	0.85	0.60	0.76	1.02	0.72	1.07	1.12	1.10	1.13	1.05
	802.0	0.85	0.53	0.74	1.67	0.76	0.85	0.56	0.73	1.11	0.68	1.00	0.95	1.02	1.50	1.11
Mean (P_m)												1.09	1.09	1.06	1.17	1.05
COV (V_p)												0.09	0.08	0.05	0.21	0.05
Resistance factor (ϕ)												0.90	0.90	0.90	0.85	0.90
Reliability index (β)												2.78	2.83	2.80	2.58	2.76

Table 3.15: Proposed post-fire reduction factor predictive equations for YSt-310 cold-formed steel.

Reduction factors k^{*}_{Pred}	Prediction equations	Temperature, T (°C)
$\frac{E^{*}_{T}}{E}$	$= \begin{cases} -0.00053 \times T + 1.0121 \\ 0.85 \end{cases}$	$23 \le T < 308$ $308 \le T \le 802$
$\frac{\sigma^{*}_{0.2,T}}{\sigma_{0.2}}$	$= \begin{cases} 1 \\ -0.0009 \times T + 1.277 \end{cases}$	$23 \le T \le 308$ $308 < T \le 802$
$\frac{\sigma^{*}_{u,T}}{\sigma_{u}}$	$= \begin{cases} 1 \\ -0.0007 \times T + 1.29 \end{cases}$	$23 \le T \le 411.5$ $411.5 < T \le 802$
$\frac{\varepsilon^{*}_{f,T}}{\varepsilon_{f,T}}$	$= \begin{cases} -0.00165 \times T + 1.04 \\ 0.0000015 \times T^{2} - 0.0005 \times T + 0.55 \end{cases}$	$23 \le T < 308$ $308 \le T \le 802$
$\frac{H^{*}_{v,T}}{H_{v,T}}$	$= \begin{cases} 1 \\ -0.0008 \times T + 1.32 \end{cases}$	$23 \le T \le 411.5$ $411.5 < T \le 802$

Table 3.16: Stress-strain material models for post-fire mechanical properties of YSt-310 cold-formed steels tubular sections

For T = 23 °C

$$\varepsilon = \frac{\sigma}{E} + 0.002\left(\frac{\sigma}{\sigma_{0.2}}\right)^{n} \quad \text{for } \sigma \le \sigma_{0.2}$$

$$\varepsilon = \frac{\sigma - \sigma_{0.2}}{E_{0.2}} + \left(\varepsilon_u - \varepsilon_{0.2} - \frac{\sigma_u - \sigma_{0.2}}{E_{0.2}}\right)\left(\frac{\sigma - \sigma_{0.2}}{\sigma_u - \sigma_{0.2}}\right)^{m} \quad \text{for}$$

in which, (3.7)

$$n = \frac{\ln(4)}{\ln\left(\frac{\sigma_{0.2}}{\sigma_{0.05}}\right)}; \qquad E_{0.2} = \frac{E}{1 + 0.002n\frac{E}{\sigma_{0.2}}}; \qquad m = 1 + 2.8\frac{\sigma_{0.2}}{\sigma_u}$$

where $E_{0.2}$ is the tangent modulus at 0.2% proof stress

Table 3.16: (Continued.) Stress-strain material model for post-fire mechanical properties of YSt-310 cold-formed steels tubular sections

For $308\ ^{\circ}\text{C} \le T \le 802\ ^{\circ}\text{C}$:

$$\varepsilon_T^* = \frac{\sigma_T^*}{E_T^*} \qquad \text{for } \sigma_T^* \le \sigma_{0.2,T}^*$$

$$\varepsilon_T^* = \varepsilon_{u,T}^* - \left(\varepsilon_{u,T}^* - \varepsilon_{p,T}^*\right)\left(\frac{\sigma_{u,T}^* - \sigma_T^*}{\sigma_{u,T}^* - \sigma_{0.2,T}^*}\right)^{\frac{1}{p}} \qquad \text{for } \sigma_{0.2,T}^* < \sigma_T^* \le \sigma_{u,T}^* \tag{3.8}$$

in which,

$$\varepsilon_{p,T}^* = \varepsilon_{y,T}^*\left(0.0151 \times T - 0.2225\right); \qquad p = \frac{E_{p,T}^*\left(\varepsilon_{u,T}^* - \varepsilon_{p,T}^*\right)}{\sigma_{u,T}^* - \sigma_{y,T}^*};$$

$$E_{p,T}^* = E_T^*\left(-0.00001 \times T + 0.023\right);$$

where $\varepsilon_{p,T}^*$ and $E_{p,T}^*$ are the strain and elastic modulus at the onset of strain hardening

Table 3.17: Proposed post-fire reduction factor predictive equations for cold-formed steels

Reduction factors (k^*_{Pred})	Prediction equations	Temperature, T (°C)
$\frac{E^*_T}{E}$	$= \begin{cases} -0.00053 \times T + 1.0121 \\ 0.85 \end{cases}$	$20 \le T < 300$ $300 \le T \le 802$
$\frac{\sigma^*_{0.2,T}}{\sigma_{0.2}}$	$= \begin{cases} 1 \\ -0.0000003 \times T^2 - 0.0006 \times T + 1.2033 \end{cases}$	$20 \le T \le 300$ $300 < T \le 802$
$\frac{\sigma^*_{u,T}}{\sigma_u}$	$= \begin{cases} 1 \\ -0.0006 \times T + 1.1753 \end{cases}$	$20 \le T \le 300$ $300 < T \le 802$
$\frac{\varepsilon^*_{f,T}}{\varepsilon_{f,T}}$	$= \begin{cases} -0.00165 \times T + 1.04 \\ 0.0000015 \times T^2 - 0.0005 \times T + 0.55 \end{cases}$	$20 \le T < 300$ $300 \le T \le 802$

Table 3.18: Comparisons of post-fire reduction factors of cold-formed steel tubular sections

Sections and source	Temp. (°C)	k^*_{Expt}				k^*_{Pred}				k^*_{Expt}/k^*_{Pred}			
		E^*_T	$\sigma^*_{0.2,T}$	$\sigma^*_{u,T}$	ε^*_T	E^*_T	$\sigma^*_{0.2,T}$	$\sigma^*_{u,T}$	ε^*_T	E^*_T	$\sigma^*_{0.2,T}$	$\sigma^*_{u,T}$	ε^*_T
50 × 50 × 2.9	23	1.00	1.00	1.00	1.00	1.00	1.00	1.00	1.00	1.00	1.00	1.00	1.00
	308	0.91	1.09	1.07	0.64	0.85	0.99	0.99	0.54	1.07	1.10	1.08	1.19
	411.5	0.90	1.03	1.06	0.67	0.85	0.90	0.93	0.60	1.06	1.13	1.14	1.12
	516.5	0.89	0.90	0.99	0.70	0.85	0.81	0.87	0.69	1.05	1.11	1.14	1.02
	563.5	0.96	0.88	0.98	0.88	0.85	0.77	0.84	0.74	1.12	1.15	1.16	1.18
	616.5	1.09	0.84	0.94	0.77	0.85	0.72	0.81	0.81	1.28	1.17	1.17	0.94
	663.5	1.01	0.79	0.89	0.96	0.85	0.67	0.78	0.88	1.18	1.18	1.14	1.09
	713	0.91	0.72	0.86	1.06	0.85	0.62	0.75	0.96	1.07	1.16	1.16	1.11
	753	0.97	0.67	0.86	1.09	0.85	0.58	0.72	1.02	1.14	1.16	1.18	1.06
	802	1.02	0.69	0.85	1.09	0.85	0.53	0.69	1.11	1.20	1.31	1.22	0.98
60 × 40 × 2.9	23	1.00	1.00	1.00	1.00	1.00	1.00	1.00	1.00	1.00	1.00	1.00	1.00
	308	0.94	1.01	1.03	0.95	0.85	0.99	0.99	0.54	1.11	1.03	1.04	1.76
	411.5	0.90	0.95	1.00	0.83	0.85	0.90	0.93	0.60	1.06	1.05	1.07	1.39
	516.5	1.16	0.82	0.94	1.16	0.85	0.81	0.87	0.69	1.36	1.01	1.09	1.68
	563.5	0.92	0.82	0.93	1.24	0.85	0.77	0.84	0.74	1.08	1.07	1.11	1.66
	616.5	1.01	0.83	0.92	0.93	0.85	0.72	0.81	0.81	1.19	1.15	1.14	1.14
	663.5	0.91	0.71	0.82	0.83	0.85	0.67	0.78	0.88	1.07	1.06	1.05	0.94
	713	0.92	0.65	0.78	1.33	0.85	0.62	0.75	0.96	1.08	1.04	1.04	1.39
	753	0.93	0.58	0.74	1.06	0.85	0.58	0.72	1.02	1.10	1.01	1.02	1.04
	802	1.04	0.55	0.72	1.62	0.85	0.53	0.69	1.11	1.22	1.03	1.03	1.46

Table 3.18: (Continued.) Comparison of post-fire reduction factors of cold-formed steel sections

Sections and source	Temp. (°C)	k^*_{Expt}				k^*_{Pred}				k^*_{Expt}/k^*_{Pred}			
		E^*_T	$\sigma^*_{0.2,T}$	$\sigma^*_{u,T}$	ε^*_T	E^*_T	$\sigma^*_{0.2,T}$	$\sigma^*_{u,T}$	ε^*_T	E^*_T	$\sigma^*_{0.2,T}$	$\sigma^*_{u,T}$	ε^*_T
66 × 33 × 2.6	23	1.00	1.00	1.00	1.00	1.00	1.00	1.00	1.00	1.00	1.00	1.00	1.00
	308	0.90	1.11	1.09	0.54	0.85	0.99	0.99	0.54	1.05	1.12	1.10	1.01
	411.5	0.85	1.03	1.06	0.60	0.85	0.90	0.93	0.60	1.01	1.14	1.14	1.00
	516.5	0.88	0.90	1.00	0.83	0.85	0.81	0.87	0.69	1.04	1.10	1.15	1.19
	563.5	0.76	0.76	1.01	0.96	0.85	0.77	0.84	0.74	0.90	0.99	1.21	1.30
	616.5	0.90	0.91	0.98	0.73	0.85	0.72	0.81	0.81	1.06	1.27	1.22	0.90
	663.5	0.86	0.82	0.90	0.71	0.85	0.67	0.78	0.88	1.01	1.22	1.16	0.81
	713	0.87	0.75	0.87	0.98	0.85	0.62	0.75	0.96	1.02	1.20	1.16	1.02
	753	0.91	0.67	0.84	1.16	0.85	0.58	0.72	1.02	1.07	1.16	1.16	1.13
	802	0.85	0.53	0.74	1.67	0.85	0.53	0.69	1.11	1.00	1.01	1.07	1.50
75 × 75 × 2.5 – G450 Kesawan and Mahendran (2018)	20	1.00	1.00	1.00	–	1.00	1.00	1.00	–	1.00	1.00	1.00	–
	300	0.98	1.00	1.00	–	0.85	1.00	1.00	–	1.15	1.00	1.00	–
	400	0.98	0.97	0.97	–	0.85	0.91	0.94	–	1.15	1.06	1.04	–
	500	0.91	0.91	0.96	–	0.85	0.83	0.88	–	1.07	1.10	1.10	–
	600	1.02	0.82	0.92	–	0.85	0.73	0.82	–	1.20	1.12	1.13	–
	650	1.01	0.80	0.86	–	0.85	0.69	0.79	–	1.19	1.17	1.10	–
	700	–	0.74	0.82	–	–	0.64	0.76	–	–	1.16	1.09	–
	750	0.75	0.61	0.72	–	0.85	0.58	0.73	–	0.88	1.05	0.99	–
	800	0.77	0.58	0.70	–	0.85	0.53	0.70	–	0.91	1.09	1.01	–

Table 3.18: (Continued.) Comparison of post-fire reduction factors of cold-formed steel sections

Sections and source	Temp. (°C)	k^*_{Expt}				k^*_{Pred}				k^*_{Expt}/k^*_{Pred}			
		E^*_T	$\sigma^*_{0.2,T}$	$\sigma^*_{u,T}$	ε^*_T	E^*_T	$\sigma^*_{0.2,T}$	$\sigma^*_{u,T}$	ε^*_T	E^*_T	$\sigma^*_{0.2,T}$	$\sigma^*_{u,T}$	ε^*_T
75 × 75 × 2.0 – G450	20	1.00	1.00	1.00	–	1.00	1.00	1.00	–	1.00	1.00	1.00	–
Kesawan and Mahendran	400	0.93	0.99	0.97	–	0.85	0.91	0.94	–	1.09	1.08	1.04	–
(2018)	500	0.94	0.97	0.96	–	0.85	0.83	0.88	–	1.11	1.17	1.10	–
	600	1.03	0.88	0.94	–	0.85	0.73	0.82	–	1.21	1.20	1.15	–
	650	0.95	0.84	0.90	–	0.85	0.69	0.79	–	1.12	1.23	1.15	–
	700	–	0.68	0.75	–	–	0.64	0.76	–	–	1.07	0.99	–
	750	0.82	0.66	0.74	–	0.85	0.58	0.73	–	0.96	1.13	1.02	–
	800	0.81	0.61	0.72	–	0.85	0.53	0.70	–	0.95	1.15	1.04	–
75 × 75 × 6.0 – G350	20	1.00	1.00	1.00	–	1.00	1.00	1.00	–	1.00	1.00	1.00	–
Kesawan and Mahendran	300	0.92	1.10	1.06	–	0.85	1.00	1.00	–	1.08	1.10	1.06	–
(2018)	400	–	1.09	1.08	–	–	0.91	0.94	–	–	1.19	1.15	–
	600	1.10	0.90	0.99	–	0.85	0.73	0.82	–	1.29	1.23	1.21	–
	650	1.09	0.85	0.93	–	0.85	0.69	0.79	–	1.28	1.24	1.18	–
	700	1.12	0.84	0.93	–	0.85	0.64	0.76	–	1.32	1.32	1.23	–
	750	0.98	0.73	0.87	–	0.85	0.58	0.73	–	1.15	1.25	1.20	–

Table 3.18: (Continued.) Comparison of post-fire reduction factors of cold-formed steel sections

Sections and source	Temp. (°C)	k^*_{Expt}				k^*_{Pred}				k^*_{Expt}/k^*_{Pred}			
		E^*_T	$\sigma^*_{0.2,T}$	$\sigma^*_{u,T}$	ε^*_T	E^*_T	$\sigma^*_{0.2,T}$	$\sigma^*_{u,T}$	ε^*_T	E^*_T	$\sigma^*_{0.2,T}$	$\sigma^*_{u,T}$	ε^*_T
100 × 50 × 2.0 – G350	20	1.00	1.00	1.00	–	1.00	1.00	1.00	–	1.00	1.00	1.00	–
Kesawan and Mahendran	300	–	1.00	0.99	–	–	1.00	1.00	–	–	1.00	0.99	–
(2018)	400	1.05	0.97	0.96	–	0.85	0.91	0.94	–	1.24	1.06	1.03	–
	500	1.00	0.88	0.92	–	0.85	0.83	0.88	–	1.18	1.06	1.05	–
	600	1.19	0.80	0.88	–	0.85	0.73	0.82	–	1.40	1.09	1.08	–
	650	1.04	0.75	0.86	–	0.85	0.69	0.79	–	1.22	1.09	1.10	–
	700	1.19	0.72	0.78	–	0.85	0.64	0.76	–	1.40	1.13	1.03	–
	750	0.93	0.62	0.74	–	0.85	0.58	0.73	–	1.09	1.06	1.02	–
100 × 50 × 2.0 – G450	20	1.00	1.00	1.00	–	1.00	1.00	1.00	–	1.00	1.00	1.00	–
Kesawan and Mahendran	400	1.06	0.90	0.90	–	0.85	0.91	0.94	–	1.25	0.98	0.96	–
(2018)	500	0.98	0.82	0.86	–	0.85	0.83	0.88	–	1.15	0.99	0.98	–
	600	0.89	0.78	0.85	–	0.85	0.73	0.82	–	1.05	1.06	1.04	–
	650	1.05	0.74	0.81	–	0.85	0.69	0.79	–	1.24	1.08	1.03	–
	750	0.85	0.61	0.71	–	0.85	0.58	0.73	–	1.00	1.05	0.98	–
800 × 800 × 20 – Q235	20	1.00	1.00	1.00	1.00	1.00	1.00	1.00	1.00	1.00	1.00	1.00	1.00
Lu *et al.* (2016)	300	0.98	0.97	0.98	1.03	0.85	1.00	1.00	0.54	1.15	0.97	0.98	1.92
	500	1.00	0.86	0.92	1.30	0.85	0.83	0.88	0.68	1.17	1.04	1.05	1.92
	700	0.99	0.80	0.89	1.40	0.85	0.64	0.76	0.94	1.16	1.26	1.17	1.50
	800	1.01	0.72	0.88	1.47	0.85	0.53	0.70	1.11	1.19	1.35	1.26	1.32

Table 3.18: (Continued.) Comparison of post-fire reduction factors of cold-formed steel sections

Sections and source	Temp. (°C)	k^*_{Expt}				k^*_{Pred}				k^*_{Expt}/k^*_{Pred}			
		E^*_T	$\sigma^*_{0.2,T}$	$\sigma^*_{u,T}$	ε^*_T	E^*_T	$\sigma^*_{0.2,T}$	$\sigma^*_{u,T}$	ε^*_T	E^*_T	$\sigma^*_{0.2,T}$	$\sigma^*_{u,T}$	ε^*_T
50 × 50 × 3.0–S355	20	1.00	1.00	–	–	1.00	1.00	–	–	1.00	1.00	–	–
Outinen and Mäkeläinen (2004)	334	1.07	0.95	–	–	0.85	0.97	–	–	1.26	0.98	–	–
	369	0.88	0.92	–	–	0.85	0.94	–	–	1.04	0.98	–	–
	498	1.54	0.83	–	–	0.85	0.83	–	–	1.81	1.00	–	–
	498	1.02	0.82	–	–	0.85	0.83	–	–	1.20	0.99	–	–
	532	0.86	0.92	–	–	0.85	0.80	–	–	1.01	1.15	–	–
	532	1.00	0.88	–	–	0.85	0.80	–	–	1.18	1.10	–	–
	569	0.88	0.9	–	–	0.85	0.76	–	–	1.03	1.18	–	–
	602	0.71	0.84	–	–	0.85	0.73	–	–	0.83	1.15	–	–
	611	0.96	0.85	–	–	0.85	0.72	–	–	1.13	1.18	–	–
	611	0.89	0.88	–	–	0.85	0.72	–	–	1.04	1.21	–	–
	617	0.79	0.87	–	–	0.85	0.72	–	–	0.92	1.21	–	–
	643	0.87	0.84	–	–	0.85	0.69	–	–	1.02	1.21	–	–
	658	1.07	–	–	–	0.85	–	–	–	1.26	–	–	–
	674	0.89	0.93	–	–	0.85	0.66	–	–	1.04	1.41	–	–
	710	1.02	0.82	–		0.85	0.63	–	–	1.20	1.31	–	–
No. of observation										85	88	73	35
Mean										1.11	1.11	1.08	1.22
COV										0.12	0.09	0.07	0.24
Resistance factor (ϕ)										0.90	0.90	0.90	0.85
Reliability index (β)										2.73	2.86	2.83	2.54

This page is intentionally left blank.

Chapter 4

Stub columns

4.1 INTRODUCTION

Column is an important structural member which primarily carries compressive load along the major axis of the member. In general, the structural performances of columns under various loading conditions are experimentally or numerically (using finite element tools) estimated, and design equations are developed for effective use of the material and safety. In this chapter, the structural capacity of YSt-310 cold-formed steel tubular stub columns under concentric loading is explored through experimental and numerical investigations. Full range stress-strain curves and key material parameters (such as Elastic modulus, 0.2% proof stress, ultimate stress and corresponding strain etc.) at ambient temperature evaluated in Chapter 3 of this thesis has been utilised to developed finite element (FE) models. Column capacities for sections, which are not covered in the test, have been generated through validated FE models using the commercial FE software Abaqus (2010). The applicability of current updated international design standard such as EC3-1-1 (2005), AISI S100-16 (2016), which follows Effective Width Methods (EWM); and design rules such as Direct Strength Method (DSM) presented in AISI S100-16 (2016) and Continuous Strength

Method (CSM) developed by Gardner (2002, 2008) and his co-workers, on YSt-310 cold-formed steel has been assessed by comparing with the results generated from the FE analysis as well as experimental column resistances. Modified design rules have been developed based on the present analysis results.

In Section 4.2 of this chapter, an experimental programme to estimate the structural performance of YSt-310 SHSs and RHSs steel stub column under concentric loading has been conducted. Firstly, initial local geometric imperfections of the stub column specimens have been measured prior to testing using a non-contact three dimensional (3D) laser scanner. Secondly, the extent of corner strength enhancement due to cold-forming towards the flat region has been estimated through Vickers microhardness test. Thirdly, the structural behaviour of YSt-310 cold-formed steel stub columns with different cross-sectional dimensions has been tested through compression testing machines. The measured geometric imperfection amplitudes, the plots of the extent of corner strength enhancements based on hardness values and the load *vs* end shortening curves generated from the tests are reported in this section.

In Section 4.3 of this chapter, a finite element (FE) study (considering both geometric and material non-linearity) to evaluate the structural performance of wide range of cross-sections (both SHSs and RHSs), which are not covered in the test programme, have been investigated through validated FE models. The FE study has been conducted using the general-purpose commercial FE analysis software Abaqus (2010). Complete details of developing and validation the FE models are presented in this section.

In Section 4.4 of this chapter, the stub column capacities generated from the experimental programme as well as the numerical investigations are compared with the predictions in current design standards such as EC3-1-1 (2005), DSM in AISI S100-16 (2016), modified DSMs by Rossi and Rasmussen (2013) and Arrayago *et al.* (2017) and proposed design equations such as CSM by Zhao *et al.* (2017).

4.2 EXPERIMENTAL INVESTIGATION

4.2.1 Preparation of stub columns

A total of 12 stub column specimens have been prepared from their parent 6000 mm uncut length tubes. The stub columns have been cut using a rotary hacksaw with a nominal length of four times the minimum cross-section dimension. The ends of the columns have been milled flat (tolerance of ±0.1 mm) to allow proper seating on the bearing plates of the compression testing machine, which will ensure uniform load distribution during testing, following the procedure detailed in Theofanous and Gardner (2009) and Gardner *et al.* (2010). Column lengths have been chosen in such a way that they are short enough to avoid global flexural buckling but yet long enough to include representative distribution of geometric imperfections and residual stresses, as mention in Section 2.3. The first stub column specimen is represented by SC1 and the repeated specimen is represented by SC2 as listed in Table 4.1. The geometric dimensions measured prior to testing are summarized in Table 4.1, where L, r_i, A_g are the stub column length, inner corner radius and gross cross-sectional area respectively.

4.2.2 Microhardness test

The extent of strength enhancement beyond the corner region due to cold-forming has been reported by earlier researchers (e.g. Macdonald *et al.*, 1997; Cruise and Gardner, 2008) using Vickers microhardness test, since corner coupon test provides only the magnitude of the average corner strength. Microhardness test has been conducted to capture the variation of hardness profile with a finer resolution. The Vickers microhardness tester has been used in this present study, following the procedure detailed in Section 3.5.5. The surface hardness has been measured on three different cross sections: 66 × 33 × 2.6, 60 × 40 × 2.9 and 40 × 40 × 3.2, repeated for each section where the first section is represented by S1 and the second is represented by S2. The convention used to number corner positions is shown in Figure 4.1. Six samples having approximately 30 mm length have been cut from the parent 6000 mm length uncut tube and milled flat on both sides of the section. The surfaces have been

then polished on a rotating water lubricated disk equipped with silicon carbide paper of grit size ranging 100 to 1200. The grinding process not only makes an even and scratch free surface but also remove the plastic deformation resulted during the milling operation. A thin line has been marked at the mid-thickness of the specimens to identify easily through the optical microscope and further the cross-section has been divided into four quarters due to the limitation in movement of the sample (due to limited bed size of the optical microscope). A typical image showing the creation of diamond shaped indent is shown in Figure 4.2. The indent has been made at different locations at mid-thickness $\left(=r_i+0.5\times t=1.5\times t\right)$, as shown in Figure 4.1, with a separation of about 2–5 mm in the flat region and a finer separation of about 0.5–1 mm near the corner and weld regions. The present hardness study is meant to estimate the extent of strength enhancement due to cold forming; however, the relationship between strength and hardness is not assessed in the present study (positive relationships between hardness and strength were reported by other researchers, e.g. Tabor, 1951).

In order to estimate the extent of strength enhancement, the hardness value, H_v generated from the microhardness test have been plotted against the section length normalised by the section thickness in Figures 4.3–4.5 for 66 × 33 × 2.6, 40 × 40 × 3.2 and 60 × 40 × 2.9 cross-sections respectively. The origin of these graphs indicates the centre of the corner and it is represented by a solid vertical line. Another two vertical dotted lines have also been plotted at ~ ± 1.2*t*, which is approximately the junction of corner and flat edges. It is observed from Figures 4.3–4.5, that the spread of the corner strength enhancement can be seen to lie within a zone of ~ ± 3.0*t* from the centre of the corner, although relatively higher influence can be witnessed within ~ ± 1.2*t*. It is also observed that hardness values in the corner region are higher than the flat region and concentrated within the vicinity of corner region. Hardness values in the weld region are almost equal to the corner hardness value, but the extent is ~ 0.5*t* (i.e. approximately for a distance of half the thickness). A combined hardness distribution against the section length normalised by each section size for all the cross-sections considered is plotted in Figure 4.6. A three dimensional (3D) hardness distribution over the entire cross-section is plotted for 66 × 33 × 2.6-S2 in Figure 4.7.

The enhancement of strengths near the corners and weld region can be readily seen from Figure 4.7.

4.2.3 Local geometric imperfection

In the present study, a non-contact 3D Laser Scanner using Picza LPX–25ORE scanner having a resolution capacity of 0.2 to 60 degrees circumferential and 0.2 to 406.4 mm height has been employed to measure the local geometric imperfection of SHS and RHS stub columns. A representative measurement for each cross-section has been conducted on one of the stub column specimens. The flat milled specimen has been placed at the middle of the scanner platform and rotary scanning has been performed to capture the outer surface profile at a grid size of 1.0 mm x 1.0 mm. The surface profiles have been generated in the form of polylines joining all the nodes as shown in Figure 4.8 (a). The imperfection amplitude has been measured along the centreline of all four faces of the section, as shown by the red line in Figure 4.8 (b). A schematic longitudinal profile (not to scale) measured at the centreline is shown in Figure 4.8 (c). The effects of end flaring as suggested by earlier researcher such as Cruise and Gardner (2006), Theofanous *et al.* (2009a) etc., and bends due to residual stress and milling operation have been removed by considering only 50% of the specimen length.

In the current study, the average of the deviations from the line joining the tips of central 50% of the member length (i.e. leaving 25% of the length at both the ends), for each face of the four faces has been estimated (see Figure 4.9). The measured initial localised geometric imperfection, ω_d of a member is defined as average of the four average deviations for each faces of the section. The results of the geometric imperfection are summarised in Table 4.1. A typical measured two dimensional (2D) longitudinal sectional profile of the four faces of SHS–80 × 40 × 2.6 stub column specimen is shown in Figure 4.9. From Table 4.1, it can be seen that value of local imperfection ranges from ω_d = 0.012–0.047 mm (or t/60–t/248). These values of imperfection amplitudes are slightly lower than those measured by Theofanous and

Gardner (2009) for stainless steel tubular sections (~*t*/47–*t*/55). At the first instance, this difference can be attributed to the measurement procedure adopted herein where average deviations are considered instead of the maximum deviation. It may be noted, in the numerical modelling, effect of imperfection magnitudes (e.g. *t*/10–*t*/100) did not have significant effect on the predicted values of ultimate load capacity (see e.g. Zhu and Wilkinson, 2006; Theofanous and Gardner, 2009 etc.), although some variation on post-ultimate behaviours were reported (see Zhu and Wilkinson, 2006).

4.2.4 Stub column test

Concentrically loaded stub column tests have been performed on each of the SHS and RHS. Two tests have been conducted for each of the specimens except for 60 × 60 × 2.6 and 80 × 40 × 2.6 specimens, where the test results have been discarded due to a technical error during the test. Two hydraulic loading frames, one with a capacity of 250 kN (with a facility of conducting both load and displacement control tests) and another with 1000 kN, (with a capability of conducting only load control test) have been used to estimate the load resistance versus end-shortening behaviour of all stub columns. The compression test setups for 250 kN and 1000 kN are respectively shown in Figures 4.10 and 4.11. Two specimens having cross-sections represented by 66 × 33 × 2.6-SC1 and 66 × 33 × 2.6-SC2 (i.e. thinner specimens) have been tested in 250 kN hydraulic testing machine under displacement-control procedure at a constant rate of 0.45 mm/min and the remaining 10 stub columns have been tested using 1000 kN hydraulic testing machine under load-control procedure at a constant optimal speed of ~ 1 kN/sec. The end-shortenings of specimens have been recorded by using a 50 mm gauge length extensometer and two LVDTs for 250 kN and 1000 kN hydraulic testing machine respectively. Typical deformed shapes of three stub columns are shown in Figure 4.12. Load-end shortening behaviours of all the sections are depicted in Figures 4.13 and 4.14. A moderate degree of strain hardening has been observed from the load-deformation curves. The results of the stub column tests are presented in Table 4.1, in the form of ultimate loads (P_{Test}) and the corresponding displacements (δ_u).

4.3 FINITE ELEMENT MODELLING

4.3.1 General

The commercial finite element tool Abaqus (2010) version 6.9 has been used to generate stub column capacities (for wide range of cross-sections) which have not been covered in the stub column tests, after carefully calibrating the numerical procedure with the experimental results. The measured sectional geometry, local geometric imperfection, and non-linear material properties from different tensile coupon test results have been incorporated in the finite element model. Full cross-section FE models, based on the centreline dimensions have been developed and, the length of each model has been taken as the measured untested column length listed in Table 4.1. The modelling approach followed two-step procedures: firstly the buckling mode shapes have been generated and secondly the non-linear load-end shortening behaviour has been investigated, using Eigenvalue analysis tools and static Riks method available in the Abaqus (2010). The numerical analysis procedure followed in this thesis were used by earlier researchers such as Theofanous and Gardner (2009); Patton and Singh (2012); Zhu and Young (2012); Sachidananda and Singh (2017) etc. In the following sections the FE modelling procedures are discussed.

4.3.2 Finite element type

Because of the thin-walled nature, a reduced integration 4-noded doubly curved S4R shell element has been utilised to model the SHS and RHS stub columns. The S4R shell element with six (three translational and three rotational) degrees of freedom for each node is known to provide accurate results for similar studies done on thin-walled tubular structures (see Theofanous and Gardner, 2009; Theofanous and Gardner, 2010; Patton and Singh, 2012; Zhu and Young, 2012; Zhao *et al.*, 2017; Sachidananda and Singh (2017 etc.). An element size of approximately two times the thickness of the section with an aspect ratio of ~ 1.0 has been adopted in the flat portion based on mesh convergence study. However for the curved portion, a finer mesh has been used to accurately represent the curved geometry (see Theofanous and Gardner, 2009).

4.3.3 Flat and corner material properties

The behaviour and performance of structural steel member are depended on the material property and assigning of material properties at appropriate portions of the section will help to accurately simulate the real test specimens. It has been noted from earlier similar researches concerning modelling of thin-walled cold-formed sections that the corner material property be extended toward the flat regions on either side of the corners up to a distance equal to two times the thickness of the cross-section (e.g. Gardner and Nethercot, 2004a; Cruise and Gardner, 2008; Theofanous and Gardner, 2009; Ma *et al.*, 2016; Zhao *et al.*, 2017). On the other hand, Huang and Young (2012) reported incorporation of flat and corner material properties to the flat and corner regions only. In the present study, the distribution of flat and corner material properties around the cross-section has been considered based on the microhardness test reported in Section 4.2.2. The flat and corner material properties have been assigned to the flat and corner region of the section considered respectively without extending the corner material properties to the flat portion.

4.3.4 Weld material properties

Cold-formed and built-up (e.g. Zhu *et al.*, 2016) tubular sections are made by cold-forming process and finally closed with the help of different welding techniques such as butt, seam welding etc. Due to the welding process, the stress-strain properties of the coupon cut from the weld portion is different from flat material properties as observed in Section 3.3.4. The use of weld material properties in the finite element modelling of thin-walled structures has been reported by very few researchers such as Zhu *et al.* (2016), however the comparison of numerical models, with or without weld material properties has not been reported to the author's knowledge. Hence, in Section 4.3.7, comparison of FE models with and without the consideration of weld material properties is investigated for – 60 × 40 × 2.9-SC1 and 66 × 33 × 2.6-SC1 rectangular sections.

Abaqus property module allows assigning multi-linear stress-strain properties and for each material considered separate entries in the elastic and plastic range are made. The recorded Young's modulus, E and Poisson's ratio (υ) of 0.3 have been incorporated first in the elastic range and the non-linear stress-strain material properties from the tensile coupon test of flat, corner and weld which have been converted to true stress σ_{true} and logarithmic plastic strain ε_{true}^{pl} curves using the following Equations 4.1 and 4.2 respectively, have been incorporated in the plastic range.

$$\sigma_{true} = \sigma_{eng}\left(1+\varepsilon_{eng}\right) \tag{4.1}$$

$$\varepsilon_{true}^{pl} = \ln\left(1+\varepsilon_{eng}\right) - \left(\frac{\sigma_{true}}{E}\right) \tag{4.2}$$

where, σ_{eng} and ε_{eng} are the recorded engineering stress and strain from tensile coupon test respectively.

4.3.5 Local geometric imperfection and residual stress

Initial imperfections are important parameters which influence the ultimate resistance and post buckling deformation mechanism of cold-formed steel (see Schafer and Peköz, 1999), which are introduced to a member primarily due to fabrication, transportation and storage. Initial local geometric imperfection has been introduced in the finite element model with three imperfection magnitude variations: the measured imperfection magnitude, ω_d from the untested specimens (see Table 4.1), $t/100$ and ω_0 (imperfection amplitude predicted by Dawson and Walker, 1972 model adapted by Gardner and Nethercot, 2004a for stainless steel members as given in Equation 4.3). The lowest buckling mode shape from the Eigenvalue analysis has been utilized to perturb the imperfect geometry of the column.

$$\omega_0 = 0.023\left(\frac{\sigma_{0.2}}{\sigma_{cr}}\right)t \tag{4.3}$$

where $\sigma_{0.2}$ is the measured 0.2% proof stress of flat tensile coupon test given in Table 3.4 and σ_{cr} is the elastic critical buckling stress of the most slender flat plate element in the member.

In the present study, the effect of residual stress is not accounted in the FE models, following similar studies in the literature such as Ellobody and Young (2005a), Huang and Young (2014b), Anwar-us-saadat *et al.* (2016), Ma *et al.* (2016) etc., as the effect of residual stress to the overall behaviour and ultimate load resistance is reported to be negligible. Further, it has been noted from previous studies such as Young and Lui (2005), Theofanous and Gardner (2009), Theofanous and Gardner (2010) etc., that residual stress may not be explicitly modelled in the FE modelling as the material properties from tensile coupon test has already incorporated the effect residual stress.

4.3.6 Loading and boundary conditions

The boundary and loading conditions of stub columns tested have been simulated for fixed ended column, by restraining all degrees of freedom except the translation in the loading direction. The top and bottom edge geometry of the finite element model have been tied to two reference points, RP–1 and RP–2 respectively, using kinematic coupling method available in Abaqus (2010) library. The degrees of freedom of the two reference points are restrained in all direction, except the translational degree of freedom of RP–2 has been allowed to displace in the column length direction. A central normal load han been applied concentrically through RP–2 using load control loading method.

4.3.7 Validation of FE procedure

This section presents the calibration of the numerical modelling procedure to perform parametric study. The load capacity P_{FE} and deformation pattern predicted by the developed SHS and RHS FE models are compared with the stub column test results. The sensitivity of numerical simulations, particularly by the three imperfection

magnitudes and effect of the inclusion of weld material property on the FE modelling approach have been sought. A comparative analysis has been investigated on the full load-deformation curve, including initial elastic curve, strain hardening, ultimate load and post-buckling responses. Figures 4.15 and 4.16 depict the comparison of load-end shortening curves generated from FE simulations against the stub columns test results. The comparison of deformed shapes from test and FE for 80 × 40 × 2.6-SC1 and 66 × 33 × 2.6-SC1 are shown in Figures 4.17 (a) and (b) respectively. It has been observed from the comparison that the stub columns are mostly failed by local buckling with an appreciable degree of yielding. Table 4.2 summarised the ratio of ultimate loads predicted by FE to that of load recorded from the stub column test results for three different imperfection magnitudes and two sections with weld and without weld. It can be seen from Table 4.2 that the ultimate column resistances predicted by FE simulations are in good agreement with the test results. The mean values of the ratio of FE to the test ultimate load are 1.007, 1.009 and 1.005 with corresponding COVs of 0.024, 0.022, and 0.024 for three different local imperfection amplitudes: ω_d, ω_0 and $t/100$, respectively. The predictions using the three imperfection amplitudes are observed to be close and the differences are negligible, suggesting that the ultimate load capacity are not significantly influenced by the range of imperfection magnitudes considered in this study. Similar observations have also been made by Zhu and Wilkinson (2018). However, as observed in Table 4.2, with ω_0 the FE predictions are closest to experimental results, hence in all the subsequent analyses, reported herein, imperfection magnitudes computed based on modified Dawson and Walker model (detailed in Gardner and Nethercot, 2004b) i.e. ω_0 are considered.

Typical load-deformation curves predicted by FE models for the two sections – 60 × 40 × 2.9-SC1 and 66 × 33 × 2.6-SC1 are compared with corresponding experimental results in Figure 4.15, considering with and without weld material properties in the FE models. It can be observed from Figure 4.15 that, both the experimental ultimate load and post-buckling curves have been well predicted by the current FE models. However, it has been seen from Table 4.2 that, there is a slight enhancement in the predicted values when the weld material properties are considered in the FE models.

Considering the minimal effect on the ultimate resistance and overall load-deformation characteristic, it is concluded that numerical model without weld material property is able to capture experimental curve accurately. Hence, for the parametric study carried out in the following part of this thesis, weld material properties have been ignored.

4.3.8 Parametric study

Upon carefully calibrated the FE modelling approach for stub column with the experimental results, the numerical procedure has been utilised for parametric study. The ultimate loads and corresponding displacements have been estimated from the FE analysis. The material properties incorporated in the FE analysis for parametric study have been the measured flat and corner material properties of 66 × 33 × 2.6-SC1 sections since the validation of FE modelling for this section has been accurately captured with the test result. The imperfection amplitudes predictive model adapted by Gardner and Nethercot (2004) has been followed in the parametric study since it gives good prediction as compared to the other two imperfection amplitudes (see Table 4.2), as also reported by other researchers such as Theofanous and Gardner (2009), Theofanous and Gardner (2010), Patton and Singh (2012), Sonu and Singh (2017b), Arrayago *et al.* (2017), Zhao *et al.* (2017), Sachidananda and Singh (2017) etc.

Over a wide range of cross-sections and thickness variation, which have been not covered in the experimental programme, FE models have been developed with an intention particularly to look the overall load deformation and strain hardening characteristics of cold-formed YSt-310 SHS and RHS structural steel sections. The cross-sections considered in the present analysis are taken from those provided in the Tata Steel production manual, see Tata Steel (2013), except for some sections for which the thicknesses have been considered up to 50.0 mm, though only up to 10 mm are available in the Tata Structura manual. The SHS cross-sectional sizes range from 25 mm to 250 mm whereas for the RHS, the width, B and depth, D ranges from 50 mm to 300 mm and 25 mm to 200 mm respectively, resulting in minimum and

maximum aspect ratios of 1.5 and 2.0 respectively. The thickness, *t* of the cross-sections considered in the present study ranges from 2.0 mm to 50.0 mm, to cover a wide range of cross-sectional slenderness. The length of the stub column *L* in the finite element models has been set equal to four times the minimal of cross-sectional size. Following the validation process, a mesh size of two times the cross-sectional thickness has been adopted in the flat portion whereas a finer mesh has been applied to depict the curvature accurately. A total of 12 stub columns test and 173 finite elements (provided in Table 4.3) generated results have been compared with EC3-1-1 (2005); design rules – CSM detailed in Zhao *et al.* (2017); DSM presented in AISI S100-16 (2016) and modified DSM by Rossi and Rasmussen (2013) and Arrayago *et al.* (2017). Further, based on the statistical analysis results, design recommendations are proposed to suit the design of cold-formed YSt-310 structural steels.

4.4 CURRENT DESIGN CODE AND RULES

4.4.1 General

The applicability of current international design code and methods to YSt-310 cold-formed constructional steel, with primary focus on load capacity and deformation behaviour for wide range of cross-sectional slenderness has been assessed by comparing results from the stub column test and finite element analysis. A total of 12 stub column test and 173 FE generated column resistances/capacities have been compared with the design predictions by EC3-1-1 (2005); CSM by Zhao *et al.* (2017); DSM in AISI S100-16 (2016) and modified DSM by Rossi and Rasmussen (2013)and Arrayago *et al.* (2017). The applicability of above considered design code and rules as well as proposed modified versions are assessed through reliability analysis.

4.4.1.1 European code

The European design code EC3-1-1 (2005) for carbon steel relies on the idealised elastic-perfectly plastic stress-strain material model and is most suitable for hot-rolled steel. To account for the effect of local buckling, four types of cross-sections are

classified using a non-dimensional parameter, $c/t\varepsilon$ where c and t are the flat element length and thickness of the cross-section and $\varepsilon = \sqrt{235/f_y}$, f_y is the material yield stress. The effect of element interaction present in the case of RHS, where a more slender element is restrained by the less slender element (see Seif and Schafer, 2010), has been accounted while estimating $c/t\varepsilon$ parameter following Wang *et al.* (2017). The equivalent flat element width, $b_{eq,flat} = c$ for RHS has been calculated using Equation 4.4:

$$b_{eq,flat} = c = b_{eq,cl} \times \frac{b_{flat}}{b_{cl}} \tag{4.4}$$

where, $b_{eq,cl} = \sqrt{\frac{k\pi^2 Et^2}{12(1-\nu^2)} \times \frac{1}{\sigma_{cr,cs}}}$ and in Equation (4.4), b_{flat}, b_{cl} and $b_{eq,cl}$ are the web flat, centreline and equivalent width respectively. The cross-section elastic buckling stress, $\sigma_{cr,cs}$ has been estimated from Abaqus (2010) based on centre line geometry, allowing element interaction suggested by Seif and Schafer (2010). k is the buckling factor which depends on the boundary condition and stress ratio, ψ. The value of k and ψ are taken as 4 and 1 respectively based on EC3-1-5 (2006). For all the calculations, the value of Young's modulus measured from flat tensile coupon test (see Table 3.4) is considered.

The present study of YSt-310 cold-formed RHS and SHS comprises of Class–1 ($c/t\varepsilon \leq 33$), Class–2 ($c/t\varepsilon \leq 38$), Class–3 ($c/t\varepsilon \leq 42$) and Class–4 ($c/t\varepsilon > 42$) cross-sections. The un-factored design strength of a uniform compression member based on Clause 6.2.4 of EC3-1-1 (2005), P_{EC3} is given in Equation 4.5.

$$P_{EC3} = \begin{cases} A_g f_y, & \text{for Class–1, 2 or 3 cross-sections} \\ A_{eff} f_y, & \text{for Class–4 cross-sections} \end{cases} \tag{4.5}$$

Where A_g is the cross-sectional area for Class–1, 2 or 3 sections, considering the section as fully effective and no deduction in the area while estimating the compressive strength whereas A_{eff} is the effective cross-sectional area for Class–4 sections, considering some part of flat plate as ineffective and deducted in calculating the section resistance. The effective area A_{eff} of compressive zone of a plate element is estimated using Clause 4.4 of EC3-1-5 (2006) using Equation 4.6.

$$A_{eff} = \sum \rho A_p + \sum A_{cr} \tag{4.6}$$

where A_p and A_{cr} are the gross cross-sectional area of plated (flat) elements and corners area respectively and ρ is the reduction factor parameter given by Equation 4.7 for internal compression element. The corner areas have been considered to be fully effective and therefore no reduction has been applied.

$$\rho = \begin{cases} 1.0 & \text{for } \bar{\lambda}_p \le 0.673 \\ \dfrac{\bar{\lambda}_p - 0.055(3+\psi)}{(\bar{\lambda}_p)^2} \le 1.0 & \text{for } \bar{\lambda}_p > 0.673 \end{cases} \tag{4.7}$$

$$\sigma_{cr} = \frac{k\pi^2 E}{12(1-\nu^2)}\left(\frac{t}{c}\right)^2 \tag{4.8}$$

where $\bar{\lambda}_p$ is the local slenderness calculated as $\bar{\lambda}_p = \sqrt{f_y / \sigma_{cr}}$, where σ_{cr} is the plate elastic buckling stress estimated based on the centreline dimension for RHS by using Abaqus (2010) and flat element width c $(= B - 2r_i - 2t)$ for SHS using Equation 4.8.

4.4.1.2 Continuous strength method

The present design standards for cold-formed carbon steel do not account for strain hardening behaviour, instead followed the idealised linear-perfectly plastic material model, thereby resulting overly conservative and scattered predictions for

compressive cross-section at lower cross-section slenderness range (detailed in Zhao *et al.*, 2017). The continuous strength method proposed by Gardner and his co-workers (see Gardner 2002, 2008; Afshan and Gardner, 2013), on the other hand is a deformation based design approach which relies on bilinear stress-strain material model, accurately representing the rounded material characteristic seen in cold-formed and stainless sections. The applicability of CSM, which has been originally developed for the design of non-slender stainless steel plated sections has been extended to design for slender plated cross-section by researchers such as Ahmed *et al.* (2016), Zhao *et al.* (2017) etc. In CSM, the cross-sectional classification to handle local buckling has been replaced by a 'base curve', derived from stub column and beam test data of carbon and stainless steel sections. The base curve is a continuous relationship between full cross-section slenderness $\bar{\lambda}_p$ and deformation capacity expressed in terms of strain ratio $\left(\varepsilon_{csm}/\varepsilon_y\right)$. The deformation capacity normalised by the yield strain $\varepsilon_y = \left(f_y/E\right)$ measures the capability of the section to undergo strain hardening and increased load due to strain hardening. The deformation capacity $\left(\varepsilon_{csm}/\varepsilon_y\right)$ of a cross-section is calculated using Equation 4.9 for different cross-sectional slenderness ranges and ultimate load P_u to yield load $P_y = f_y A_g$ ratio of the stub column.

$$\frac{\varepsilon_{csm}}{\varepsilon_y} = \begin{cases} \dfrac{\varepsilon_{lb} - 0.002}{\varepsilon_y} & \text{for } \bar{\lambda}_p \le 0.68 \text{ and } P_u \ge P_y \\ \dfrac{P_u}{P_y} & \text{for } \bar{\lambda}_p > 0.68 \text{ or } P_u < P_y \end{cases} \tag{4.9}$$

where, $\bar{\lambda}_p = \sqrt{f_y/\sigma_{cr,cs}}$ is the cross-sectional slenderness calculated based on the centreline dimension. In Equation 4.9, $\varepsilon_{lb} = \delta_u/L$ and δ_u are the local buckling strain and deformation at ultimate load respectively. Full cross-section elastic critical buckling stress $\sigma_{cr,cs}$ can be estimated through elastic buckling analysis using finite

strip method (such as CUFSM by Schafer and Ádány, 2006) or finite element analysis tool (e.g. Abaqus, 2010), in similar line as defined in Section 4.4.1.1.

The base curves (detailed in Afshan and Gardner, 2013; Zhao *et al.*, 2017) for both non-slender and slender sections are given by Equations 4.10 and 4.11 respectively.

$$\frac{\varepsilon_{csm}}{\varepsilon_y} = \frac{0.25}{\bar{\lambda}_p^{3.6}} \qquad \text{for } \bar{\lambda}_p \le 0.68 \text{ but } \frac{\varepsilon_{csm}}{\varepsilon_y} \le \min\left(15, \frac{C_1\varepsilon_u}{\varepsilon_y}\right) \tag{4.10}$$

$$\frac{\varepsilon_{csm}}{\varepsilon_y} = \left(1 - \frac{0.222}{\bar{\lambda}_p^{1.050}}\right)\frac{1}{\bar{\lambda}_p^{1.050}} \qquad \text{for } \bar{\lambda}_p > 0.68 \tag{4.11}$$

where ε_u is the predicted ultimate tensile strain. Two upper bounds are set on the deformation capacity in Equation 4.10 to limit the extend up to which deformation of non-slender cross-section can occur. The first limit of 15 represents the material ductility requirement as per EC3-1-1 (2005) and it is applicable for all metallic materials and the second limit of $\left(C_1\varepsilon_u/\varepsilon_y\right)$ verifies that the cross-sectional resistance does not over predict by using the adopted linear hardening material model. The CSM design stress f_{csm}, strain hardening slope E_{sh} and predicted strain corresponding to ultimate tensile stress ε_u for non-slender cross-section have been calculated using Equations 4.12–4.14.

$$f_{csm} = f_y + E_{sh}\varepsilon_y\left(\frac{\varepsilon_{csm}}{\varepsilon_y} - 1\right) \tag{4.12}$$

$$E_{sh} = \frac{f_u - f_y}{C_2\varepsilon_u - \varepsilon_y} \tag{4.13}$$

$$\varepsilon_u = C_3\left(1 - \frac{f_y}{f_u}\right) + C_4 \tag{4.14}$$

The constants C_1, C_2, C_3 and C_4 are the material related coefficients and are calculated based on tensile coupon test results as detailed in Zhao *et al.* (2017). In the present study the value of C_1, C_2, C_3 and C_4 are 0.4, 0.45, 0.60 and 0.0 respectively as listed in Zhao *et al.* (2017), for cold-formed carbon steel. As mentioned earlier CSM replaced the traditional lengthy effective width calculation method which is being followed in most of the design codes. The column capacity as per CSM is evaluated based on the gross cross-sectional area A_g. The expression to evaluate column capacity, P_{csm} of a member predicted by CSM (detailed in Zhao *et al.*, 2017) is given in Equation 4.15.

$$P_{csm} = \begin{cases} A_g f_{csm} & \text{for } \bar{\lambda}_p \le 0.68 \\ \dfrac{\varepsilon_{csm}}{\varepsilon_y} A_g f_y & \text{for } \bar{\lambda}_p > 0.68 \end{cases} \quad (4.15)$$

CSM has been developed to estimate the design compressive strength of various materials such as cold-formed steel S235 (see in Gardner *et al.*, 2011), various duplex (such as Huang, 2013; Saliba and Gardner, 2013; Sachidananda and Singh, 2017), ferritic and austenitic stainless steel by Afshan and Gardner (2013), aluminium alloy by Su *et al.* (2014). The applicability of this design rule on YSt-310 cold-formed steel is being accessed in this present study.

4.4.1.3 Direct strength method

The design capacity of a concentrically loaded compression member based on Direct Strength Method (DSM) detailed in Section E of AISI S100-16 (2016) are given in Equations 4.16 and 4.17. The nominal axial compressive strength P_{DSM} shall be taken as the smallest of the axial strength for yielding and global buckling (P_{ne}), local buckling (P_{nl}) and distortional buckling (P_{nd}) column capacity. However, in the present study, as closed sections being concerned, the distortional buckling capacity is very large and therefore distortional buckling is ignored. Therefore, the nominal

capacity of a compression member shall be the minimum of yielding and global buckling (P_{ne}) and local buckling (P_{nl}).

$$P_{DSM} = \min\left(P_{ne}, P_{nl}\right) \tag{4.16}$$

where,

$$P_{ne} = A_g F_n$$

$$P_{nl} = \begin{cases} P_{ne} & \text{for } \lambda_l \le 0.776 \\ \left[1 - 0.15\left(\frac{P_{crl}}{P_{ne}}\right)^{0.4}\right]\left(\frac{P_{crl}}{P_{ne}}\right)^{0.4} P_{ne} & \text{for } \lambda_l > 0.776 \end{cases} \tag{4.17}$$

$$F_n = \begin{cases} \left(0.658^{\lambda_c^2}\right) f_y & \text{for } \lambda_c \le 1.5 \\ \left(\frac{0.877}{\lambda_c^2}\right) f_y & \text{for } \lambda_c > 1.5 \end{cases}$$

In Equation 4.17, $\lambda_l = \sqrt{P_{ne}/P_{crl}}$; $\lambda_c = \sqrt{f_y / f_{cre}}$; $f_{cre} = (\pi^2 E / (KL/r_g)^2$ where P_{crl}, K, L and r_g are the critical elastic local column buckling load, effective length factor, length of the column and radius of gyration of the cross-section about the minor axis of buckling respectively.

4.4.1.4 Modified DSM

The present DSM provision implemented in AISI S100-16 (2016) and its earlier editions does not account for the strain hardening effects in the design of short cold-formed steel columns. Design predictions using DSM for short columns show a great degree of conservativeness. To improve the column capacity prediction at low slenderness range or stocky cross-sections, Rossi and Rasmussen (2013) replaced the classical horizontal yield limit by a linear expression composed with cross-section slenderness, ultimate stress and proof stress of tensile test for stainless steel sections

as shown in Equation 4.18. Further, Arrayago *et al.* (2017) proposed a full-range DSM curve based on carbon steel strength curve with few modification but following similar procedure proposed by Rossi and Rasmussen (2013), as given in Equation 4.19. The proposed model has been found to give good prediction for SHS and RHS made of different stainless steel material – Austenitic, Ferritic, Duplex and lean Duplex stainless steel. Since the stress-strain behaviour of YSt-310 has similar material profile as compared to stainless steel material model, the applicability and reliability of the proposed model for YSt-310 structural steel is studied in the present study.

$$\frac{P_{nl-RR}}{P_y} = \begin{cases} 1+\left(1-2.11\lambda_l\right)\left(\dfrac{\sigma_u}{\sigma_{0.2}}-1\right) & \text{for } \lambda_l \le 0.474 \\ \dfrac{0.95}{\lambda_l^{0.8}} - \dfrac{0.22}{\lambda_l^{1.6}} & \text{for } \lambda_l > 0.474 \end{cases} \tag{4.18}$$

$$\frac{P_{nl-ARR}}{P_y} = \begin{cases} 1+\left(1-1.29\lambda_l\right)\left(\dfrac{\sigma_u}{\sigma_{0.2}}-1\right) & \text{for } \lambda_l \le 0.776 \\ \dfrac{1}{\lambda_l^{0.8}} - \dfrac{0.15}{\lambda_l^{1.6}} & \text{for } \lambda_l > 0.776 \end{cases} \tag{4.19}$$

where P_{nl-RR} and P_{nl-ARR} are the proposed cross-sectional resistance proposed by Rossi and Rasmussen (2013) and Arrayago *et al.* (2017), σ_u and $\sigma_{0.2}$ are the ultimate and yield stress of tensile test respectively. Weighted average ultimate and yield stresses material properties from tensile coupon tests have been utilised for generating the design curves since the ultimate and yield stresses for test and FE results are different for each section.

4.5 RELIABILITY ANALYSIS

The applicability of present design standard and design rules including the proposed equations are assessed by using reliability analysis. The results from the test and FE

analysis results have been compared with the design predictions by EC3-1-1 (2005); CSM by Zhao *et al.* (2017); DSM detailed in AISI S100-16 (2016); and modified DSM by Rossi and Rasmussen (2013) and Arrayago *et al.* (2017). The mean (P_m) and coefficient of variation (V_p) of the ratio of test and FE results to the design predictions have been estimated and are shown in Tables 4.4–4.9. The reliability analysis procedure provided in Section B of commentary on AISI S100-16C (2016) for design of cold-formed steel structural member has been followed, similar to those detailed in Section 3.4.7 of this thesis. The load combination of 1.35DL + 1.5LL has been utilised for EC3-1-1 (2005) and CSM in Zhao *et al.* (2017) whereas 1.2DL + 1.6LL has been adopted for DSM from AISI specification AISI S100-16 (2016) and modified DSM by Rossi and Rasmussen (2013) and Arrayago *et al.* (2017). Resistance factors (ϕ) of 0.91 has been used for EC3-1-1 (2005) and CSM while 0.85 has been employed for DSM. For the purpose of direct comparison and consistency, a load combination of 1.2DL + 1.6LL and constant resistance factors (ϕ) of 0.85 has been adopted to assess the reliability of all design equations. Similar load combinations and resistance factors have been adopted by earlier researchers such as Zhu and Young (2012); Huang (2013) etc. Design equations are considered to be reliable if the target reliability index of 2.5 is achieved.

4.6 COMPARISION OF TEST AND FE STUB COLUMN STRENGTHS WITH DESIGN PREDICTIONS

4.6.1 General

This section presents the assessment of unfactored column strength predicted by EC3-1-1 (2005); CSM detailed in Zhao *et al.* (2017); DSM presented in AISI specification AISI S100-16 (2016); and modified DSM by Rossi and Rasmussen (2013) and Arrayago *et al.* (2017) with the experimental and FE generated columns resistances. A total of 12 test and 173 FE generated stub column capacity results have been utilised. The detailed comparison of design predictions with test results is shown in Table 4.4, whereas, the comparison of FE results with design predictions is presented

(in summary) in Table 4.5. The column design predictions have been calculated using 0.2% proof stress taken as the respective weighted average (based on the cross-sectional area) of flat, corner and weld material properties (detailed in Tables 3.4–3.6) for each cross-section for comparison with the experimental stub column resistances; whereas the weighted average material property of 66 × 33 × 2.6 cross-section has been used to for comparison with the finite element results (as the same weighted average material property has been incorporated in the finite element modelling). The effective length factor of stub columns has been taken as unity as detailed in Chapter C of AISI S100-16 (2016). The comparison is presented in the form of P_{Test}/P_{EC3}, P_{Test}/P_{CSM}, P_{Test}/P_{DSM}, $P_{Test}/P_{DSM–RR}$, and $P_{Test}/P_{DSM–ARR}$ where P_{Test}, P_{EC3}, P_{CSM}, P_{DSM}, $P_{DSM\text{-}RR}$, and $P_{DSM\text{-}ARR}$ are the load capacities corresponding to experimental tests, EC3, CSM, DSM, modified DSM by Rossi and Rasmussen (2013) and modified DSM by Arrayago *et al.* (2017) respectively. The notation P_{FE} and P_u are used to mean the ultimate capacities; P_{FE} is used when the comparisons are made only for FE generated results, whilst P_u corresponds to both FE and test capacities (when mixed data) are used (both test and FE results). Discussions on individual comparisons are presented in the following sub-sections (Sections 4.6.2–4.6.5). The mean (P_m) values and coefficient of variation (V_p) of the ratios of experimental and FE column strengths to the predicted design strengths and corresponding reliability indices are shown in Tables 4.4–4.9. The comparison of results for test and FE are shown in Tables 4.4 and 4.5 respectively, while Tables 4.6 and 4.7 show the combined test and FE comparison results for non-slender and slender cross-sections respectively. It can be noted that in Tables 4.6 and 4.7, since slenderness limits are different (e.g. $\overline{\lambda}_p \leq 0.673$; $\overline{\lambda}_p \leq 0.68$, $\lambda_l \leq 0.776$ for EC3-1-1 (2005), CSM and DSM respectively), for each design predictions; hence the number of observations falling under the classification of slender and non-slender/stocky classifications are different for each predictions. The comparison of both test and FE results is summarised in Table 4.8. Finally, for the purpose of direct comparison of all design predictions, considering same resistance factor of $\phi = 0.85$ for both the test and FE results, are shown in Table 4.9.

4.6.2 Comparison with Eurocode

The cross-section resistance of a structural member in compression is limited by local buckling in both elastic and inelastic ranges depending on the susceptibility of the most slender constituent elements in the cross-section. To assess the Class–3 cross-section slenderness based on Eurocode 3, EC3-1-1 (2005), local slenderness parameter $c/t\varepsilon$ has been plotted against the ultimate load P_u normalised by squash load $A_g f_y$, where f_y is the weighted average material properties (as shown in Figure 4.18). From Figure 4.18 it is seen that the current Eurocode 3 Class–3 limit for internal compression elements, $c/t\varepsilon = 42$ is found to be inappropriate, but a lower value of $c/t\varepsilon = 38$ (depicted in Figure 4.18) is found to be more suitable for YSt-310 cold-formed carbon steel. Similar results have been also observed for other ordinary carbon steel and high strength steel by Wang *et al.* (2017). Using the same test and FE generated results; the Eurocode 3 effective width equation for Class–4 internal compression elements has been also assessed in this section. In Figure 4.19, the ultimate load normalised by squash load, $A_g f_y$ has been plotted against cross-section slenderness, $\overline{\lambda}_p$ calculated separately for RHS and SHS as explained above in Section 4.4.1.1. It is evident from the Figure 4.19 that ~ 80% of the data points for slender, $\overline{\lambda}_p > 0.673$ cross-sections generated in this present study lie below the codified effective equation curve (i.e. Eurocode 3 curve), resulting in slight non-conservative design predictions. On the other hand, the codified effective width curve for non-slender $\overline{\lambda}_p \leq 0.673$ cross-sections occurs far below the test as well as FE generated values, leading to an overly conservative prediction. The reliability index for non-slender/stocky cross-sections are observed to be greater ($\beta = 3.06$; see Table 4.6) than the target reliability index. However, the mean value of P_u/P_{EC3} ratios for slender cross-sections is 0.92 with COV of 0.07 for all specimens and the corresponding reliability index is found to be 1.97, which is lesser than the target reliability index, β_o value of 2.5 (see Table 4.7).

4.6.3 Comparison with CSM

The applicability of CSM (see in Zhao *et al.*, 2017) for the design of YSt-310 cold-formed structural steel stub column both for non-slender and slender cross-section has been assessed in this section. The deformation capacities *vs*. cross-section slenderness are plotted for all specimens under consideration, together with the base curve in Figure 4.20. Comparison of CSM design predictions with all the test and FE samples are shown in Figures 4.21 and 4.22 for non-slender and slender cross-sections respectively. The mean and COV values are observed to be 1.16 and 0.07; and 1.04 and 0.06, respectively for non-slender and slender sections, presented in Tables 4.6 and 4.7 respectively. A slight conservative prediction of about ~ –16% for non-slender cross-section has been observed although fairly accurate prediction is seen in slender cross-section. The reliability indexes of all comparisons are higher than the target reliability index $(\beta_o = 2.5)$. Considering the less scatterings, reliable prediction, as well as relatively ease in calculation procedure; CSM is recommended to be used for design of YSt-310 cold-formed carbon steel stub column.

4.6.4 Comparison with DSM

This section evaluates the applicability of DSM in AISI S100-16 (2016) for the design of YSt-310 cold-formed carbon steel stub column sections. The column resistances generated from both test and FE, P_u normalized by column resistance for yielding and global buckling, P_{ne} are plotted in Figure 4.23. From Figure 4.23, it can be observed that ~ 50% of the data points are below the DSM predicted curve for slender cross-section $(\lambda_l > 0.776)$, leading to non-conservative prediction. On the other hand, the traditional horizontal line for non-slender section $(\lambda_l \le 0.776)$, is far below the generated data points, resulting to an overly conservative prediction of about ~ –24% (or mean = 1.24; see Table 4.6). The comparison shown in Table 4.7 for slender section gives mean value of 0.96 and COV of 0.12, with reliability index of 2.39, which is lesser than the target reliability index $(\beta_o = 2.5)$, and therefore not reliable.

4.6.5 Comparison with modified DSM

To account for the effect of strain hardening, researchers such as Rossi and Rasmussen (2013) replaced the classical horizontal yield limit by a linear equation expressed as a function of cross-section slenderness, ultimate stress and proof stress of tensile test for stainless steel sections (see Equation 4.18); and further, Arrayago *et al.* (2017) proposed a full-range DSM curve for carbon steel strength curve (see Equation 4.19). In this section, the above proposed modified DSM equations (i.e. Equations 4.18 and 4.19) are analysed to check their applicability for YSt-310 cold-formed carbon steel stub columns. It may be noted that the average value of $\sigma_u/\sigma_{0.2}$ ratio from the weighted material properties of all cross-sections have been used to generate the DSM (Rossi and Rasmussen, 2013; Arrayago *et al.*, 2017) column design curve. The test and FE column resistances normalised by squash load are plotted against the cross-section slenderness (λ_l) in Figure 4.24. The slenderness limit separating the slender and non-slender/stocky cross-sections in the modified DSM (or DSM_{RR}) by Rossi and Rasmussen (2013) is observed to be inappropriate for YSt-310 cold-formed carbon steel. The results are expected as the proposed design rule was developed based on various stainless steel experimental data. Further, it is observed from Tables 4.4–4.9 that the modified DSM prediction proposed by Rossi and Rasmussen (2013) is found to give conservative prediction ranging from ~ 14% to 21%. The proposed modified DSM (or DSM_{ARR}) design rule by Arrayago *et al.* (2017) is also presented in Figure 4.24. It is observed form the figure that the proposed design curve lies above the majority of the test and FE generated data for slender, $\lambda_l > 0.776$ cross-sections, leading to non-conservative prediction for compressive members. The mean and COV for slender cross-sections are computed to be 0.95 and 0.12 respectively, with reliability index of 2.35 (see Table 4.7), which is lesser than the target reliability index. The proposed modified DSM_{ARR} model by Arrayago *et al.* (2017) is found to give slightly conservative of ~ –14% for stocky (i.e. $\lambda_l \leq 0.776$) cross-section, with a reliability index of 3.25 (see Table 4.6).

4.6.6 Proposed modified DSM

The modified model by Arrayago *et al.* (2017) derived from the Modified DSM prediction by Rossi and Rasmussen (2013) is found to give conservative (i.e. mean = 1.14) prediction for non-slender and non-conservative (i.e. mean = 0.95) prediction for slender section (see Tables 4.6 and 4.7; also discussed above). Hence, an attempt has been made in this study, by adopting a non-linear regression fit to provide a best fit to the test as well as FE generated data points, based on the original DSM curve in AISI S100-16 (2016) The proposed modified (DSM*) nominal member capacity is then expressed by Equation 4.20.

$$\frac{P_{DSM}^{*}}{P_{ne}} = \begin{cases} \dfrac{0.9516}{\lambda_l^{0.2016}} & \text{for } \lambda_l \le 0.776 \\ \dfrac{0.776}{\lambda_l^{0.8}} + \dfrac{0.03}{\lambda_l^{1.6}} & \text{for } \lambda_l > 0.776 \end{cases} \tag{4.20}$$

Comparison of the member capacity predicted by the proposed modified DSM, P_{DSM}^{*} (i.e. Equation 4.20) with test and FE results are shown in Tables 4.3–4.9 and Figure 4.24. The mean values of 1.03 and 1.05, with COV values of 0.04 and 0.12 for non-slender and slender sections respectively, are obtained (see Tables 4.6 and 4.7). It can be observed from Figure 4.24 as well as from Tables 4.4–4.9 that the proposed design rule provides a more accurate and less scatter prediction, as compared to the modified DSM given in Equations 4.18 and 4.19. The proposed modified DSM design rule, P_{DSM}^{*} is reliable as the reliability indices (β = 2.72–2.96) are observed to be greater than the target value of 2.5 for all comparisons shown in Tables 4.4–4.9.

4.7 SUMMARY

A comprehensive experimental and numerical programme to investigate the structural behaviour of YSt-310 cold-formed SHS and RHS is presented in this chapter. Extent

of corner strength enhancement due to cold-forming in the whole cross-section, at a finer resolution has been conducted using Vickers's microhardness tester and the results are presented in the form of two (2D) and three (3D) dimensional plots. The geometric imperfection magnitudes of SHS and RHS stub columns using non-contact 3D Laser scanner are also presented. Additionally, cross-section capacities of the stub columns have also been investigated experimentally and numerically (through carefully calibrated finite element procedure to cover a wide range of cross-sections which has not been not included in the experimental programme). The results from the experimental/test as well as FE generated column capacities have been utilised to compare the design strengths predicted by EC3-1-1 (2005); CSM by Zhao *et al.* (2017); DSM in AISI S100-16 (2016); and modified DSMs proposed by Rossi and Rasmussen (2013) and Arrayago *et al.* (2017). Based on the analysis of test, FE study and assessment of design equations, following concluding remarks have been presented:

a) The spread of the corner strength enhancement due to cold-forming has been seen to lie within a zone of ~ ± 3.0*t* from the centre of the corner, although relatively higher influence can be witnessed within ~ ± 1.2*t*.

b) Based on the 3D laser imperfection measurement, local geometric imperfections for YSt-310 cold-formed steel columns have been seen in the range ~0.012–0.047 (*t*/60–*t*/248).

c) Class–3 cross-sectional slenderness limit presented in EC3-1-1 (2005) has been assessed, for YSt-310 cold-formed tubular sections. A slenderness limit, i.e. $c/t\varepsilon$ = 38 has been proposed and found to be more suitable for YSt-310 cold-formed tubular sections.

d) The design strengths predict by EC3-1-1 (2005), CSM detailed in Zhao *et al.* (2017), DSM presented in AISI S100-16 (2016), modified DSM by Rossi and Rasmussen (2013); and Arrayago *et al.* (2017), have been found to provide conservative predictions for non-slender cross-sections. However, for the case of slender cross-section, CSM and modified DSM proposed by Rossi and

Rasmussen (2013) have been seen to provide accurate and conservative design predictions.

e) A modified design equation based on DSM approach has been proposed considering the current test and FE column capacities and found to provide conservative prediction with least scatterness as compared to existing design equations of unperforated stub columns.

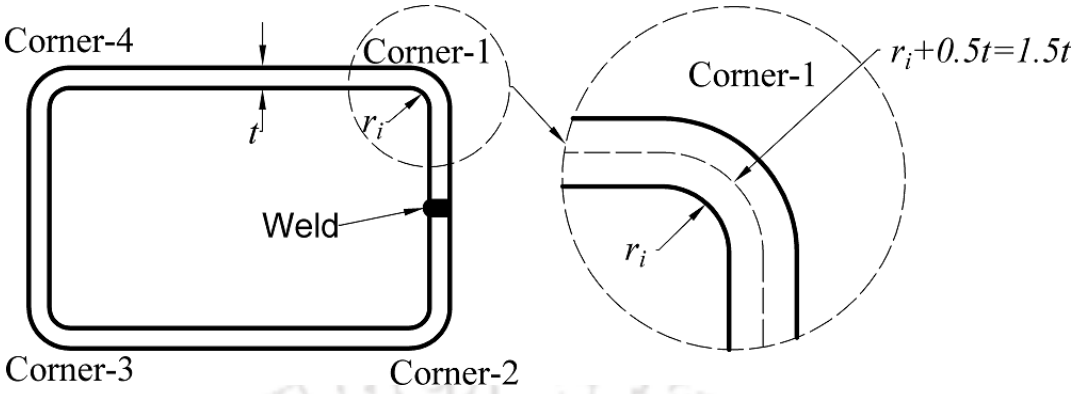

Figure 4.1: Convention used for numbering corner locations

Figure 4.2: A typical picture showing the creation of diamond indent

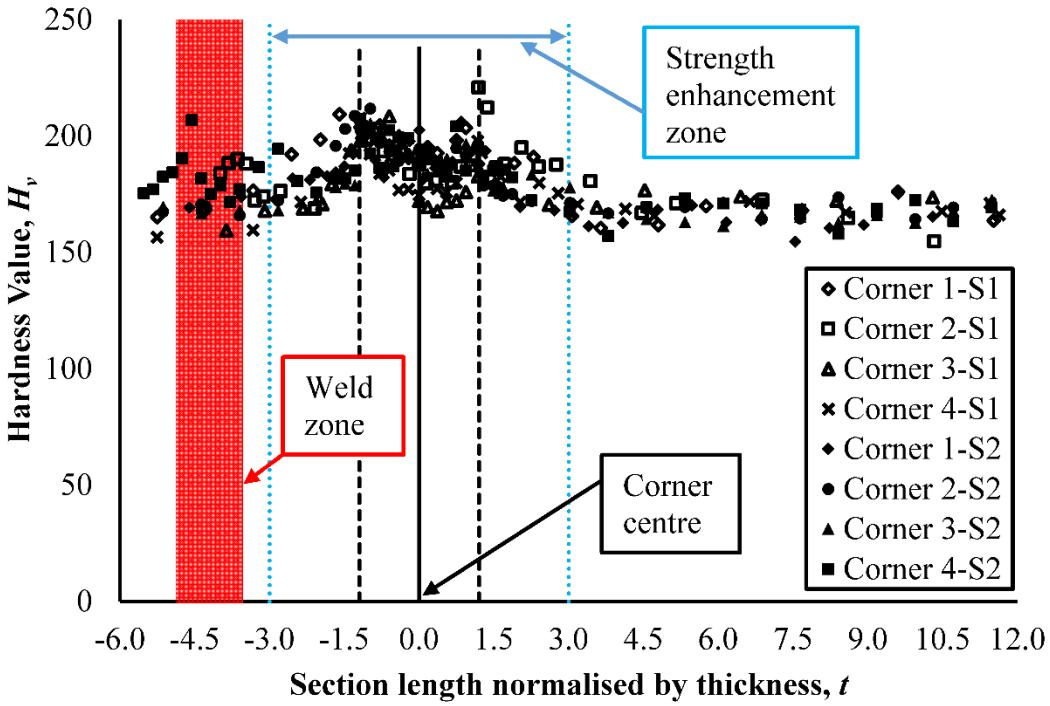

Figure 4.3: Hardness distributions across the cross-section length normalized by thickness for sample 66 × 33 × 2.6

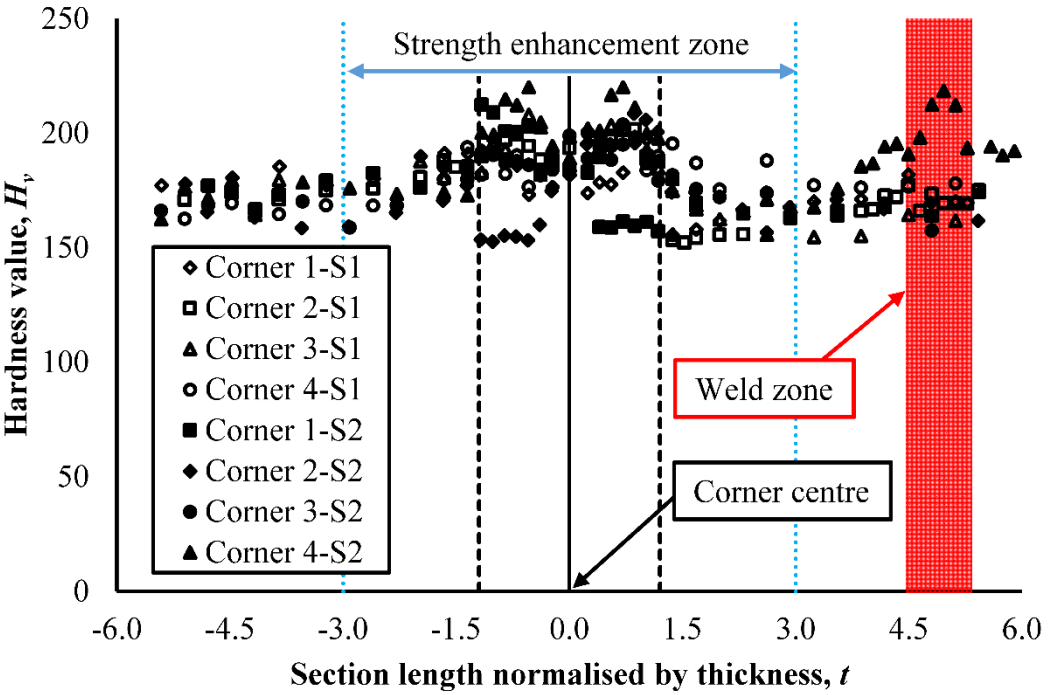

Figure 4.4: Hardness distributions across the cross-section length normalized by thickness for sample 40 × 40 × 3.2

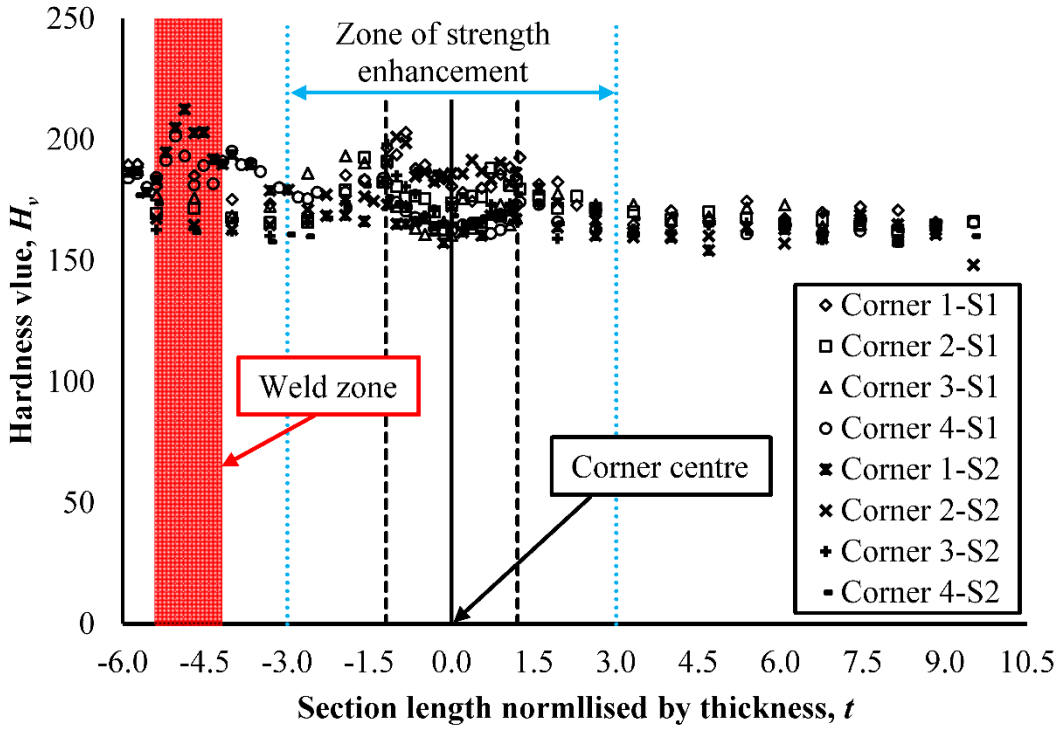

Figure 4.5: Hardness distributions across the cross-section length normalized by thickness for sample 60 × 40 × 2.9

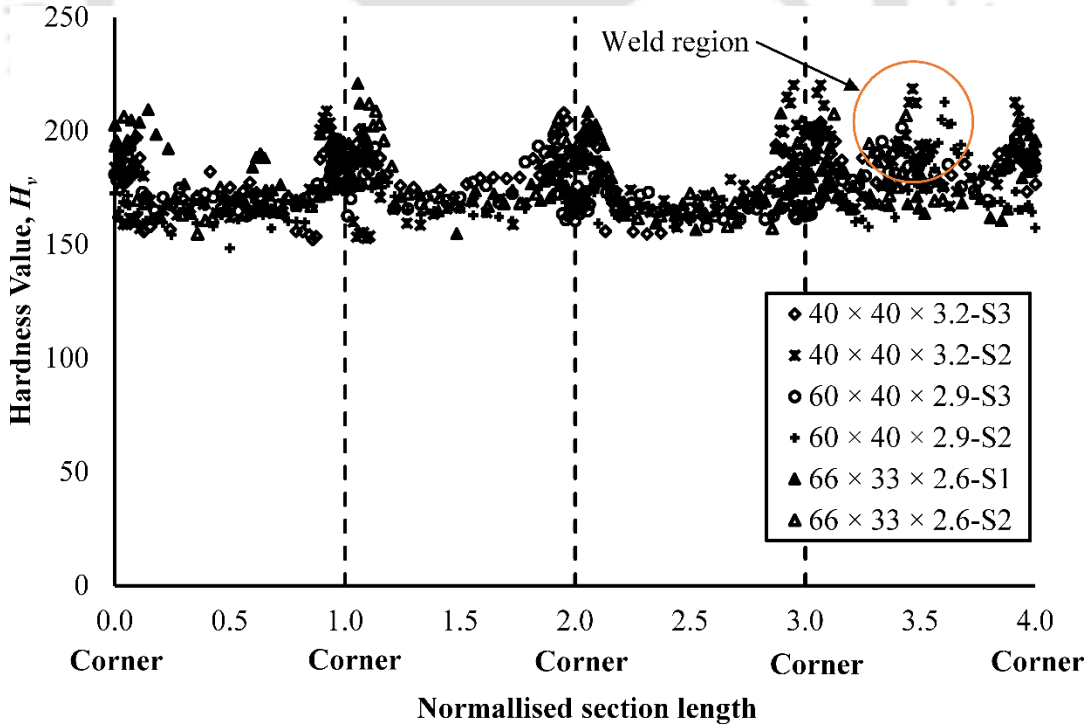

Figure 4.6: Hardness value (H_v) distribution over normalized section length

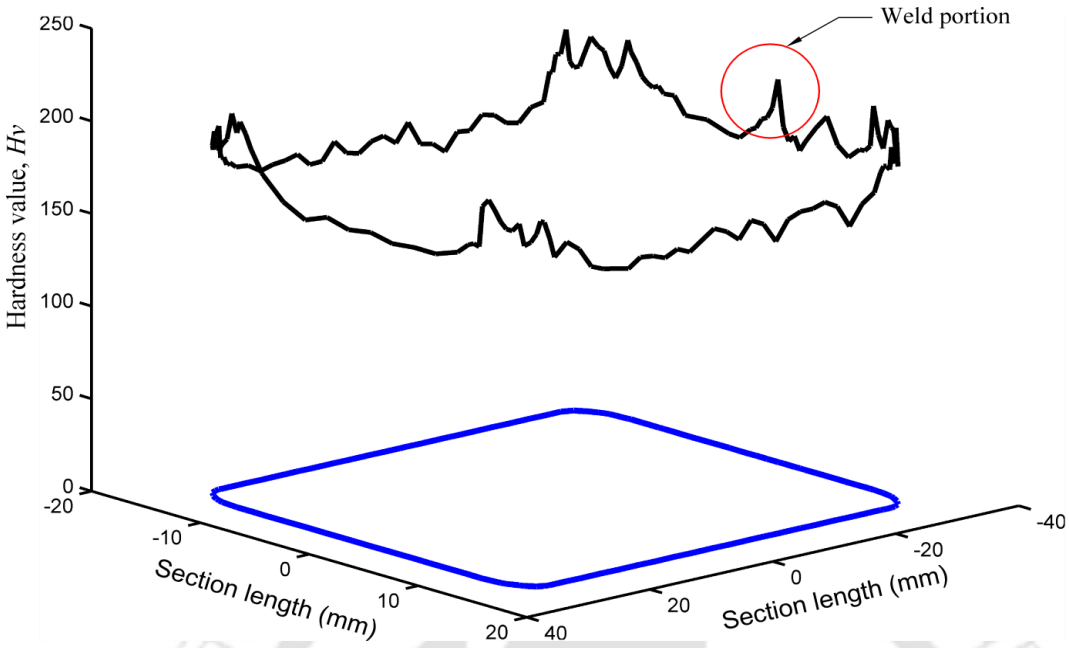

Figure 4.7: 3D hardness distributions for 66 × 33 × 2.6-S2

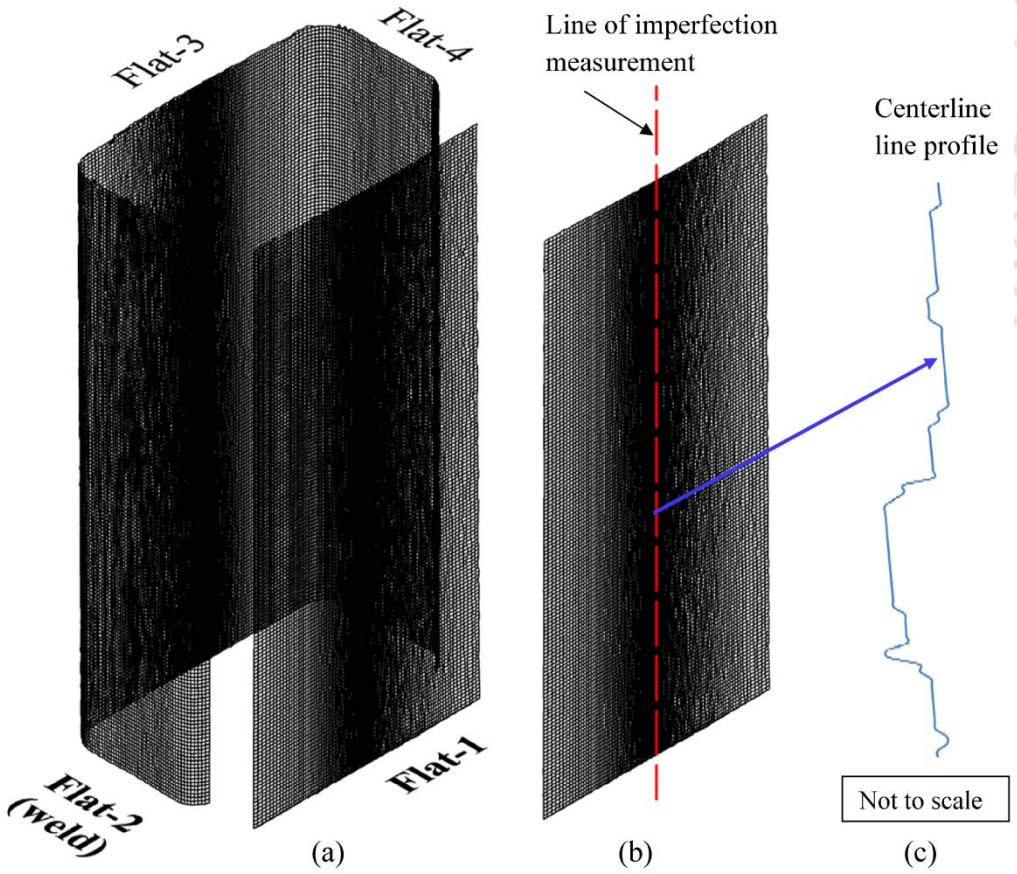

Figure 4.8: Measurement of geometric imperfection: (a) extracting flat portion (b) measurement of geometric imperfection (c) a schematic longitudinal profile

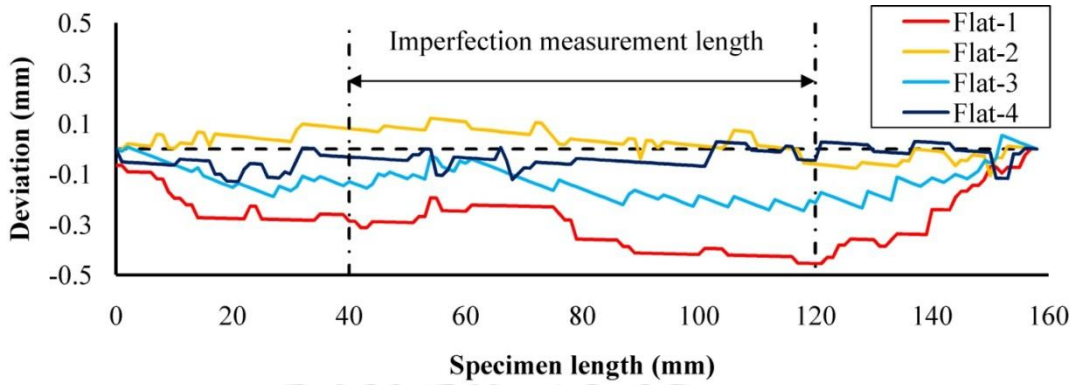

Figure 4.9: Measured geometric imperfection for section 80 × 40 × 2.6

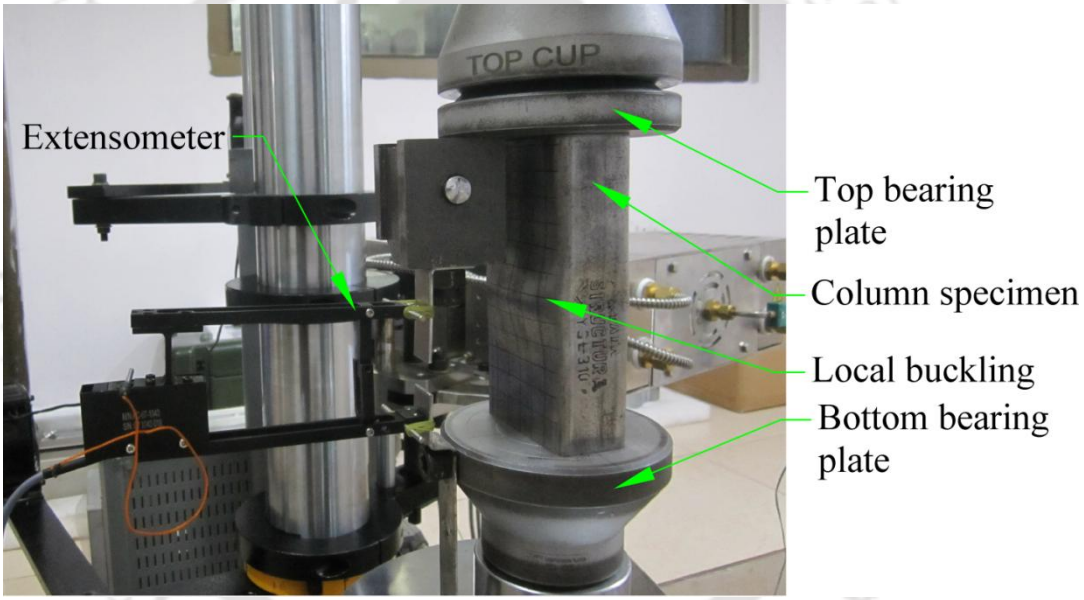

Figure 4.10: Stub columns compression test setup for 250 kN displacement control universal testing machine (UTM)

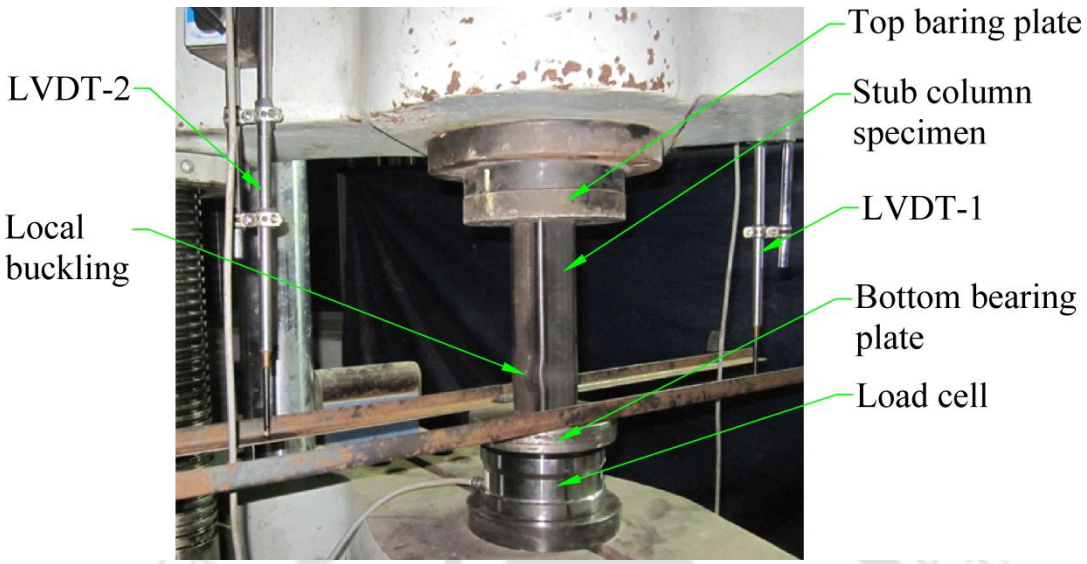

Figure 4.11: Stub columns compression test setup for 1000 kN load UTM

(a) (b) (c)

Figure 4.12: Typical local buckling failure mode for stub columns of (a) 50 × 50 × 2.9, (b) 60 × 40 × 2.9 and (c) 60 × 60 × 2.6

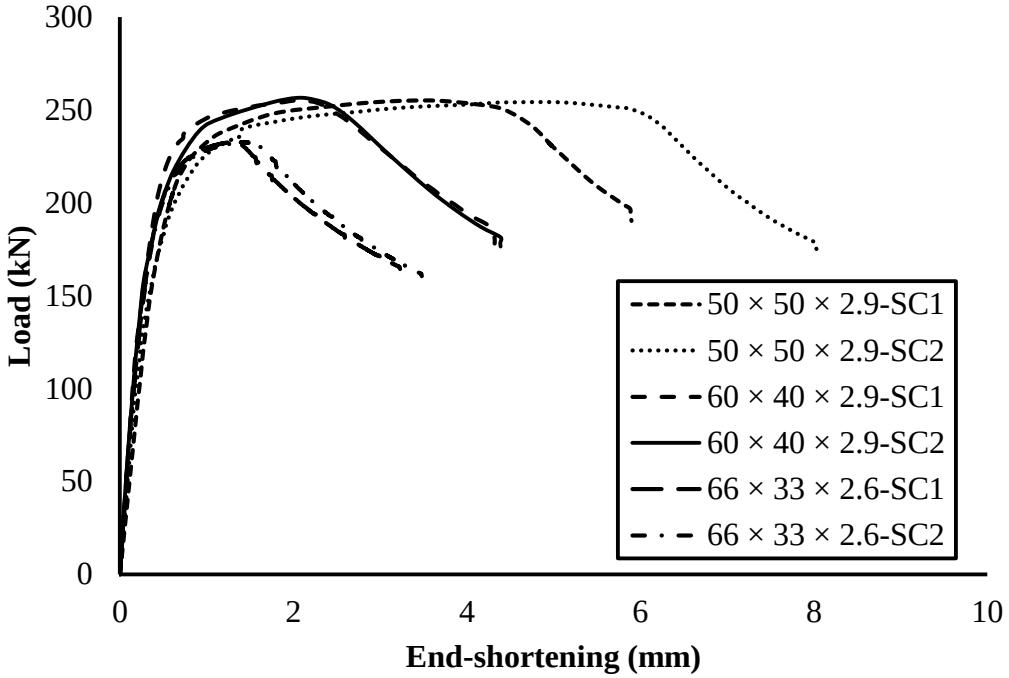

Figure 4.13: Load-end shortening curve for 50 × 50 × 2.9, 60 × 40 × 2.9 and 66 × 33 × 2.6 sections.

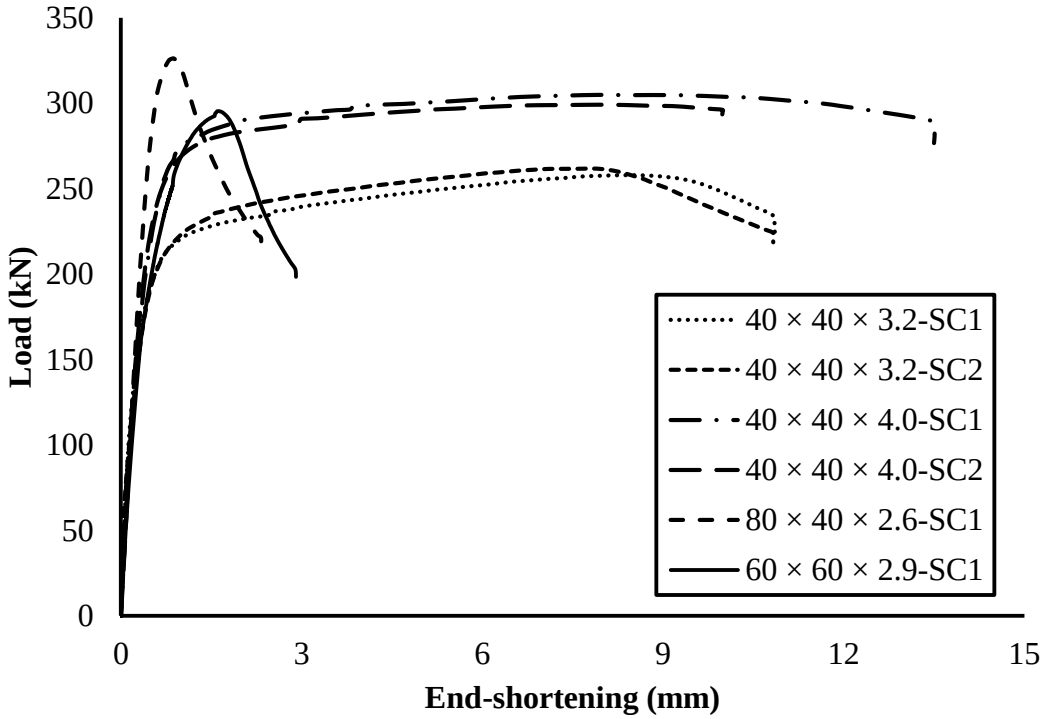

Figure 4.14: Load-end shortening curve for 40 × 40 × 3.2, 40 × 40 × 4.0, 80 × 40 × 2.6 and 60 × 60 × 2.6 sections

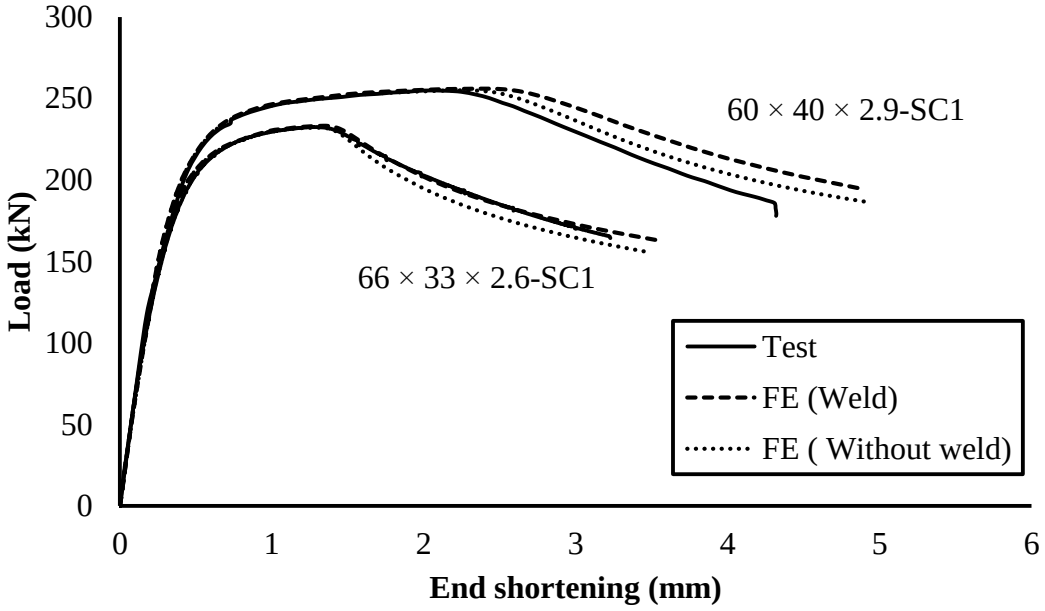

Figure 4.15: Comparison of experimental and numerical load-end shortening curves for sections including weld material property

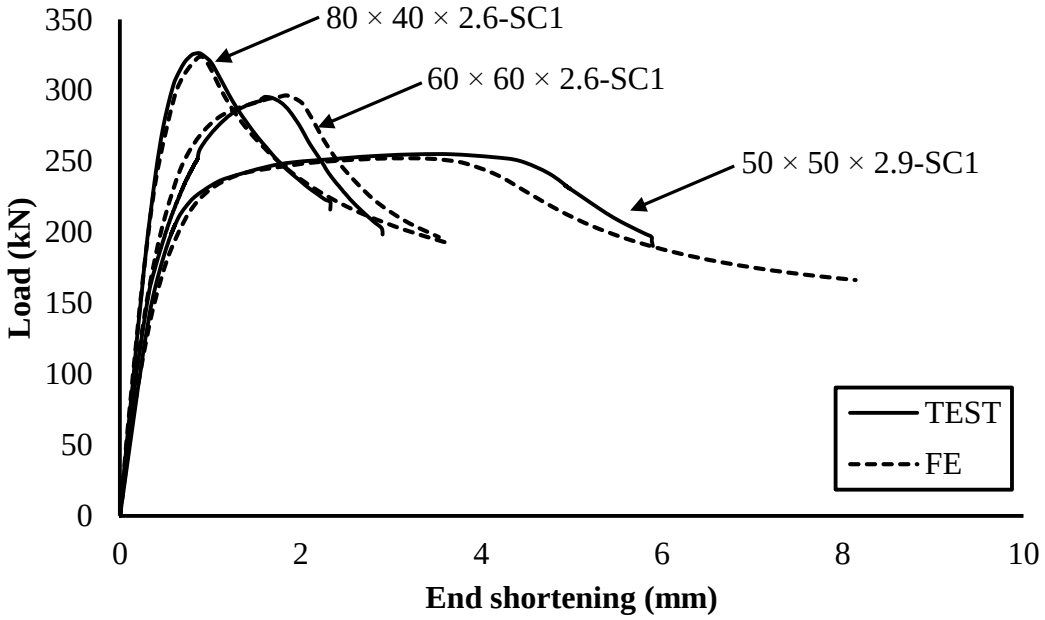

Figure 4.16: Comparison of experimental and numerical load-end shortening curves (without weld)

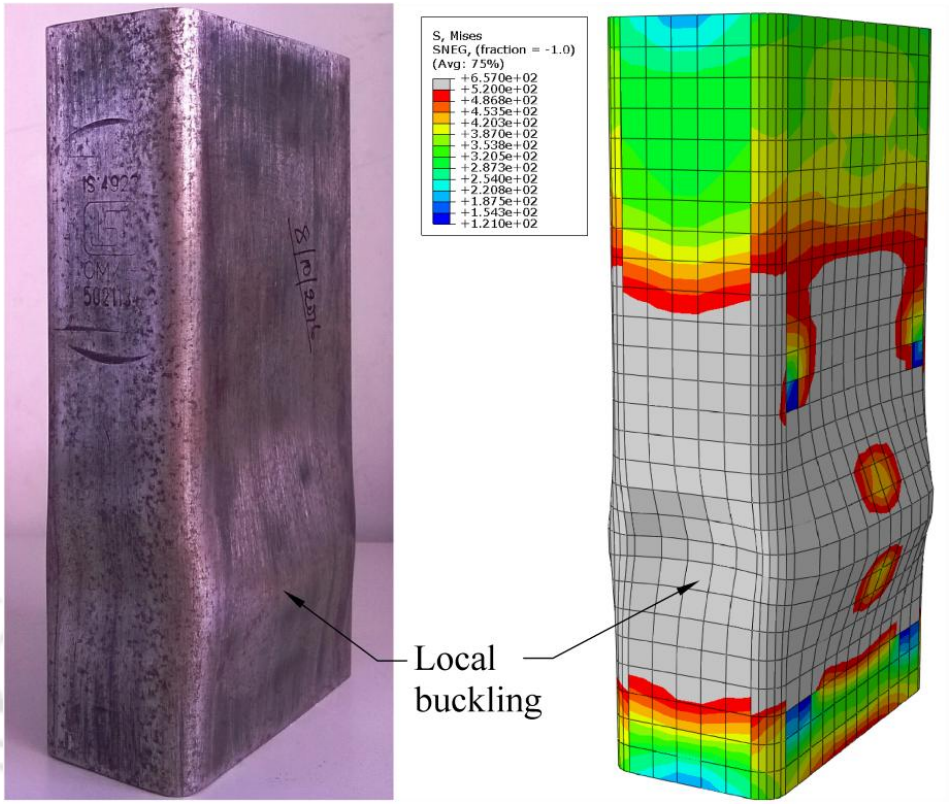

(a)

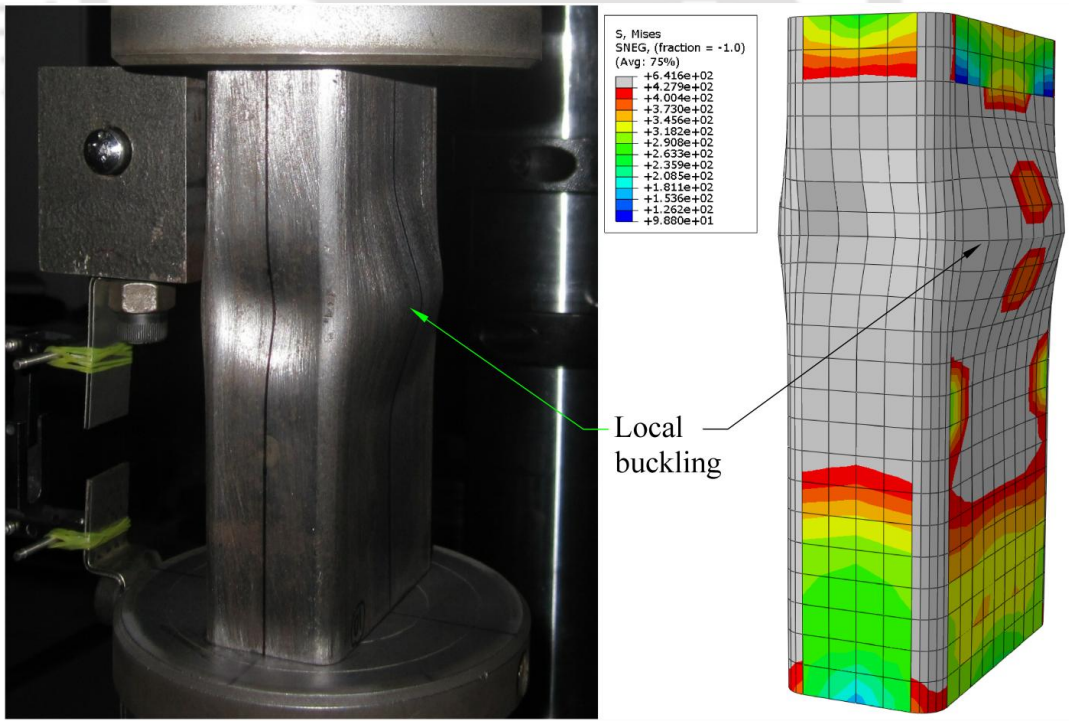

(b)

Figure 4.17: Comparison of experimental and FE deformation for (a) 80 × 40 × 2.6-SC1 and (b) 66 × 33 × 2.6-SC1

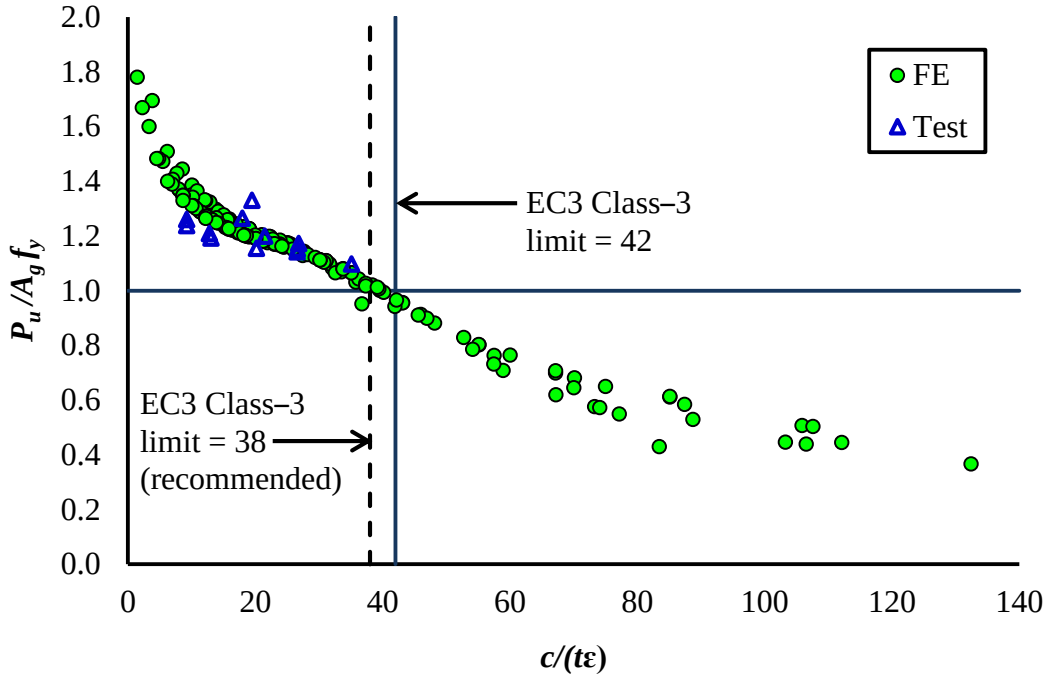

Figure 4.18: Assessment of EC3: Part 1–1 (2005) Class–3 slenderness limit with the FE and test results

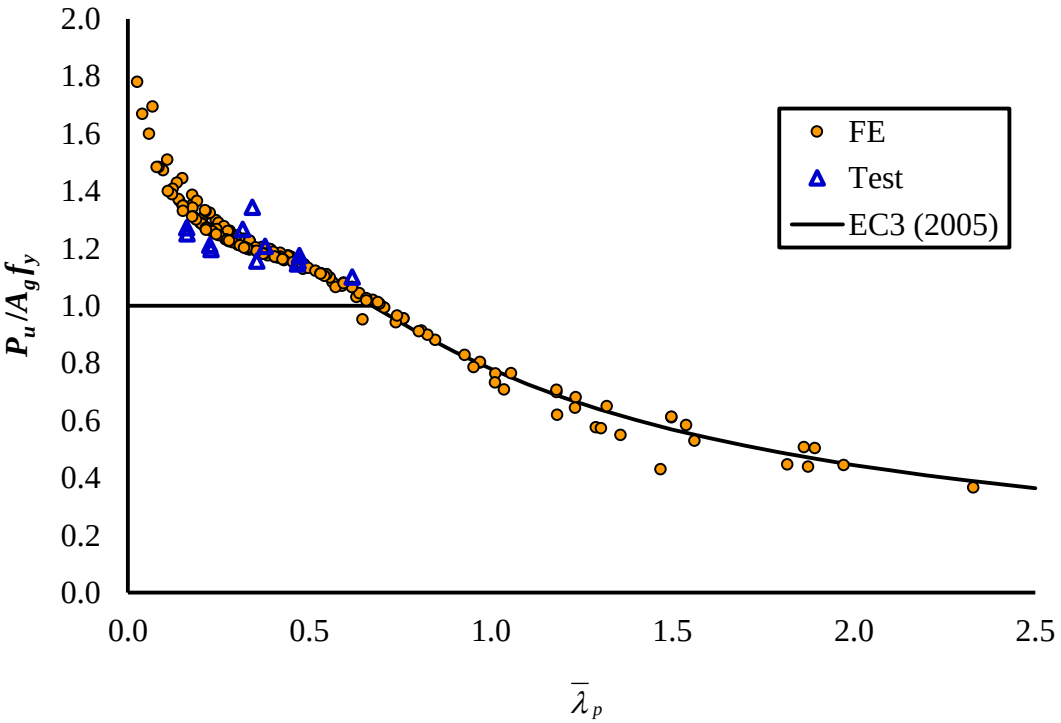

Figure 4.19: Assessment of EC3 effective width equation for internal flat element in compression.

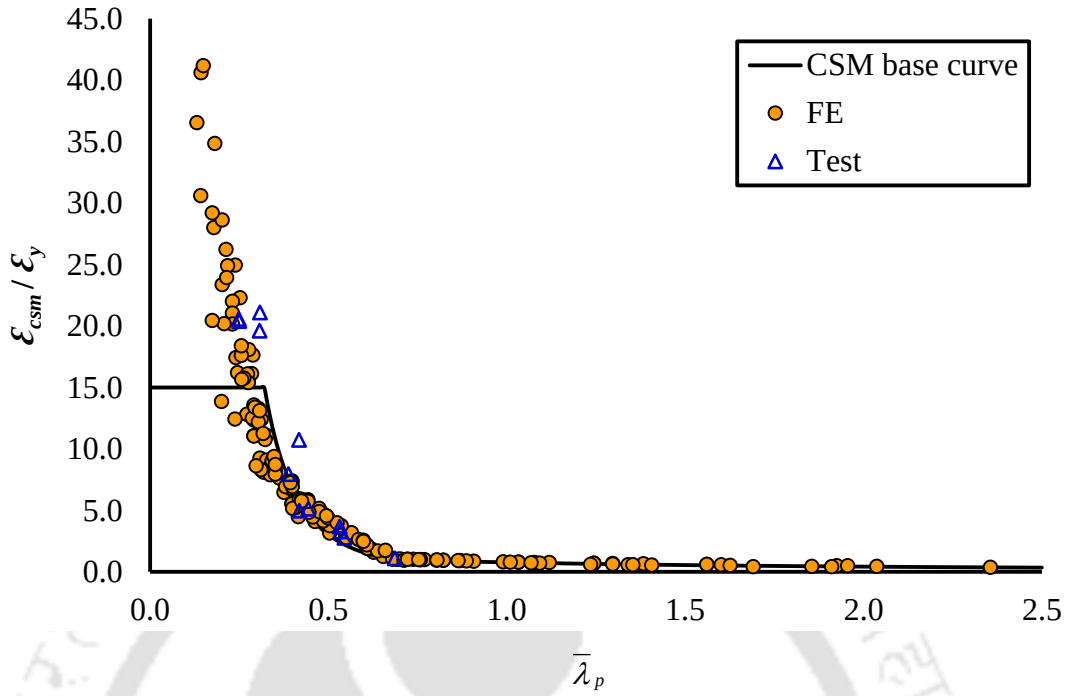

Figure 4.20: Comparison of CSM base curve with test and FE data points

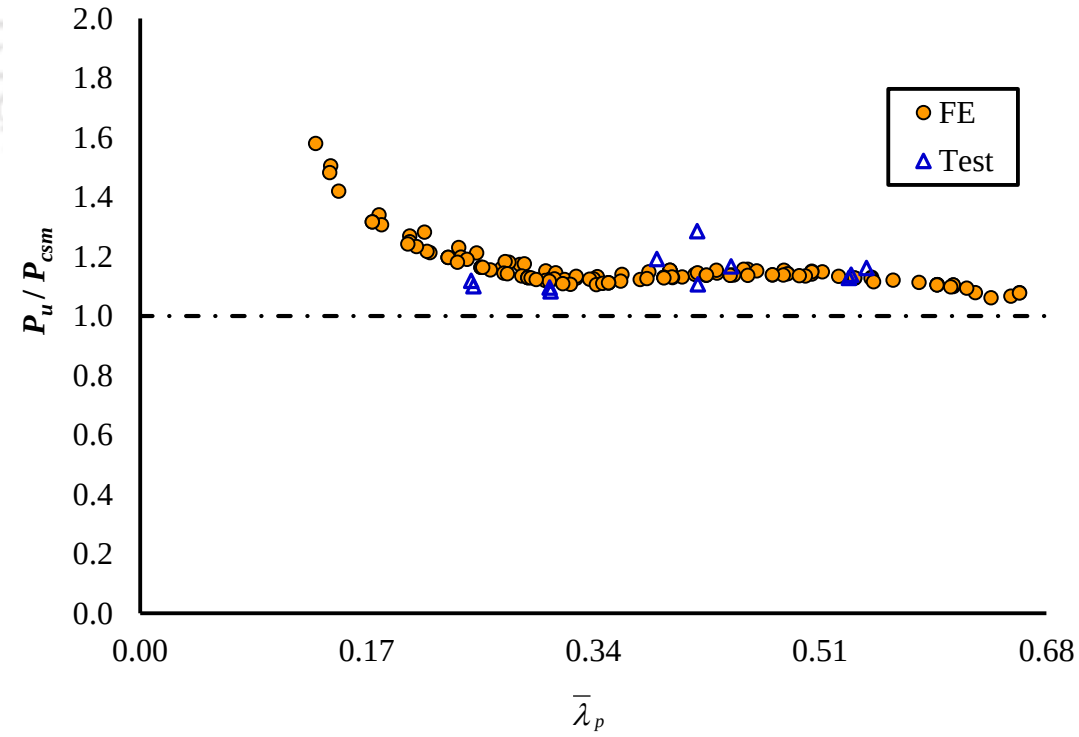

Figure 4.21: Assessment of CSM design prediction with test and results for non-slender cross-sections $\left(\overline{\lambda}_p \le 0.68\right)$

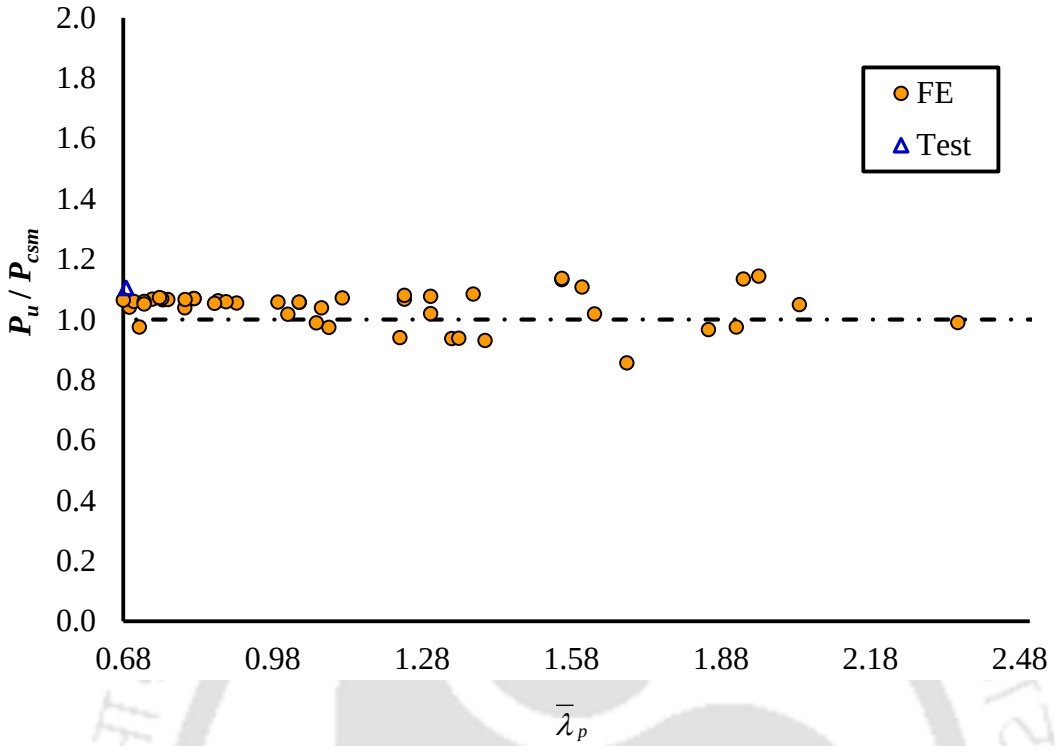

Figure 4.22: Assessment of CSM design prediction with test and FE results for slender cross-sections $\left(\bar{\lambda}_p > 0.68\right)$

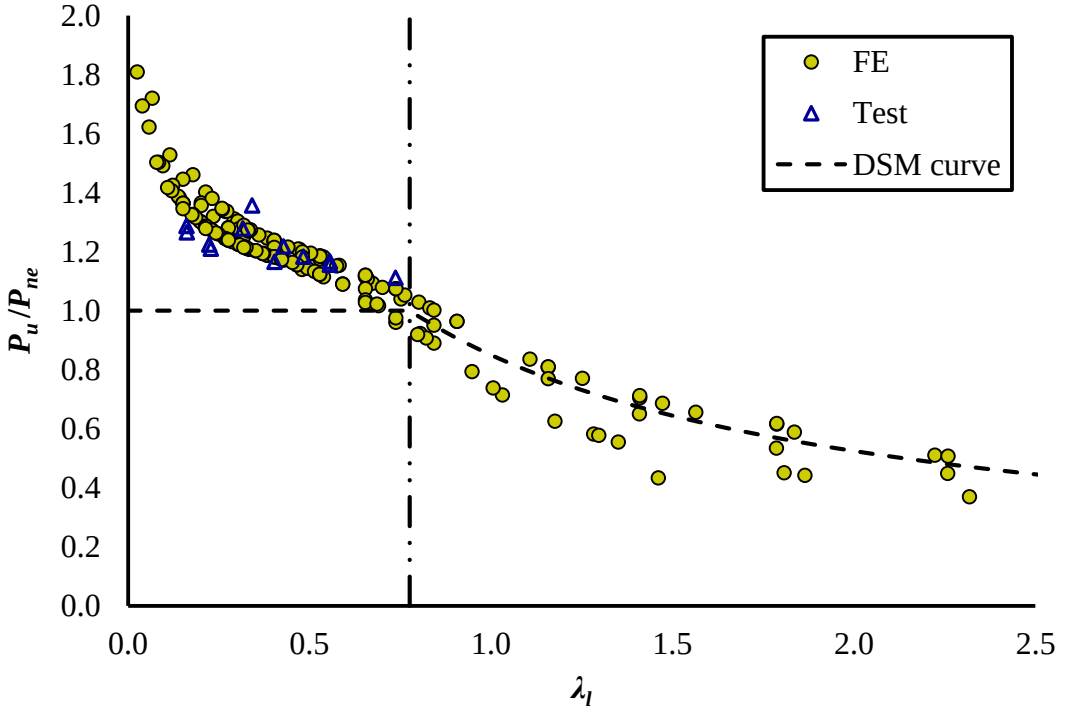

Figure 4.23: Assessment of DSM with test and FE results

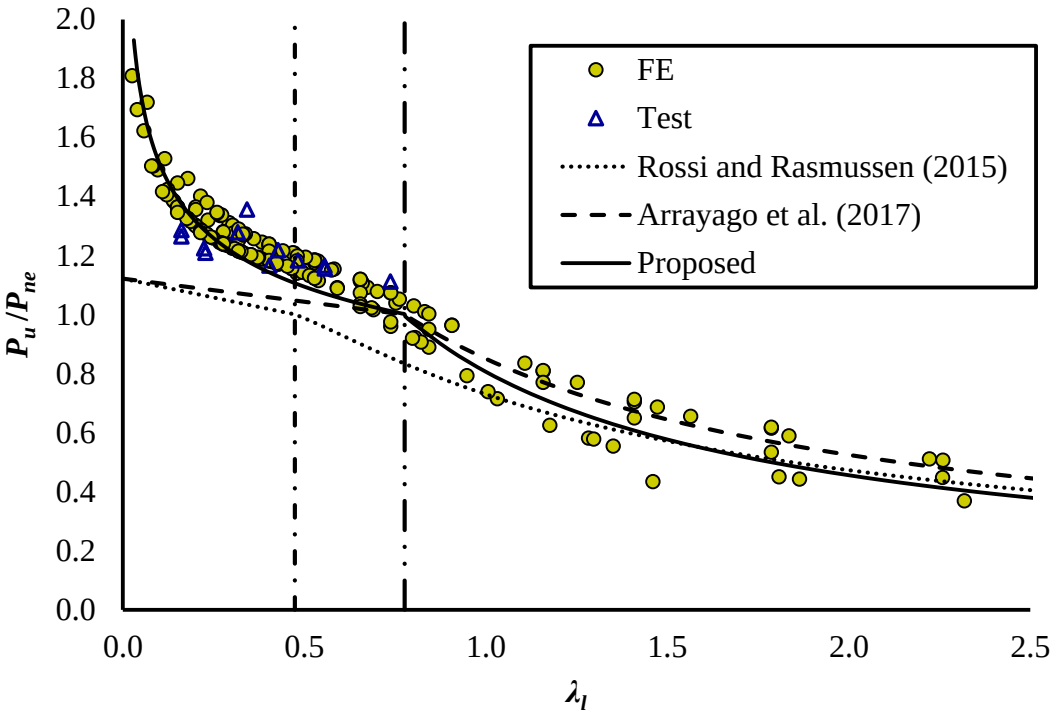

Figure 4.24: Assessment of modified DSM approach with test and FE results

Table 4.1: Measured section dimensions, geometric imperfection and results of stub columns

Cross-sections	B (mm)	D (mm)	L (mm)	t (mm)	r_i (mm)	ω_d (mm)	P_{Test} (kN)	δ_u (mm)
40 × 40 × 3.2-SC1	40.50	40.40	160.1	3.14	3.2	0.01264	258.08	8.47
40 × 40 × 3.2-SC2	40.32	40.15	160.2	3.17	3.2	–	261.70	7.89
40 × 40 × 4.0-SC1	40.28	40.16	160.5	3.84	4.0	0.02158	304.93	7.94
40 × 40 × 4.0-SC2	40.18	40.36	160.7	3.82	4.0	–	298.95	7.88
50 × 50 × 2.9-SC1	49.67	49.88	200.2	2.86	2.9	0.0265	254.96	3.68
50 × 50 × 2.9-SC2	49.75	49.65	200.9	2.68	2.9	–	254.22	4.83
60 × 40 × 2.9-SC1	60.10	40.12	160.5	2.86	2.9	0.04765	254.90	2.00
60 × 40 × 2.9-SC2	60.43	40.25	160.2	2.75	2.9	–	256.49	2.04
60 × 60 × 2.6-SC1	60.15	59.98	200.8	2.53	2.6	0.01300	295.45	1.61
66 × 33 × 2.6-SC1	65.90	33.10	132.2	2.52	2.6	0.01715	232.51	1.27
66 × 33 × 2.6-SC2	66.20	33.40	132.0	2.53	2.6	–	232.85	1.39
80 × 40 × 2.6-SC1	80.09	39.64	161.0	2.54	2.6	0.02276	326.91	0.88

Table 4.2: Validation of FE models against the test results considering either with weld or without weld material in the FE models

Cross-sections	P_{TEST} (kN)	With or without weld material	P_{FE}/P_{TEST}		
			Imperfection amplitudes		
			ω_d	ω_0	t/100
40 × 40 × 3.2-SC1	258.077	*Without weld*	1.035	1.034	1.035
40 × 40 × 4.0-SC1	304.930	*Without weld*	1.058	1.058	1.058
50 × 50 × 2.9-SC1	254.960	*Without weld*	0.991	0.989	0.989
60 × 60 × 2.6-SC1	295.450	*Without weld*	1.002	1.005	0.991
80 × 40 × 2.6-SC1	326.910	*Without weld*	0.989	0.993	0.991
60 × 40 × 2.9-SC1	254.902	*With weld*	0.997	1.000	0.996
		Without weld	0.990	0.999	0.995
66 × 33 × 2.6-SC1	232.512	*With weld*	1.001	1.003	0.996
		Without weld	0.997	0.998	0.991
Mean (P_m)			1.007	1.009	1.005
COV (V_p)			0.024	0.022	0.024

Table 4.3: Generated stub column capacities and corresponding displacements from FE models

Cross-section	Length (mm)	P_{FE} (kN)	δ_u (mm)	P^*_{DSM} (kN)	$\frac{P_{FE}}{P^*_{DSM}}$
50 × 25 × 2.0	100.00	140.36	0.93	130.01	1.09
50 × 25 × 2.6	100.00	187.65	1.77	175.10	1.08
50 × 25 × 3.2	100.00	235.74	3.27	220.78	1.08
50 × 25 × 4.0	100.00	301.94	5.96	281.92	1.08
50 × 25 × 4.5	100.00	344.48	6.26	319.99	1.09
60 × 40 × 2.6	160.00	245.25	1.86	230.29	1.07
60 × 40 × 2.9	160.00	275.75	2.18	261.02	1.06
60 × 40 × 3.6	160.00	346.52	3.65	333.81	1.05
60 × 40 × 4.0	160.00	387.85	3.74	375.88	1.04
60 × 40 × 4.5	160.00	440.86	5.06	428.81	1.04
60 × 40 × 5.0	160.00	496.57	6.76	481.97	1.04
66 × 33 × 2.6	132.00	242.46	1.46	222.60	1.10
66 × 33 × 2.9	132.00	273.42	1.76	252.14	1.09
66 × 33 × 3.6	132.00	343.84	2.59	321.92	1.08
66 × 33 × 4.5	132.00	441.03	5.18	412.54	1.08
66 × 33 × 5.0	132.00	496.18	7.06	462.99	1.08
80 × 40 × 2.6	160.00	276.36	0.91	262.16	1.06
80 × 40 × 3.2	160.00	362.45	1.77	332.82	1.10
80 × 40 × 4.0	160.00	460.36	2.37	428.87	1.08
80 × 40 × 4.8	160.00	559.02	3.68	526.13	1.07
80 × 40 × 5.4	160.00	643.45	6.84	599.44	1.08
96 × 48 × 3.2	192.00	415.34	1.23	388.70	1.08
96 × 48 × 4.0	192.00	544.41	2.30	502.14	1.09
96 × 48 × 4.8	192.00	663.98	3.23	617.57	1.08
96 × 48 × 6.0	192.00	846.78	5.88	792.79	1.08
122 × 61 × 3.6	244.00	559.22	1.19	545.23	1.03
122 × 61 × 4.5	244.00	762.35	2.05	705.35	1.09
122 × 61 × 5.4	244.00	941.41	3.21	868.75	1.09
122 × 61 × 7.0	244.00	1243.75	5.62	1164.07	1.08
145 × 82 × 4.8	328.00	980.21	2.06	921.13	1.07
145 × 82 × 5.4	328.00	1135.01	2.77	1055.32	1.08
145 × 82 × 7.0	328.00	1507.31	4.06	1420.28	1.07
145 × 82 × 9.0	328.00	1977.44	6.79	1885.55	1.06
172 × 92 × 2.6	368.00	380.15	1.10	324.32	1.18
172 × 92 × 3.2	368.00	545.98	1.13	475.69	1.15
172 × 92 × 4.8	368.00	1070.17	1.56	1012.04	1.06
172 × 92 × 5.4	368.00	1251.47	1.81	1193.43	1.06

172 × 92 × 8.0	368.00	2016.94	5.59	1874.03	1.08
172 × 92 × 10.0	368.00	2557.75	8.17	2410.71	1.07
172 × 92 × 12.0	368.00	3154.38	16.10	2952.41	1.08
200 × 100 × 2.6	400.00	389.84	1.05	324.60	1.21
200 × 100 × 3.2	400.00	555.45	1.34	475.41	1.17
200 × 100 × 4.0	400.00	810.07	1.06	717.88	1.13
200 × 100 × 5.0	400.00	1193.35	1.42	1086.97	1.10
200 × 100 × 5.4	400.00	1343.61	1.62	1255.15	1.07
200 × 100 × 6.0	400.00	1576.81	2.02	1493.62	1.06
200 × 100 × 8.0	400.00	2260.96	4.28	2080.12	1.09
200 × 100 × 10.0	400.00	2868.79	5.92	2680.43	1.08
200 × 100 × 12.0	400.00	3514.07	11.06	3288.30	1.08
200 × 100 × 14.0	400.00	4171.21	15.10	3899.41	1.08
240 × 120 × 2.6	480.00	407.76	1.26	334.74	1.22
240 × 120 × 3.2	480.00	601.67	1.36	489.64	1.23
240 × 120 × 4.0	480.00	854.03	1.15	738.08	1.16
240 × 120 × 5.0	480.00	1253.43	1.31	1115.01	1.13
240 × 120 × 6.0	480.00	1717.99	1.61	1565.24	1.10
240 × 120 × 7.0	480.00	2166.72	2.29	2081.71	1.05
240 × 120 × 8.0	480.00	2608.72	3.15	2429.40	1.08
240 × 120 × 10.0	480.00	3410.02	5.79	3138.36	1.09
240 × 120 × 12.0	480.00	4153.94	9.18	3859.82	1.08
240 × 120 × 14.0	480.00	4876.19	9.73	4588.79	1.07
300 × 150 × 3.2	600.00	623.30	1.57	508.42	1.23
300 × 150 × 4.0	600.00	943.45	1.63	765.07	1.24
300 × 150 × 5.0	600.00	1349.44	2.00	1153.25	1.17
300 × 150 × 6.0	600.00	1826.57	2.03	1615.24	1.14
300 × 150 × 8.0	600.00	2965.29	2.39	2759.19	1.08
300 × 150 × 9.0	600.00	3547.11	3.04	3360.64	1.06
300 × 150 × 10.0	600.00	4076.80	3.85	3795.93	1.08
300 × 150 × 13.0	600.00	5537.90	6.89	5127.87	1.09
300 × 150 × 15.0	600.00	6490.60	11.36	6030.97	1.08
300 × 200 × 3.2	800.00	613.72	2.18	566.23	1.09
300 × 200 × 4.0	800.00	908.36	1.84	852.59	1.07
300 × 200 × 5.0	800.00	1372.43	1.83	1286.17	1.07
300 × 200 × 6.0	800.00	1937.18	2.03	1802.84	1.08
300 × 200 × 8.0	800.00	3143.41	2.72	3084.65	1.02
300 × 200 × 9.0	800.00	3547.96	3.53	3760.08	0.95
300 × 200 × 10.0	800.00	4379.40	4.75	4250.69	1.04
300 × 200 × 13.0	800.00	6129.05	9.27	5757.20	1.07
300 × 200 × 15.0	800.00	7159.40	12.57	6783.38	1.06

300 × 200 × 20.0	800.00	10203.85	16.98	9397.12	1.04
300 × 200 × 25.0	800.00	12995.30	31.52	12049.31	1.03
300 × 200 × 30.0	800.00	15869.85	44.79	14717.27	1.04
300 × 200 × 35.0	800.00	18876.20	53.33	17391.72	1.04
300 × 200 × 45.0	800.00	25149.70	76.62	22788.74	1.05
25 × 25 × 2.0	100.00	97.36	3.05	98.97	0.99
25 × 25 × 2.6	100.00	129.67	5.95	133.50	0.98
25 × 25 × 3.2	100.00	163.72	8.25	169.16	0.98
32 × 32 × 2.0	128.00	122.55	2.17	122.10	1.01
32 × 32 × 2.6	128.00	162.18	3.95	165.05	0.99
32 × 32 × 3.2	128.00	203.12	6.76	209.17	0.98
38 × 38 × 2.6	152.00	190.12	3.47	191.10	1.00
38 × 38 × 3.2	152.00	237.85	5.96	242.47	0.99
38 × 38 × 4.0	152.00	303.55	8.71	312.70	0.98
40 × 40 × 2.6	160.00	199.76	3.31	199.61	1.01
40 × 40 × 3.2	160.00	248.89	4.41	253.36	0.99
40 × 40 × 4.0	160.00	317.46	8.10	326.83	0.98
40 × 40 × 4.5	160.00	363.59	10.90	373.72	0.98
50 × 50 × 2.6	200.00	246.14	2.46	240.94	1.03
50 × 50 × 2.9	200.00	276.25	2.81	273.44	1.02
50 × 50 × 3.6	200.00	348.22	5.37	350.83	1.00
50 × 50 × 4.5	200.00	442.52	8.53	452.89	0.98
50 × 50 × 5.0	200.00	496.01	9.71	510.67	0.98
60 × 60 × 2.6	240.00	287.96	2.02	280.61	1.03
60 × 60 × 3.2	240.00	364.52	3.74	357.29	1.03
60 × 60 × 4.0	240.00	461.62	5.05	462.41	1.01
60 × 60 × 4.8	240.00	560.00	6.61	570.05	0.99
60 × 60 × 5.4	240.00	636.91	10.67	652.17	0.98
72 × 72 × 3.2	288.00	430.05	2.93	416.20	1.04
72 × 72 × 4.0	288.00	548.52	4.49	539.43	1.02
72 × 72 × 4.8	288.00	663.75	5.87	665.86	1.00
72 × 72 × 6.0	288.00	844.39	10.82	860.12	0.99
80 × 80 × 3.2	320.00	468.56	2.41	454.34	1.04
80 × 80 × 4.0	320.00	605.04	4.45	589.34	1.03
80 × 80 × 4.8	320.00	734.13	5.65	727.99	1.02
80 × 80 × 5.4	320.00	831.81	7.57	833.90	1.00
80 × 80 × 7.0	320.00	1098.22	12.28	1122.73	0.99
91.5 × 91.5 × 3.6	366.00	598.93	2.59	582.97	1.03
91.5 × 91.5 × 4.5	366.00	778.23	4.78	756.28	1.04
91.5 × 91.5 × 5.4	366.00	941.79	5.10	934.30	1.02
91.5 × 91.5 × 7.0	366.00	1243.47	11.05	1259.57	0.99

100 × 100 × 4.0	400.00	732.10	3.17	709.90	1.04
100 × 100 × 5.0	400.00	946.60	5.34	920.84	1.04
100 × 100 × 6.0	400.00	1147.13	7.52	1137.48	1.02
100 × 100 × 8.0	400.00	1556.16	13.34	1583.48	0.99
113.5 × 113.5 × 4.8	454.00	1010.86	4.24	976.01	1.04
113.5 × 113.5 × 5.4	454.00	1153.21	5.50	1119.66	1.04
113.5 × 113.5 × 7.0	454.00	1521.70	8.18	1512.64	1.01
113.5 × 113.5 × 9.0	454.00	1987.68	14.95	2019.32	0.99
132 × 132 × 2.6	528.00	362.34	1.08	409.83	0.89
132 × 132 × 4.8	528.00	1133.26	3.16	1106.33	1.03
132 × 132 × 5.4	528.00	1312.88	4.28	1269.86	1.04
132 × 132 × 7.0	528.00	1754.24	6.96	1717.92	1.03
132 × 132 × 10.0	528.00	2562.27	17.04	2592.12	1.00
150 × 150 × 2.6	600.00	366.77	1.36	417.26	0.88
150 × 150 × 4.0	600.00	890.27	1.68	933.86	0.96
150 × 150 × 5.0	600.00	1281.24	2.70	1289.98	1.00
150 × 150 × 6.0	600.00	1647.12	4.75	1597.28	1.04
150 × 150 × 8.0	600.00	2277.34	9.17	2233.09	1.03
150 × 150 × 11.0	600.00	3192.44	16.79	3224.68	1.00
180 × 180 × 2.9	720.00	384.84	1.94	524.70	0.74
180 × 180 × 4.0	720.00	864.93	1.47	954.63	0.91
180 × 180 × 5.0	720.00	1381.61	2.15	1452.59	0.96
180 × 180 × 5.4	720.00	1571.94	2.59	1641.13	0.96
180 × 180 × 6.0	720.00	1829.32	2.95	1857.57	0.99
180 × 180 × 8.0	720.00	2690.32	7.70	2601.23	1.04
180 × 180 × 10.0	720.00	3429.61	11.04	3371.47	1.02
180 × 180 × 12.0	720.00	4154.58	15.98	4161.66	1.01
220 × 220 × 2.9	880.00	491.04	2.54	541.10	0.91
220 × 220 × 4.0	880.00	866.86	2.08	980.88	0.89
220 × 220 × 5.0	880.00	1364.82	2.07	1487.34	0.92
220 × 220 × 6.0	880.00	1995.67	2.58	2095.94	0.96
220 × 220 × 7.0	880.00	2587.52	3.57	2627.27	0.99
220 × 220 × 8.0	880.00	3143.78	5.31	3073.14	1.03
220 × 220 × 10.0	880.00	4129.36	9.86	3988.93	1.04
220 × 220 × 13.0	880.00	5463.00	15.84	5409.10	1.02
220 × 220 × 15.0	880.00	8636.25	33.60	8869.13	0.98
220 × 220 × 20.0	880.00	10939.95	42.80	11435.17	0.96
220 × 220 × 25.0	880.00	13375.85	61.10	14087.71	0.96
220 × 220 × 30.0	880.00	16018.75	85.42	16876.90	0.96
250 × 250 × 2.6	1000.00	411.94	2.80	452.01	0.92
250 × 250 × 3.2	1000.00	605.05	2.93	661.92	0.92

250 × 250 × 4.5	1000.00	1101.08	2.73	1243.20	0.89
250 × 250 × 6.0	1000.00	1993.43	2.31	2127.33	0.94
250 × 250 × 7.0	1000.00	2678.59	2.89	2844.63	0.95
250 × 250 × 8.0	1000.00	3379.91	4.15	3415.46	1.00
250 × 250 × 10.0	1000.00	4573.20	7.71	4436.89	1.04
250 × 250 × 12.0	1000.00	5653.00	12.55	5488.41	1.04
250 × 250 × 15.0	1000.00	7153.95	18.72	7109.23	1.01
250 × 250 × 20.0	1000.00	9667.10	21.91	9896.78	0.98
250 × 250 × 25.0	1000.00	12232.70	30.69	12766.68	0.97
250 × 250 × 30.0	1000.00	14834.95	34.01	15712.69	0.95
250 × 250 × 35.0	1000.00	17594.65	49.23	18753.52	0.95
250 × 250 × 45.0	1000.00	23279.55	72.65	25401.06	0.93
250 × 250 × 50.0	1000.00	26300.90	86.41	29404.87	0.90

Table 4.4: Assessment of design predictions from current design equations as well as proposed equations against the test results

Specimens	P_{Test} (kN)	$\frac{P_u}{P_{EC3}}$	$\frac{P_{Test}}{P_{CSM}}$	$\frac{P_{Test}}{P_{DSM}}$	$\frac{P_{Test}}{P_{DSM-RR}}$	$\frac{P_{Test}}{P_{DSM-ARR}}$	$\frac{P_{Test}}{P^*_{DSM}}$
40 × 40 × 3.2-SC1	258.08	1.20	1.08	1.21	1.13	1.10	0.94
40 × 40 × 3.2-SC2	261.70	1.21	1.10	1.22	1.14	1.12	0.95
40 × 40 × 4.0-SC1	304.93	1.27	1.12	1.29	1.15	1.13	0.94
40 × 40 × 4.0-SC2	298.95	1.25	1.10	1.27	1.13	1.11	0.92
50 × 50 × 2.9-SC1	254.96	1.27	1.19	1.28	1.19	1.14	1.07
50 × 50 × 2.9-SC2	254.22	1.34	1.29	1.36	1.28	1.21	1.15
60 × 40 × 2.9-SC1	254.90	1.16	1.11	1.17	1.14	1.11	1.02
60 × 40 × 2.9-SC2	256.49	1.21	1.17	1.22	1.20	1.16	1.08
60 × 60 × 2.6-SC1	295.45	1.18	1.16	1.18	1.18	1.12	1.07
66 × 33 × 2.6-SC1	232.51	1.16	1.14	1.17	1.21	1.11	1.09
66 × 33 × 2.6-SC2	232.85	1.15	1.13	1.16	1.20	1.10	1.08
80 × 40 × 2.6-SC1	326.91	1.10	1.10	1.11	1.29	1.10	1.10
No. of observations		12.0	12.0	12.0	12.0	12.0	12.0
Mean (P_m)		1.21	1.14	1.22	1.19	1.13	1.03
COV (V_p)		0.06	0.05	0.06	0.04	0.03	0.07
Resistant factor (ϕ)		0.91	0.91	0.85	0.85	0.85	0.85
Reliability index (β)		3.10	2.89	3.57	3.55	3.36	2.84

Table 4.5: Assessment of design predictions from current design equations as well as proposed equations against FE

	$\frac{P_{FE}}{P_{EC3}}$	$\frac{P_{FE}}{P_{CSM}}$	$\frac{P_{FE}}{P_{DSM}}$	$\frac{P_{FE}}{P_{DSM-RR}}$	$\frac{P_{FE}}{P_{DSM-ARR}}$	$\frac{P_{FE}}{P^{*}_{DSM}}$
No. of observations	173	173	173	173	173	173
Mean (P_m)	1.16	1.13	1.18	1.18	1.10	1.03
COV (V_p)	0.15	0.08	0.15	0.08	0.11	0.07
Resistant factor (ϕ)	0.91	0.91	0.85	0.85	0.85	0.85
Reliability index (β)	2.57	2.78	2.95	3.38	2.97	2.87

Table 4.6: Comparison of FE and test results with design predictions for non-slender/ stocky cross-sections

	$\frac{P_{u}}{P_{EC3}}$	$\frac{P_{u}}{P_{CSM}}$	$\frac{P_{u}}{P_{DSM}}$	$\frac{P_{u}}{P_{DSM-RR}}$	$\frac{P_{u}}{P_{DSM-ARR}}$	$\frac{P_{u}}{P^{*}_{DSM}}$
No. of observations	144	138	147	105	147	147
Mean (P_m)	1.24	1.16	1.24	1.21	1.14	1.03
COV (V_p)	0.10	0.07	0.11	0.06	0.08	0.04
Resistant factor (ϕ)	0.91	0.91	0.85	0.85	0.85	0.85
Reliability index (β)	3.06	2.92	3.43	3.57	3.25	2.96

Table 4.7: Comparison of FE and test results with design predictions for slender cross-sections

	$\frac{P_{u}}{P_{EC3}}$	$\frac{P_{u}}{P_{CSM}}$	$\frac{P_{u}}{P_{DSM}}$	$\frac{P_{u}}{P_{DSM-RR}}$	$\frac{P_{u}}{P_{DSM-ARR}}$	$\frac{P_{u}}{P^{*}_{DSM}}$
No. of observations	41	47	38	80	38	38
Mean (P_m)	0.92	1.04	0.96	1.14	0.95	1.05
COV (V_p)	0.07	0.06	0.12	0.09	0.12	0.12
Resistant factor (ϕ)	0.91	0.91	0.85	0.85	0.85	0.85
Reliability index (β)	1.97	2.50	2.39	3.20	2.35	2.72

Table 4.8: Comparison of all FE and test results with design predictions

	$\frac{P_u}{P_{EC3}}$	$\frac{P_u}{P_{CSM}}$	$\frac{P_u}{P_{DSM}}$	$\frac{P_u}{P_{DSM-RR}}$	$\frac{P_u}{P_{DSM-ARR}}$	$\frac{P_u}{P^*_{DSM}}$
No. of observations	185	185	185	185	185	185
Mean (P_m)	1.17	1.13	1.18	1.18	1.10	1.03
COV (V_p)	0.15	0.08	0.15	0.08	0.11	0.07
Resistant factor (ϕ)	0.91	0.91	0.85	0.85	0.85	0.85
Reliability index (β)	2.60	2.78	3.01	3.38	2.97	2.87

Table 4.9: Comparison of all FE and test results with design predictions for resistance factor of $\phi = 0.85$

	$\frac{P_u}{P_{EC3}}$	$\frac{P_u}{P_{CSM}}$	$\frac{P_u}{P_{DSM}}$	$\frac{P_u}{P_{DSM-RR}}$	$\frac{P_u}{P_{DSM-ARR}}$	$\frac{P_u}{P^*_{DSM}}$
No. of observations	185	185	185	185	185	185
Mean (P_m)	1.17	1.13	1.18	1.18	1.10	1.03
COV (V_p)	0.15	0.08	0.15	0.08	0.11	0.07
Resistant factor (ϕ)	0.85	0.85	0.85	0.85	0.85	0.85
Reliability index (β)	2.84	3.05	3.01	3.38	2.97	2.87

This page is intentionally left blank

Chapter 5

Perforated Stub Columns

5.1 INTRODUCTION

As mentioned in Chapter 2, experimental test results on the structural performance of YSt-310 cold-formed steel perforated tubular stub columns has not been reported so far. Therefore, in this chapter, an experimental and numerical investigation into the structural performance of stub columns, having two opposite central circular perforations of same diameter, under concentric loading has been attempted. Firstly, the experimental program to understand the behaviour of perforated stub columns are presented. This is followed by a parametric study using validated FE models, to estimate the performance of perforated stub columns which have not covered in the experimental program has been studied using numerical analysis.

In brief, Section 5.2 of this chapter describes the experimental program to investigate the capacity of perforated stub columns at ambient temperature.

The results of experimental investigations have been presented and discussed in Section 5.3. New equations to predict local geometric imperfection amplitude have been proposed based on 3D laser scanning local imperfection results. The column

capacity test results have been utilised to validate numerical models and also to assess the applicability of existing equations in design standards and proposed formulae for perforated columns.

In Section 5.4, finite element study to estimate the capacity of perforated stub columns, which have not been included in the experimental program, is presented. In Section 5.5, the ultimate column capacities generated from both test and numerical investigations have been utilised to assess the applicability of existing design equations set out in design standards and proposed equations in literature. Based on the analysis, modified design equations have been proposed in this section.

5.2 EXPERIMENTAL INVESTIGATION

5.2.1 General

An experimental study into the member capacity of stub SHS and RHS columns containing two opposite central circular perforations of equal diameter has been conducted. Figure 5.1 shows the dimension levelling system adopted in this chapter, where B, D, t, d, w, r_i and L are the width, depth, thickness, diameter of perforation, flat element width, outer corner radius and overall member length of the stub column. A detailed description of the test setups and testing procedures are reported as follows:

5.2.2 Test material

The test materials used in the present study have been obtained from the same batch previously utilised in Chapters 3 and 4. The ambient temperature flat and corner material properties detailed in Tables 3.4 and 3.5 are utilised to investigate structural behaviour and numerical study of perforated cold-formed steel stub columns. The unperforated column capacities, presented in Table 4.1 of Chapter 4, are employed to explore the effect due to the introduction of perforations with various diameters on the ultimate capacity of perforated stub columns. To account for the effect of corner

strength enhancement, the area-weighted average of flat and corner yield stress has been used throughout the present study.

5.2.3 Stub column preparation

Five cold-formed tubular sections, namely SHS 50 × 50 ×2.9, SHS 60 × 60 × 2.6, RHS 66 × 33 × 2.6, RHS 60 × 40 × 2.9 and RHS 80 × 40 × 2.6 have been considered for the circular perforated stub column tests. The method described in Section 4.2.1 of Chapter 4 for preparation of stub column is followed herein. Two opposite centrally located circular perforations of equal diameter have been made at mid-height on the faces perpendicular to the face containing seam weld using CO2 Laser cutting machine. Similarly researchers such as Saad-Eldeen *et al.* (2016) used laser cutting technique as a tool to make perforation on the untested sample, to avoid any deformation and residual stress development during the cutting process. It is assumed that the effect of heat induced during the cutting operation on the material strength is minimal. The size of the circular perforations has been made in such a way that the perforations size ratio ranges from $0.1 \leq d/w \leq 0.9$. The plate slenderness ratio (w/t) of specimens in the present study ranges from 13.13 to 27.9. The specimens are named based on the cross-sectional sizes, thickness, perforation size ratio (d/w) and sample number, in such a way that the members can be identified easily. For example, 60 × 40 × 2.9d/w0.9-2 represents a rectangular tubular/hollow section with width (B) of 60 mm, depth (D) of 40 mm, thickness (t) of 2.9 mm, perforation diameter to flat plate width ratio (d/w) of 0.9 and 2 for second (repeated) sample. The two centrally located circular perforation has been made on the larger flat width of the RHS. The largest diameter of the perforation is 0.9 times the flat width of the section. The measured cross-sectional dimensions of perforated stub columns are listed in Table 5.1. It may be noted that due to shortage of material, some stub columns for 50 × 50 × 2.9 and 66 × 33 × 2.6 with perforation size ratios, d/w ~ 0.1–0.3 and 0.1–0.5 respectively have been not included in the present test programme. The cross-sectional area of unperforated and perforated (measured at the location of perforation) stub columns are represented by A_g and A_{net} respectively.

5.2.4 Local Geometric imperfection

Buckling load and overall behaviour of structural members can be captured accurately using finite element models by inputting proper local and global imperfection amplitudes (see Pastor *et al.*, 2014). Therefore, measurement of local and global imperfection amplitude is an inevitable practice in the current design and analysis trend of cold-formed structural members. In the present study, local geometric imperfection of 21 stub columns have been measured using a non-contact three dimensional (3D) laser scanner, following the same procedure outlined in Section 4.2.3 of Chapter 4, before and after the perforation have been made. A typical three dimensional (3D) wire frame structure generated from the laser scanner is shown in Figure 5.2 (a) for 80 × 40 × 2.6*d*/*w*0.7-1 perforated stub column. Measurement of local geometric imperfection has been performed along the centreline of all four flat faces of the stub columns and a typical perforated flat face is shown in Figure 5.2 (b). The coordinates of nodes at mid-width for all four faces have been recorded from the central 50% of member length (leaving 25% of member length at both ends). This practice is to avoid the effect of end flaring (see Cruise and Gardner, 2006; Theofanous *et al.*, 2009a) at both ends due to residual stress and milling operations. A typical local geometric imperfection profile of four faces for 80 × 40 × 2.6*d*/*w*0.7-1 is shown in Figure 5.2 (c) and the dotted lines represent the perforated portions of flat faces of the cross-section.

5.2.5 Strain measurement

The strain distributions near the perforation and mid-height of unperforated faces along the direction of column length during compression test has been captured on two specimens namely 60 × 40 × 2.9*d*/*w*0.7-2 and 60 × 40 × 2.9*d*/*w*0.9-2, using unidirectional single element strain gauges having gauge length of 6 mm. The strain gauges have been positioned at mid-height on the outer surface of the specimen. Seven single element strain gauges have been utilised to measure strain distribution for 60 × 40 × 2.9*d*/*w*0.7-2 and five for 60 × 40 × 2.9*d*/*w*0.9-2. The locations of strain gauges are shown in Figure 5.3 for 60 × 40 × 2.9*d*/*w*0.7-2. The location of strain gauges for

60 × 40 × 2.9*d*/*w*0.9-2 is similar as that of 60 × 40 × 2.9*d*/*w*0.7-2 except that strain gauge at location 6 and 7 have not been provided (due to the presence of manufacturer's marking on the outer surface) for this particular specimen.

5.2.6 Stub column tests

Similar to the stub column test for unperforated members detailed in Section 4.2.4, the ultimate capacity of perforated stub columns has been estimated by using the two hydraulic loading frames. A typical experimental setup for 250 kN loading 60 × 40 × 2.6*d*/*w*0.9-2 and 1000 kN loading 60 × 60 × 2.6*d*/*w*0.3-1 testing machines are shown in Figures 5.4 (a) and (b) respectively. An initial load of ~ 1 kN has been applied to remove any possible gaps between the specimen edges and the bearing plate. The concentric incremental load has been applied to a certain limit where sufficient post-ultimate range is captured. The readings from load cells, displacement transducers, extensometer and strain gauges have been recorded at regular interval automatically by using a data acquisition system.

5.3 RESULTS AND DISCUSSION

The results from the experimental programme are summarised in this section.

5.3.1 Local geometric imperfection

As mentioned in Section 4.2.3, the average of the deviations of all nodes from the line joining the tips of central 50% of member length has been determined for each face of the cross-section and is termed as imperfection amplitude of each face. The mean of imperfection amplitudes of four faces is defined as the local geometric imperfection of a column member in the current study. The measured imperfection amplitude for each faces and mean values for unperforated, ω_d and perforated, ω_{dp} cross-sections are summarised in Tables 5.2 and 5.3 respectively. The change in local imperfection amplitude after the laser cutting process is then compared. The amount of imperfection amplitude changes from unperforated to perforated member has been

calculated by deducting the magnitude from perforated, ω_{dp} to unperforated, ω_d value and expressed in terms of percentage change from unperforated member (summarised in Table 5.4). For the specimen tested, a variation in the range of –62.90 to 159.21 with a high degree of scatter of coefficient of variance of 1.91 is observed from Table 5.4. From Table 5.4, it can be readily seen that a definite correlation or trend of imperfection magnitude with perforation size cannot be established, as the percentage variation in imperfection amplitude appears a bit random in nature. This may be due to combined effects from residual stress, heat induced at the time of cutting process, transportation etc.

5.3.1.1 Unperforated plate elements

The local geometric imperfections of unperforated sections from Section 4.2.3 (provided in Table 4.1) and present test data have been used to calibrate predictive model proposed by Dawson and Walker (1972) for cold-formed steel tubular sections provided in Equations 5.1 and 5.2. The local geometric imperfection amplitudes (ω_d) are normalised by each cross-sectional thickness and plotted against $(f_y / f_{cr})^{0.5}$ and (f_y / f_{cr}) to estimate the coefficients β and γ of predictive models.

$$\omega_d / t = \beta (f_y / f_{cr})^{0.5} \quad (5.1)$$

$$\omega_d / t = \gamma (f_y / f_{cr}) \quad (5.2)$$

in which,

$$f_{cr} = k \frac{\pi^2 E}{12(1-\upsilon^2)} \left(\frac{t}{w}\right)^2 . \quad (5.3)$$

Where f_y, E, k, t, υ and w are 0.2% proof stress (weighted average), Young's modulus of steel (used for flat coupon test), plate buckling coefficient (4 for stiffened plate elements), thickness of member, Poisson's ratio of steel (considered as 0.3) and flat plate element width of the cross-section measured before the test as $w = (D - 2r_i - 2t)$, where symbols are defined in Figure 5.1 (a).

The correlations between $(f_y/f_{cr})^{0.5}$ and (f_y/f_{cr}) against ω_d/t for estimating β and γ is respectively plotted in Figures 5.5 and 5.6. Similar work has been reported by Gardner *et al.* (2010) for cold-formed carbon steel and hot-rolled steel. Based on the least square linear regression analysis the coefficients, β and γ are estimated to be 0.0167 and 0.0235. It is also observed from the analysis that Equation 5.1 provides a better prediction (higher R^2 value of 1.88) on the measured local imperfection amplitudes as compared to Equation 5.2. The value of $\gamma = 0.0235$ from the present study is very closed to that of modified Dawson and Walker (1972) predictive equation proposed by Gardner and Nethercot (2004) of stainless steel where the value of $\gamma = 0.023$. This could be the reason when numerical validation performed in Section 4.3.5 using the predictive equation by Gardner and Nethercot (2004) has been well predicted for cold-formed carbon steel.

5.3.1.2 Perforated plate elements

The measured local geometric imperfection of perforated plates (ω_{dp}) from the present study have been utilised to estimate the coefficients (β and γ) of predictive model proposed by Dawson and Walker (1972) by replacing f_{cr} with critical elastic buckling for thin plate having perforation, f_{crl}. Simplified equations proposed by Moen and Schafer (2009) for calculation of critical elastic buckling for thin plate with perforations given in Equation 5.4 has been utilised. The critical elastic buckling of plate without perforation has been calculated using Equation 5.3. The smallest value from the critical elastic buckling of perforated and unperforated elements of the member has been selected for estimation of β and γ. The measured imperfection amplitudes, (ω_{dp}) are normalised with cross-sectional thickness and plotted with $(f_y/f_{cr})^{0.5}$ and (f_y/f_{cr}) based on Equations 5.1 and 5.2.

$$f_{crl} = \min(f_{cr}, f_{crh}) \tag{5.4}$$

in which,

f_{cr} = critical elastic buckling of plate without perforation (Equation 5.3);

f_{crh} = critical elastic buckling of plate with perforation;

$$f_{crh} = k_h \frac{\pi^2 E}{12(1-\upsilon^2)}\left(\frac{t}{w_h}\right)^2. \quad (5.5)$$

where k_h, plate buckling coefficient of unstiffened plate estimated based on the expressions approximated by Yu and Schafer (2007) (given in Equations 5.6 and 5.7) and w_h is the equivalent unstiffened plate element width on either side of the perforation (at the perforation location), calculated as $w_h = (w/2 - \pi d/8)$ for the current study, as shown in Figure 5.7. The plate buckling coefficient from Yu and Schafer (2007) takes into account the influence of perforation size and improves from AISI S100-16 (2016), which conservatively assumes a lower bound value of 0.43 for unstiffened plate elements, irrespective of perforation size.

For $d/w_h \geq 1$, $$k_h = 0.425 + \frac{0.2}{(d/w_h)^{0.95} - 0.6}, \quad (5.6)$$

For $d/w_h < 1$, $$k_h = 0.925. \quad (5.7)$$

The relationships between $(f_y/f_{crl})^{0.5}$ and (f_y/f_{crl}) against ω_{dp}/t, for estimating β and γ are plotted in Figures 5.8 and 5.9 respectively. The values of β and γ are found out to be 0.0211 and 0.0303 respectively, based on the least square linear regression analysis. As compared to unperforated members, the coefficients β and γ of predictive models are ~ 29% and 26% respectively higher in perforated members. Thus, it may be concluded that laser cutting process increases the local geometric imperfection amplitude of cold-formed steel tubular sections.

5.3.2 Compression test results

The load versus end-shortening curves of columns having similar cross-sectional dimensions and member length, but different circular perforation size at mid-height

of the column (d/w ~ 0.1 to 0.9) obtained from the compression tests are plotted, in the same graph to compare the effect of perforation size on the column capacity, for all five cross-sections separately in Figures 5.10–5.14 for 50 × 50 × 2.9 (d/w ~ 0.5–0.9), 60 × 40 × 2.9, 60 × 60 × 2.6, 66 × 33 × 2.6 (d/w ~ 0.7–0.9) and 80 × 40 × 2.6 respectively and the ultimate column capacities $\left(P_{Test-P}\right)$ are summarised in Table 5.5. It can be observed distinctly from the comparisons that the column stiffness, ultimate capacity and ductility decreases as the diameter of circular perforation size increases. The decrease in ultimate load with increasing perforation size ratio is due to the fact that the stiffness of flat plate elements having perforation decreases and the member fails. The deformed shapes of 60 × 40 × 2.6 and 80 × 40 × 2.6 cross-sections with different d/w ratios ranging from 0.1–0.9 are shown in Figures 5.15 and 5.16 respectively. It can be observed from the deformed shapes that all cross-sections have material yielding failure at the perforation location.

5.3.3 Effect of d/w on the capacity of stub columns

In this section, the effect of perforation size to flat width ratio, d/w on the ultimate capacity of stub columns is presented. The ultimate loads of perforated members recorded from the experimental investigation have been normalised with the columns capacities of identical members without perforation, P_{Test} from Chapter 4 detailed in Table 4.1, to estimate the percentage reduction in column capacity due to the presence of central perforation with different (d/w) size ratio at mid-height of column and are plotted in Figure 5.17 for three different cross-sections (for which maximum flat width of the member to thickness ratio, w/t ranges from 19.08 to 26.77) namely 60 × 60 × 2.6, 60 × 40 × 2.9 and 80 × 40 × 2.6. It can be observed from the figure that, for the central circular perforation ratio of 10 %, the ultimate capacity of a member is not affected. However, the percentage reduction on column capacities for 30%, 50%, 70% and 90% perforation size ratio ranges from 7.13% to 11.24%, 13.96% to 21.59%, 26.59% to 35.38% and 37.47 to 51.09% respectively. In short, a mild non-linear drop in the member capacity has been observed as the perforation size, d increases from 0.1 to 0.9 of the widest flat element width, w.

5.3.4 Strain distribution at perforations location

The axial strain distributions captured by strain gauges near central circular perforation at mid-height of two columns: 60 × 40 × 2.9*d*/*w*0.7-02 and 60 × 40 × 2.9*d*/*w*0.9-02 are plotted against the applied load and reported in Figures 5.18 and 5.19 respectively. It is observed from the figures that percentage strain measured by strain gauges at various locations at mid-height of the columns are linear and uniformly distributed at low compressive load ~ 50 kN but gradually transited to non-uniform and non-linear as the compressive load increases. The strain distribution measured by strain gauge(s) near the edge of central circular perforation at locations 4 and 6 for 60 × 40 × 2.9*d*/*w*0.7-02 and 4 for 60 × 40 × 2.9*d*/*w*0.9-02 (refer Figure 5.3) are observed to be generally higher than that of strain measured other locations. Therefore, stresses near the edges of perforation (strain gauge location at 4 and 6) are expected to be higher than other strain gauge locations and onset of localised deformation at these locations (before starting at mid-depth location) are visually observed on the deformed shapes of 80 × 40 × 2.6*d*/*w*0.3-01 as shown in Figure 5.20. Strain distribution measured by strain gauges at the corner location (strain gauge at 3) is found to be lesser than that measure by strain gauges at the mid-depth (location at 1). This may due to higher stress resistance of corner region than flat region as observed in Section 3.3.3. The strain at mid-width of the column near the circular perforation (strain gauge location at 5) is very small for 60 × 40 × 2.9*d*/*w*0.7-02 and negligible for 60 × 40 × 2.9*d*/*w*0.9-02 as illustrated in Figures 5.18 and 5.19 respectively, which implies that the material at this location does not take (very small) any load throughout the compression testing process. Therefore, there may be a possibility of decreasing the weight of the member by making the perforation in the form of an elliptical shape but keeping the perforation width and load capacity same, thus increasing the stiffness to weight ratio. However, determination of elliptical perforation size so as to keeping the member capacity remains same is beyond the scope of this present study.

5.4 FINITE ELEMENT ANALYSIS

Since the present test data are limited, column capacities for wide range of cross-sectional slenderness (B/t ranges from 6.67 to 150) and perforation size ratios (e.g., d/w = 0.2, 0.4, 0.6, 0.8 etc.), which are not considered in the experimental program, have been extended through validated FE models using the general purpose commercial non-linear FE program Abaqus (2010). In the following sections, the procedures considered in developing FE models are discussed. Further, the present perforated stub column test and generated FE column capacities have been utilised in assessing the existing design equations in literature and design standards as well as establishing the design equations for perforation size ratio, $d/w \leq 0.9$.

5.4.1 Finite element modelling

In brief, this section discusses the procedure followed in developing and validation of FE models. Firstly, the FE models have been developed using the measured geometric properties provided in Table 5.1 and the stress-strain curves (both flat and corner material properties) presented in Figures 3.7 and 3.8 have been incorporated. The FE modelling procedure presented in previous chapter (see Section 4.3) has been again followed to model the perforated stub columns. Additionally, the following considerations have been made while developing the FE models: (i) Two opposite central circular perforations having same diameter (detailed in Table 5.1) have been made at mid-height of the stub column (on the longer width in the case of RHS), (ii) A finer element size of approximately equal to the material thickness has been employed near the periphery of the circular perforations (to simulate the curve geometry), (iii) Structured meshing technique available in Abaqus (2010) has been utilised to discretise the complete FE model, and (iv) Local geometric imperfection amplitude for perforated stub columns as provided in Equation 5.8, developed based on the experimental 3D scanning results (discussed more detailed in Section 5.3.1.2 above) has been employed in the least Eigen mode (local buckling) to perturb the imperfect geometry of real stub column.

$$\omega_{dp} = 0.0303\left(\frac{f_y}{f_{crl}}\right)t \tag{5.8}$$

5.4.2 Validation of FE perforated model

The load *vs.* end-shortening curves generated from the FE models have been utilised to validate the FE modelling procedure by comparing against the test results, as shown in Figures 5.21–5.25, whereas the comparison of the experimental and numerical failure modes are shown in Figures 5.26–5.28. Table 5.5 presents the ratio of experimental ($P_{Test\text{-}P}$) to numerical ($P_{FE\text{-}P}$) ultimate loads and the corresponding displacements at ultimate load. Based on the full range load-end shortening curves, ultimate and corresponding displacement as well as deformed shapes comparison against the test results, it can be concluded, a good agreement between the test results and those generated from the FE simulations has been achieved; thus validating the FE modelling procedure.

5.4.3 Parametric study

Upon validation of the FE model, the FE modelling protocol has been further utilised for parametric study. It may be mentioned here that an attempt has been made to utilise the average experimental material properties through existing two-stage stress-strain material model such as modified Ramberg–Osgood model for cold-formed steels developed by Gardner and Yun (2018), however, it has been found that the material model is only able to represent well the flat material stress-strain curve as compared to corner stress-strain curve. Therefore, the material properties adopted in the FE models for parametric study are based on the experimentally recorded stress-strain curves (both flat and corner elements) of 60 × 60 × 2.6 cross-section, as the average yield stress and ultimate strength of the experimental results are approximately close to that of 60 × 60 × 2.6 cross-section. The cross-sections considered for the parametric studies have outer widths ranging from 60 mm to 300 mm, while the outer depths ranges from 40 mm to 200 mm, thereby resulting in aspect ratio ranging from 1.0 to 2.0. The FE stub column length has been set equal to four times the minimum of the

cross-sectional dimensions. The thickness of the stub columns have been varied from 1.0 to 45.0 mm to cover a wide range of cross-sectional slenderness (i.e. w/t ranges from 2.67 to 146). In addition, FE models have been developed for stub columns for perforation size ratios, d/w = 0.2, 0.4, 0.6 and 0.8, which have not been included in the experimental program; and analysed to determine the effect of perforation size on the ultimate capacity of stub columns. A total of 233 column capacities have been generated through the validated stub columns numerical models and the column capacities are presented in Table 5.6. The nomenclatures of the cross-sections are represented by sectional dimensions, for example in 300 × 200 × 2.0-FE denotes a stub column having width, depth and thickness of 300.0 mm, 200.0 mm and 2.0 mm respectively. The "FE" signifies that the column capacity is generated from finite element analysis.

5.4.4 Effect of perforation size ratio on the ultimate capacity of stub column using test and FE results

In continuation to the analyses mentioned in Section 5.3.3, the amount of reduction in the column capacity due to the introduction of perforation has been assessed by normalizing the perforated column capacities, P_{u-P} from the test and FE analyses, with the corresponding non-perforated stub column capacities, P_u. Various sizes of perforation sizes i.e. d/w ratios ranges from 0.1 to 0.9 and additional slender cross-sections (100 × 100 × 2.0 and 300 × 200 × 2.0, for which w/t ranges from 46.0 to 146) which have not included in the test program, have also been considered. Figure 5.29 shows the influence of d/w on the ultimate column capacity for four cross-sections. It is evident from the figure that the influence of perforation size ratio on the ultimate column capacity purely depends on the plate slenderness ratio, w/t of the member. For 50 × 50 × 2.9 and 60 × 60 × 2.6 cross-section (w/t of 13.24 and 19.07 respectively), the reduction in column capacity is found to be ~ 40.0% at d/w = 0.9, as compared to that of 100 × 100 × 2.0 (w/t of 46.0) and 300 × 250 × 2.0 (w/t of 146.0) sections for which the reduction is ~ 30.0% at d/w = 0.9. Moreover, it is also observed that the reduction pattern in the case of three cross-sections: 50 × 50 × 2.9, 60 × 60 × 2.6 and 100 × 100 × 2.0 (w/t < 146.0) are found to be non-linear, whereas for 300 × 250 × 2.0

the reduction is quite small (~ 5.0%) at d/w = 0.7 and then suddenly dropped by ~ 20.0% and 30.0% at d/w = 0.8 and 0.9 respectively.

5.5 DESIGN METHODS FOR PERFORATED STEEL COLUMNS

The applicability of present design equations in design code AISI S100-16 (2016) and proposed equations by researchers such as Miller and Peköz (1994); Shanmugam *et al.* (1999); Dhanalakshmi and Shanmugam (2001); Shanmugam and Dhanalakshmi (2001); and Moen and Schafer (2011) are compared with the member capacities from present test data base for perforation size ratio (d/w) up to 0.9 in this section. It is to be noted that the present design code AISI S100-16 (2016) and proposed equations Shanmugam *et al.* (1999); Dhanalakshmi and Shanmugam (2001); AISI S100-16 (2016) provides equations for design of perforated cold-formed steel columns having perforation size to flat element width ratio (d/w) up to 0.7. The limits of perforation size ratio (d/w) for each design equation are specified in the corresponding section.

5.5.1 Design equations by Shanmugam *et al.* (1999)

Plates with centrally located square or circular perforation subjected to compressive load with different boundary conditions were analysed to capture the post-buckling and ultimate strength through finite element method by Shanmugam *et al.* (1999). The effect of parameters such as plate slenderness ($20 < w/t < 70$), shape and size of perforation ($d/w \leq 0.7$), boundary conditions along the edges and the nature of loading on the plate behaviour were studied. Based on the extensive FEM results, a simplified design formula in terms of perforation area ratio and plate slenderness was developed to predict the ultimate load of perforated plates through a best fit regression analysis. The ultimate column capacity (P_{STT}) of perforated plate is given by the following Equation 5.9:

$$; \frac{P_{STT}}{P_{sq}} = k_1\left[\frac{A_0}{A_s}\right] + k_2\left[\frac{A_0}{A_s}\right]^{1/2} + k_3$$

For $0 < d/w < 0.4$

$$k_1 = -4m^2 + 1.58m - 0.1286;$$

$$k_2 = 3m^2 - 1.52m - 0.8674$$

$$k_3 = -m^2 + 0.49m + 0.9585$$

For $0.4 < d/w < 0.7$ (5.9)

$$k_1 = 0;$$

$$k_2 = -0.96;$$

$$k_3 = 0.973$$

in which,

A_0 = Total surface area of perforations;

A_s = Total surface area of the member;

$m = (w/t)/100;$

where k_1, k_2 and k_3 are different sets of coefficients and P_{sq} is the squash load.

5.5.2 Design equations by Dhanalakshmi and Shanmugam (2001)

Behaviour of cold-formed equal-angle stub columns subjected to axial or eccentric loading was studied experimentally by Dhanalakshmi and Shanmugam (2001). The study covered a wide range of parameters which includes plate slenderness ratio ranging from 20 to 60, perforation shape, size ($d/w \leq 0.6$) and number. Based on the extensive parametric data, a simplified design equation (Equation 5.10) was developed to determine ultimate strength (P_{DS}) of perforated equal-angle stub columns as follows:

$$\frac{P_{DS}}{P_{sq}} = k_1\left(\frac{A_o}{A_s}\right) + k_2\left(\frac{A_o}{A_s}\right)^{1/2} + k_3;$$

in which,

A_0 = Surface area of perforations

A_s = Total surface area of the member

(5.10)

$$k_1 = -4.5579m^2 + 4.4862m - 1.3724;$$

$$k_2 = -0.8107m^2 + 1.0577m - 0.3354;$$

$$k_3 = 2.5357m^2 - 2.8364m + 1.0908;$$

$$m = (w/t)/100;$$

where k_1, k_2 and k_3 are different sets of coefficients and P_{sq} is the squash load.

5.5.3 Design equations by Shanmugam and Dhanalakshmi (2001)

A simplified design equation for design of cold-formed steel stub columns with perforation of all kinds of shapes, through comprehensive parametric study using finite element models on plain and lipped channel sections, was proposed by Shanmugam and Dhanalakshmi (2001). The design equation was developed based on two basic parameters namely: plate slenderness ratio (w/t) and perforation area ratio (A_0/A_S). The study covered slenderness ratio of 29.3 to 133.7 and perforation size ratio, $d/w \leq 0.6$. The ultimate load, P_{SD} of perforated stub columns proposed by Shanmugam and Dhanalakshmi (2001) is given by Equation 5.11 as follows:

$$\frac{P_{SD}}{P_{sq}} = k_1\left[\frac{A_0}{A_s}\right] + k_2\left[\frac{A_0}{A_s}\right]^{1/2} + k_3$$

in which, (5.11)

A_0 = Total surface area of perforations

A_s = Total surface area of the stub column

$$k_1 = 1.185m^3 - 3.8487m^2 + 3.7321m - 1.2336;$$

$$k_2 = 0.1111m^2 + 0.0932m - 0.7763;$$

$$k_3 = 0.11m^2 - 0.5681m + 1.1412;$$

$$m = (w/t)/100;$$

where k_1, k_2 and k_3 are different sets of coefficients and P_{sq} is the squash load.

5.5.4 Design equations in AISI Standard

Design formulae are provided in American Iron and Steel Institute, AISI S100-16 (2016) to estimate the column capacity of cold-formed steel structural members with perforations, which are based on Effective Width Method (EWM) and Direct Strength Method (DSM). Based on Section E of AISI S100-16 (2016), the nominal axial strength of a member in compression shall be the minimum of axial capacity of a member for yielding and global buckling (P_{ne}), local buckling interacting with yielding and global buckling (P_{nl}) and distortional buckling (P_{nd}). In current experimental programme, as doubly symmetric closed sections being focused, distortional buckling capacity is very large and hence ignored.

5.5.4.1 Determination of global buckling

The nominal axial capacity (P_{ne}) for yielding and global buckling is estimated based on Section E2 of AISI S100-16 (2016) as follows:

$$P_{ne} = A_g F_n \tag{5.12}$$

in which,

A_g = gross cross-sectional area,

F_n = compressive stress and calculated as follows:

For $\lambda_c \leq 1.5$; $F_n = \left(0.658^{\lambda_c^2}\right) f_y$, (5.13)

For $\lambda_c \leq 1.5$; $F_n = \left(\frac{0.877}{\lambda_c^2}\right) f_y$,

where,

$\lambda_c = \sqrt{f_y / F_{cre}}$,

F_{cre} = Elastic global buckling stress estimated based on Appendix 2 of AISI S100-16 (2016),

f_y = Yield stress.

5.5.4.2 Determination of local buckling

The nominal axial capacity (P_{nl}) for local buckling interacting with yielding and global buckling is calculated based on either through EWM on Section E3.1 or DSM on Section E3.2 of AISI S100-16 (2016).

5.5.4.2.1 Determination of local buckling based on Effective Width Method (EWM)

The nominal axial capacity for local buckling ($P_{nl\text{-}EWM}$) based on Effective Width Method (EWM) is estimated using Equation 5.14 given as follows:

$P_{nl-EWM} = A_e F_n \leq P_{ne}$ (5.14)

in which,

P_{ne} *and* F_n are defined in Equations 5.12 and 5.13 respectively,

A_e = Effective area calculated as member thickness times the summation of the effective width, *b* of each element comprising the cross-section plus corner portions, considering corner portions are fully effective.

The effective width of all elements is estimated based on Appendix 1 of AISI S100-16 (2016). The effective width of an unperforated plate element is calculated based on following Section 5.5.5.1 of this thesis. However, for perforated stiffened elements with $0 \le d/w \le 0.5$ and $w/t \le 70$, the effective width is calculated based on Equation 5.15 as follows:

For $\lambda \le 0.673$, $\quad b = (w - d)$

For $\lambda > 0.673$, $\quad b = \frac{w}{\lambda}\left\{1 - \frac{0.22}{\lambda} - \frac{(0.8d)}{w} + \frac{(0.085d)}{w\lambda}\right\}$ (5.15)

in which,

$$\lambda = \sqrt{F_n / f_{crl}}; \tag{5.16}$$

$$f_{crl} = k\frac{\pi^2 E}{12(1-\mu^2)}\left(\frac{t}{w}\right)^2;$$

where,

F_n = Global column stress defined in Equation 5.13,

k = Plate buckling coefficient (taken as 4 for stiffened elements),

E = Young's modulus,

μ = Poisson's ratio of steel.

5.5.4.2.2 Determination of local buckling based on Direct Strength Method (DSM)

The nominal axial capacity for local buckling ($P_{nl\text{-}DSM}$) based on Direct Strength Method (DSM) of AISI S100-16 (2016) is from the modifications proposed by Moen and Schafer (2011) for design of cold-formed steel columns with perforations and estimated from formulae given in Equation 5.17 as follows:

For $\lambda_l \le 0.776$; $\quad P_{nl} = P_{ne} \le P_{ynet}$,

For $\lambda_l > 0.776$; $\quad P_{nl} = \left\{1 - 0.15\left(\frac{P_{crl}}{P_{ne}}\right)^{0.4}\right\}\left(\frac{P_{crl}}{P_{ne}}\right)^{0.4} P_{ne} \le P_{ynet}$, (5.17)

in which,

$\lambda_l = \sqrt{P_{ne} / P_{crl}}$;

$P_{ynet} = A_{net} f_y$; (5.18)

$A_{net} = A_g - A_p$;

where,

P_{ne}= Global column strength defined in Equation 5.12,

$P_{crl} = A_g f_{crl}$, (5.19)

$A_p = 2 * d * t$.

The local buckling stress, f_{crl} for all elements with perforations is estimated as both for unstiffened elements at the perforation location and as a separate element where perforation is not located. For elements at the perforation location, the buckling stress has been calculated by multiplying the ratio of A_{net} /A_g, to account for net cross-sectional area, based on Section 2.3.2.2 of Appendix 2 of AISI S100-16 (2016).

5.5.4.2.3 Determination of local buckling stress based on Moen and Schafer (2009)

A simplified expression for estimating critical elastic buckling stress, f_{crl} of stiffened and unstiffened thin plates with perforations was developed by Moen and Schafer (2009). For a thin uniformly compressed simply supported plate element with one perforation or multiple perforations, the critical elastic buckling, f_{crl} is evaluated based on the equation given in Equation 5.4 and further utilised in Equation 5.19 (instead of local buckling stress, f_{crl} calculated based on AISI S100-16 (2016) specification to evaluate local buckling ($P_{nl\text{-}DSM\text{-}MS}$) following the DSM approach based on Equation 5.17.

5.5.5 Design equation proposed by Miller and Peköz (1994)

A simplified formula for the treatment of perforated plate was developed by Miller and Peköz (1994). The approach consisted of the following assumptions,

$$\text{if } (w - b_{DW}) > W_p \text{ then } b = b_{DW}$$
$$\text{if } (w - b_{DW}) \leq W_p \text{ then } b = w - W_p \tag{5.20}$$

where w is the flat width of the plate, b_{DW} is the effective design width, b is the effective width and W_p is the width of the perforation. Expressions are given in many design codes to estimate the effective width, b for an unperforated plate under compressions as follows:

5.5.5.1 Calculation of effective design width based on European, American and Australian standards

The European code, EC3-1-5 (2006), North American specification, AISI S100-16 (2016) and Australian/New Zealand standard, AS/NZS 4600 (2005) provide guidelines for determination of effective cross-sectional width. The effective width, b of an internal flat compression element is given by Equation 5.21 as follows:

$$b_{DW} = \rho w \tag{5.21}$$

in which,

For $\bar{\lambda}_p \leq 0.673$; $\rho = 1$,

For $\bar{\lambda}_p > 0.673$; $\rho = \left(1 - 0.22/\bar{\lambda}_p\right)/\bar{\lambda}_p \leq 1$,

where, w is the flat of the platted element, and $\bar{\lambda}_p = \sqrt{f_y / f_{cr}}$, where f_y is the yield stress and f_{cr} is calculated using Equation 5.3. The column capacities by Miller and

Peköz (1994) simplified formula using the above effective design equation is represented by $P_{MP\text{-}EC3}$.

5.5.5.2 Calculation of effective design width based on British Standard

The British standard, BS 5950-5 (1998) provides guidelines to estimate effective design width, *b* as follows:

For $f_y / f_{cr} \leq 0.123$, $\quad b_{DW} = w$,

For $f_y / f_{cr} > 0.123$, $\quad b_{DW} = w\left[1+14\left\{\left(\frac{f_y}{f_{cr}}\right)^{1/2} - 0.35\right\}^4\right]^{-0.2}$ (5.22)

where f_y is the yield stress and f_{cr} is calculated using Equation 5.3. The column capacities by Miller and Peköz (1994) simplified formula using the above effective design equation is represented by $P_{MP\text{-}BS}$.

5.6 RELIABILITY ANALYSIS

To assess the applicability of present design code AISI S100-16 (2016) and proposed equations by researchers (Miller and Peköz, 1994; Shanmugam *et al.*, 1999; Dhanalakshmi and Shanmugam, 2001; Shanmugam and Dhanalakshmi, 2001; and Moen and Schafer, 2011), reliability analysis detailed in Section B of commentary on AISI S100-16C (2016) specifications has been performed, using the statistical parameters such as mean (P_m) and coefficient of variance (V_p) from the comparison of test and design prediction ratios. Detailed analysis procedure and assumptions are provided in Section 3.4.7 of this thesis. For the purpose of direct comparison, the dead load (DL) and live load (LL) factor of 1.2 and 1.6 respectively have been utilised as load combinations and a resistance factor of (ϕ) of 0.85 for all design equations, has been adopted for all design equations. For reliability index greater than 2.5, the design equation is considered to be reliable.

5.7 DESIGN OF PERFORATED STEEL STUB COLUMNS

5.7.1 Assessment of current design methods for perforated steel members against test results

5.7.1.1 For perforation size ratio: $0.1 \leq d/w \leq 0.9$

The present test results cover perforation size ratio (d/w) up to 0.9 and applicability of present design equations are assessed up to this limit in this section. The ultimate columns capacities ($P_{Test–P}$) normalised by Direct Strength Method (DSM) of AISI S100-16 (2016), $P_{nl–DSM}$ and Direct Strength Method (DSM) of AISI S100-16 (2016) with critical elastic buckling stress proposed by Moen and Schafer (2009) plotted against cross-section slenderness (λ_l) are shown in Figures 5.30 and 5.31 respectively. A highly scattered but conservative column strength prediction by DSM in AISI S100-16 (2016) is observed from Figure 5.30. It may be because of the plate buckling coefficient, k of unstiffened plate conservatively taken as 0.43 regardless of perforation dimension. However as suggested by Moen and Schafer (2009), improvements have been observed as shown in Figure 5.31, when critical buckling stress, f_{crl} has been calculated based on Equation 5.4 utilising the plate buckling coefficient, k approximated by Yu and Schafer (2007), detailed in Section 5.3.1.2 of this chapter. The comparison of the predictions from original DSM in AISI S100-16 (2016), $P_{nl\text{-}DSM}$ and DSM of AISI S100-16 (2016) with critical elastic buckling stress proposed by Moen and Schafer (2009), $P_{nl\text{-}DSM\text{-}MS}$ is presented in Figure 5.32.

The experimental ultimate capacities ($P_{Test–P}$) of cold-formed steel tubular stub columns having two opposite central circular perforations at mid-height are compared with those of perforated column strengths available in design code AISI S100-16 (2016) and published research papers (Miller and Peköz, 1994; Shanmugam *et al.*, 1999; Dhanalakshmi and Shanmugam, 2001; Shanmugam and Dhanalakshmi, 2001; and Moen and Schafer, 2011), as provided in Table 5.7. It is to be mentioned here that the ultimate column capacity ($P_{nl\text{-}DSM\text{-}MS}$) estimated from the DSM prediction for local buckling interacting with yielding and global buckling calculated based on the critical

elastic buckling stress proposed by Moen and Schafer (2009) are found to be equivalent to P_{ne} (see Equation 5.17) as $\lambda_l \leq 0.776$, but they are limited to P_{ynet}, since $P_{ne} \leq P_{ynet}$. Therefore, the column capacity ($P_{nl\text{-}DSM\text{-}MS}$) is same as that predicted with net cross-sectional area, P_{ynet}. Similar results are also obtained (see in Table 5.7) from that of equation proposed by Miller and Peköz (1994) based on EC3-1-5 (2006), AISI S100-16 (2016) and AS/NZS 4600 (2005) represented by $P_{MP\text{-}EC3}$ as well as BS 5950-5 (1998), $P_{MP\text{-}BS}$. Therefore, effective width of the plate elements of the cross-sections is fully effective and controlled by the perforation width, W_p. This may be due to the fact that the stub columns in the present study are all belonged to the Class–3 cross-sectional classification (see in Section 4.6). The mean values of the ratios of test and predicted column capacities, $P_{Test\text{–}P}/P_{STT}$, $P_{Test\text{–}P}/P_{DS}$, $P_{Test\text{–}P}/P_{SD}$, $P_{Test\text{–}P}/P_{nl\text{-}EWM}$, $P_{Test\text{–}P}/P_{nl\text{-}DSM}$, $P_{Test\text{–}P}/P_{nl\text{-}DSM\text{-}MS}$, $P_{Test\text{–}P}/P_{MP\text{-}EC3}$ and $P_{Test\text{–}P}/P_{MP\text{-}BS}$, are found to be 1.00, 1.57, 1.03, 1.24, 1.59, 1.23, 1.23 and 1.23 with their corresponding coefficient of variances (COVs) of 0.11, 0.16, 0.07, 0.04, 0.20, 0.04, 0.04 and 0.04, respectively. It is observed from the comparison that all the design equations in codes and literature (proposed by researchers) are conservative. The design equations proposed by Shanmugam and Dhanalakshmi (2001) is found to be slightly conservative by 3%, whereas design equation by Dhanalakshmi and Shanmugam (2001), EWM in AISI S100-16 (2016) and DSM in AISI S100-16 (2016) are overly conservative by 57%, 24% and 59% respectively with high degree of COVs except for EWM in AISI S100-16 (2016) which has lower COV of 0.04. The design formula proposed by Miller and Peköz (1994) and DSM in AISI S100-16 (2016) using critical buckling stress by Moen and Schafer (2009) are found to be conservative by 23% with the lower value of COVs. The target reliability indexes are found to be greater than 2.5 for all design equations and hence reliable.

5.7.1.2 For perforation size ratio: $0.1 \leq d/w \leq 0.7$

The applicability of present design equations (Shanmugam *et al.*, 1999; Dhanalakshmi and Shanmugam, 2001; Shanmugam and Dhanalakshmi, 2001; AISI S100-16, 2016) based on each perforation size limits are discussed in this section. As mentioned earlier, the design equations presented by Shanmugam *et al.* (1999), Dhanalakshmi

and Shanmugam (2001), Shanmugam and Dhanalakshmi (2001) and EWM in AISI S100-16 (2016) specify the perforation size ratio (d/w) limits up to 0.7, 0.6, 0.6 and 0.5 respectively. Therefore the accuracy of the design predictions are compared with the test results with perforation size ratio, (d/w) ≤ 0.7 and are listed in Table. 5.8. The mean values of ultimate capacity to design prediction, P_{Test-P}/P_{STT}, P_{Test-P}/P_{DS}, P_{Test-P}/P_{SD}, and $P_{Test-P}/P_{nl\text{-}EWM}$ are 1.05, 1.78, 1.09 and 1.22 and corresponding COVs are 0.06, 0.13, 0.02 and 0.04 respectively. Based on the comparison, the design equations proposed by Shanmugam *et al.* (1999), Shanmugam and Dhanalakshmi (2001) and EWM in AISI S100-16 (2016) estimate conservative prediction of 5%, 9% and 22% with lower values of COVs for design of perforated cold-formed steel columns having perforation size ratio (d/w) up to 0.7, 0.6 and 0.5 respectively. However, the design predictions proposed by Dhanalakshmi and Shanmugam (2001) is overly conservative of about 78% with higher degree of COV. Overall, the design equations are found to be reliable as the target reliability indexes are greater than 2.5.

5.7.2 Assessment of current design methods for perforated steel members against test and FE results

5.7.2.1 For perforation size ratio: $0.1 \leq d/w \leq 0.9$

The applicability of the presently available design equations for perforated steel compression members is further assessed using the column capacities generated from the test and FE models,(collectively represented by P_{u-P}) for perforation size ratio d/w ≤ 0.9 and is presented Tables 5.9. It is to be noted that the design prediction by Shanmugam *et al.* (1999) for perforation size ratio, $d/w \leq 0.3$ and $w/t \geq 129.5$ provide negative ultimate column capacities and therefore, they are excluded in the comparison. The mean values of the ratios of test and FE column capacities against the predictions, P_{u-P}/P_{STT}, P_{u-P}/P_{DS}, P_{u-P}/P_{SD}, P_{u-P}/P_{nl-EWM}, P_{u-P}/P_{nl-DSM}, $P_{u-P}/P_{nl-DSM-MS}$, P_{u-P}/P_{MP-EC3} and P_{u-P}/P_{MP-BS}, are found to be 0.99, 1.42, 1.02, 1.27, 1.75, 1.22, 1.25 and 1.27 with their corresponding coefficient of variances (COVs) of 0.34, 0.32, 0.26, 0.22, 0.19 , 0.27, 0.23 and 0.21, respectively. It can be observed from the comparison that most of the design equations provide either overly conservative or

scattered predictions (except the design equation by Shanmugam *et al.*, 1999, for which the prediction is unconservative). The reliability index of design equations proposed by Dhanalakshmi and Shanmugam (2001), Miller and Peköz (1994) as well as those provided by DSM and EWM in AISI S100-16 (2016) are found greater than the target reliability index of 2.5. However, the design equations proposed by Shanmugam *et al.* (1999) and Shanmugam and Dhanalakshmi (2001) and those set out by DSM in AISI S100-16 (2016) using critical buckling stress by Moen and Schafer (2009) are found to be lesser than the target reliability index and hence not reliable. Additionally, the design predictions by original DSM in AISI S100-16 (2016), $P_{nl\text{-}DSM}$ are compared with those generated from DSM of AISI S100-16 (2016) with critical elastic buckling stress proposed by Moen and Schafer (2009), $P_{nl\text{-}DSM\text{-}MS}$ are compared and presented in Figure 5.33. It can be seen that the predictions by DSM of AISI S100-16 (2016) with critical elastic buckling stress proposed by Moen and Schafer (2009), $P_{nl\text{-}DSM\text{-}MS}$ provide improved mean value of 1.22 as compared to that of DSM in AISI S100-16 (2016), $P_{nl\text{-}DSM}$ for which the mean value is 1.78, although the former provides larger COV than the later. Hence a design equation based on the original DSM in AISI S100-16 (2016) considering the critical buckling stress recommended by Moen and Schafer (2009) is proposed based on the test and FE column capacities and the details are discussed in Section 5.7.3 below.

5.7.2.2 For perforation size ratio: $0.1 \leq d/w \leq 0.7$

Similar to the discussion in Section 5.7.1.2, the applicability of present design equations which are limited to perforation size ratio, $d/w \leq 0.7$ are assessed considering both the test and FE column capacities. Table 5.10 presents the comparison of design predictions by Shanmugam *et al.* (1999); Dhanalakshmi and Shanmugam (2001); Shanmugam and Dhanalakshmi (2001) and EWM in AISI S100-16 (2016) against the combined column capacities, P_{u-P} (both from FE and test). It can be seen that all the four design predictions provide conservative predictions but high COVs. The design prediction provided by Dhanalakshmi and Shanmugam (2001) and EWM in AISI S100-16 (2016) are able to achieve the target reliability

index of 2.5 while the prediction presented by Shanmugam *et al.* (1999) and Shanmugam and Dhanalakshmi (2001) failed to provide reliable prediction.

5.7.3 Proposed design equation

As seen in Sections 5.7.1 and 5.7.2 above, the presently available design equations for perforated compression members are not applicable for perforation size ratio, $d/w \leq 0.9$. Therefore, in this section, an attempt has been made to develop an accurate and effective design equation for design of perforated columns having two opposite circular perforations (of equal diameter) at mid-height of the column covering the perforation size ratio, $d/w \leq 0.9$. The proposed design equation, presented in Equation 5.23, is based on the current DSM method detailed in AISI S100-16 (2016) considering the critical elastic buckling stress recommended by Moen and Schafer (2009). It may be mentioned that the proposed design equations and modification to the existing design equation are based on the ultimate column capacities generated from the current test and FE analyses and a new set of coefficients are generated considering best fit regression analysis. It may also be noted that, to account for the effect of stain hardening in low slenderness range, the classical horizontal yield limit has been replaced by a non-linear curve.

$$\text{For } \lambda_l \leq 0.776 \qquad P^*_{DSM} = P_{ne}\left\{\frac{K_1}{\lambda_l^{K_2}}\right\}$$

$$\text{For } \lambda_l > 0.776 \qquad P^*_{DSM} = P_{ne}\left\{\frac{K_3}{\lambda_l^{0.8}} + \frac{K_4}{\lambda_l^{1.6}}\right\} \tag{5.23}$$

where K_1, K_2, K_3 and K_4 are the sets of coefficient of the design equations developed based on the different perforation size ratios, d/w. For different perforation size ratios d/w, the values of coefficients presented in Table 5.11 can be used to generate the design predictive capacity of perforated stub columns having the same d/w values. The relationships between the coefficients against the perforation size ratio d/w are shown in Figures 5.34–5.36. The comparison of the test and FE column capacities and

proposed design prediction curves, for different perforation size ratio d/w are also shown in Figures 5.37–5.41. The test and FE generated column capacities for both non-slender and slender cross-sections are also compared with proposed design predictions as shown in Figure 5.42 and 5.43 respectively. Additionally, Figure 5.44 presents the comparison of DSM in (AISI S100, 2016) prediction using critical elastic buckling stress suggested by Moen and Schafer (2009) and proposed modified DSM prediction against the test and FE results. The predicted column capacities from the proposed design equation are provided and compared with the test and FE column capacities in Table 5.6 and the mean and COV are also given in Table 5.9. It can be seen that the design equations are able to predict accurate design prediction values with a mean value of 1.02 and COV value of 0.06. The proposed modified design equations are able to achieve the target reliability index (i.e. β = 2.5) and hence reliable.

5.8 CONCLUSIONS

A comprehensive study on the ultimate column strength assessment of 31 tests on cold-formed steel SHS and RHS stub columns having two opposite centrally located circular perforations of perforation diameters to width ratios, $d/w \leq 0.9$, has been performed experimentally at the Department of Civil Engineering, Indian Institute of Technology Guwahati. The local geometric imperfections, load-end shortening curves, strain distributions at mid-height of column and typical failure modes observed from the present test programme are documented in this chapter. The measured local geometric imperfections of unperforated and perforated members have been utilised to estimate the coefficients β and γ of Dawson and Walker (1972) for local imperfection predictions. Based on the perforated stub column test results and comparison with design predictions following conclusions are highlighted:

i) The introduction of perforation increases the local geometric imperfection amplitude of cold-formed steel tubular sections.
ii) Central perforation ratios, d/w up to 10 % are observed not to affect the ultimate capacity of SHS/RHS stub columns. Hence, employing a smaller perforation size,

$d \leq 0.1w$, does not have significant effect on the ultimate load of perforated SHS/RHS stub columns.

iii) Average percentage reduction on column capacities based on current test results for perforation size ratios (d/w) of 30%, 50%, 70% and 90% are ~ 9.57%, 18.24%, 31.15% and 40.00% respectively. A mild non-linear drop in the load capacity of perforated stub columns is observed as the perforation size ratio, d/w increases from 0.1 to 0.9.

iv) Most of the presently available design equations provide conservative and reliable but scattered predictions for the design of cold-formed steel SHS/RHS structural stub columns with central circular perforation size ratio, d/w up to 0.9.

v) An accurate and effective design equation for design of perforated columns having two opposite circular perforations (of equal diameters) at mid-height of the column covering the perforation size ratio, $d/w \leq 0.9$, based on the current DSM method detailed in AISI S100-16 (2016) considering the critical elastic buckling stress recommended by Moen and Schafer (2009), is proposed in this chapter.

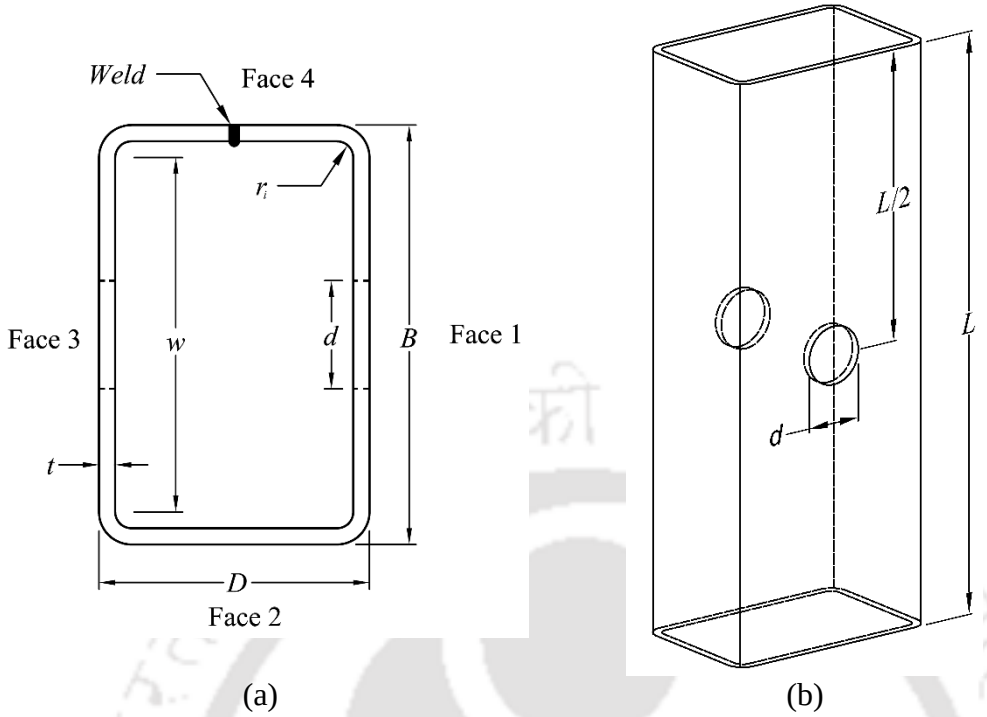

Figure 5.1: Section definitions of perforated stub column: (a) plan and (b) three dimensional views

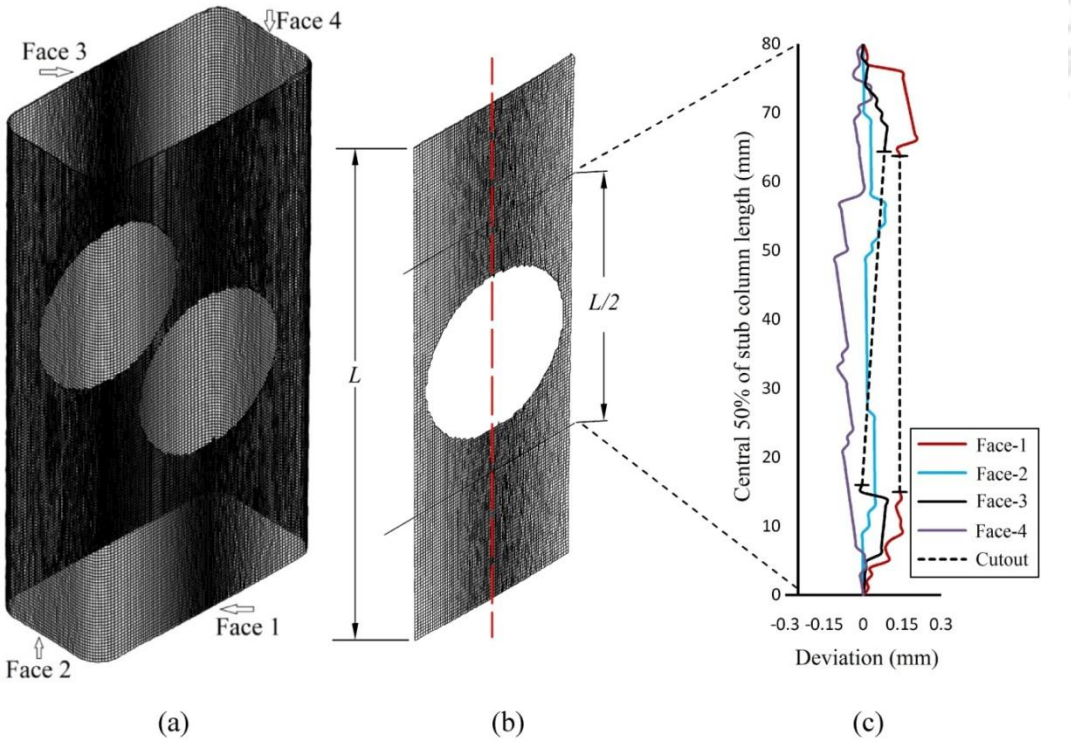

Figure 5.2: Typical diagram showing measurement of local geometric imperfection for 80 × 40 × 2.6*d*/*w*0.7-1: (a) 3D wire frame scan image (b) perforated face and (c) surface profiles for four faces.

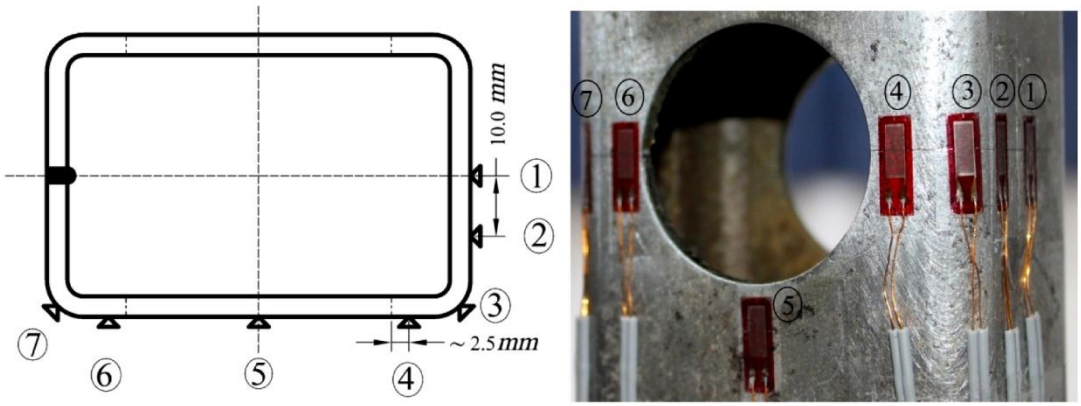

Figure 5.3: Location of Strain gauge for 60 × 40 × 2.9*d*/*w*0.7-02 stub column

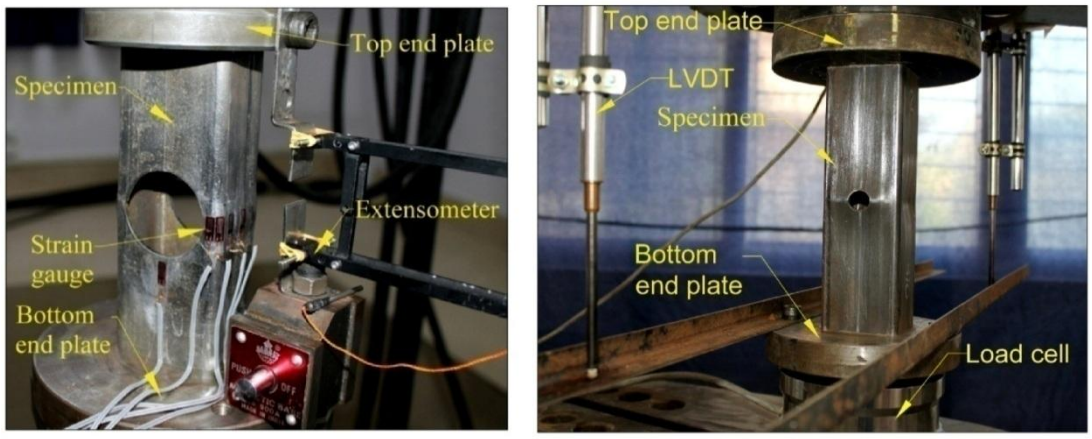

(a) (b)

Figure 5.4: Experimental setup of cold-formed tubular stub columns with circular perforation: (a) 60 × 40 × 2.6*d*/*w*0.9-2 compressing on 250 kN loading frame and (b) 60 × 60 × 2.6*d*/*w*0.3-1 on 1000 kN loading frame.

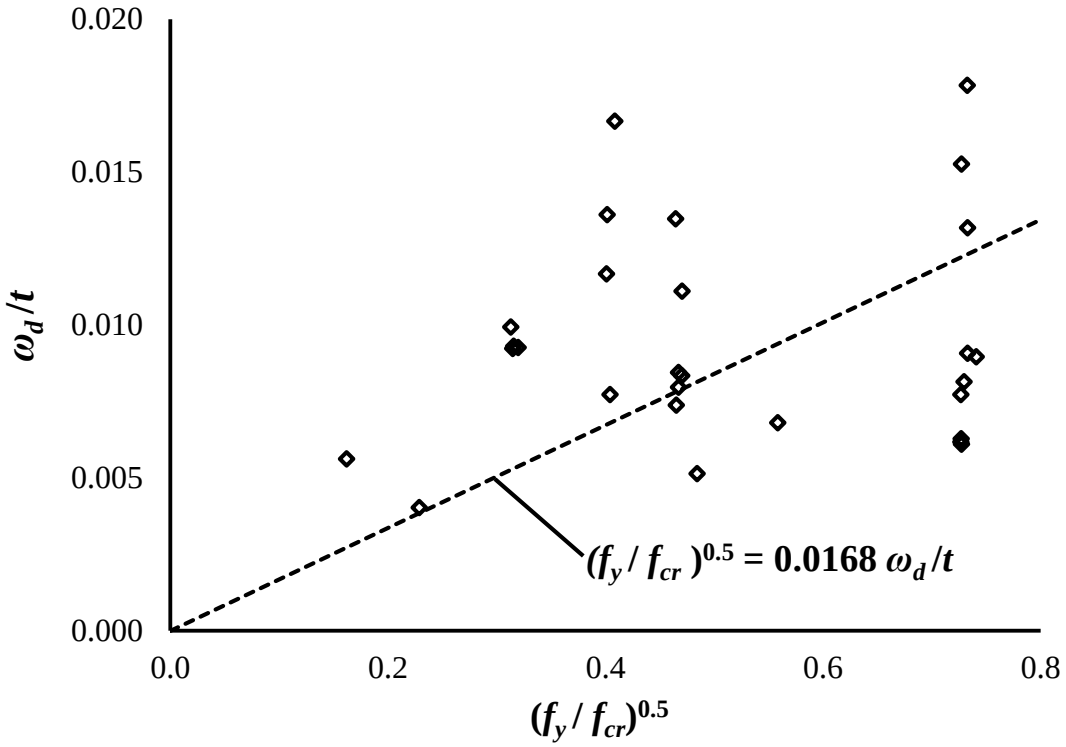

Figure 5.5: Inter-relationship between ω_d/t and $(f_y/f_{cr})^{0.5}$ for estimation of γ for unperforated columns

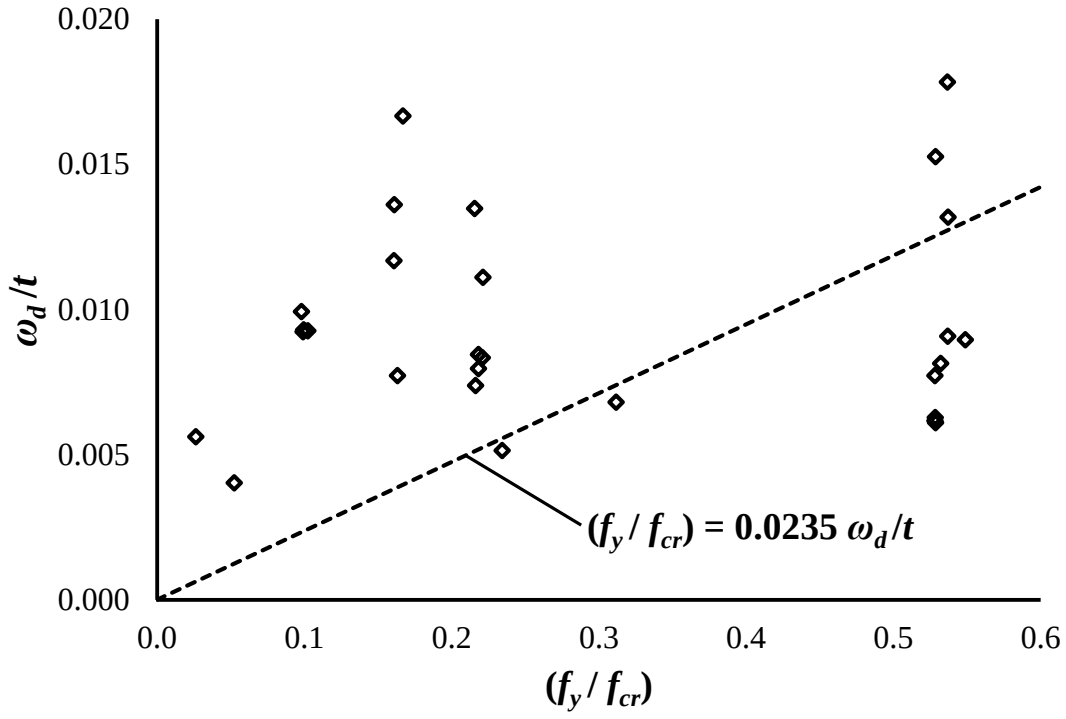

Figure 5.6: Inter-relationship between ω_d/t and $\left(f_y/f_{cr}\right)$ for estimation of β for unperforated columns

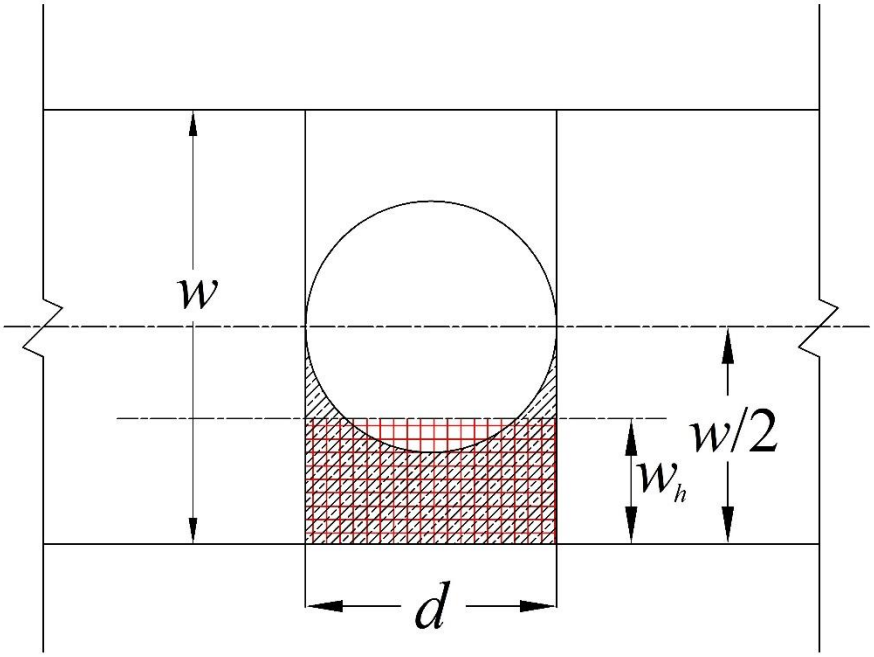

Figure 5.7: Typical representation for calculation of equivalent unstiffened plate element width, w_h at the location of hole

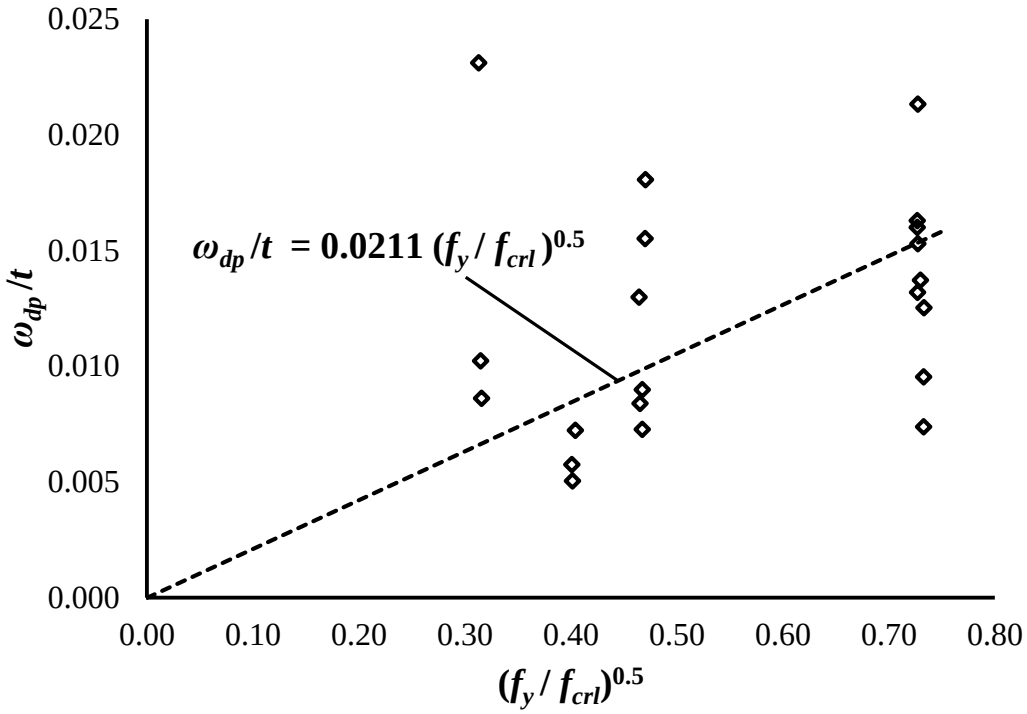

Figure 5.8: Interrelationship between ω_{dp}/t and $(f_y/f_{crl})^{0.5}$ for estimation of γ for perforated columns

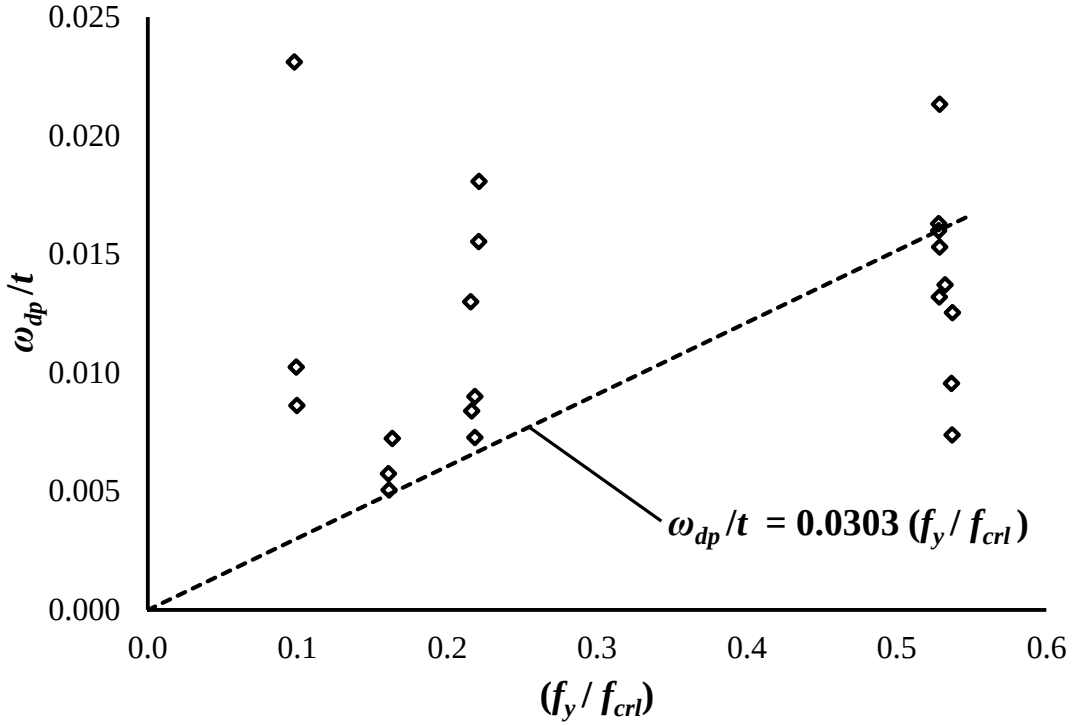

Figure 5.9: Interrelationship between ω_{dp}/t and $\left(f_y / f_{crl}\right)$ for estimation of β for perforated columns

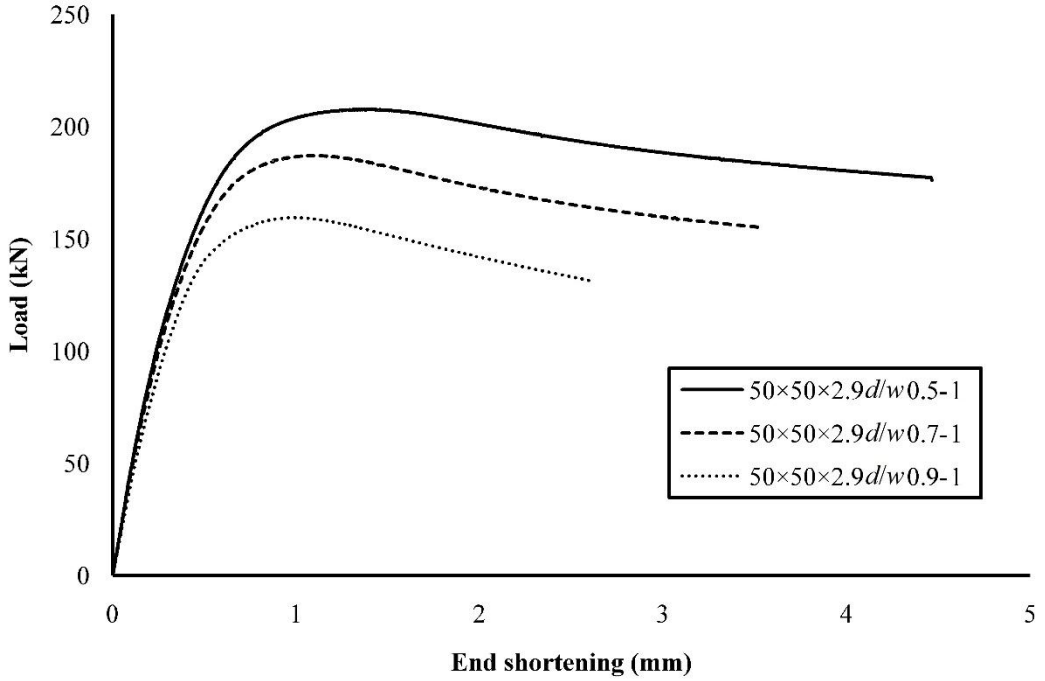

Figure 5.10: Load-end shortening curves for different (d/w) ratios of 50 × 50 × 2.9 cross-sections

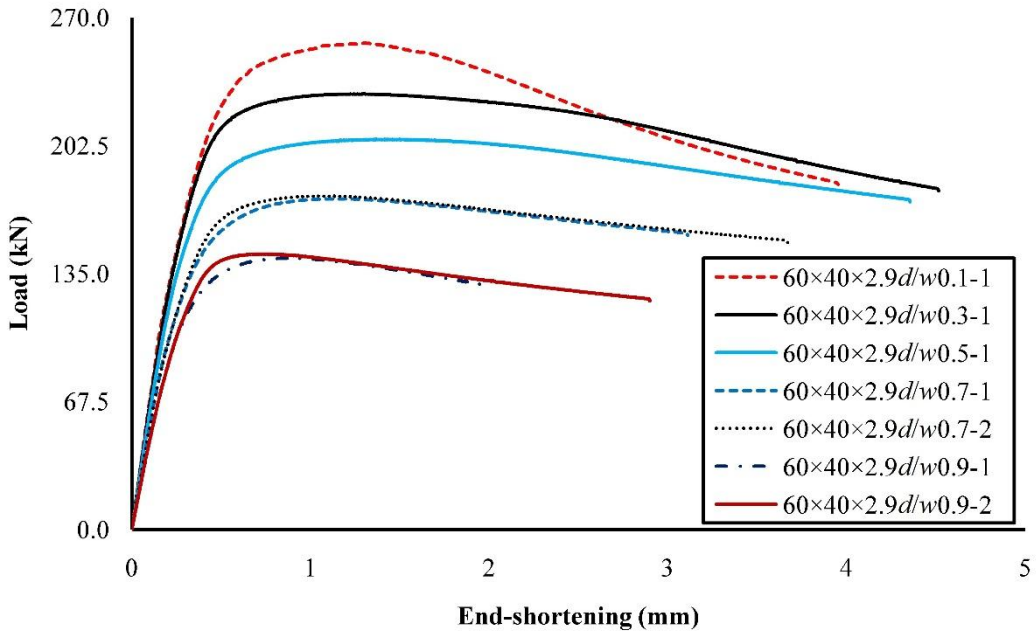

Figure 5.11: Load-end shortening curves for different (d/w) ratios of 60 × 40 × 2.9 cross-sections

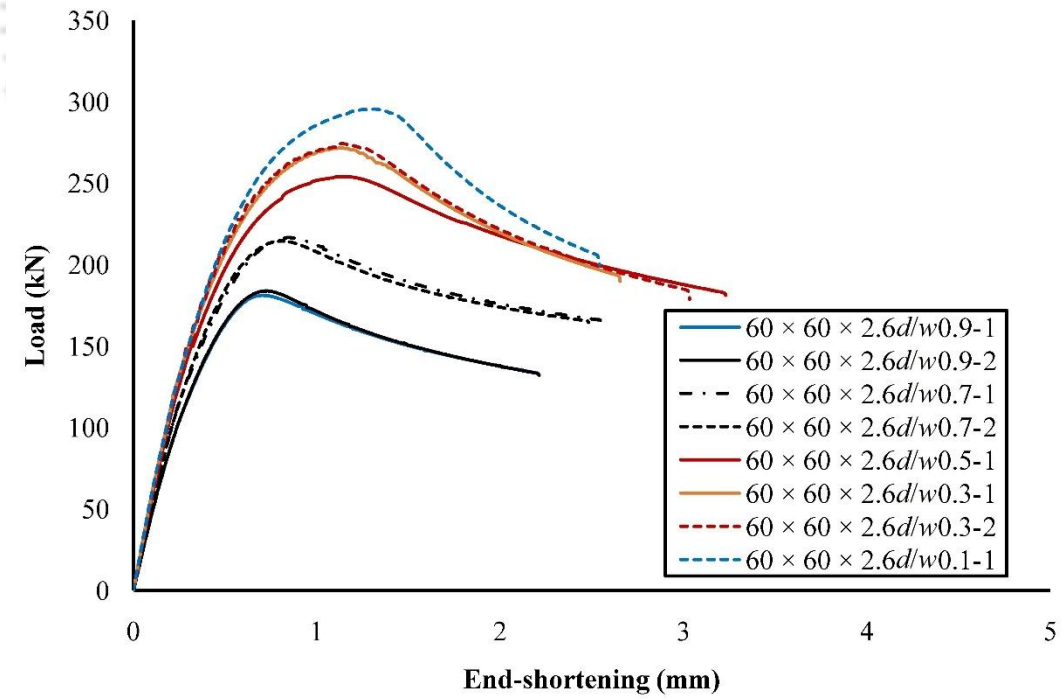

Figure 5.12: Load-end shortening curves for different (d/w) ratios of 60×60×2.6 cross-sections

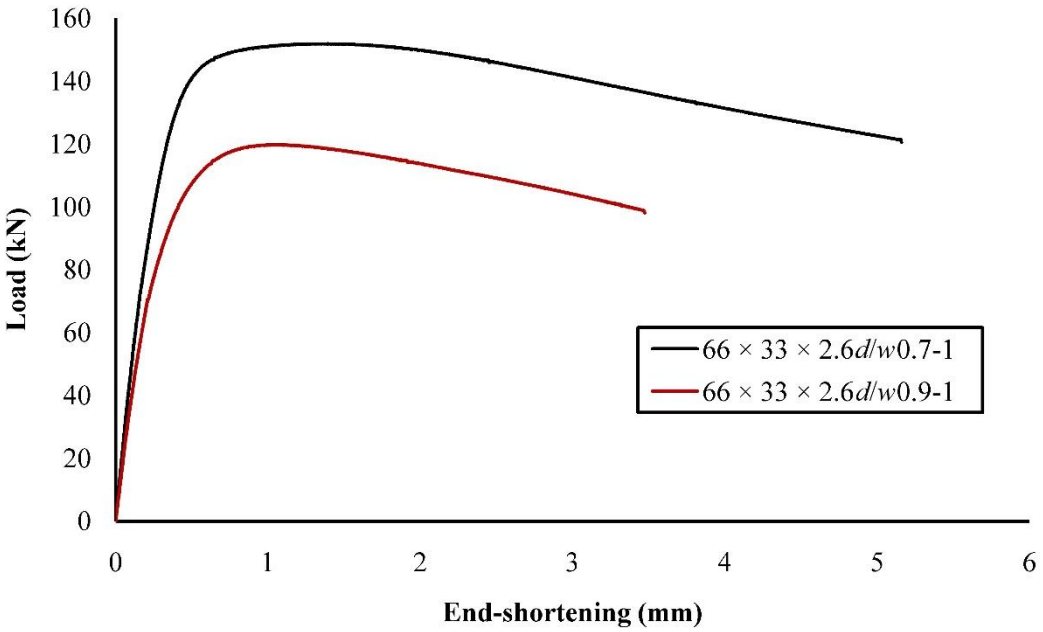

Figure 5.13: Load-end shortening curves for different (*d*/*w*) ratios of 66×33×2.6 cross-sections

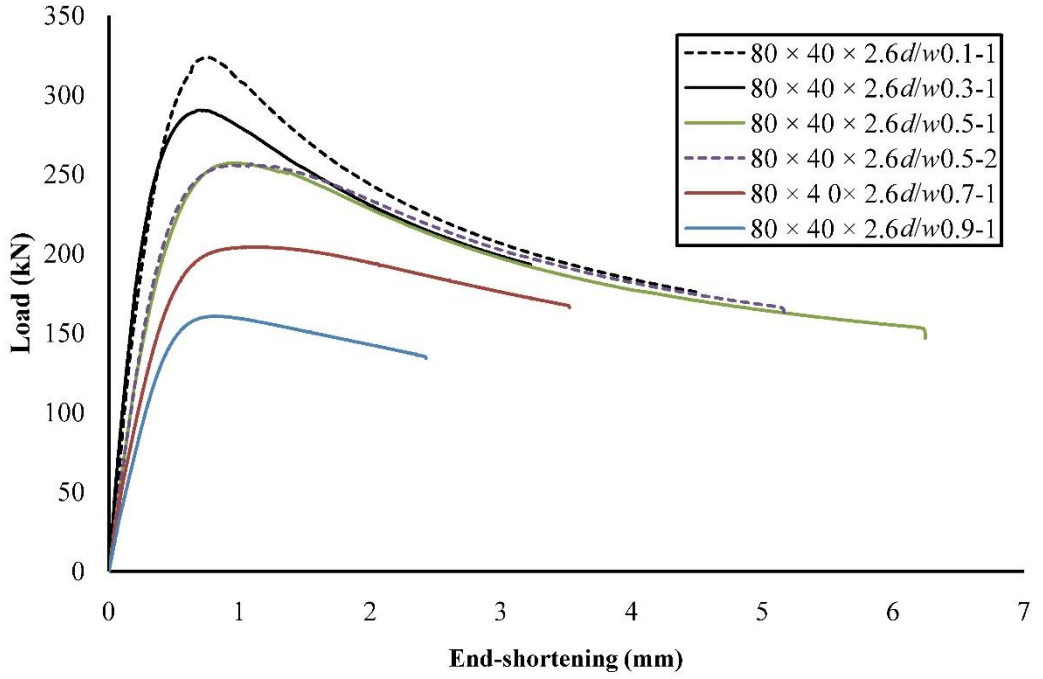

Figure 5.14: Load-end shortening curves for different (*d*/*w*) ratios of 80 × 40 × 2.6 cross-sections

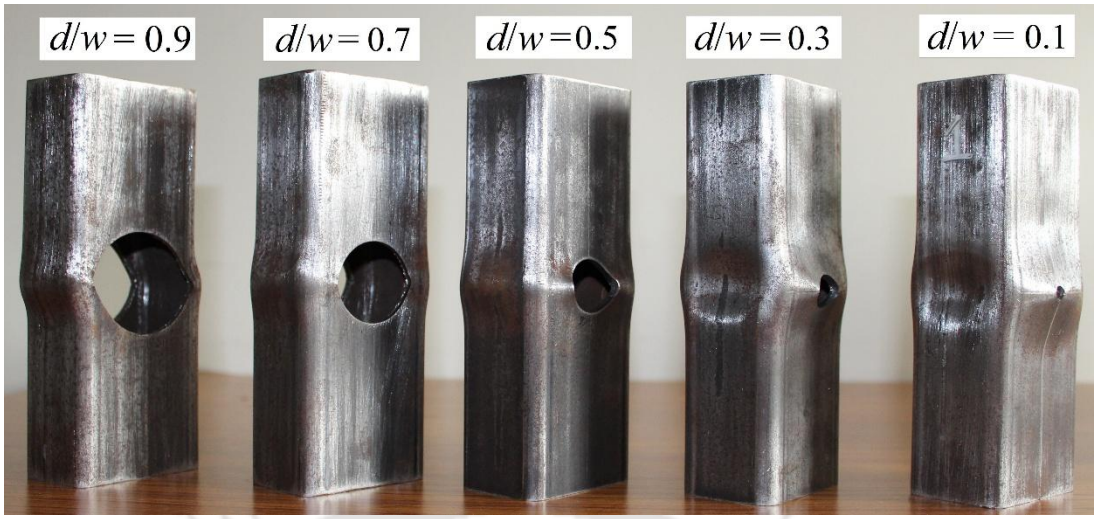

Figure 5.15: Deformed shapes of 60 × 40 × 2.6 with different hole to width size (*d*/*w*) ratio ranging from 0.1–0.9

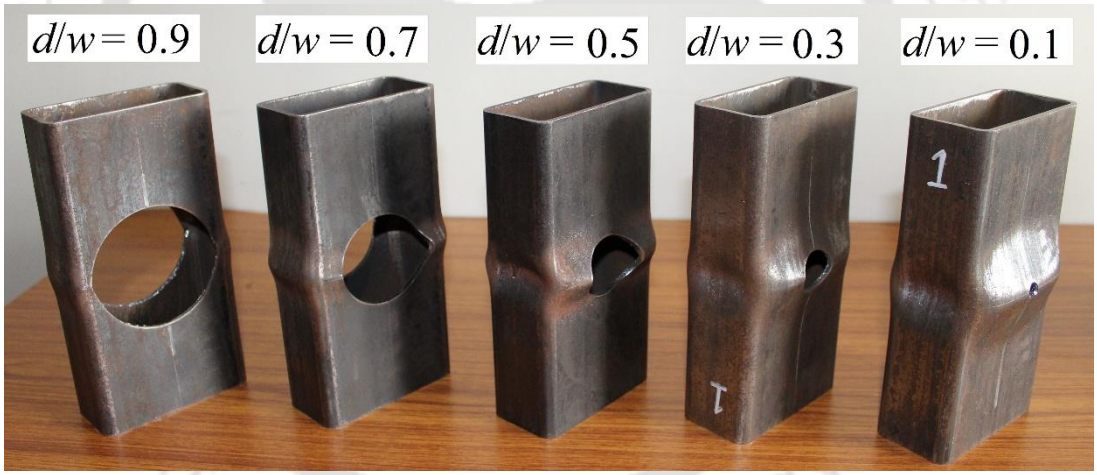

Figure 5.16: Deformed shapes of 80 × 40 × 2.6 with different hole to width size (*d*/*w*) ratio ranging from 0.1–0.9

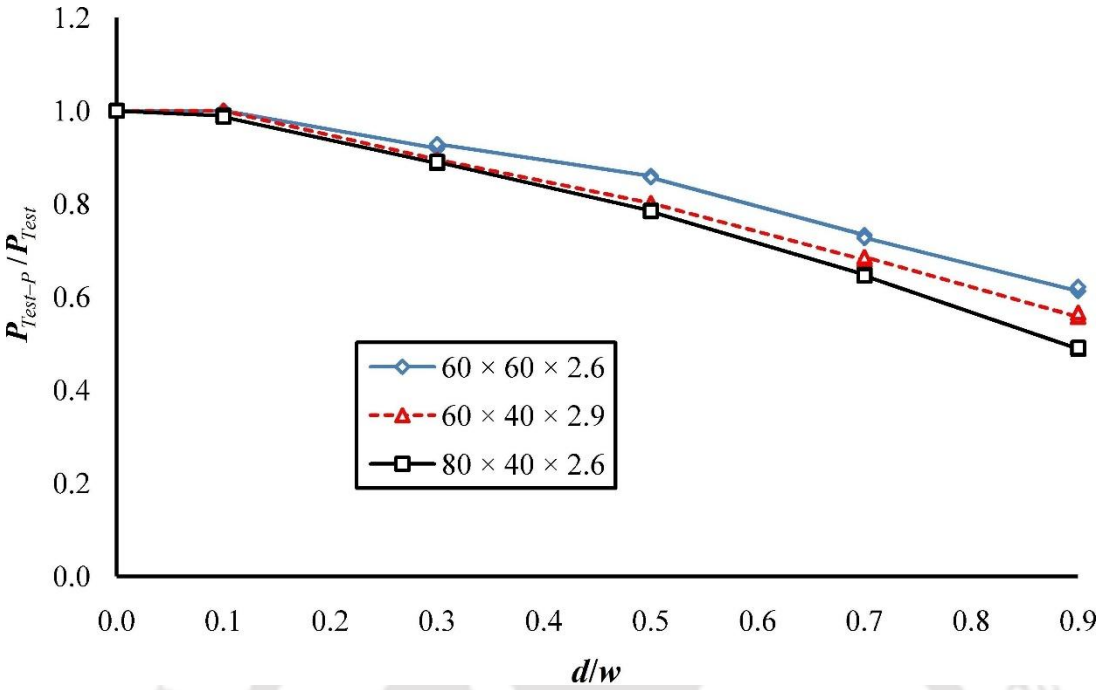

Figure 5.17: Influence of opening size on column strength for three cross-sections: 60 × 60 × 2.6, 60 × 40 × 2.9 and 80 × 40 × 2.6

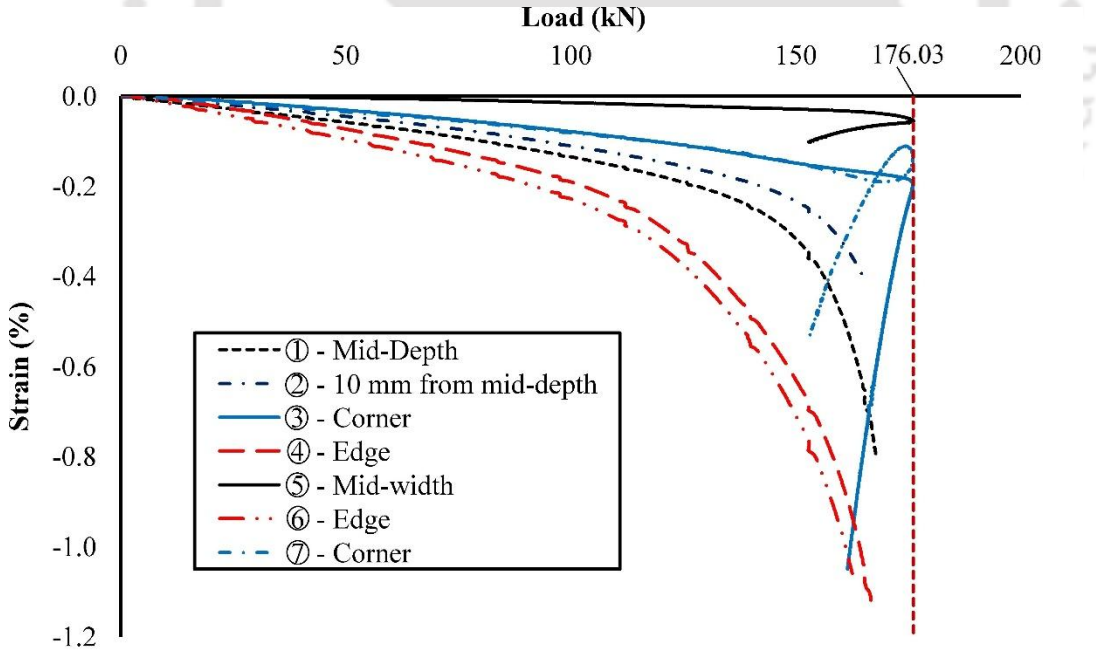

Figure 5.18: Axial strain distribution at perforation locations for stub column, 60 × 40 × 2.9*d*/*w*0.7-2

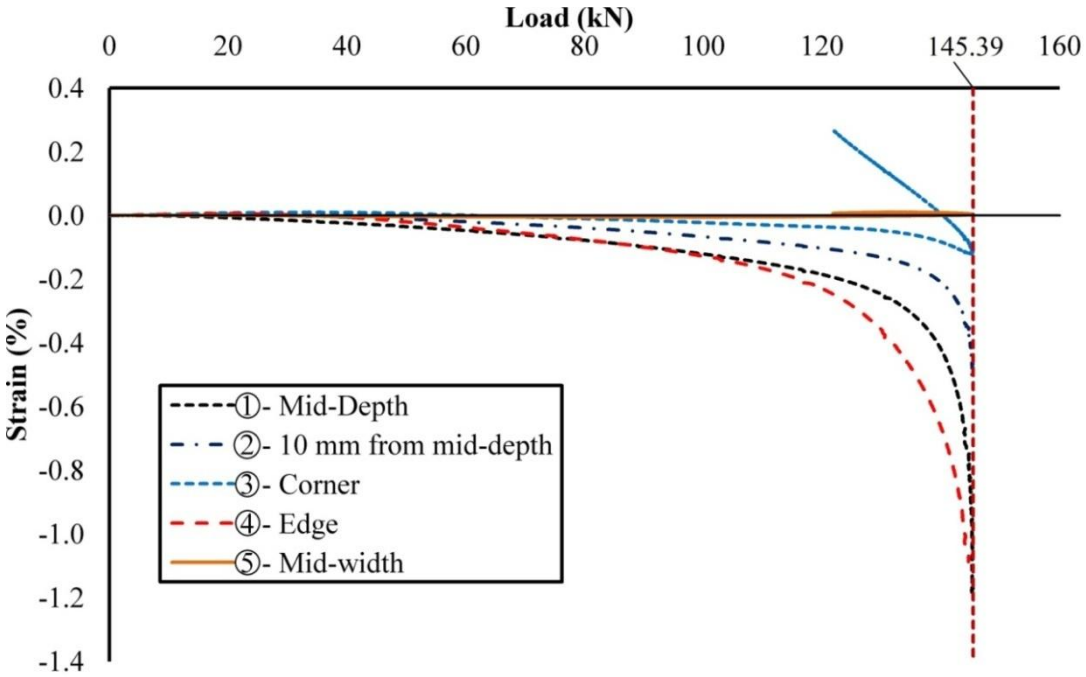

Figure 5.19: Axial strain distribution at perforation locations for stub column, 60 × 40 × 2.9*d*/*w*0.9-2

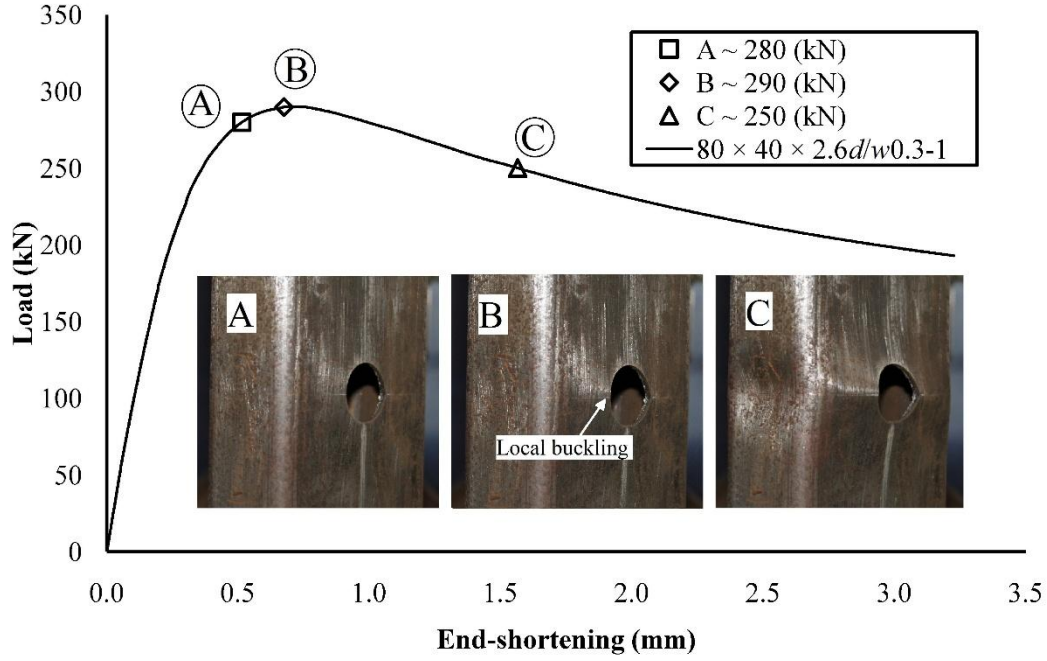

Figure 5.20: Load-end shortening curve and deformation at mid-height of 80 × 80 × 2.6*d*/*w*0.3-1 at various load levels: (A) before ultimate load (~ 280 kN), (B) at ultimate load (~ 290 kN) and (C) after ultimate load (~ 250 kN)

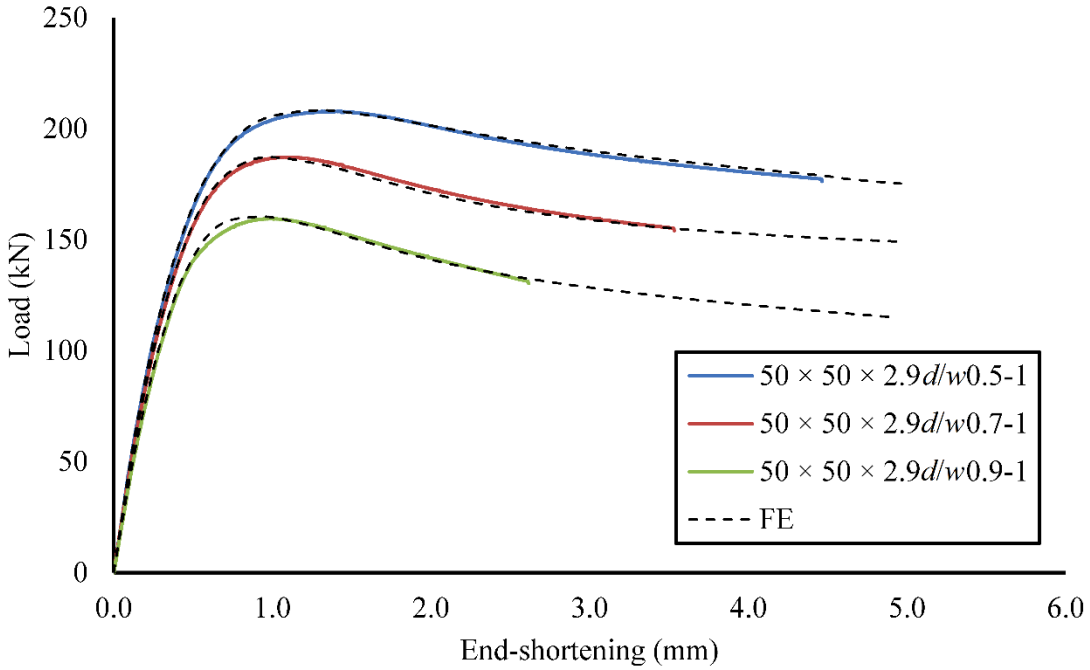

Figure 5.21: Comparison of Test and finite element (FE) load end-shortening curves for 50 × 50 × 2.9 cross-section

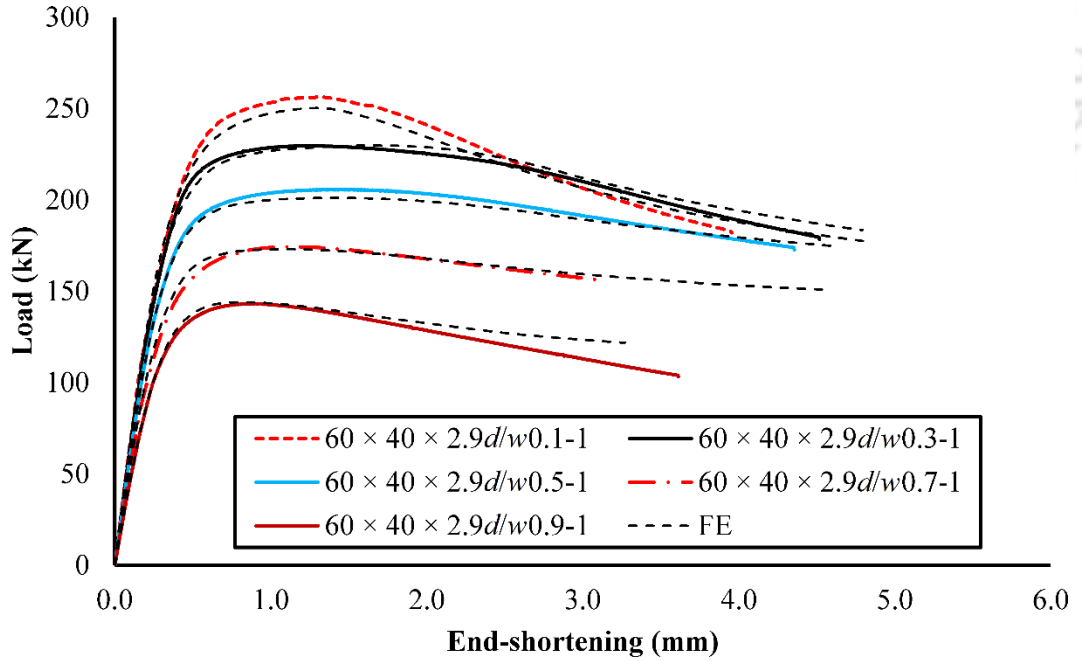

Figure 5.22: Comparison of Test and finite element (FE) load end-shortening curves for 60 × 40 × 2.9 cross-section

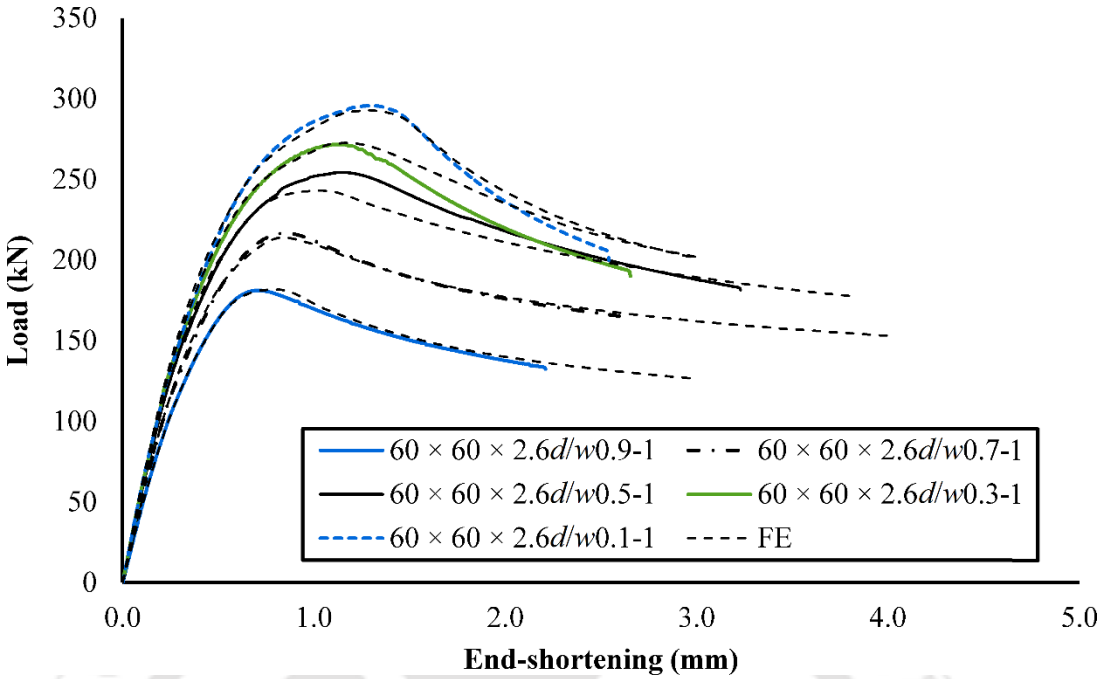

Figure 5.23: Comparison load end-shortening curves generated from experiment and FE of 60 × 60 ×2.6 cross-section stub column.

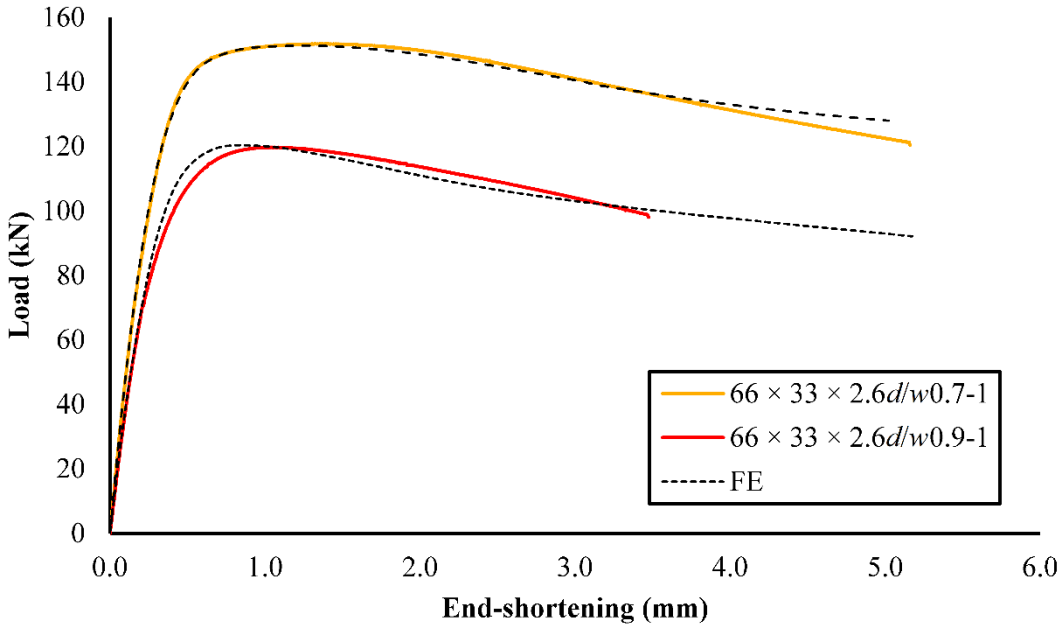

Figure 5.24: Comparison load end-shortening curves generated from experiment and FE of 66 × 33 ×2.6 cross-section stub column.

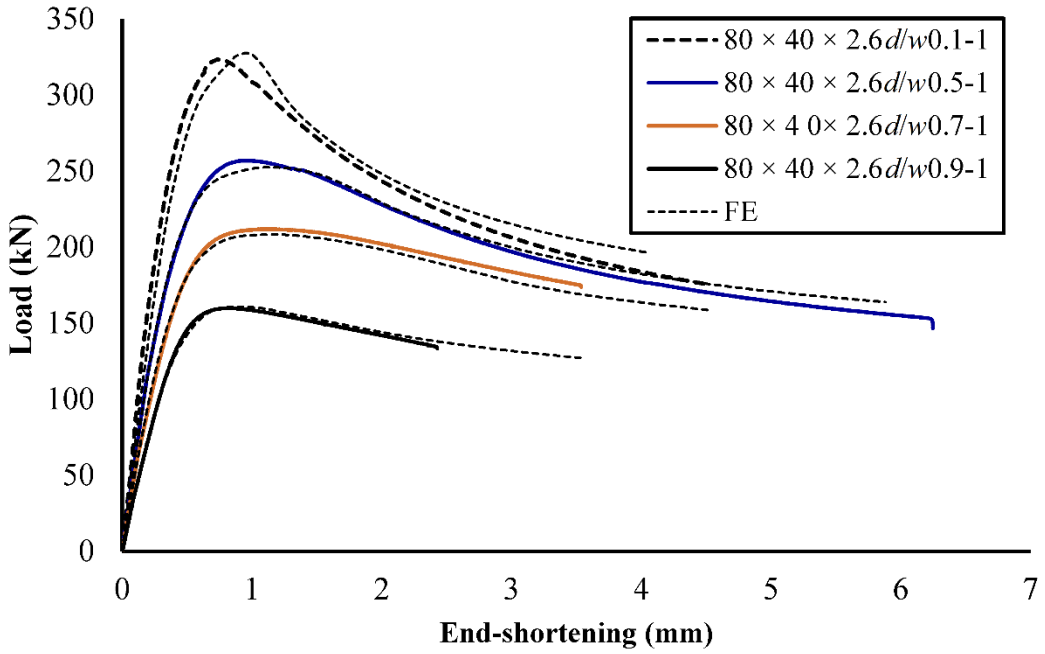

Figure 5.25: Comparison load end-shortening curves generated from experiment and FE of 80 × 40 ×2.6 cross-section stub column.

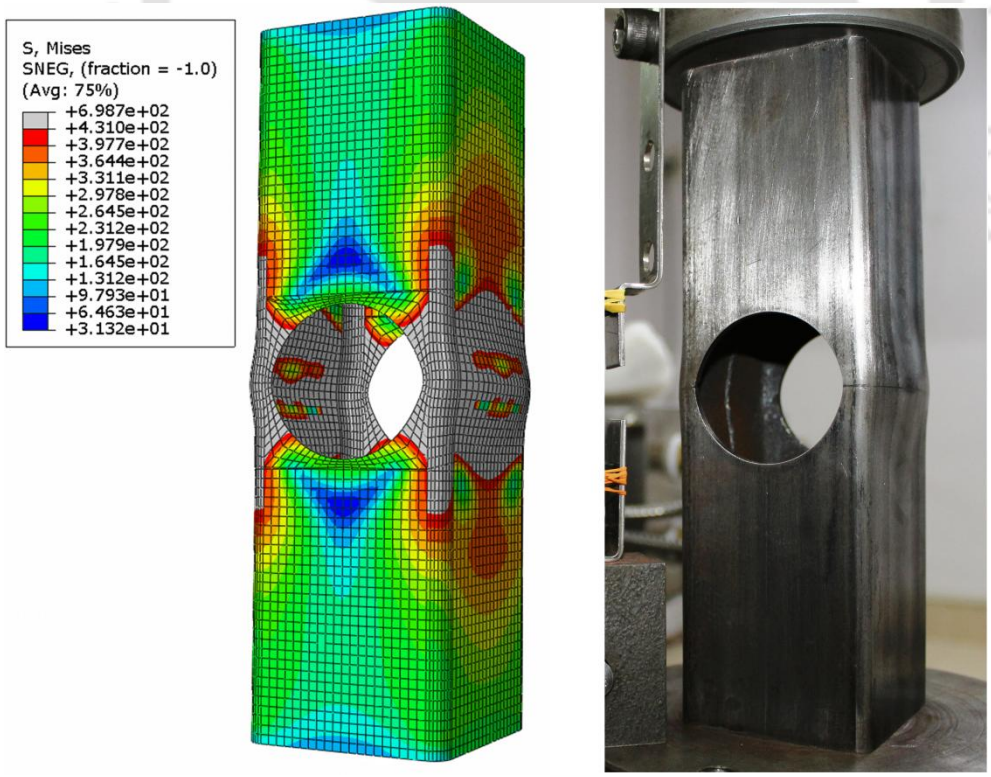

Figure 5.26: Comparison of post-ultimate deformed shapes – FE model and tested specimen for 60 × 60 × 2.6*d*/*w*0.9-1

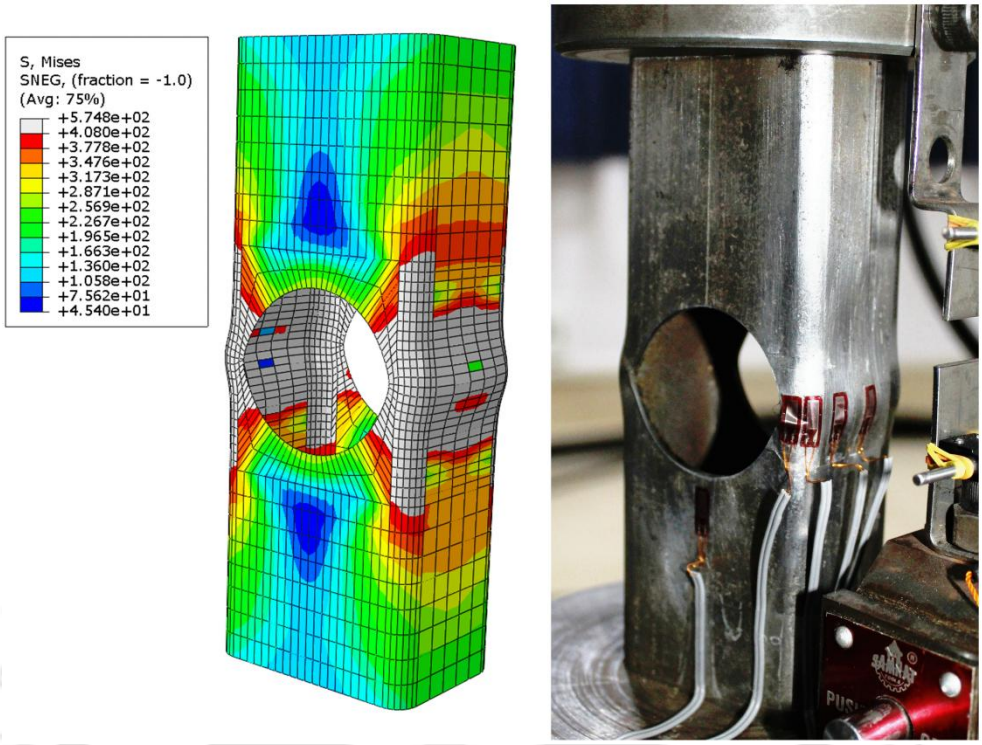

Figure 5.27: Comparison of post-ultimate deformed shapes – FE model and tested specimen for 60 × 40 × 2.9*d*/*w*0.9-2

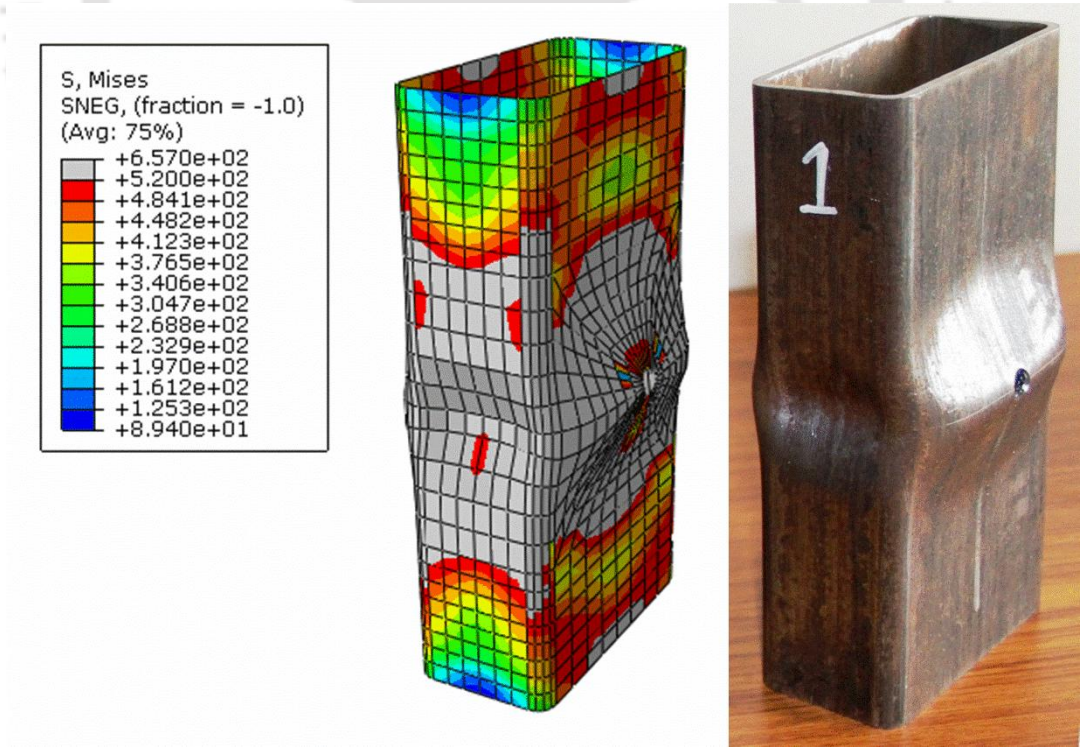

Figure 5.28: Comparison of post-ultimate deformed shapes – FE model and tested specimen for 80 × 40 × 2.6*d*/*w*0.1-1

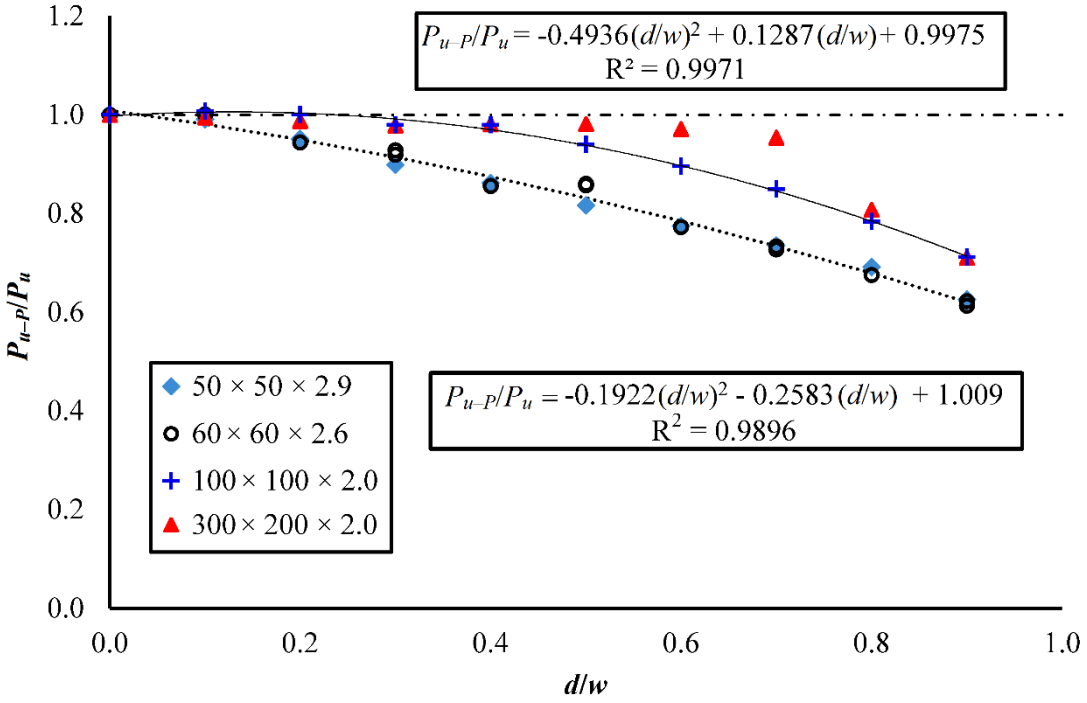

Figure 5.29: Normalized ultimate load capacities for columns with different perforation (d/w) ratios.

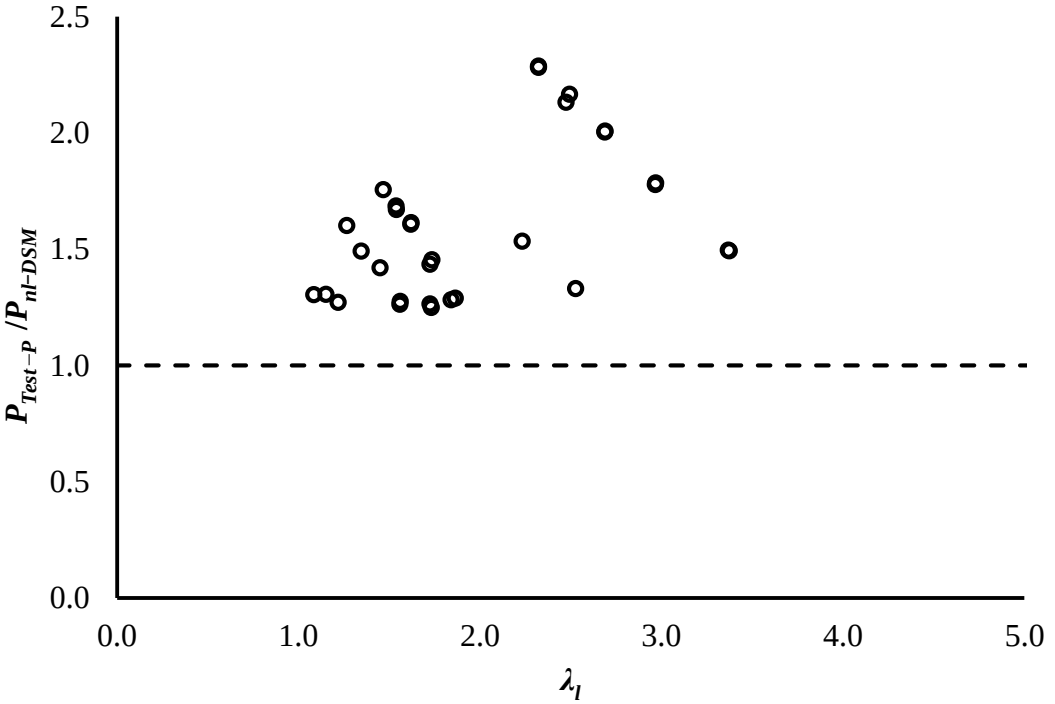

Figure 5.30: Assessment of AISI S100 (2016) DSM prediction with test results

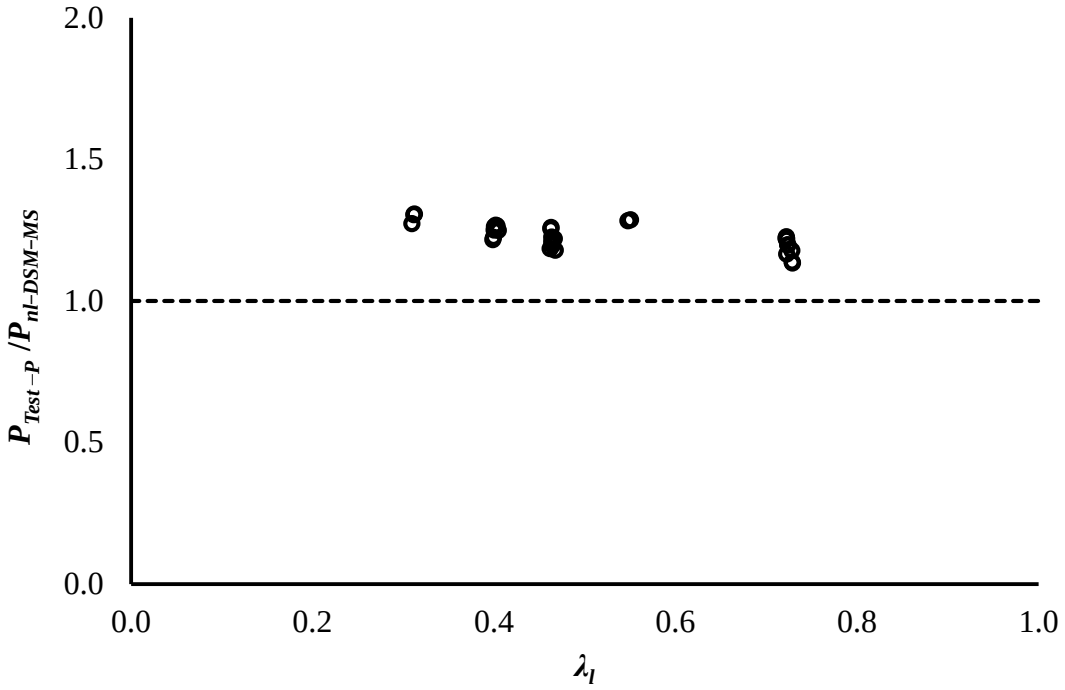

Figure 5.31: Assessment of AISI DSM (2016) prediction using critical elastic buckling stress by Moen and Schafer (2009) with test results.

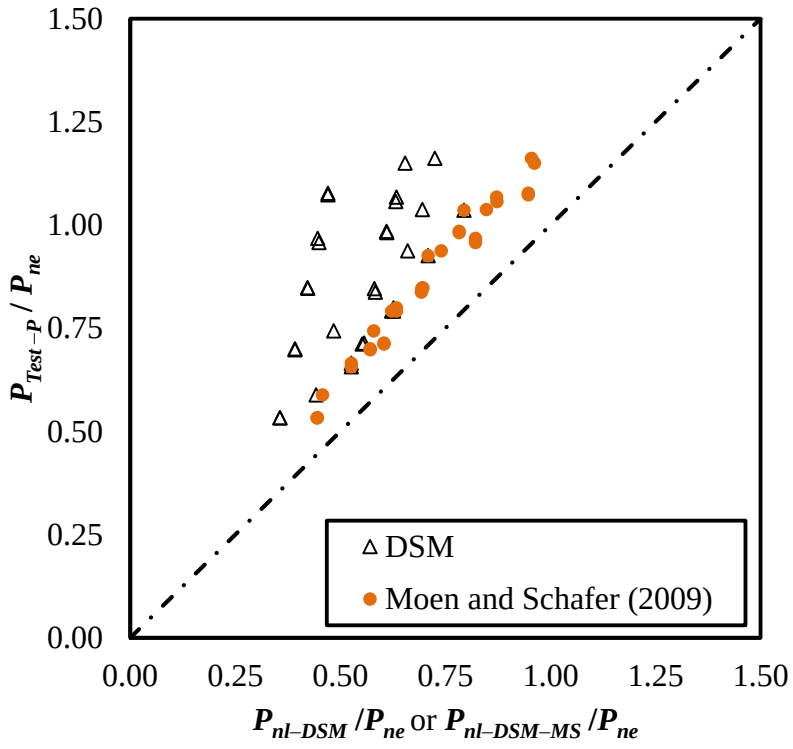

Figure 5.32: Assessment of DSM in AISI S100 (2016) and DSM with critical elastic buckling stress by Moen and Schafer (2009) predictions against the test results

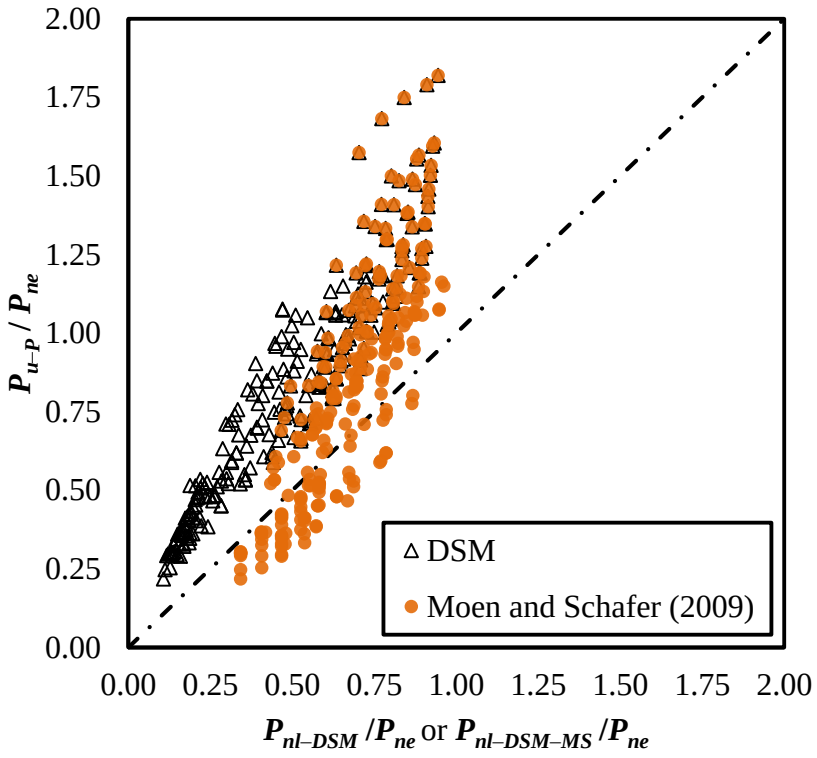

Figure 5.33: Assessment of AISI DSM (2016) prediction with test and FE column capacities

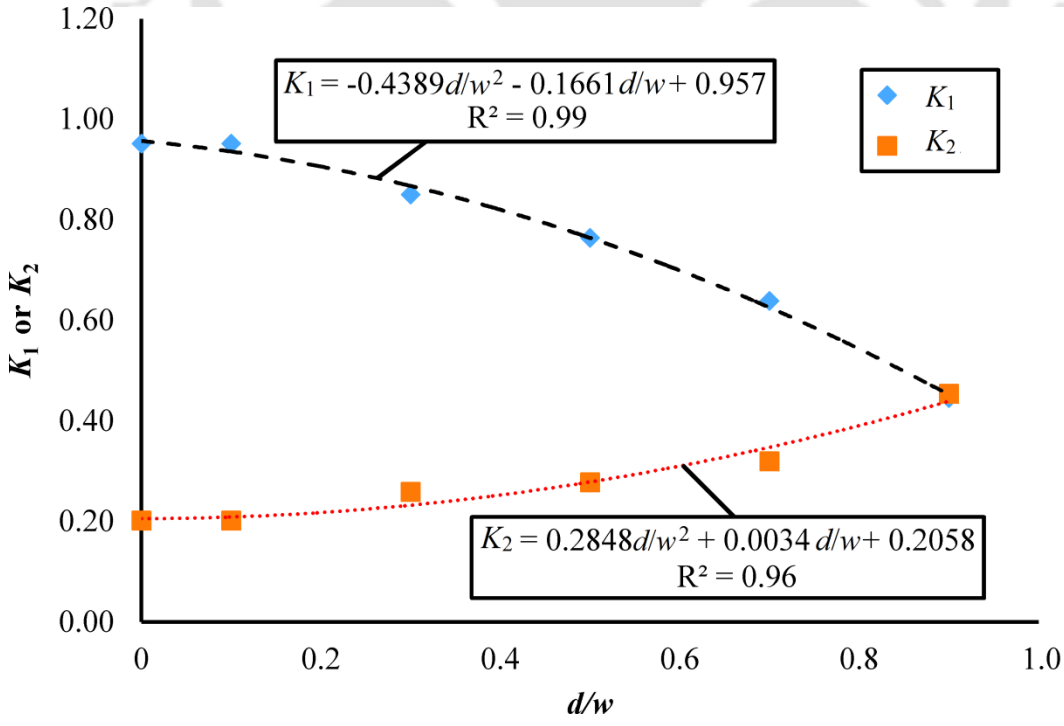

Figure 5.34: Relationship between K_1 and K_2 coefficients against perforation size ratio, d/w

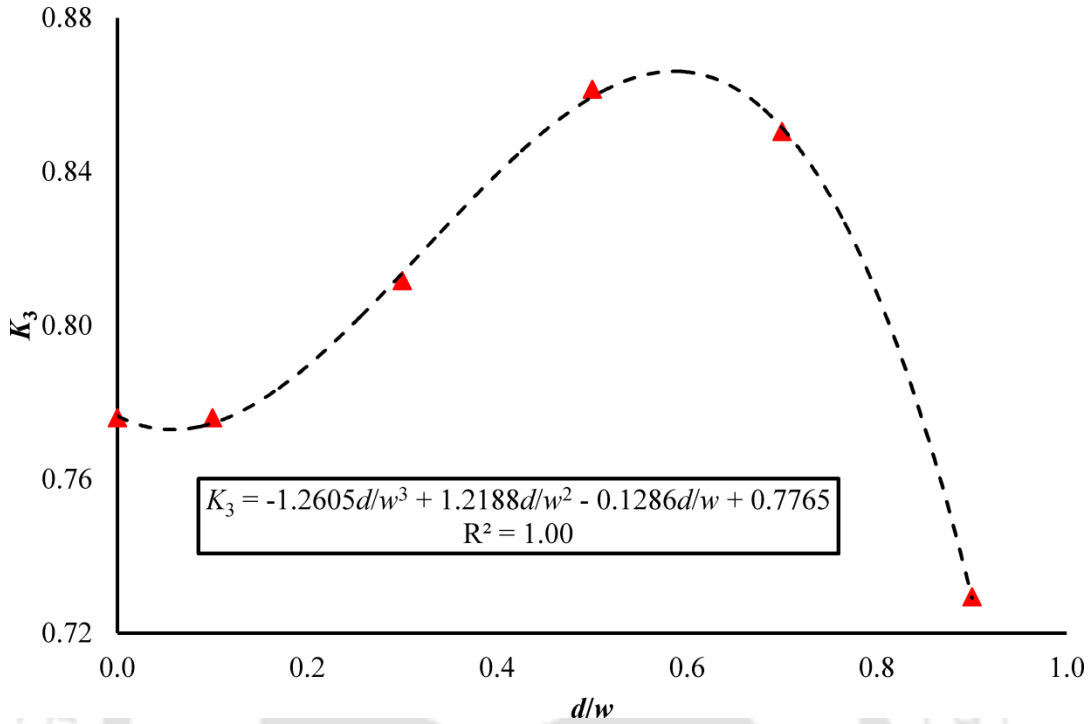

Figure 5.35: Relationship between K_3 and perforation size ratio, d/w

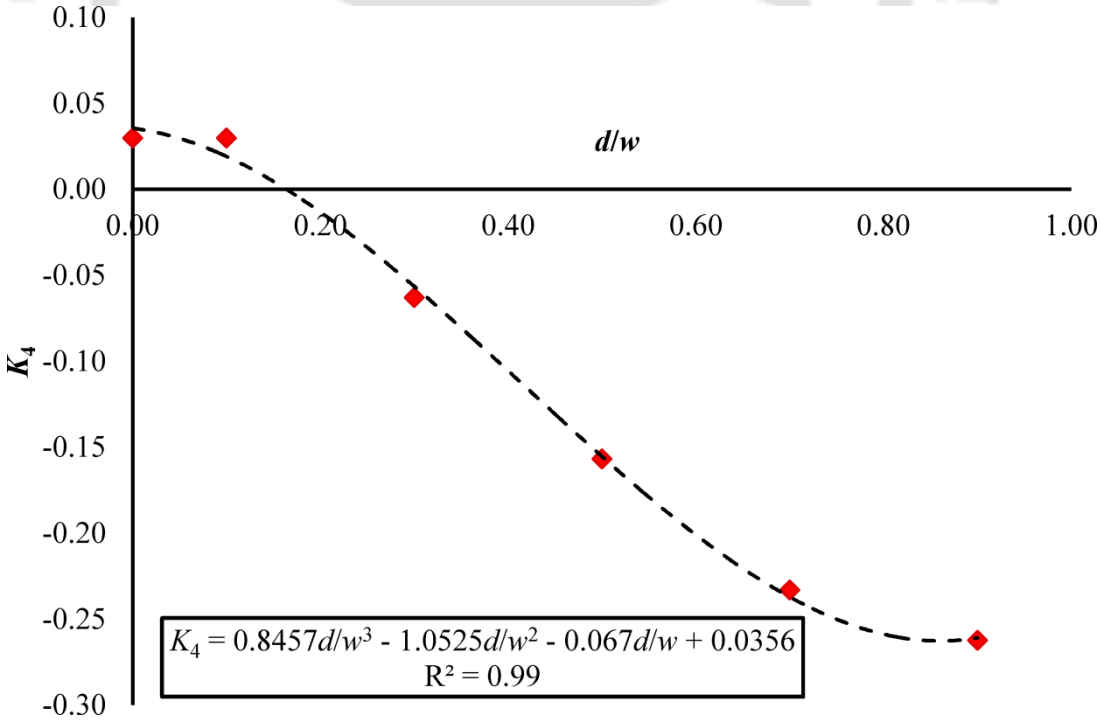

Figure 5.36: Relationship between K_4 and perforation size ratio, d/w

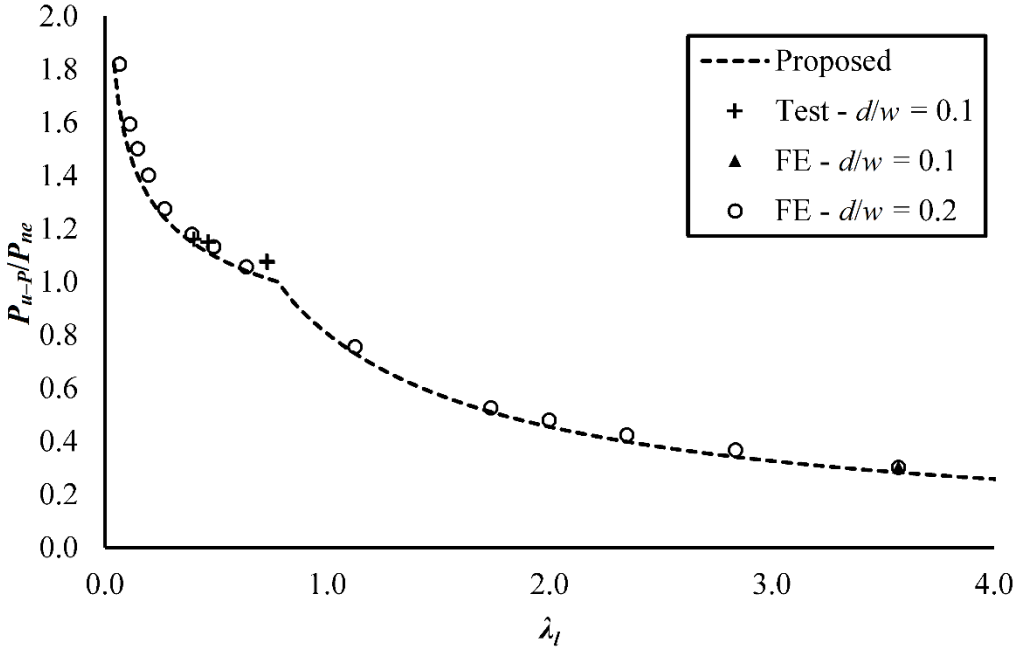

Figure 5.37: Assessment of unperforated design curve against the ultimate capacities of cold-formed steel stub columns having perforations with size ratio, *d*/*w* up to 0.2

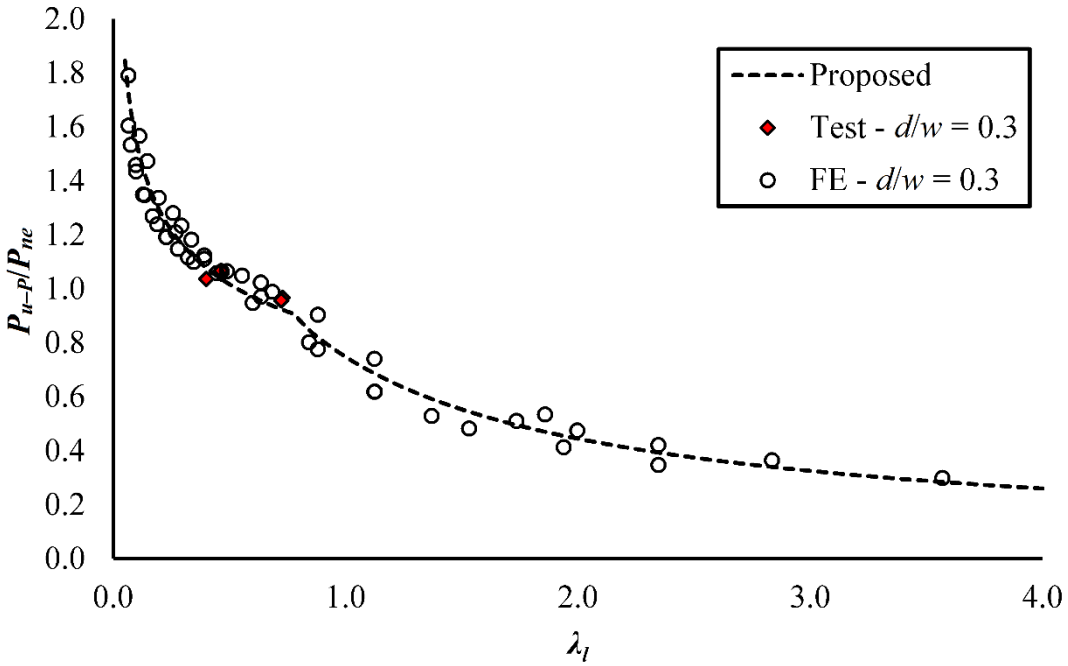

Figure 5.38: Assessment of proposed design curve for perforated cold-formed steel stub columns having perforations *d*/*w* up to 0.3

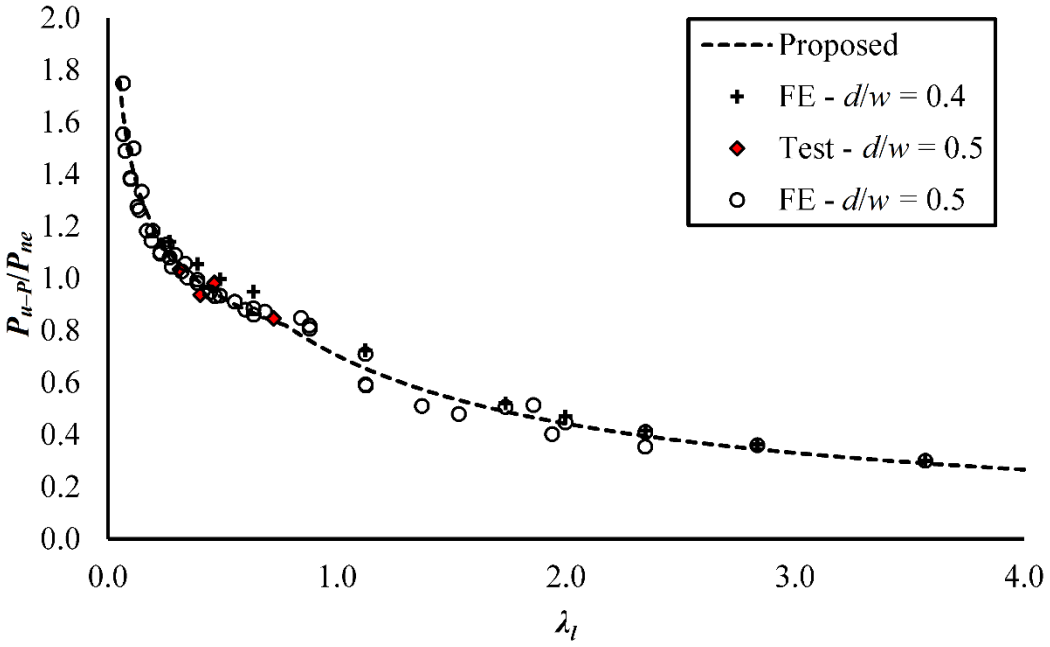

Figure 5.39: Assessment of proposed design curve for perforated cold-formed steel stub columns having perforations *d*/*w* up to 0.5

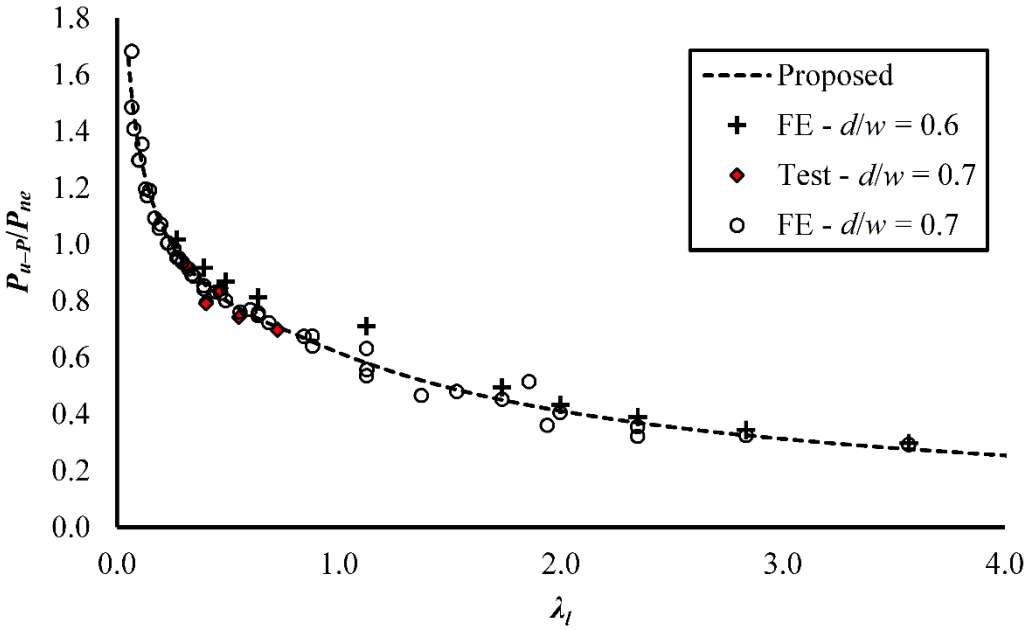

Figure 5.40: Assessment of proposed design curve for perforated cold-formed steel stub columns having perforations *d*/*w* up to 0.7

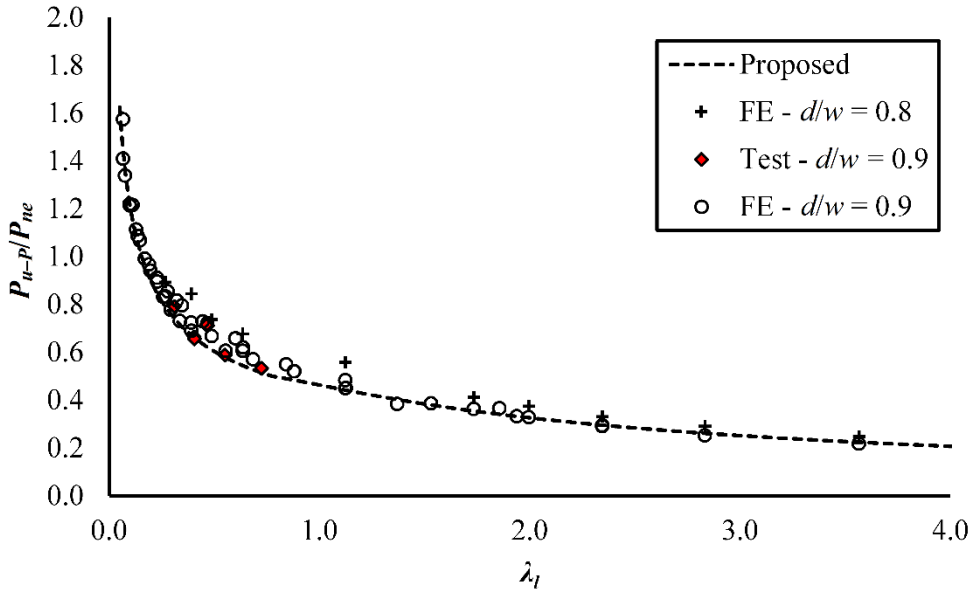

Figure 5.41: Assessment of proposed design curve for perforated cold-formed steel stub columns having perforations *d*/*w* up to 0.9

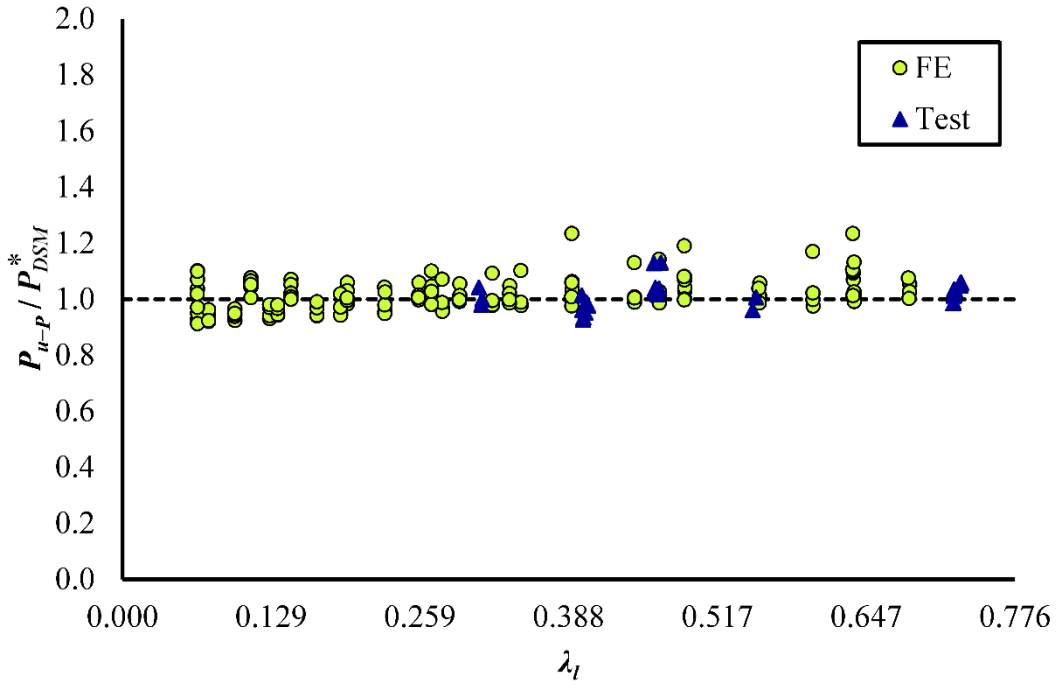

Figure 5.42: Comparison of test and numerical perforated column capacities with design predictions for $\lambda_l \leq 0.776$

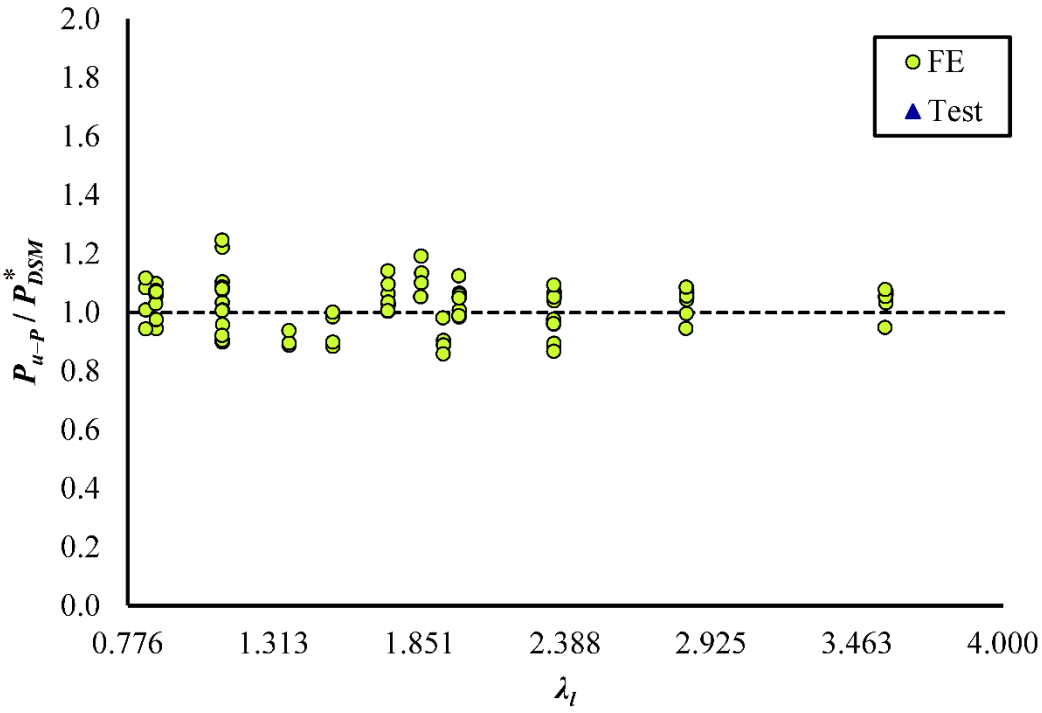

Figure 5.43: Comparison of test and numerical perforated column capacities with design predictions for $\lambda_l > 0.776$

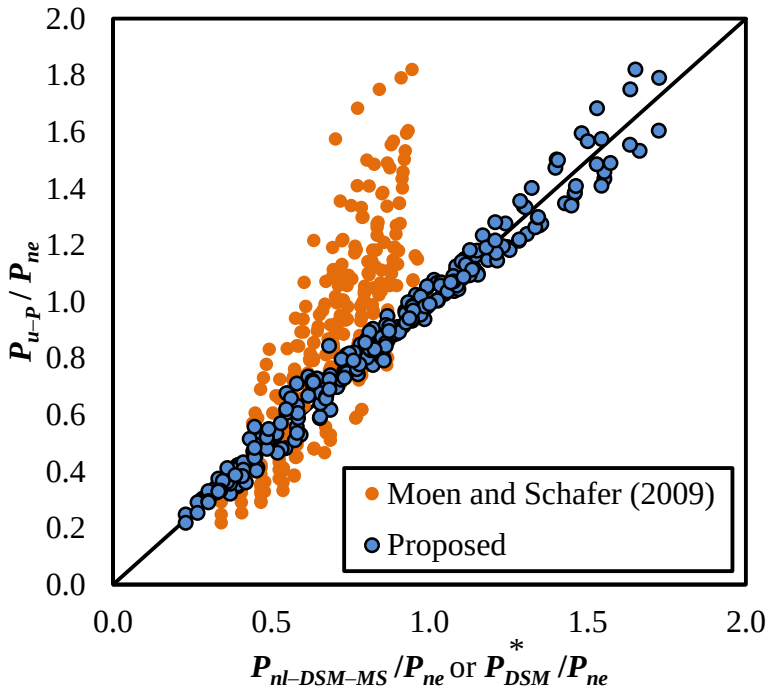

Figure 5.44: Assessment of DSM in AISI S100 (2016) prediction using critical elastic buckling stress by Moen and Schafer (2009) and proposed modified DSM prediction against the test and FE result

Table 5.1: Section dimensions of stub columns

Cross-sections	B (mm)	D (mm)	t (mm)	L (mm)	r_i (mm)	w (mm)	d (mm)	d/w	w/t
50 × 50 × 2.9d/w0.5-1	49.56	49.82	2.89	200.20	2.9	37.98	19.2	0.51	13.1
50 × 50 × 2.9d/w0.7-1	49.82	49.88	2.90	199.96	2.9	38.22	26.9	0.70	13.2
50 × 50 × 2.9d/w0.9-1	49.62	49.82	2.91	200.36	2.9	38.00	34.6	0.91	13.1
60 × 60 × 2.6d/w0.1-1	60.00	60.10	2.61	200.00	2.6	48.98	5.00	0.10	18.8
60 × 60 × 2.6d/w0.3-1	60.00	60.10	2.61	200.22	2.6	48.98	14.9	0.30	18.8
60 × 60 × 2.6d/w0.3-2	59.90	60.12	2.61	200.10	2.6	48.88	14.9	0.30	18.7
60 × 60 × 2.6d/w0.5-1	60.04	60.08	2.62	199.96	2.6	49.00	24.8	0.51	18.7
60 × 60 × 2.6d/w0.5-2	60.00	60.10	2.62	200.00	2.6	48.96	24.8	0.51	18.7
60 × 60 × 2.6d/w0.7-1	60.00	60.18	2.60	199.94	2.6	49.00	34.7	0.71	18.8
60 × 60 × 2.6d/w0.7-2	59.92	60.12	2.61	200.08	2.6	48.90	34.7	0.71	18.7
60 × 60 × 2.6d/w0.9-1	59.94	60.00	2.59	200.00	2.6	48.96	44.6	0.91	18.9
60 × 60 × 2.6d/w0.9-2	59.94	60.00	2.62	200.00	2.6	48.90	44.6	0.91	18.7
60 × 40 × 2.9d/w0.1-1	60.13	40.13	2.91	160.23	2.9	48.51	4.80	0.10	16.7
60 × 40 × 2.9d/w0.3-1	60.18	40.28	2.91	160.06	2.9	48.56	14.5	0.30	16.7
60 × 40 × 2.9d/w0.5-1	60.14	40.16	2.89	160.10	2.9	48.56	24.2	0.50	16.8
60 × 40 × 2.9d/w0.7-1	60.11	40.30	2.90	160.10	2.9	48.51	33.9	0.70	16.7
60 × 40 × 2.9d/w0.7-2	60.16	40.21	2.90	160.22	2.9	48.56	33.9	0.70	16.7
60 × 40 × 2.9d/w0.9-1	60.11	40.22	2.87	159.32	2.9	48.57	43.6	0.90	16.9
60 × 40 × 2.9d/w0.9-2	60.14	40.23	2.88	160.30	2.9	48.56	43.6	0.90	16.8
66 × 33 × 2.6d/w0.7-1	66.34	33.38	2.57	132.34	2.6	55.40	38.9	0.70	21.6
66 × 33 × 2.6d/w0.9-1	66.44	33.40	2.56	130.40	2.6	55.52	50.0	0.90	21.7
80 × 40 × 2.6d/w0.1-1	80.78	39.32	2.59	160.04	2.6	69.80	7.00	0.10	26.9
80 × 40 × 2.6d/w0.1-2	80.80	39.40	2.59	160.04	2.6	69.82	7.00	0.10	27.0

Table 5.1: (Continued) Section dimensions of stub columns

Cross-sections	B (mm)	D (mm)	t (mm)	L (mm)	r_i (mm)	w (mm)	d (mm)	d/w	w/t
80 × 40 × 2.6d/w0.3-1	80.80	39.44	2.61	160.06	2.6	69.78	20.9	0.30	26.7
80 × 40 × 2.6d/w0.3-2	80.76	39.52	2.59	160.06	2.6	69.78	20.9	0.30	26.9
80 × 40 × 2.6d/w0.5-1	80.82	39.40	2.61	160.00	2.6	69.80	34.8	0.50	26.7
80 × 40 × 2.6d/w0.5-2	80.78	39.42	2.61	160.14	2.6	69.76	34.8	0.50	26.7
80 × 40 × 2.6d/w0.7-1	80.82	39.48	2.61	161.50	2.6	69.80	48.7	0.70	26.7
80 × 40 × 2.6d/w0.7-2	80.78	39.56	2.61	160.10	2.6	69.76	48.7	0.70	26.7
80 × 40 × 2.6d/w0.9-1	80.76	39.34	2.60	161.22	2.6	69.76	62.6	0.90	26.8
80 × 40 × 2.6d/w0.9-2	80.72	39.56	2.60	160.10	2.6	69.72	62.6	0.90	26.8

Table 5.2: Summary of measured local geometric imperfection for unperforated stub columns

Cross-sections	*Imperfection amplitude in average deviation* (mm)				
	Face-1	*Face*-2	*Face*-3	*Face*-4	*Mean*
50 × 50 × 2.9*d*/*w*0.5-1	0.061	0.029	0.015	0.004	0.027
50 × 50 × 2.9*d*/*w*0.7-1	0.034	0.032	0.033	0.008	0.027
50 × 50 × 2.9*d*/*w*0.9-1	0.069	0.015	0.010	0.021	0.029
60 × 60 × 2.6*d*/*w*0.1-1	0.028	0.008	0.032	0.015	0.021
60 × 60 × 2.6*d*/*w*0.3-1	0.008	0.015	0.031	0.034	0.022
60 × 60 × 2.6*d*/*w*0.5-1	0.037	0.004	0.021	0.015	0.019
60 × 60 × 2.6*d*/*w*0.7-1	0.020	0.005	0.006	0.055	0.022
60 × 60 × 2.6*d*/*w*0.9-1	0.057	0.005	0.019	0.033	0.029
60 × 60 × 2.6*d*/*w*0.9-2	0.015	0.069	0.040	0.017	0.035
60 × 40 × 2.9*d*/*w*0.1-1	0.044	0.066	0.005	0.021	0.034
60 × 40 × 2.9*d*/*w*0.3-1	0.063	0.001	0.059	0.035	0.040
60 × 40 × 2.9*d*/*w*0.5-1	0.021	0.020	0.028	0.020	0.022
80 × 40 × 2.6*d*/*w*0.1-1	0.020	0.043	0.027	0.003	0.023
80 × 40 × 2.6*d*/*w*0.1-2	0.073	0.032	0.014	0.017	0.034
80 × 40 × 2.6*d*/*w*0.3-1	0.010	0.004	0.033	0.018	0.016
80 × 40 × 2.6*d*/*w*0.3-2	0.076	0.027	0.061	0.021	0.046
80 × 40 × 2.6*d*/*w*0.5-1	0.012	0.010	0.039	0.003	0.016
80 × 40 × 2.6*d*/*w*0.5-2	0.009	0.009	0.007	0.039	0.016
80 × 40 × 2.6*d*/*w*0.7-1	0.089	0.031	0.022	0.017	0.040
80 × 40 × 2.6*d*/*w*0.7-2	0.034	0.006	0.022	0.019	0.020
80 × 40 × 2.6*d*/*w*0.9-1	0.022	0.003	0.043	0.016	0.021

Table 5.3: Summary of measured local geometric imperfection for perforated stub columns

Cross-sections	*Imperfection amplitude in average deviation* (mm)				
	Face-1	*Face*-2	*Face*-3	*Face*-4	*Mean*
50 × 50 × 2.9*d*/*w*0.5-1	0.027	0.030	0.038	0.006	0.025
50 × 50 × 2.9*d*/*w*0.7-1	0.026	0.027	0.038	0.027	0.030
50 × 50 × 2.9*d*/*w*0.9-1	0.003	0.029	0.103	0.133	0.067
60 × 60 × 2.6*d*/*w*0.1-1	0.009	0.011	0.064	0.010	0.023
60 × 60 × 2.6*d*/*w*0.3-1	0.022	0.028	0.013	0.013	0.019
60 × 60 × 2.6*d*/*w*0.5-1	0.015	0.015	0.034	0.024	0.022
60 × 60 × 2.6*d*/*w*0.7-1	0.020	0.055	0.036	0.051	0.040
60 × 60 × 2.6*d*/*w*0.9-1	0.051	0.078	0.020	0.038	0.047
60 × 60 × 2.6*d*/*w*0.9-2	0.050	0.060	0.000	0.025	0.034
60 × 40 × 2.9*d*/*w*0.1-1	0.014	0.006	0.035	0.012	0.017
60 × 40 × 2.9*d*/*w*0.3-1	0.003	0.031	0.022	0.002	0.015
60 × 40 × 2.9*d*/*w*0.5-1	0.030	0.022	0.018	0.013	0.021
80 × 40 × 2.6*d*/*w*0.1-1	0.046	0.011	0.014	0.005	0.019
80 × 40 × 2.6*d*/*w*0.1-2	0.023	0.048	0.037	0.022	0.032
80 × 40 × 2.6*d*/*w*0.3-1	0.012	0.011	0.072	0.043	0.034
80 × 40 × 2.6*d*/*w*0.3-2	0.037	0.027	0.013	0.021	0.025
80 × 40 × 2.6*d*/*w*0.5-1	0.083	0.031	0.044	0.002	0.040
80 × 40 × 2.6*d*/*w*0.5-2	0.065	0.021	0.026	0.054	0.042
80 × 40 × 2.6*d*/*w*0.7-1	0.112	0.023	0.042	0.045	0.056
80 × 40 × 2.6*d*/*w*0.7-2	0.059	0.026	0.067	0.018	0.043
80 × 40 × 2.6*d*/*w*0.9-1	0.058	0.034	0.004	0.046	0.036

Table 5.4: Summary of measured local geometric imperfection for perforated stub columns

Cross-sections	*% increase in imperfection amplitude* $\frac{\omega_{dp}-\omega_{d}}{\omega_{d}}\times 100\%$
50 × 50 × 2.9*d*/*w*0.5-1	–7.31
50 × 50 × 2.9*d*/*w*0.7-1	10.82
50 × 50 × 2.9*d*/*w*0.9-1	132.68
60 × 60 × 2.6*d*/*w*0.1-1	12.98
60 × 60 × 2.6*d*/*w*0.3-1	–13.97
60 × 60 × 2.6*d*/*w*0.5-1	13.68
60 × 60 × 2.6*d*/*w*0.7-1	86.20
60 × 60 × 2.6*d*/*w*0.9-1	62.60
60 × 60 × 2.6*d*/*w*0.9-2	–3.61
60 × 40 × 2.9*d*/*w*0.1-1	–50.76
60 × 40 × 2.9*d*/*w*0.3-1	–62.90
60 × 40 × 2.9*d*/*w*0.5-1	–6.42
80 × 40 × 2.6*d*/*w*0.1-1	–18.63
80 × 40 × 2.6*d*/*w*0.1-2	–4.92
80 × 40 × 2.6*d*/*w*0.3-1	109.99
80 × 40 × 2.6*d*/*w*0.3-2	–46.48
80 × 40 × 2.6*d*/*w*0.5-1	150.84
80 × 40 × 2.6*d*/*w*0.5-2	159.21
80 × 40 × 2.6*d*/*w*0.7-1	39.72
80 × 40 × 2.6*d*/*w*0.7-2	110.90
80 × 40 × 2.6*d*/*w*0.9-1	68.45
Mean (P_m)	35.38
COV (V_p)	1.91

Table 5.5: Comparison of ultimate load ($P_{FE–P}$) and corresponding displacements ($\delta_{FE–P}$) generated FE against the test results.

Cross-sections	$P_{Test–P}$ (kN)	$\delta_{u–P}$ (mm)	$P_{Test–P}/P_{FE–P}$	$\delta_{u–P}/\delta_{FE–P}$
50 × 50 × 2.9d/w0.5-1	207.99	1.416	1.00	1.13
50 × 50 × 2.9d/w0.7-1	187.16	1.086	1.00	1.22
50 × 50 × 2.9d/w0.9-1	159.44	1.005	0.99	1.08
60 × 60 × 2.6d/w0.1-1	295.65	1.302	1.01	1.05
60 × 60 × 2.6d/w0.3-1	271.65	1.126	1.00	0.94
60 × 60 × 2.6d/w0.3-2	274.38	1.130	1.01	0.95
60 × 60 × 2.6d/w0.5-1	254.21	1.161	1.05	1.11
60 × 60 × 2.6d/w0.5-2	253.30	†	1.04	–
60 × 60 × 2.6d/w0.7-1	216.72	0.853	1.02	1.10
60 × 60 × 2.6d/w0.7-2	214.89	0.810	1.01	1.05
60 × 60 × 2.6d/w0.9-1	181.20	0.709	1.00	0.86
60 × 60 × 2.6d/w0.9-2	183.95	0.725	1.00	0.89
60 × 40 × 2.9d/w0.1-1	256.56	1.303	1.02	1.00
60 × 40 × 2.9d/w0.3-1	229.63	1.220	1.00	0.70
60 × 40 × 2.9d/w0.5-1	205.75	1.499	1.02	0.97
60 × 40 × 2.9d/w0.7-1	174.43	1.147	1.01	1.09
60 × 40 × 2.9d/w0.7-2	176.03	1.055	1.02	1.00
60 × 40 × 2.9d/w0.9-1	143.09	0.878	0.99	1.05
60 × 40 × 2.9d/w0.9-2	145.39	0.765	1.01	0.92
66 × 33 × 2.6d/w0.7-1	151.82	1.394	1.00	1.18
66 × 33 × 2.6d/w0.9-1	119.72	1.048	1.00	1.05
80 × 40 × 2.6d/w0.1-1	323.49	0.745	0.99	0.79
80 × 40 × 2.6d/w0.1-2	322.79	†	0.98	–
80 × 40 × 2.6d/w0.3-1	290.18	0.691	1.00	0.75
80 × 40 × 2.6d/w0.3-2	291.06	†	1.00	–
80 × 40 × 2.6d/w0.5-1	256.83	0.955	1.02	0.76
80 × 40 × 2.6d/w0.5-2	256.33	1.090	1.01	0.87
80 × 40 × 2.6d/w0.7-1	211.93	1.154	1.02	1.00
80 × 40 × 2.6d/w0.7-2	211.24	†	1.01	–
80 × 40 × 2.6d/w0.9-1	159.88	0.822	1.00	0.83
80 × 40 × 2.6d/w0.9-2	160.56	†	1.00	–
Mean (P_m)			1.01	0.97
COV (V_p)			0.01	0.14

† – Displacements corresponding to ultimate load are not shown due to suspected technical error.

Table 5.6: Comparison of test and FE perforated column capacities with design predictions proposed in this chapter.

Cross-section	d/w	L (mm)	P_{u-P} (kN)	P^*_{DSM} (kN)	$\frac{P_{u-P}}{P^*_{DSM}}$
60 × 40 × 2.9-1	0.10	160.23	256.56	252.92	1.01
60 × 60 × 2.6-1	0.10	200.00	295.65	285.49	1.04
80 × 40 × 2.6-1	0.10	160.04	323.49	304.67	1.06
80 × 40 × 2.6-2	0.10	160.04	322.79	304.94	1.06
300 × 200 × 2.0-FE	0.10	800.00	264.90	247.44	1.07
300 × 200 × 2.0-FE	0.20	800.00	263.04	247.42	1.06
300 × 200 × 2.5-FE	0.20	800.00	398.41	371.55	1.07
300 × 200 × 3.0-FE	0.20	800.00	550.01	518.38	1.06
300 × 200 × 3.5-FE	0.20	800.00	723.66	687.47	1.05
300 × 200 × 4.0-FE	0.20	800.00	902.87	878.46	1.03
300 × 200 × 6.0-FE	0.20	800.00	1922.06	1857.87	1.03
300 × 200 × 10.0-FE	0.20	800.00	4350.12	4291.52	1.01
300 × 200 × 12.5-FE	0.20	800.00	5723.50	5554.98	1.03
300 × 200 × 15.0-FE	0.20	800.00	7022.95	6846.18	1.03
300 × 200 × 20.0-FE	0.20	800.00	9753.30	9480.56	1.03
300 × 200 × 25.0-FE	0.20	800.00	12882.60	12151.29	1.06
300 × 200 × 30.0-FE	0.20	800.00	15895.30	14835.11	1.07
300 × 200 × 35.0-FE	0.20	800.00	18872.90	17522.20	1.08
300 × 200 × 45.0-FE	0.20	800.00	25282.00	22932.82	1.10
60 × 40 × 2.9-1	0.30	160.06	229.63	238.64	0.96
60 × 60 × 2.6-1	0.30	200.22	271.65	266.58	1.02
60 × 60 × 2.6-2	0.30	200.10	274.38	266.52	1.03
60 × 60 × 1.0-FE	0.30	200.00	54.56	61.12	0.89
60 × 60 × 1.2-FE	0.30	200.00	76.21	84.43	0.90
60 × 60 × 1.5-FE	0.30	200.00	118.38	125.20	0.95
60 × 60 × 2.0-FE	0.30	200.00	194.38	191.56	1.01
60 × 60 × 2.6-FE	0.30	200.00	272.44	265.07	1.03
60 × 60 × 3.5-FE	0.30	200.00	374.37	382.41	0.98
60 × 60 × 4.5-FE	0.30	200.00	497.93	520.78	0.96
60 × 60 × 5.5-FE	0.30	200.00	627.48	666.32	0.94
60 × 60 × 6.5-FE	0.30	200.00	762.62	818.70	0.93
60 × 60 × 7.5-FE	0.30	200.00	904.40	978.46	0.92
60 × 60 × 8.5-FE	0.30	200.00	1057.25	1147.20	0.92
80 × 40 × 2.6-2	0.30	160.06	291.06	277.72	1.05
80 × 40 × 2.6-1	0.30	160.06	290.18	280.23	1.04
80 × 40 × 1.0-FE	0.30	160.00	55.04	48.48	1.14
80 × 40 × 2.0-FE	0.30	160.00	180.71	164.34	1.10
80 × 40 × 2.5-FE	0.30	160.00	243.54	231.06	1.05
80 × 40 × 3.0-FE	0.30	160.00	305.32	288.49	1.06

80 × 40 × 4.0-FE	0.30	160.00	423.17	408.18	1.04
80 × 40 × 4.5-FE	0.30	160.00	492.87	469.86	1.05
80 × 40 × 5.0-FE	0.30	160.00	562.40	532.49	1.06
80 × 40 × 5.5-FE	0.30	160.00	631.69	595.88	1.06
100 × 100 × 1.0-FE	0.30	400.00	60.19	68.32	0.88
100 × 100 × 1.2-FE	0.30	400.00	85.57	94.53	0.91
100 × 100 × 1.5-FE	0.30	400.00	124.35	140.57	0.88
100 × 100 × 2.0-FE	0.30	400.00	210.66	234.09	0.90
100 × 100 × 2.6-FE	0.30	400.00	351.43	371.98	0.94
100 × 100 × 3.5-FE	0.30	400.00	550.60	563.83	0.98
100 × 100 × 4.5-FE	0.30	400.00	776.08	769.40	1.01
100 × 100 × 5.5-FE	0.30	400.00	968.04	985.36	0.98
100 × 100 × 6.5-FE	0.30	400.00	1172.34	1210.07	0.97
100 × 100 × 7.5-FE	0.30	400.00	1378.82	1442.48	0.96
100 × 100 × 8.5-FE	0.30	400.00	1592.90	1681.96	0.95
100 × 100 × 10.5-FE	0.30	400.00	2058.08	2181.19	0.94
100 × 100 × 12.5-FE	0.30	400.00	2544.55	2709.05	0.94
100 × 100 × 15.0-FE	0.30	400.00	3182.38	3420.85	0.93
300 × 200 × 2.0-FE	0.30	800.00	260.51	248.04	1.05
300 × 200 × 2.5-FE	0.30	800.00	395.81	369.28	1.07
300 × 200 × 3.0-FE	0.30	800.00	546.56	510.91	1.07
300 × 200 × 3.5-FE	0.30	800.00	716.44	671.98	1.07
300 × 200 × 4.0-FE	0.30	800.00	876.97	851.69	1.03
300 × 200 × 6.0-FE	0.30	800.00	1880.30	1744.43	1.08
300 × 200 × 10.0-FE	0.30	800.00	4213.33	3936.29	1.07
300 × 200 × 12.5-FE	0.30	800.00	5384.75	5172.14	1.04
300 × 200 × 15.0-FE	0.30	800.00	6614.80	6456.15	1.02
300 × 200 × 20.0-FE	0.30	800.00	9243.65	9134.00	1.01
300 × 200 × 25.0-FE	0.30	800.00	12289.75	11922.24	1.03
300 × 200 × 30.0-FE	0.30	800.00	15588.65	14796.94	1.05
300 × 200 × 35.0-FE	0.30	800.00	18539.55	17751.14	1.04
300 × 200 × 45.0-FE	0.30	800.00	24868.70	23960.24	1.04
300 × 200 × 2.0-FE	0.40	800.00	261.28	253.02	1.03
300 × 200 × 2.5-FE	0.40	800.00	393.39	373.52	1.05
300 × 200 × 3.0-FE	0.40	800.00	538.59	512.45	1.05
300 × 200 × 3.5-FE	0.40	800.00	708.68	668.36	1.06
300 × 200 × 4.0-FE	0.40	800.00	894.12	840.01	1.06
300 × 200 × 6.0-FE	0.40	800.00	1836.80	1662.08	1.11
300 × 200 × 10.0-FE	0.40	800.00	3904.16	3567.52	1.09
300 × 200 × 12.5-FE	0.40	800.00	5040.25	4711.41	1.07
300 × 200 × 15.0-FE	0.40	800.00	6277.60	5906.48	1.06
300 × 200 × 20.0-FE	0.40	800.00	8720.35	8417.12	1.04
50 × 50 × 2.9-1	0.51	200.20	207.99	212.18	0.98
60 × 40 × 2.9-1	0.50	160.10	205.75	215.97	0.95

60 × 60 × 2.6-1	0.50	199.96	254.21	244.24	1.04
60 × 60 × 2.6-2	0.50	200.00	253.30	244.25	1.04
60 × 60 × 2.6-FE	0.50	200.00	238.53	241.66	0.99
60 × 60 × 1.0-FE	0.50	200.00	52.66	59.27	0.89
60 × 60 × 1.2-FE	0.50	200.00	72.43	80.45	0.90
60 × 60 × 1.5-FE	0.50	200.00	122.98	116.09	1.06
60 × 60 × 2.0-FE	0.50	200.00	172.32	173.60	0.99
60 × 60 × 3.5-FE	0.50	200.00	344.32	351.17	0.98
60 × 60 × 4.5-FE	0.50	200.00	459.69	481.41	0.95
60 × 60 × 5.5-FE	0.50	200.00	584.69	619.54	0.94
60 × 60 × 6.5-FE	0.50	200.00	721.06	765.34	0.94
60 × 60 × 7.5-FE	0.50	200.00	870.63	919.45	0.95
60 × 60 × 8.5-FE	0.50	200.00	1027.40	1083.64	0.95
80 × 40 × 2.6-1	0.49	160.00	256.83	253.16	1.01
80 × 40 × 2.6-2	0.49	160.14	256.33	253.15	1.01
80 × 40 × 1.0-FE	0.50	160.00	52.91	48.01	1.10
80 × 40 × 2.0-FE	0.50	160.00	163.88	152.31	1.08
80 × 40 × 2.5-FE	0.50	160.00	214.90	209.05	1.03
80 × 40 × 3.0-FE	0.50	160.00	264.98	262.07	1.01
80 × 40 × 4.0-FE	0.50	160.00	374.41	373.31	1.00
80 × 40 × 4.5-FE	0.50	160.00	440.41	430.97	1.02
80 × 40 × 5.0-FE	0.50	160.00	496.69	489.72	1.01
80 × 40 × 5.5-FE	0.50	160.00	557.79	549.40	1.02
100 × 100 × 1.0-FE	0.50	400.00	61.37	68.52	0.90
100 × 100 × 1.2-FE	0.50	400.00	83.52	93.86	0.89
100 × 100 × 1.5-FE	0.50	400.00	123.62	137.46	0.90
100 × 100 × 2.0-FE	0.50	400.00	202.13	223.02	0.91
100 × 100 × 2.6-FE	0.50	400.00	371.96	342.87	1.08
100 × 100 × 3.5-FE	0.50	400.00	511.12	511.54	1.00
100 × 100 × 4.5-FE	0.50	400.00	694.87	702.08	0.99
100 × 100 × 5.5-FE	0.50	400.00	883.44	903.52	0.98
100 × 100 × 6.5-FE	0.50	400.00	1067.06	1114.30	0.96
100 × 100 × 7.5-FE	0.50	400.00	1266.77	1333.44	0.95
100 × 100 × 8.5-FE	0.50	400.00	1472.39	1560.37	0.94
100 × 100 × 10.5-FE	0.50	400.00	1927.49	2036.91	0.95
100 × 100 × 12.5-FE	0.50	400.00	2416.75	2545.74	0.95
100 × 100 × 15.0-FE	0.50	400.00	3081.85	3240.00	0.95
300 × 200 × 2.0-FE	0.50	800.00	261.47	252.99	1.03
300 × 200 × 2.5-FE	0.50	800.00	390.12	373.46	1.04
300 × 200 × 3.0-FE	0.50	800.00	532.99	512.37	1.04
300 × 200 × 3.5-FE	0.50	800.00	673.89	668.26	1.01
300 × 200 × 4.0-FE	0.50	800.00	870.32	839.88	1.04
300 × 200 × 6.0-FE	0.50	800.00	1802.46	1661.81	1.08
300 × 200 × 10.0-FE	0.50	800.00	3641.70	3566.83	1.02

300 × 200 × 12.5-FE	0.50	800.00	4718.31	4710.54	1.00
300 × 200 × 15.0-FE	0.50	800.00	5844.20	5905.43	0.99
300 × 200 × 20.0-FE	0.50	800.00	8255.30	8415.74	0.98
300 × 200 × 25.0-FE	0.50	800.00	10872.15	11052.78	0.98
300 × 200 × 30.0-FE	0.50	800.00	14103.60	13794.68	1.02
300 × 200 × 35.0-FE	0.50	800.00	17741.40	16636.45	1.07
300 × 200 × 45.0-FE	0.50	800.00	24297.90	22692.20	1.07
300 × 200 × 2.0-FE	0.60	800.00	258.73	240.80	1.07
300 × 200 × 2.5-FE	0.60	800.00	372.64	352.58	1.06
300 × 200 × 3.0-FE	0.60	800.00	505.22	479.76	1.05
300 × 200 × 3.5-FE	0.60	800.00	651.59	620.53	1.05
300 × 200 × 4.0-FE	0.60	800.00	847.93	773.28	1.10
300 × 200 × 6.0-FE	0.60	800.00	1804.12	1475.18	1.22
300 × 200 × 10.0-FE	0.60	800.00	3340.31	3036.01	1.10
300 × 200 × 12.5-FE	0.60	800.00	4384.05	4053.36	1.08
300 × 200 × 15.0-FE	0.60	800.00	5457.45	5128.78	1.06
300 × 200 × 20.0-FE	0.60	800.00	7775.10	7423.43	1.05
50 × 50 × 2.9-1	0.70	199.96	187.16	187.12	1.00
60 × 40 × 2.9-1	0.70	160.10	174.43	188.44	0.93
60 × 40 × 2.9-2	0.70	160.22	176.03	188.28	0.93
60 × 60 × 2.6-1	0.70	199.94	216.72	208.68	1.04
60 × 60 × 2.6-2	0.70	200.08	214.89	209.38	1.03
60 × 60 × 1.0-FE	0.70	200.00	48.07	53.61	0.90
60 × 60 × 1.2-FE	0.70	200.00	68.54	71.42	0.96
60 × 60 × 1.5-FE	0.70	200.00	97.56	99.94	0.98
60 × 60 × 2.0-FE	0.70	200.00	151.76	147.76	1.03
60 × 60 × 2.6-FE	0.70	200.00	211.67	208.34	1.02
60 × 60 × 3.5-FE	0.70	200.00	306.31	307.46	1.00
60 × 60 × 4.5-FE	0.70	200.00	420.27	427.51	0.98
60 × 60 × 5.5-FE	0.70	200.00	540.48	557.09	0.97
60 × 60 × 6.5-FE	0.70	200.00	675.96	696.19	0.97
60 × 60 × 7.5-FE	0.70	200.00	817.50	845.75	0.97
60 × 60 × 8.5-FE	0.70	200.00	971.04	1007.94	0.96
66 × 33 × 2.6-1	0.70	132.34	151.82	158.01	0.96
80 × 40 × 2.6-1	0.69	161.50	211.93	214.30	0.99
80 × 40 × 2.6-2	0.69	160.10	211.24	214.46	0.98
80 × 40 × 1.0-FE	0.70	160.00	52.91	44.37	1.19
80 × 40 × 2.0-FE	0.70	160.00	135.08	131.03	1.03
80 × 40 × 2.5-FE	0.70	160.00	177.98	177.29	1.00
80 × 40 × 3.0-FE	0.70	160.00	221.30	224.22	0.99
80 × 40 × 4.0-FE	0.70	160.00	316.62	324.04	0.98
80 × 40 × 4.5-FE	0.70	160.00	371.63	376.43	0.99
80 × 40 × 5.0-FE	0.70	160.00	427.04	430.21	0.99
80 × 40 × 5.5-FE	0.70	160.00	484.38	485.24	1.00

100 × 100 × 1.0-FE	0.70	400.00	55.74	64.16	0.87
100 × 100 × 1.2-FE	0.70	400.00	74.80	87.00	0.86
100 × 100 × 1.5-FE	0.70	400.00	123.62	125.45	0.99
100 × 100 × 2.0-FE	0.70	400.00	182.61	197.95	0.92
100 × 100 × 2.6-FE	0.70	400.00	295.97	293.14	1.01
100 × 100 × 3.5-FE	0.70	400.00	446.65	436.40	1.02
100 × 100 × 4.5-FE	0.70	400.00	609.61	606.43	1.01
100 × 100 × 5.5-FE	0.70	400.00	780.95	788.58	0.99
100 × 100 × 6.5-FE	0.70	400.00	971.04	981.45	0.99
100 × 100 × 7.5-FE	0.70	400.00	1161.08	1184.20	0.98
100 × 100 × 8.5-FE	0.70	400.00	1358.76	1396.35	0.97
100 × 100 × 10.5-FE	0.70	400.00	1788.91	1848.77	0.97
100 × 100 × 12.5-FE	0.70	400.00	2264.16	2341.80	0.97
100 × 100 × 15.0-FE	0.70	400.00	2944.66	3031.08	0.97
300 × 200 × 2.0-FE	0.70	800.00	254.06	240.73	1.06
300 × 200 × 2.5-FE	0.70	800.00	351.42	352.49	1.00
300 × 200 × 3.0-FE	0.70	800.00	461.11	479.63	0.96
300 × 200 × 3.5-FE	0.70	800.00	611.20	620.36	0.99
300 × 200 × 4.0-FE	0.70	800.00	776.52	773.06	1.00
300 × 200 × 6.0-FE	0.70	800.00	1603.73	1474.76	1.09
300 × 200 × 10.0-FE	0.70	800.00	3076.28	3035.09	1.01
300 × 200 × 12.5-FE	0.70	800.00	4047.40	4052.17	1.00
300 × 200 × 15.0-FE	0.70	800.00	5081.45	5127.35	0.99
300 × 200 × 20.0-FE	0.70	800.00	7286.55	7421.55	0.98
300 × 200 × 25.0-FE	0.70	800.00	9839.60	9877.00	1.00
300 × 200 × 30.0-FE	0.70	800.00	12601.05	12475.66	1.01
300 × 200 × 35.0-FE	0.70	800.00	16024.55	15216.99	1.05
300 × 200 × 45.0-FE	0.70	800.00	23363.35	21227.19	1.10
300 × 200 × 2.0-FE	0.80	800.00	215.03	199.33	1.08
300 × 200 × 2.5-FE	0.80	800.00	314.67	289.48	1.09
300 × 200 × 3.0-FE	0.80	800.00	427.33	390.60	1.09
300 × 200 × 3.5-FE	0.80	800.00	563.55	500.85	1.13
300 × 200 × 4.0-FE	0.80	800.00	706.82	618.54	1.14
300 × 200 × 6.0-FE	0.80	800.00	1413.70	1133.20	1.25
300 × 200 × 10.0-FE	0.80	800.00	2782.17	2252.26	1.24
300 × 200 × 12.5-FE	0.80	800.00	3712.83	3115.36	1.19
300 × 200 × 15.0-FE	0.80	800.00	5017.45	4062.46	1.24
300 × 200 × 20.0-FE	0.80	800.00	6813.10	6185.22	1.10
50 × 50 × 2.9-1	0.91	200.36	159.44	152.96	1.04
60 × 40 × 2.9-2	0.90	160.30	145.39	147.15	0.99
60 × 40 × 2.9-1	0.90	159.32	143.09	146.40	0.98
60 × 60 × 2.6-1	0.90	200.00	181.20	160.25	1.13
60 × 60 × 2.6-2	0.90	200.00	183.95	162.98	1.13
60 × 60 × 1.0-FE	0.90	200.00	39.53	42.08	0.94

60 × 60 × 1.2-FE	0.90	200.00	55.41	54.88	1.01
60 × 60 × 1.5-FE	0.90	200.00	79.31	74.04	1.07
60 × 60 × 2.0-FE	0.90	200.00	124.18	109.62	1.13
60 × 60 × 2.6-FE	0.90	200.00	184.26	161.16	1.14
60 × 60 × 3.5-FE	0.90	200.00	273.61	250.10	1.09
60 × 60 × 4.5-FE	0.90	200.00	373.94	364.20	1.03
60 × 60 × 5.5-FE	0.90	200.00	490.06	494.25	0.99
60 × 60 × 6.5-FE	0.90	200.00	629.14	641.30	0.98
60 × 60 × 7.5-FE	0.90	200.00	765.23	807.80	0.95
60 × 60 × 8.5-FE	0.90	200.00	922.89	998.22	0.92
66 × 33 × 2.6-1	0.89	130.40	119.72	118.92	1.01
80 × 40 × 2.6-1	0.89	161.22	159.88	155.00	1.03
80 × 40 × 2.6-2	0.89	160.10	160.56	155.33	1.03
80 × 40 × 1.0-FE	0.90	160.00	37.56	35.63	1.05
80 × 40 × 2.0-FE	0.90	160.00	103.86	96.95	1.07
80 × 40 × 2.5-FE	0.90	160.00	140.13	130.13	1.08
80 × 40 × 3.0-FE	0.90	160.00	176.14	169.35	1.04
80 × 40 × 4.0-FE	0.90	160.00	259.05	256.54	1.01
80 × 40 × 4.5-FE	0.90	160.00	303.99	304.10	1.00
80 × 40 × 5.0-FE	0.90	160.00	353.66	354.10	1.00
80 × 40 × 5.5-FE	0.90	160.00	409.21	406.44	1.01
100 × 100 × 1.0-FE	0.90	400.00	50.28	52.24	0.96
100 × 100 × 1.2-FE	0.90	400.00	68.85	70.11	0.98
100 × 100 × 1.5-FE	0.90	400.00	99.59	99.42	1.00
100 × 100 × 2.0-FE	0.90	400.00	153.08	152.09	1.01
100 × 100 × 2.6-FE	0.90	400.00	240.71	215.32	1.12
100 × 100 × 3.5-FE	0.90	400.00	382.08	326.29	1.17
100 × 100 × 4.5-FE	0.90	400.00	534.31	472.09	1.13
100 × 100 × 5.5-FE	0.90	400.00	700.61	635.01	1.10
100 × 100 × 6.5-FE	0.90	400.00	872.79	814.11	1.07
100 × 100 × 7.5-FE	0.90	400.00	1053.44	1008.99	1.04
100 × 100 × 8.5-FE	0.90	400.00	1243.76	1219.69	1.02
100 × 100 × 10.5-FE	0.90	400.00	1658.51	1690.86	0.98
100 × 100 × 12.5-FE	0.90	400.00	2126.43	2237.23	0.95
100 × 100 × 15.0-FE	0.90	400.00	2794.37	3058.76	0.91
300 × 200 × 2.0-FE	0.90	800.00	189.24	199.24	0.95
300 × 200 × 2.5-FE	0.90	800.00	273.72	289.35	0.95
300 × 200 × 3.0-FE	0.90	800.00	381.58	390.43	0.98
300 × 200 × 3.5-FE	0.90	800.00	495.24	500.62	0.99
300 × 200 × 4.0-FE	0.90	800.00	622.56	618.25	1.01
300 × 200 × 6.0-FE	0.90	800.00	1225.09	1132.65	1.08
300 × 200 × 10.0-FE	0.90	800.00	2491.54	2251.27	1.11
300 × 200 × 12.5-FE	0.90	800.00	3369.05	3114.07	1.08
300 × 200 × 15.0-FE	0.90	800.00	4306.87	4060.88	1.06

300 × 200 × 20.0-FE	0.90	800.00	6360.25	6183.08	1.03
300 × 200 × 25.0-FE	0.90	800.00	8638.10	8590.64	1.01
300 × 200 × 30.0-FE	0.90	800.00	11289.05	11281.16	1.00
300 × 200 × 35.0-FE	0.90	800.00	14368.20	14275.40	1.01
300 × 200 × 45.0-FE	0.90	800.00	21852.65	21419.57	1.02

Table 5.7: Summary of compression test of perforated cold-formed stub columns and comparison with design prediction for perforation size ratio, $d/w \leq 0.9$

Cross-sections	w/t	P_{Test-P}	P_{Test-P}							
		(kN)	P_{STT}	P_{DS}	P_{SD}	P_{nl-EWM}	P_{nl-DSM}	$P_{nl-DSM-MS}$	P_{MP-EC3}	P_{MP-BS}
50 × 50 × 2.9d/w0.5-1	13.23	207.99	1.12	1.43	1.08	1.32	1.30	1.30	1.30	1.30
50 × 50 × 2.9d/w0.7-1	13.20	187.16	1.04	1.33	1.03	1.32	1.31	1.31	1.31	1.31
50 × 50 × 2.9d/w0.9-1	13.13	159.44	0.92	1.19	0.94	1.28	1.27	1.27	1.27	1.27
60 × 60 × 2.6d/w0.1-1	19.03	295.65	1.15	1.79	1.13	1.20	1.74	1.20	1.20	1.20
60 × 60 × 2.6d/w0.3-1	19.03	271.65	1.10	1.69	1.09	1.22	1.66	1.21	1.21	1.21
60 × 60 × 2.6d/w0.3-2	19.04	274.38	1.11	1.70	1.10	1.23	1.67	1.22	1.22	1.22
60 × 60 × 2.6d/w0.5-1	18.95	254.21	1.09	1.62	1.08	1.27	1.60	1.26	1.26	1.26
60 × 60 × 2.6d/w0.5-2	18.95	253.30	1.08	1.62	1.08	1.26	1.59	1.25	1.25	1.25
60 × 60 × 2.6d/w0.7-1	19.15	216.72	0.97	1.46	1.00	1.23	1.44	1.22	1.22	1.22
60 × 60 × 2.6d/w0.7-2	19.04	214.89	0.96	1.44	0.99	1.22	1.42	1.21	1.21	1.21
60 × 60 × 2.6d/w0.9-1	19.16	181.20	0.86	1.30	0.91	1.19	1.28	1.18	1.18	1.18
60 × 60 × 2.6d/w0.9-2	18.92	183.95	0.86	1.30	0.92	1.19	1.27	1.18	1.18	1.18
60 × 40 × 2.9d/w0.1-1	16.67	256.56	1.18	1.69	1.13	1.23	1.59	1.22	1.22	1.22
60 × 40 × 2.9d/w0.3-1	16.69	229.63	1.11	1.56	1.08	1.24	1.48	1.22	1.22	1.22
60 × 40 × 2.9d/w0.5-1	16.80	205.75	1.08	1.49	1.06	1.28	1.41	1.27	1.27	1.27
60 × 40 × 2.9d/w0.7-1	16.73	174.43	0.97	1.34	0.99	1.26	1.25	1.25	1.25	1.25
60 × 40 × 2.9d/w0.7-2	16.74	176.03	0.98	1.36	1.00	1.28	1.27	1.26	1.26	1.26
60 × 40 × 2.9d/w0.9-1	16.92	143.09	0.86	1.22	0.93	1.26	1.25	1.25	1.25	1.25
60 × 40 × 2.9d/w0.9-2	16.80	145.39	0.86	1.23	0.94	1.28	1.26	1.26	1.26	1.26
66 × 33 × 2.6d/w0.7-1	21.79	151.82	1.03	1.55	1.05	1.30	1.52	1.28	1.28	1.28
66 × 33 × 2.6d/w0.9-1	21.92	119.72	0.90	1.41	1.00	1.30	1.32	1.29	1.28	1.28
80 × 40 × 2.6d/w0.1-1	27.18	323.49	1.10	2.13	1.11	1.15	2.27	1.14	1.14	1.14

Table 5.7: (Continued) Summary of compression test of perforated cold-formed stub columns and comparison with design prediction for perforation size ratio, $d/w \leq 0.9$

Cross-sections	w/t	P_{Test-P} (kN)	P_{Test-P}							
			P_{STT}	P_{DS}	P_{SD}	P_{nl-EWM}	P_{nl-DSM}	$P_{nl-DSM-MS}$	P_{MP-EC3}	P_{MP-BS}
80 × 40 × 2.6d/w0.1-2	27.19	322.79	1.09	2.12	1.11	1.14	2.26	1.13	1.13	1.13
80 × 40 × 2.6d/w0.3-1	26.97	290.18	1.06	1.96	1.08	1.18	2.11	1.17	1.17	1.17
80 × 40 × 2.6d/w0.3-2	27.17	291.06	1.07	1.99	1.09	1.19	2.15	1.18	1.18	1.18
80 × 40 × 2.6d/w0.5-1	26.97	256.83	1.04	1.85	1.07	1.23	1.99	1.22	1.22	1.22
80 × 40 × 2.6d/w0.5-2	26.96	256.33	1.04	1.84	1.07	1.23	1.99	1.22	1.22	1.22
80 × 40 × 2.6d/w0.7-1	26.97	211.93	0.94	1.66	1.01	1.24	1.77	1.23	1.23	1.23
80 × 40 × 2.6d/w0.7-2	26.96	211.24	0.93	1.66	1.01	1.24	1.76	1.22	1.22	1.22
80 × 40 × 2.6d/w0.9-1	27.06	159.88	0.79	1.43	0.91	1.21	1.48	1.20	1.20	1.20
80 × 40 × 2.6d/w0.9-2	27.05	160.56	0.79	1.44	0.91	1.21	1.48	1.20	1.20	1.20
Mean (P_m)			1.00	1.57	1.03	1.24	1.59	1.23	1.23	1.23
COV (V_p)			0.11	0.16	0.07	0.04	0.20	0.04	0.04	0.04
Reliability index (β)			2.58	3.90	2.86	3.73	3.63	3.70	3.70	3.70

Table 5.8: Summary of compression test of perforated cold-formed stub columns and comparison with design prediction for perforation size ratio, $d/w \leq 0.7$

Cross-sections	w/t	P_{Test-P} (kN)	P_{Test-P}			
			P_{STT}	P_{DS}	P_{SD}	P_{nl-EWM}
			$d/w \leq 0.7$	$d/w \leq 0.6$	$d/w \leq 0.6$	$d/w \leq 0.5$
50 × 50 × 2.9d/w0.5-1	13.23	207.99	1.12	1.43	1.08	1.32
50 × 50 × 2.9d/w0.7-1	13.20	187.16	1.04	–	–	–
60 × 60 × 2.6d/w0.1-1	19.03	295.65	1.15	1.89	1.13	1.20
60 × 60 × 2.6d/w0.3-1	19.03	271.65	1.10	1.78	1.09	1.22
60 × 60 × 2.6d/w0.3-2	19.04	274.38	1.11	1.79	1.10	1.23
60 × 60 × 2.6d/w0.5-1	18.95	254.21	1.09	1.71	1.08	1.27
60 × 60 × 2.6d/w0.5-2	18.95	253.30	1.08	1.70	1.08	1.26
60 × 60 × 2.6d/w0.7-1	19.15	216.72	0.97	–	–	–
60 × 60 × 2.6d/w0.7-2	19.04	214.89	0.96	–	–	–
60 × 40 × 2.9d/w0.1-1	16.67	256.56	1.18	1.61	1.13	1.23
60 × 40 × 2.9d/w0.3-1	16.69	229.63	1.11	1.49	1.08	1.24
60 × 40 × 2.9d/w0.5-1	16.80	205.75	1.08	1.42	1.06	1.28
60 × 40 × 2.9d/w0.7-1	16.73	174.43	0.97	–	–	–
60 × 40 × 2.9d/w0.7-2	16.74	176.03	0.98	–	–	–
66 × 33 × 2.6d/w0.7-1	21.79	151.82	1.03	–	–	–
80 × 40 × 2.6d/w0.1-1	27.18	323.49	1.10	2.13	1.11	1.15
80 × 40 × 2.6d/w0.1-2	27.19	322.79	1.09	2.12	1.11	1.14
80 × 40 × 2.6d/w0.3-1	26.97	290.18	1.06	1.96	1.08	1.18
80 × 40 × 2.6d/w0.3-2	27.17	291.06	1.07	1.99	1.09	1.19

Table 5.8: (Continued) Summary of compression test of perforated cold-formed stub columns and comparison with design prediction for perforation size ratio, $d/w \leq 0.7$

Cross-sections	w/t	P_{Test-P} (kN)	P_{Test-P}			
			P_{STT}	P_{DS}	P_{SD}	P_{nl-EWM}
			$d/w \leq 0.7$	$d/w \leq 0.6$	$d/w \leq 0.6$	$d/w \leq 0.5$
80 × 40 × 2.6d/w0.5-1	26.97	256.83	1.04	1.85	1.07	1.23
80 × 40 × 2.6d/w0.5-2	26.96	256.33	1.04	1.84	1.07	1.23
80 × 40 × 2.6d/w0.7-1	26.97	211.93	0.94	–	–	–
80 × 40 × 2.6d/w0.7-2	26.96	211.24	0.93	–	–	–
Number of observations (n)			23.0	15.0	15.0	15.0
Mean (P_m)			1.05	1.78	1.09	1.22
COV (V_p)			0.06	0.13	0.02	0.04
Reliability index (β)			2.97	4.53	3.23	3.65

Table 5.9: Summary of comparison of stub column ultimate capacities from test and FE with design prediction for $d/w \leq 0.9$

	P_{u-P}								
	P_{STT}	P_{DS}	P_{SD}	P_{nl-EWM}	P_{nl-DSM}	$P_{nl-DSM-MS}$	P_{MP-EC3}	P_{MP-BS}	P^{*}_{DSM}
Number of data	261	264	264	264	264	264	264	264	264
Mean (P_m)	0.99	1.42	1.02	1.27	1.75	1.22	1.25	1.27	1.02
COV (V_p)	0.34	0.32	0.26	0.22	0.19	0.27	0.23	0.21	0.06
Reliability Index (β)	1.61	2.58	1.98	2.83	4.10	2.44	2.73	2.90	2.87

Table 5.10: Summary of comparison of stub column ultimate capacities from test and FE with design prediction for $d/w \leq 0.7$

	P_{u-P}			
	P_{STT}	P_{DS}	P_{SD}	P_{nl-EWM}
Perforation size ratio, d/w	$d/w \leq 0.7$	$d/w \leq 0.6$	$d/w \leq 0.6$	$d/w \leq 0.5$
Number of data	196	144	144	121
Mean (P_m)	1.03	1.49	1.04	1.28
COV (V_p)	0.32	0.34	0.26	0.21
Reliability Index (β)	1.77	2.58	1.98	2.91

Table 5.11: Coefficient for design of perforated cold-formed steel tubular sections with circular perforation

Perforation size ratio, (d/w)	*Coefficients*			
	K_1	K_2	K_3	K_4
$0.2 < d/w \leq 0.3$	0.8506	0.2587	0.8116	– 0.0629
$0.3 < d/w \leq 0.5$	0.7643	0.2780	0.8614	– 0.1566
$0.5 < d/w \leq 0.7$	0.6386	0.3194	0.8504	– 0.2330
$0.7 < d/w \leq 0.9$	0.4459	0.4542	0.7091	– 0.2456

Chapter 6

Conclusions

The present thesis work reported a series of carefully conducted test results, to study the material characteristics and column (unperforated and perforated) performances of YSt-310 cold-formed steel, thereby contribution majorly to the data pool of experimental results for cold-formed steel tubular structures. The main conclusions drawn from the current study are presented in this chapter. This chapter has been divided into two main sections: a) the first section summarised the key findings of the research project and salient conclusions drawn from each chapter, and b) the second section provides an insight of possible extension to present work and future scope on cold-formed steel tubular section.

6.1 RESEARCH SUMMARY

Tubular structures are widely popular and have been a preferred choice for engineers and architects because of their aesthetically pleasing nature and excellent structural performance (as compared to opened sections). Hence, tubular sections such as the traditional circular, square and rectangular sections; and newly added sections such as elliptical, flat-oval, semi-oval have been widely employed in many infrastructural

projects, as it can be witnessed from many of the architectural marvels all around the world. Despite such widespread uses, the present international design standards for the design of steel structures have mostly been developed based on hot-finished or hot-rolled steel materials and hence, relied principally on the idealised stress-strain material (i.e. elastic-perfectly plastic) model. The design concept has been applied to cold-formed steel tubular sections, ignoring the beneficial effects of material strength enhancement due to cold-working and hence, resulting in overly conservative design predictions for cold-formed steel structural members. Therefore, research work on investigating the material strength enhancement and member behaviour has become necessary to assess the applicability of currently adopted design codes (which are based on hot-rolled steels) and develop specific design equations for cold-formed steel tubular members.

In India, construction industries are predominantly dominated by reinforced concrete structures, mainly due to relatively long experiences and cheaper unskilled workforce available. However, in the recent years, appreciable development in steel constructions is observed where structural steels (particularly cold-formed steel tubular structures) have been utilised in public building (*viz.*, skywalks, airports, stadia, railway platforms, shopping malls etc.), residential and industrial buildings. Amongst the various grades (e.g., YSt-210, YSt-355 etc.) of structural tubular steels, YSt-310 cold-formed steel tubular sections is one of the most widely used structural steels in India. Although, YSt-310 constructional steel is a popular choice, limited or no accurate material characteristics and column capacities are available in the public domain.

Therefore, the primary objective of the study is to determine and establish accurate material characteristics of YSt-310 cold-formed steel tubular sections. Further, using the material properties, the applicability of current design standards for the design of cold-formed steel stub columns, both unperforated and perforated, have been examined using column capacities generated from test and validated FE models and new design approaches have been recommended. In the following sub-sections, a

summary of the experimental investigations, numerical parametric study, assessment of existing design equations and proposed recommendations are presented.

6.1.1 Material characterisation

An extensive experimental programme, to establish an accurate material database for YSt-310 cold-formed steel tubular sections (manufactured by Tata Steel (2013), has been presented in Chapter 3. The test programme has been conducted at three temperature conditions, namely ambient temperature, elevated temperature and post-fire conditions.

6.1.1.1 Ambient temperature tests

At ambient temperature (~ 21 ºC), material characteristics such as chemical composition, metallographic examination and mechanical properties have been studied through optical emission spectrometer (OES), optical microscope and tensile coupon test respectively. Following conclusions have been made from the experimental investigation:

a) Based on the metallographic examination, the grains in the flat regions have been observed to be relatively larger in comparison to those of corner regions wherein the grains are smaller and elongated.

b) Tensile test has been conducted to estimate the ambient temperature mechanical properties of YSt-310 steel material, using coupons extracted from flat, corner and weld regions. Engineering stress-strain curves and then key material parameters have been evaluated. Based on the test results, the mean values of Young's modulus of flat coupons have been observed to be slightly higher than that of curved and weld coupons. In addition, strength enhancement in the corner material due to cold-forming has been noticed, in particular the average 0.2% proof stress and ultimate stress of corner material are respectively 26% and 34%

higher than those of flat coupons. Also, the material strength of corner and weld coupons have been found to be similar.

6.1.1.2 Elevated temperature material tests

Elevated temperature mechanical properties of YSt-310 cold-formed steel have been studied through steady-state elevated temperatures tensile coupon test. A total of 31 tensile coupon tests have been performed at temperature ranging from approximately ambient to 800 °C and the reduction factors of key material parameters have been estimated, namely Young's modulus; yield stress; stress corresponding to 0.5%, 1.5% and 2.0% strain; ultimate strength and corresponding strains (%); fracture strains (%) and Ramberg–Osgood hardening paerameter. Elevated temperature reduction factors of YSt-310 cold-formed steels have been compared with those presented in design guidelines and reported by earlier researchers. Based on the comparison, following concluding remarks have been made:

a) Reduction factors of key material parameters generated from the present experimental programme have been found to be in close agreement, within a scatter band, with the existing test results for cold-formed steel tubular sections, except for elastic modulus which showed to have relatively higher scatter values.

b) Except for elastic modulus, the design reduction factors for key material parameters (such as 0.2% proof stress; stresses corresponding to 0.5%, 1.5%, 2.0% strains; ultimate stress etc.) presented in most of the international design standards (developed based on the hot-rolled steel) have been observed to be unsuitable for cold-formed steels tubular sections.

c) Design reduction factors as per IS 800 (2007), for elastic modulus and yield stress are found to be unsuitable YSt-310 material. However, the design curve proposed by Chen and Young (2007) to estimate ultimate strain reduction factor for brake-pressed cold-formed steel and is found to applicable for cold-formed steel tubular sections also.

d) A new set of fire design reduction factors for 0.2% proof stress; stresses corresponding to 0.5%, 1.5% and 2.0% strains; ultimate stress and fracture strain (%), based on lower bound values of the present and existing test results, have been proposed. The proposed reductions have been seen to offer an improved mean values and reliable predictions

6.1.1.3 Post-fire material tests

Post-fire mechanical property of YSt-310 cold-formed steel tubular section has been studied through standard tensile coupon test and microhardness test at ambient temperature. Coupon specimens extracted from the flat regions have been first exposed to various elevated temperatures ranging from ~ 300–800 °C for a period of 20 min, allowed to cool down and then tensile tests have been conducted at ambient temperature. Stress-strain curves, key material parameters (e.g. elastic modulus, proof stresses, tensile strength, percentage elongation at fracture, Ramberg–Osgood material parameters etc.) and microhardness values, generated from the tests, have been analysed and the following important findings have been made:

a) The reduction in elastic modulus due to fire exposure of YSt-310 cold-formed steel material has been seen to be insignificant.

b) For exposed temperature up to ~ 400 °C, the reductions in yield strength and tensile strength is found to be negligible, however the strengths are observed to be reduced to ~ 59% and 77% respectively at the exposed temperature of ~ 800 °C.

c) Two best fit linear correlations between material strengths (yield and tensile stress) against microhardness values have been developed.

d) Using the present test and existing test results from literature, two sets of empirical equations to predict the post-fire reduction factors of cold-formed steel have been developed separately for i) YSt-310 steel material and ii) cold-formed steel of various grades presently available in the literature.

6.1.2 Unperforated stub column tests

The structural performance of YSt-310 cold-formed steel tubular stub columns has been investigated through experimental and numerical programmes, as presented in Chapter 4. The extent of strength enhancement in the corner region due to cold-forming has been investigated at a finer resolution using microhardness test. Local geometric imperfection of stub columns has been measured using a non-contact 3D laser scanner. A total of 12 stub column tests have been performed to investigate the cross-sectional capacity of YSt-310 cold-formed SHS and RHS stub columns. Using validated FE models, parametric study has been performed to study the performance of stub columns covering a wide range of cross-sectional slenderness. The column capacities generated from the test and FE models have been utilised to assess the accurateness of the current international guidelines for design of cold-formed steel columns. Based on the test and FE analysis, following concluding remarks have been presented:

f) The spread of the corner strength enhancement due to cold-forming has been seen to lie within a zone of ~ ± 3.0*t* from the centre of the corner, although relatively higher influence can be witnessed within ~ ± 1.2*t*.

g) Based on the 3D laser imperfection measurement, local geometric imperfections have been seen in the range ~0.012–0.047 (*t*/60–*t*/248).

h) The design strengths predicted by EC3-1-1 (2005), CSM (detailed in Zhao *et al.*, 2017), DSM in AISI S100-16 (2016), modified DSM by Rossi and Rasmussen (2013); and Arrayago *et al.* (2017), have been found to provide conservative predictions for non-slender cross-sections. However, for the case of slender cross-section, CSM and modified DSM proposed by Rossi and Rasmussen (2013) have been seen to provide accurate and conservative design predictions.

i) Class–3 cross-sectional slenderness limit presented in EC3-1-1 (2005) has been assessed, for YSt-310 cold-formed tubular sections. A slenderness limit, i.e. $c/t\varepsilon$

= 38 has been proposed and found to be more suitable for YSt-310 cold-formed tubular sections.

j) A modified design equation based on DSM has been proposed based on current test and FE column capacities and found to provide conservative prediction with least scatterness as compared to existing design equations of unperforated stub columns.

6.1.3 Perforated stub column test

Extensive experimental and numerical investigations into the structural behaviour of YSt-310 cold-formed steel stub columns having two opposite central circular perforations have been conducted. Experimental investigations include local geometric imperfection measurement of stub columns before and after the perforations are made and 32 perforated stub column test. Parametric study has been performed using 233 validated FE stub columns, covering a wide range of cross-sectional slenderness, w/t ranges from 2.67 to 146 and perforation diameters to width ratios, $d/w \leq 0.9$, to study the effects of perforation sizes on the ultimate capacity of columns. Based on the imperfection measurement, compression test and numerical analysis as well as assessment of current design predictions for perforated columns, following points have been obtained:

i) Introduction of two opposite central circular perforation has been found to increase the local geometric amplitudes of perforated cold-formed steel tubular stub columns. Further, based on the imperfections measured, a modified imperfection amplitude formula, based on Dawson and Walker (1972), for both unperforated and perforated cold-formed steel stub columns has been developed.

ii) Stub column test results showed that perforation size ratios, d/w up to 10 % has been observed not to affect the ultimate capacity of SHS/RHS stub columns. However, for d/w of 30%, 50%, 70% and 90%, the average percentage reduction on column capacities has been found to be ~ 9.57%, 18.24%, 31.15% and 40.00%

respectively. Overall, a mild non-linear drop in the load capacity, as *d*/*w* increases from 0.1 to 0.9, has been observed.

iii) Most of the presently available design equations have been found to provide conservative and reliable, but scattered predictions for the design of cold-formed steel SHS/RHS structural stub columns with central circular perforation size ratio, *d*/*w* up to 0.9.

iv) A modified design equation based on DSM guidelines provided in AISI S100-16 (2016), for design of perforated tubular stub columns, considering perforation size ratios and cross-section slenderness, has been proposed.

6.2 SUGESSIONS FOR FUTURE WORK

This final section of the thesis presents suggestions to potential research areas that can be conducted in the future. The section has been classified into two sub-sections: the first sub-section describes the probable areas where the present work can be extended directly; and the second sub-section deals with general thoughts that have been identified during the course of present research work.

6.2.1 Extension to present research work

The present research work on YSt-310 cold-formed steel tubular sections has been limited to stub columns at ambient temperature only, however, to the best of author's knowledge, performance of stub columns (both unperforated and perforated) considering temperature effects have not been studied previously. Therefore, the study can be extended further through experimental and numerical studies. In the case of numerical approach, the study can be directly carried out by considering FE models validated against the ambient temperature stub columns test results and replacing the ambient temperature material properties with the elevated temperature or post-fire mechanical properties provided in this thesis.

The present work on the performance of YSt-310 tubular sections has been focused on pure axial compression. The study on member behaviour considering various

loading protocols such as eccentric, bending, shear, cyclic (including both low and high cyclic) and their combinations through experimental and numerical investigations is suggested.

The effects of size two opposite central circular perforations on the compressive column capacity of tubular sections have been presented in Chapter 5 of this thesis. Hence, the study could also be enlarged to include the influence of different perforation shapes (e.g., elliptical, square, rhombus, flat oval), number (singular or multiple) etc. Moreover, the study can be extended to long columns and their behaviour can be investigated by considering various perforation effects such as shape, sizes and locations.

It has been demonstrated by many researchers as well as present study that the introduction of perforations on structural members may result in the redistribution of stress near the perforation, thereby resulting in the reduction of ultimate member capacity. Different form of stiffeners may be employed to compensate the loss in member capacity due to perforation and thus represent another scope for extension of present research work on perforation. The study can investigate the most optimal way to regain the perforated member capacity back to parent member based on the perforation shape, size etc.

The Continuous Strength Method (CSM) is a new deformation based design approach and the steps involved in the estimation of design column capacity are relatively simple, as observed in Chapter 3. The presently design method for unperforated members can be further extended for perforated members, using accurate test or FE member capacities.

6.2.2 Other thoughts

Metallic 3D printing technology is one of the most interesting and prospective research area that has come across during the course of present work. The research topic has the potential to completely transform the construction technology currently

followed all around the world, to a most efficient design-building process. Till date, the research work in the field of 3D printed tubular section, connections, tapered section, perforated members etc., are very limited and hence, the potential of 3D technology in such area may be conducted in the future.

Additionally, research works on high-strength steel and stainless steel (e.g., lean duplex stainless steel) are increasingly popular in the last decade. Attempts are being made to develop efficient design equations based on existing hot-rolled design equations. Therefore, the extension of the present work on perforated members to these materials would be an interesting topic. Moreover, the applicability of the proposed design equation for stub columns and their extension to long columns, beams and torsional member could be conducted experimentally and numerically.

Furthermore, the current research programme in confined to quasi-static loading and hence, the behaviour of structures under extreme loading such as blast, impact, hydrocarbon fire loading etc., are some of the important research areas that could be conducted in the future. Also, the studies on this thesis are generally on member level (stub columns), and thus, it can be extended to portal frames. The structural performance of frames can be used in the development of direct analysis.

References

Abaqus. (2010). Abaqus/Standard user's manual volumes I-III and ABAQUS CAE Manual, Version 6.9.

Afshan, S. and Gardner, L. (2013). The continuous strength method for structural stainless steel design. *Thin-Walled Structures*, **68**, 42–49.

Afshan, S., Rossi, B. and Gardner, L. (2013). Strength enhancements in cold-formed structural sections—Part I: Material testing. *Journal of Constructional Steel Research*, **83**, 177–188.

Ahmed, S., Ashraf, M. and Anwar-Us-Saadat, M. (2016). The Continuous Strength Method for slender stainless steel cross-sections. *Thin-Walled Structures*, **107**, 362–376.

AISC 360. (2010). Specification for Structural Steel Buildings, ANSI/AISC 360-10, American Institution of Steel Construction, Chicago.

AISI. (1968). Specifications for the Design of Cold-Formed Steel Structural Members. New York: American Iron and Steel Institute (AISI).

AISI S100-07. (2007). North American Specification for the Design of Cold-Formed Steel Structural Members. *American Iron and Steel Institute (AISI), Washington, DC, USA.*

AISI S100-16. (2016). North American Specification for the Design of Cold-Formed Steel Structural Members. *American Iron and Steel Institute (AISI), Washington, DC.*

AISI S100-16C. (2016). Commentary on North American Specification for the

Design of Cold-Formed Steel Structural Members. *American Iron and Steel Institute (AISI), Washington, DC.*

Aluminum Design Manual. (2005). The Aluminum Association (AA), Washington, D.C., USA.

Anwar-us-saadat, M., Ashraf, M. and Ahmed, S. (2016). Behaviour and design of stainless steel slender cross-sections subjected to combined loading. *Thin Walled Structures*, **104**, 225–237.

Aoki, T., Migita, Y. and Fukumoto, Y. (1991). Local buckling strength of closed polygon folded section columns. *Journal of Constructional Steel Research*, **20**, 259–270.

Arivalagan, S. and Kandasamy, S. (2010). Test of void-filled SHS beams under cyclic loading. *Journal of Reinforced Plastics and Composites*, **29**, 1534–1544.

Arrayago, I., Rasmussen, K.J.R. and Real, E. (2017). Full slenderness range DSM approach for stainless steel hollow cross-sections. *Journal of Constructional Steel Research*, **133**, 156–166.

Arrayago, I. and Real, E. (2015). Experimental study on ferritic stainless steel RHS and SHS cross-sectional resistance under combined loading. *Structures*, **4**, 69–79.

Arrayago, I., Real, E. and Gardner, L. (2015). Description of stress–strain curves for stainless steel alloys. *Materials and Design*, **87**, 540–552.

Arrayago, I., Real, E. and Mirambell, E. (2013). Constitutive equations for stainless steels: Experimental tests and new proposal. *Research and Applications in Structural Engineering, Mechanics and Computation*, 513–514.

AS/NZS 4600. (2005). Cold-formed steel structures, Australian/New Zealand Standards, New Zealand.

AS 2291. (2007). Methods for the Tensile Testing of Metals at Elevated Temperature, Australian Standard AS 2291, Standard Association of Australia, Australia.

AS 4100. (1998). Australian Standards: Steel Structures. Sydney.

ASCE. (2002). Specification for the design of cold-formed stainless steel structural members. SEI/ASCE 8-02,. *American Society of Civil Engineers, Reston, Verginia*.

Ashraf, M., Gardner, L. and Nethercot, D.A. (2005). Strength enhancement of the corner regions of stainless steel cross-sections. *Journal of Constructional Steel Research*, **61**, 37–52.

ASTM E21. (2009). ASTM, Standard Test Methods for Elevated Temperature Tension Tests of Metallic Materials. *ASTM International, West Conshohocken, PA, United States*.

ASTM E8 / E8M. (2015). E8/E8M - 15a: Standard Test Methods for Tension Testing of Metallic Materials. *ASTM International, West Conshohocken, PA, United States*.

Azhari, F., Heidarpour, A. and Zhao, X.L. (2018). Post-fire behavior of cold-formed ultra-high strength steel tubular stub columns. *Tubular Structures XVI - Proceedings of the 16th International Symposium on Tubular Structures, ISTS 2017*, 305–310.

Balarupan, M. (2015). Structural behaviour and design of cold-formed steel hollow columns under simulated fire conditions, PhD Thesis. Queensland University of Technology, Brisbane, Australia.

Becque, J., Lecce, M. and Rasmussen, K.J.R. (2008). The direct strength method for stainless steel compression members. *Journal of Constructional Steel Research*, **64**, 1231–1238.

Becque, J. and Wilkinson, T. (2017). The capacity of grade C450 cold-formed rectangular hollow section T and X connections: An experimental investigation. *Journal of Constructional Steel Research*, **133**, 345–359.

BS 5950-5. (1998). Structural use of steelwork in building - Part 5: Code of practice for design of cold formed thin gauge sections. *British Standard Institution*.

BS 5950. (2003). Structural Use of Steel Work in Buildings - Part 8: Code of Practice for Fire Restraint Design. *British Standards Institute, London*.

Cai, Y., Quach, W.-M., Chen, M.-T. and Young, B. (2019). Behavior and design of cold-formed and hot-finished steel elliptical tubular stub columns. *Journal of Constructional Steel Research*, **156**, 252–265.

Chajes, A., Britvec, S.J. and Winter, G. (1963). Effects of cold-straining on structural sheet steels. *Journal of the Structural Division*, **89**, 1–32.

Chan, T.M. and Gardner, L. (2008). Compressive resistance of hot-rolled elliptical hollow sections. *Engineering Structures*, **30**, 522–532.

Chan, T.M., Gardner, L. and Law, K.H. (2010). Structural design of elliptical hollow sections: a review. *Proceedings of the Institution of Civil Engineers - Structures and Buildings*, **163**, 391–402.

Chen, J.-F. and Cao, P.-Z. (2010). Experimental investigation into mechanical properties of steel post high temperatures. *Journal of PLA University of Science and Technology*, **11**, 328–333.

Chen, J. and Young, B. (2007). Experimental investigation of cold-formed steel material at elevated temperatures. *Thin-Walled Structures*, **45**, 96–110.

Chen, J., Young, B. and Brian, U. (2006). Behavior of High Strength Structural Steel at Elevated Temperatures. *Journal of Structural Engineering*, **132**, 1948–1954.

Chen, M.-T. and Young, B. (2018a). Cross-sectional behavior of cold-formed steel semi-oval hollow sections. *Engineering Structures*, **177**, 318–330.

Chen, M.-T. and Young, B. (2018b). Experimental and numerical investigation on cold-formed steel semi-oval hollow section compression members. *Journal of Constructional Steel Research*, **151**, 174–184.

Chen, M.-T. and Young, B. (2019). Material properties and structural behavior of cold-formed steel elliptical hollow section stub columns. *Thin-Walled Structures*, **134**, 111–126.

Chen, M.T. and Young, B. (2018c). Experimental study on cold-formed steel semi-oval hollow section columns. *In Tubular Structures XVI - Proceedings of the 16th International Symposium on Tubular Structures, ISTS 2017*. CRC Press, 549–556.

Chen, Z., Lu, J., Liu, H. and Liao, X. (2016). Experimental study on the post-fire mechanical properties of high-strength steel tie rods. *Journal of Constructional Steel Research*, **121**, 311–329.

Cheng, B., Wang, J. and Li, C. (2013). Compression behavior of perforated plates in steel tower anchorage zones of cable-stayed bridges. *Journal of Constructional Steel Research*, **90**, 72–84.

Cruise, R.B. (2007). The influence of production routes on the behaviour of stainless steel structural, PhD Thesis. Imperial College London (University of London).

Cruise, R.B. and Gardner, L. (2006). Measurement and prediction of geometric imperfections in structural stainless steel members. *Structural Engineering and Mechanics*, **24**, 63–89.

Cruise, R.B. and Gardner, L. (2008). Strength enhancements induced during cold forming of stainless steel sections. *Journal of constructional steel research*, **64**, 1310–1316.

Davison, T.A. and Birkemoe, P.C. (1983). Column behaviour of cold-formed hollow structural steel shapes. *Canadian Journal of Civil Engineering*, **10**, 125–141.

Dawson, R.G. and Walker, A.C. (1972). Post-buckling of geometrically imperfect plates. *Journal of the Structural Division*, **98**, 75–94.

DD ENV 1993-1-1. (1992). Eurocode 3: Design of steel structures — Part 1.1: General rules and rules for buildings. *European Committee for Standardization (CEN), Brussels*.

Desmond, T.P., Peköz, T. and Winter, G. (1978). Local and overall buckling of cold formed compression members. *Department of Structural Engineering Report, Cornell University*.

Desmond, T.P., Winter, G. and Peköz, T. (1981a). Edge stiffeners for thin-walled members. *Journal of the Structural Division*, **107**, 329–353.

Desmond, T.P., Winter, G. and Peköz, T. (1981b). Intermediate stiffeners for thin-walled members. *Journal of the Structural Division*, **107**, 627–648.

Dhanalakshmi, M. and Shanmugam, N.E. (2001). Design for openings in equal-angle

cold-formed steel stub columns. *Thin-walled structures*, **39**, 167–187.

Dias, W.P.S. (1992). Some properties of hardened cement paste and reinforcing bars upon cooling from elevated temperatures. *Fire and materials*, **16**, 29–35.

Ding, F., Yu, Z. and Wen, H. (2006). Experimental research on mechanical properties of Q235 steel after high temperature treatment. *Journal of building materials*, **2**.

Dwight, J.B. (1969). Welded Steel Plates in Compression. *The Structural Engineering*, **47**, 49–66.

EC3-1-1. (2005). Eurocode 3: Design of steel structures–Part 1-1: General rules and rules for buildings. *European Standard, European Committee for Standardization (CEN), Brussels*.

EC3-1-12. (2007). Eurocode 3: Design of steel structures - Part 1-12: Additional rules for the extension of EN 1993 up to steel grades S 700. *European Standard, European Committee for Standardization (CEN), Brussels*.

EC3-1-2. (2005). Eurocode 3: Design of steel structures - Part 1-2: General rules - Structural fire design. *European Standard, European Committee for Standardization (CEN), Brussels*.

EC3-1-5. (2006). Eurocode 3: Design of steel structures–Part 1-5: Plated structural elements. *European Committee for Standardization (CEN), Brussels*.

EC9-1-1. (2007). Eurocode 9: Design of aluminium structures - Part 1-1: General Structural rules. *European Committee for Standardization, CEN, Brussels, Belgium.*

Ellobody, E. and Young, B. (2005a). Behavior of cold-formed steel plain angle columns. *Journal of structural engineering*, **131**, 457–466.

Ellobody, E. and Young, B. (2005b). Structural performance of cold-formed high strength stainless steel columns. *Journal of Constructional Steel Research*, **61**, 1631–1649.

EN 1993-1-1:2005/A1. (2014). Eurocode 3: Design of steel structures - Part 1-1: General rules and rules for buildings. *European Standard, European Committee for Standardization (CEN), Brussels*.

EN 1993-1-1. (2005). Eurocode 3: Design of steel structures–Part 1-1: General rules and rules for buildings. *European Standard, European Committee for Standardization (CEN), Brussels*.

EN 1993-1-5:2006/A1. (2017). Eurocode 3: Design of steel structures–Part 1-5: Plated structural elements. *European Standard, European Committee for Standardization (CEN), Brussels*.

EN 1993-1-5. (2006). Eurocode 3: Design of steel structures–Part 1-5: Plated structural elements. *European Standard, European Committee for Standardization (CEN), Brussels*.

Faulkner, D. (1975). A review of effective plating for use in the analysis of stiffened plating in bending and compression. *Journal of Ship research*, **19**, 1–17.

Felicetti, R., Gambarova, P.G. and Meda, A. (2009). Residual behavior of steel rebars and R/C sections after a fire. *Construction and building materials*, **23**, 3546–3555.

Feng, Mou, X., Chen, A. and Ma, Y. (2016). Tests of aluminium alloy CHS columns with circular openings. *Thin-Walled Structures*, **109**, 113–131.

Feng, R. and Young, B. (2015). Experimental investigation of aluminum alloy stub columns with circular openings. *Journal of Structural Engineering*, **141**, 4015031.

Feng, Sun, W., Shen, C. and Zhu, J. (2017). Experimental investigation of aluminum square and rectangular beams with circular perforations. *Engineering Structures*, **151**, 613–632.

Frankland, J.M. (1940). The strength of ship plating under edge compression. *David Taylor Model Basin Report*, **469**.

Gao, X., Zhang, X., Liu, H., Chen, Z. and Li, H. (2018). Residual mechanical properties of stainless steels S30408 and S31608 after fire exposure. *Construction and Building Materials*, **165**, 82–92.

Gardner, L. (2002). A new approach to structural stainless steel design, PhD Thesis. Imperial College London, UK.

Gardner, L. (2008). The continuous strength method. *Proceedings of the Institution of Civil Engineers - Structures and Buildings*, **161**, 127–133.

Gardner, L. and Chan, T.-M. (2007). Cross-section classification of elliptical hollow sections. *Steel and Composite Structures*, **7**, 185–200.

Gardner, L. and Nethercot, D.A. (2004). Numerical modeling of stainless steel structural components—a consistent approach. *Journal of Structural Engineering*, **130**, 1586–1601.

Gardner, L., Saari, N. and Wang, F. (2010). Comparative experimental study of hot-rolled and cold-formed rectangular hollow sections. *Thin-Walled Structures*, **48**, 495–507.

Gardner, L. and Yun, X. (2018). Description of stress-strain curves for cold-formed steels. *Construction and Building Materials*, **189**, 527–538.

Gardner, L., Yun, X., Macorini, L. and Kucukler, M. (2017). Hot-rolled steel and steel-concrete composite design incorporating strain hardening. *In Structures*. Elsevier, 21–28.

Gardner, Wang, F. and Liew, A. (2011). Influence of strain hardening on the behavior and design of steel structures. *International Journal of Structural Stability and Dynamics*, **11**, 855–875.

GB 50429. (2007). Code for design of Aluminium Structure,. *Chinese Code, China Planning Press, Beijing*.

Ghazijahani, T.G., Jiao, H. and Holloway, D. (2014). Influence of a cutout on circular steel hollow sections under cyclic loading. *Journal of Constructional Steel Research*, **100**, 12–20.

Godat, A., Legeron, F. and Bazonga, D. (2012). Stability investigation of local buckling behavior of tubular polygon columns under concentric compression. *Thin-Walled Structures*, **53**, 131–140.

Gunalan, S. and Mahendran, M. (2014). Experimental investigation of post-fire mechanical properties of cold-formed steels. *Thin-Walled Structures*, **84**, 241–254.

Guo, Y.-J., Zhu, A.-Z., Pi, Y.-L. and Tin-Loi, F. (2007). Experimental study on compressive strengths of thick-walled cold-formed sections. *Journal of constructional steel research*, **63**, 718–723.

Hancock, G.J. and Zhao, X.-L. (1992). Research into the strength of cold-formed tubular sections. *Journal of Constructional Steel Research*, **23**, 55–72.

Hansen, T., Gath, J. and Nielsen, M.P. (2010). An improved effective width method based on the theory of plasticity. *Advanced Steel Construction*, **6**, 515–547.

Hu, S.-D., Ye, B. and Li, L.-X. (2011). Materials properties of thick-wall cold-rolled welded tube with a rectangular or square hollow section. *Construction and Building Materials*, **25**, 2683–2689.

Hu, Y., Yang, C.B., Teh, L.H. and Yang, Y.-B. (2018). Reduction factors for stainless steel bolts at elevated temperatures. *Journal of Constructional Steel Research*, **148**, 198–205.

Huang, Y. (2013). Behaviour and design of cold-formed lean duplex stainless steel members, PhD Thesis. The University of Hong Kong (Pokfulam, Hong Kong).

Huang, Y. and Young, B. (2012). Material properties of cold-formed lean duplex stainless steel sections. *Thin-walled structures*, **54**, 72–81.

Huang, Y. and Young, B. (2017). Post-fire behaviour of ferritic stainless steel material. *Construction and Building Materials*, **157**, 654–667.

Huang, Y. and Young, B. (2014a). Stress–strain relationship of cold-formed lean duplex stainless steel at elevated temperatures. *Journal of Constructional Steel Research*, **92**, 103–113.

Huang, Y. and Young, B. (2014b). Structural performance of cold-formed lean duplex stainless steel columns. *Thin-Walled Structures*, **83**, 59–69.

Huang, Y. and Young, B. (2014c). The art of coupon tests. *Journal of Constructional Steel Research*, **96**, 159–175.

Imran, M., Mahendran, M. and Keerthan, P. (2018). Mechanical properties of cold-formed steel tubular sections at elevated temperatures. *Journal of Constructional Steel Research*, **143**, 131–147.

IS 4923. (1997). Hollow Steel Sections for Structural Use – Specification. *Indian Standard, Bureau of Indian Standards, New Delhi*.

IS 800. (2007). General Construction in Steel - Code of Practice. *Indian Standard, Bureau of Indian Standards, New Delhi*.

ISO 6892-2. (2011). Metallic Materials - Tensile Testing: Part 2. Method of Test at Elevated Temperature. *British Standard Institution (BSI), London, UK*.

Jia-Lin, M., Chan, T.-M. and Young, B. (2016). Experimental investigation of cold-formed high strength steel tubular beams. *Engineering Structures*, **126**, 200–209.

Kalyanaraman, V. and Peköz, T. (1978). Analytical study of unstiffened elements. *Journal of the Structural Division*, **104**, 1507–1524.

Kalyanaraman, V., Peköz, T. and Winter, G. (1972). Performance of unstiffened compression elements. Department of Structural Engineering Report.

Kankanamge, N.D. and Mahendran, M. (2011). Mechanical properties of cold-formed steels at elevated temperatures. *Thin-Walled Structures*, **49**, 26–44.

Karman, T. Von, Sechler, E.E. and Donnell, L.H. (1932). The strength of thin plates in compression. *Trans. ASME*, **54**, 53–57.

Karren, K.W. (1967). Corner properties of cold-formed steel shapes. *Journal of the Structural Division*, **ST1**, 401–432.

Karren, K.W. and Winter, G. (1965). Effects of cold-forming on light-gage steel members.

Kavousi Sisi, A. and Mirsalehi, S.E. (2015). Prediction of microstructure and mechanical properties of line pipe welded joints based on hardness map. *Science and Technology of Welding and Joining*, **21**, 43–52.

Kesawan, S. and Mahendran, M. (2018). Post-fire mechanical properties of cold-formed steel hollow sections. *Construction and Building Materials*, **161**, 26–36.

Key, P.W., Hasan, S.W. and Hancock, G.J. (1988). Column behavior of cold-formed hollow sections. *Journal of Structural Engineering*, **114**, 390–407.

Kim, D.-K., Lee, C.-H., Han, K.-H., Kim, J.-H., Lee, S.-E. and Sim, H.-B. (2014).

Strength and residual stress evaluation of stub columns fabricated from 800MPa high-strength steel. *Journal of Constructional Steel Research*, **102**, 111–120.

Kim, U.-N., Choe, I.-H. and Paik, J.K. (2009). Buckling and ultimate strength of perforated plate panels subject to axial compression: experimental and numerical investigations with design formulations. *Ships and Offshore Structures*, **4**, 337–361.

Kirby, B.R., Lapwood, D.G. and Thomson, G. (1986). The reinstatement of fire damaged steel and iron framed structures. *British Steel Corporation, Swinden Laboratories, 1986*, 79.

Ko, W.L. (1998). Mechanical- and thermal-buckling behavior of rectangular plates with different central cutouts, NASA/TM–1998–206542 Edwards, CA., USA: Dryden Flight Research Center. National Aeronautics and Space Administration.

Kodur, V., Dwaikat, M. and Fike, R. (2010). High-temperature properties of steel for fire resistance modeling of structures. *Journal of Materials in Civil Engineering*, **22**, 423–434.

Kulatunga, M.P., Macdonald, M., Rhodes, J. and Harrison, D.K. (2014). Load capacity of cold-formed column members of lipped channel cross-section with perforations subjected to compression loading–Part I: FE simulation and test results. *Thin-Walled Structures*, **80**, 1–12.

Kumai, T. (1951). Elastic stability of the square plate with a central circular hole under edge thrust. *In Japan National Congress for Applied Mechanics*. 81–86.

Lagaros, N.D., Psarras, L.D., Papadrakakis, M. and Panagiotou, G. (2008). Optimum design of steel structures with web openings. *Engineering Structures*, **30**, 2528–2537.

Larsson, P.-L. (1987). On buckling of orthotropic compressed plates with circular holes. *Composite Structures*, **7**, 103–121.

Lecce, M. (2006). Distortional buckling of stainless steel sections, PhD Thesis. Department of Civil Engineering, University of Sydney.

Lecce, M. and Rasmussen, K. (2006). Distortional buckling of cold-formed stainless

steel sections: Finite-element modeling and design. *Journal of Structural Engineering*, **132**, 505–514.

Lee, J., Engelhardt, M.D. and Taleff, E.M. (2012). Mechanical properties of ASTM A992 steel after fire. *Engineering Journal*, **49**, 33–44.

Li, D., Huang, Z., Uy, B., Thai, H.-T. and Hou, C. (2019). Slenderness limits for fabricated S960 ultra-high-strength steel and composite columns. *Journal of Constructional Steel Research*, **159**, 109–121.

Li, H.-T. and Young, B. (2017a). Material properties of cold-formed high strength steel at elevated temperatures. *Thin-Walled Structures*, **115**, 289–299.

Li, H.-T. and Young, B. (2018). Residual mechanical properties of high strength steels after exposure to fire. *Journal of Constructional Steel Research*, **148**, 562–571.

Li, H.-T. and Young, B. (2017b). Tests of cold-formed high strength steel tubular sections undergoing web crippling. *Engineering Structures*, **141**, 571–583.

Lian, Y., Uzzaman, A., Lim, J.B.P., Abdelal, G., Nash, D. and Young, B. (2017). Web crippling behaviour of cold-formed steel channel sections with web holes subjected to interior-one-flange loading condition-Part I: Experimental and numerical investigation. *Thin-Walled Structures*, **111**, 103–112.

Liang, Y., Manninen, T., Zhao, O., Walport, F. and Gardner, L. (2019). Elevated temperature material properties of a new high-chromium austenitic stainless steel. *Journal of Constructional Steel Research*, **152**, 261–273.

Liew, A. and Gardner, L. (2015). Ultimate capacity of structural steel cross-sections under compression, bending and combined loading. *Structures*, **1**, 2–11.

Liew, J.Y.R., Shanmugam, N.E. and Lee, S.L. (1989). Local buckling of thin-walled steel box columns. *Thin-walled structures*, **8**, 119–145.

Lind, N.C., Ravindra, M.K. and Power, J. (1971). A review of the effective width formula.

Liu, D., Liu, H., Chen, Z. and Liao, X. (2017a). Structural behavior of extreme thick-walled cold-formed square steel columns. *Journal of Constructional Steel Research*, **128**, 371–379.

Liu, H., Liao, X., Chen, Z. and Huang, S.-S. (2017b). Post-fire residual mechanical properties of steel butt weld — Experimental study. *Journal of Constructional Steel Research*, **129**, 156–162.

Liu, T.C.H. and Chung, K.F. (2003). Steel beams with large web openings of various shapes and sizes: finite element investigation. *Journal of Constructional Steel Research*, **59**, 1159–1176.

Lu, J., Liu, H. and Chen, Z. (2017a). Post-fire mechanical properties of low-relaxation hot-dip galvanized prestressed steel wires. *Journal of Constructional Steel Research*, **136**, 110–127.

Lu, J., Liu, H., Chen, Z. and Bisby, L. (2017b). Experimental investigation of the residual mechanical properties of cast steels after exposure to elevated temperature. *Construction and Building Materials*, **143**, 259–271.

Lu, J., Liu, H., Chen, Z. and Liao, X. (2016). Experimental investigation into the post-fire mechanical properties of hot-rolled and cold-formed steels. *Journal of Constructional Steel Research*, **121**, 291–310.

Ma, Chan, T.-M. and Young, B. (2015). Material properties and residual stresses of cold-formed high strength steel hollow sections. *Journal of Constructional Steel Research*, **109**, 152–165.

Ma, J.-L., Chan, T.-M. and Young, B. (2016). Experimental Investigation on Stub-Column Behavior of Cold-Formed High-Strength Steel Tubular Sections. *Journal of Structural Engineering*, **142**, 4015174.

Ma, J. (2016). Behaviour and design of cold-formed high strength steel tubular members, PhD Thesis. The University of Hong Kong, Pokfulam, Hong Kong.

Macdonald, M., Taylor, G.T. and Rhodes, J. (1997). The effect of cold forming on the yield strength of thin gauge steel—hardness test approach. *Thin-walled structures*, **29**, 243–256.

Mander, J.B. (1983). Seismic Design of Bridge Piers, PhD. University of Canterbury, Christchurch, New Zealand.

Marshall, N.S. and Nurick, G.N. (1970). The effect of induced imperfections on the

formation of the first lobe of symmetric progressive buckling of thin-walled square tubes. *WIT Transactions on The Built Environment*, **35**, 0–14.

McCann, F., Gardner, L. and Kirk, S. (2015). Elevated temperature material properties of cold-formed steel hollow sections. *Thin-Walled Structures*, **90**, 84–94.

Miller, T.H. and Peköz, T. (1994). Unstiffened strip approach for perforated wall studs. *Journal of Structural Engineering*, **120**, 410–421.

Mirambell, E. and Real, E. (2000). On the calculation of deflections in structural stainless steel beams: an experimental and numerical investigation. *Journal of Constructional Steel Research*, **54**, 109–133.

Moen, C.D. (2008). Direct strength design of cold-formed steel members with perforations, PhD Thesis. Civil Engineering, Johns Hopkins University.

Moen, C.D. and Schafer, B.W. (2011). Direct strength method for design of cold-formed steel columns with holes. *Journal of Structural Engineering*, **137**, 559–570.

Moen and Schafer, B.W. (2009). Elastic buckling of thin plates with holes in compression or bending. *Thin-Walled Structures*, **47**, 1597–1607.

Moen and Schafer, B.W. (2008). Experiments on cold-formed steel columns with holes. *Thin-Walled Structures*, **46**, 1164–1182.

Narayanan, R. and Chow, F.Y. (1984). Ultimate capacity of uniaxially compressed perforated plates. *Thin-Walled Structures*, **2**, 241–264.

Narayanan, R. and Rockey, K.C. (1981). Ultimate load capacity of plate girders with webs containing circular cut-outs. *Proceedings of the institution of civil engineers*, **71**, 845–862.

Narendra, P.V.R. and Singh, K.D. (2016). Structural performance of elliptical hollow section (EHS) steel tubular braces under extremely low cycle fatigue loading-a finite element study. *Thin-Walled Structures*, **109**, 202–216.

Neves, I.C., Rodrigues, J.P.C. and Loureiro, A. de P. (1996). Mechanical properties of reinforcing and prestressing steels after heating. *Journal of Materials in Civil Engineering*, **8**, 189–194.

Nikolaou, J. and Papadimitriou, G.D. (2004). Microstructures and mechanical properties after heating of reinforcing 500 MPa class weldable steels produced by various processes (Tempcore, microalloyed with vanadium and work-hardened). *Construction and Building Materials*, **18**, 243–254.

Ortiz-Colberg, R.A. (1981). The load carrying capacity of perforated cold-formed steel columns, PhD Thesis. Ithaca, NY: Cornell University.

Outinen, J. (2007). Mechanical Properties of Structural Steels at Elevated Temperatures and After Cooling Down, PhD Thesis. Helsinki University of Technology, Helsinki, Finland.

Outinen, J., Kaitila, O. and Mäkeläinen, P. (2001). High-temperature testing of structural steel and modelling of structures at fire temperatures. Department of Civil and Environmental Engineering, Helsinki University of Technology.

Outinen, J. and Mäkeläinen, P. (2004). Mechanical properties of structural steel at elevated temperatures and after cooling down. *Fire and Materials*, **28**, 237–251.

Pastor, M.M., Casafont, M., Bonada, J. and Roure, F. (2014). Imperfection amplitudes for nonlinear analysis of open thin-walled steel cross-sections used in rack column uprights. *Thin-Walled Structures*, **76**, 28–41.

Patton, M.L. and Singh, K.D. (2012). Numerical modeling of lean duplex stainless steel hollow columns of square, L-, T-, and+-shaped cross sections under pure axial compression. *Thin-Walled Structures*, **53**, 1–8.

Pellegrino, C., Maiorana, E. and Modena, C. (2009). Linear and non-linear behaviour of steel plates with circular and rectangular holes under shear loading. *Thin-Walled Structures*, **47**, 607–616.

Pu, Y., Godley, M.H.R., Beale, R.G. and Lau, H.H. (1999). Prediction of ultimate capacity of perforated lipped channels. *Journal of structural Engineering*, **125**, 510–514.

Qiang, X., Bijlaard, F. and Kolstein, H. (2012a). Dependence of mechanical properties of high strength steel S690 on elevated temperatures. *Construction and Building Materials*, **30**, 73–79.

Qiang, X., Bijlaard, F.S.K. and Kolstein, H. (2012b). Post-fire mechanical properties of high strength structural steels S460 and S690. *Engineering Structures*, **35**, 1–10.

Qiang, X., Bijlaard, F.S.K. and Kolstein, H. (2013). Post-fire performance of very high strength steel S960. *Journal of Constructional Steel Research*, **80**, 235–242.

Rasmussen, K.J.R. and Hancock, G.J. (1993). Design of cold-formed stainless steel tubular members. II: Beams. *Journal of Structural Engineering*, **119**, 2368–2386.

Rasmussen, K.J.R. and Hancock, G.J. (1992). Plate slenderness limits for high strength steel sections. *Journal of Constructional Steel Research*, **23**, 73–96.

Rasmussen, K.J.R. and Hancock, G.J. (1995). Tests of high strength steel columns. *Journal of Constructional Steel Research*, **34**, 27–52.

Real, E., Arrayago, I., Mirambell, E. and Westeel, R. (2014). Comparative study of analytical expressions for the modelling of stainless steel behaviour. *Thin-Walled Structures*, **83**, 2–11.

Ringle, H.L. (1969). Effects of cold roll-forming on the mechanical properties of square welded steel tubes, National Steel Corporation, Research and Developement Department, Project No. 5-501. Weirton,West Virginia.

Ritchie, D. and Rhodes, J. (1975). Buckling and post-buckling behaviour of plates with holes. *The Aeronautical Quarterly*, **26**, 281–296.

Rogers, C.A. and Hancock, G.J. (1997). Ductility of G550 sheet steels in tension. *Journal of Structural Engineering*, **123**, 1586–1594.

Rossi, B., Afshan, S. and Gardner, L. (2013). Strength enhancements in cold-formed structural sections — Part II : Predictive models. *Journal of Constructional Steel Research*, **83**, 189–196.

Rossi, B., Jaspart, J.-P. and Rasmussen, K.J.R. (2009). Combined Distortional and Overall Flexural-Torsional Buckling of Cold-Formed Stainless Steel Sections: Design. *Journal of Structural Engineering*, **136**, 361–369.

Rossi, B. and Rasmussen, K.J.R. (2013). Carrying Capacity of Stainless Steel Columns in the Low Slenderness Range. *Journal of Structural Engineering*, **139**,

1088–1092.

Saad-Eldeen, S., Garbatov, Y. and Guedes Soares, C. (2016). Experimental strength assessment of thin steel plates with a central elongated circular opening. *Journal of Constructional Steel Research*, **118**, 135–144.

Sachidananda, K. and Singh, K.D. (2015). Numerical study of fixed ended lean duplex stainless steel (LDSS) flat oval hollow stub column under pure axial compression. *Thin-walled structures*, **96**, 105–119.

Sachidananda, K. and Singh, K.D. (2017). Structural behaviour of fixed ended stocky Lean Duplex Stainless Steel (LDSS) flat oval hollow column under axial compression. *Thin-Walled Structures*, **113**, 47–60.

Saliba, N. and Gardner, L. (2013). Cross-section stability of lean duplex stainless steel welded I-sections. *Journal of Constructional Steel Research*, **80**, 1–14.

Schafer and Ádány, S. (2006). Buckling analysis of cold-formed steel members using CUFSM: conventional and constrained finite strip methods. *In Proceedings of the18th international specialty conference on cold-formed steel structures*. 39–54.

Schafer, B.W. and Peköz, T. (1998a). Computational modeling of cold-formed steel: characterizing geometric imperfections and residual stresses. *Journal of Constructional Steel Research*, **47**, 193–210.

Schafer, B.W. and Peköz, T. (1998b). Direct Strength Prediction of Cold-Formed Steel Members Using Numerical Elastic Buckling Solutions. *In 14th International Specialy Conference on Cold-Formed Steel Structures*. New York: St. Louis, Missouri, 69–76.

Schafer and Peköz, T. (1999). Laterally braced cold-formed steel flexural members with edge stiffened flanges. *Journal of Structural Engineering*, **125**, 118–127.

Schlack, A.L. (1964). Elastic stability of pierced square plates. *Experimental Mechanics*, **4**, 167–172.

Schuster, R.M. (1992). Testing of perforated C-studs sections in bending, Report for the Canadian Sheet Steel Building Institute, University of Waterloo. Waterloo

Ontario.

Seif and Schafer, B.W. (2010). Local buckling of structural steel shapes. *Journal of Constructional Steel Research*, **66**, 1232–1247.

Shakerley, T.M. and Brown, C.J. (1996). Elastic buckling of plates with eccentrically positioned rectangular perforations. *International journal of mechanical sciences*, **38**, 825–838.

Shan, M.Y., A., L.R. and W., Y.W. (1996). Bending and shear behavior of web elements with openings. *Journal of Structural Engineering*, **122**, 854–859.

Shan, M.Y., Batson, K.D., LaBoube, R.A. and Yu, W.W. (1994a). Local buckling flexural strength of webs with openings. *Engineering Structures*, **16**, 317–323.

Shan, M.Y., LaBoube, R.A. and Yu, W. (1994b). Behavior of web elements with openings subjected to bending, shear and the combination of bending and shear, Final Report. 2nd ed. Civil Engineering Series 94-2. Cold-Formed Steel Series, Department of Civil Engineering, University of Missouri-Rolla, Rolla, MO.

Shanmugam, N.E. (1997). Openings in Thin-Walled steel structures. *Thin-Walled Structures*, **28**, 355–372.

Shanmugam, N.E. and Dhanalakshmi, M. (2001). Design for openings in cold-formed steel channel stub columns. *Thin-walled structures*, **39**, 961–981.

Shanmugam, N.E., Thevendran, V. and Tan, Y.H. (1999). Design formula for axially compressed perforated plates. *Thin-Walled Structures*, **34**, 1–20.

Shariati, M. and Rokhi, M.M. (2008). Numerical and experimental investigations on buckling of steel cylindrical shells with elliptical cutout subject to axial compression. *Thin-Walled Structures*, **46**, 1251–1261.

Shi, G., Zhou, W. and Lin, C. (2015). Experimental investigation on the local buckling behavior of 960 MPa high strength steel welded section stub columns. *Advances in Structural Engineering*, **18**, 423–437.

Silvestre, N., Pires, T. and Duarte, A.P.C. (2013). Numerical analysis of semi-elliptical hollow section columns. *Proceedings of the Institution of Civil Engineers-Structures and Buildings*, **166**, 424–433.

Singh, T.G. and Singh, K.D. (2019). Semi-elliptical LDSS Hollow Stub Columns Under Axial Compression. *In Recent Advances in Structural Engineering, Volume 1*. Springer, 327–337.

Sivakumaran, K.S. and Zielonka, K.M. (1989). Web crippling strength of thin-walled steel members with web opening. *Thin-Walled Structures*, **8**, 295–319.

Smith, C.I., Kirby, B.R., Lapwood, D.G., Cole, K.J., Cunningham, A.P. and Preston, R.R. (1981). The reinstatement of fire damaged steel framed structures. *Fire Safety Journal*, **4**, 21–62.

Somodi, B. and Kövesdi, B. (2017). Residual stress measurements on cold-formed HSS hollow section columns. *Journal of Constructional Steel Research*, **128**, 706–720.

Sonu, J.K. and Singh, K.D. (2017a). Shear behaviour of single perforated lean duplex stainless steel (LDSS) rectangular hollow beams. *Thin-Walled Structures*, **119**, 851–867.

Sonu, J.K. and Singh, K.D. (2017b). Shear characteristics of Lean Duplex Stainless Steel (LDSS) rectangular hollow beams. *Structures*, **10**, 13–29.

Su, M.-N., Young, B. and Gardner, L. (2014). Testing and design of aluminum alloy cross sections in compression. *Journal of Structural Engineering*, **140**, 4014047.

Su, M.-N., Young, B. and Gardner, L. (2016). The continuous strength method for the design of aluminium alloy structural elements. *Engineering Structures*, **122**, 338–348.

Tabor, D. (1951). The hardness of metals. London, UK: Oxford university press.

Tao, Z., Wang, X.-Q., Hassan, M.K., Song, T.-Y. and Xie, L.-A. (2018). Behaviour of three types of stainless steel after exposure to elevated temperatures. *Journal of Constructional Steel Research*.

Tao, Z., Wang, X.-Q. and Uy, B. (2012). Stress-strain curves of structural and reinforcing steels after exposure to elevated temperatures. *Journal of Materials in Civil Engineering*, **25**, 1306–1316.

Tata Steel. (2013). Tata steel production manual for YSt 310 Rectangular, Square and

Circular steel hollow section. Kolkata: Tata Steel Limited.

Tata Structura Tubes Division. (2019). Tata Steel Available at: http://www.tatastructura.com/ [Accessed April 23, 2019].

Theofanous, M., Chan, T.M. and Gardner, L. (2009a). Flexural behaviour of stainless steel oval hollow sections. *Thin-Walled Structures*, **47**, 776–787.

Theofanous, M., Chan, T.M. and Gardner, L. (2009b). Structural response of stainless steel oval hollow section compression members. *Engineering Structures*, **31**, 922–934.

Theofanous, M. and Gardner, L. (2010). Experimental and numerical studies of lean duplex stainless steel beams. *Journal of Constructional Steel Research*, **66**, 816–825.

Theofanous, M. and Gardner, L. (2009). Testing and numerical modelling of lean duplex stainless steel hollow section columns. *Engineering Structures*, **31**, 3047–3058.

Tran, A.T., Veljkovic, M., Rebelo, C. and da Silva, L.S. (2016). Resistance of cold-formed high strength steel circular and polygonal sections - Part 2: Numerical investigations. *Journal of Constructional Steel Research*, **125**, 227–238.

Umbarkar, K.R., Patton, L.M. and Singh, K.D. (2013). Effect of single circular perforation in lean duplex stainless steel (LDSS) hollow circular stub columns under pure axial compression. *Thin Walled Structures*, **68**, 18–25.

Uzzaman, A., Lim, J.B.P., Nash, D., Rhodes, J. and Young, B. (2012). Web crippling behaviour of cold-formed steel channel sections with offset web holes subjected to interior-two-flange loading. *Thin-Walled Structures*, **50**, 76–86.

Vann, W.P. (1971). Compressive buckling of perforated plate elements. *In First Specialty conference on cold-formed structures*. Rolla, 58–64.

Vilnay, O. and Rockey, K.C. (1981). A generalised effective width method for plates loaded in compression. *Journal of Constructional Steel Research*, **1**, 3–12.

Wang, J., Afshan, S., Schillo, N., Theofanous, M., Feldmann, M. and Gardner, L. (2017). Material properties and compressive local buckling response of high

strength steel square and rectangular hollow sections. *Engineering Structures*, **130**, 297–315.

Wang, L. and Young, B. (2017). Design of cold-formed steel built-up sections with web perforations subjected to bending. *Thin-Walled Structures*, **120**, 458–469.

Wang, W., Liu, T. and Liu, J. (2015). Experimental study on post-fire mechanical properties of high strength Q460 steel. *Journal of Constructional Steel Research*, **114**, 100–109.

Wang, X., Tao, Z., Song, T. and Han, L. (2014). Stress – strain model of austenitic stainless steel after exposure to elevated temperatures. *Journal of Constructional Steel Research*, **99**, 129–139.

Wei, Y., Guo, Y., Sun, Q. and Zhang, B. (2013). Study on local stability of Q690 high-strength steel tube under axial compression. *China Civil Engineering Journal*, **46**, 1–12.

Winful, D.A., Cashell, K.A., Afshan, S., Barnes, A.M. and Pargeter, R.J. (2017). Elevated temperature material behaviour of high-strength steel. *Proceedings of the Institution of Civil Engineers - Structures and Buildings*, **170**, 777–787.

Winter, G. (1947). Strength of thin steel compression flanges. *Trans. ASCE*, **112**, 527.

Winter, G. and Pian, R.H.J. (1946). Crushing Strength of thin steel webs. Ithaca, N.Y., N.Y.: Cornell University.

Yang, D. and Hancock, G.J. (2004). Compression tests of cold-reduced high strength steel sections. I: stub columns. *Journal of Structural Engineering*, **130**, 1772–1781.

Yang, F., Liu, Y. and Xin, H. (2018). Negative bending capacity prediction of composite girders based on continuous strength method. *Thin-Walled Structures*, **129**, 278–288.

Yao, Z. and Rasmussen, K.J.R. (2014). Design of Perforated thin-walled steel columns. Sydney.

Yao, Z. and Rasmussen, K.J.R. (2012). Inelastic local buckling behaviour of perforated plates and sections under compression. *Thin-Walled Structures*, **61**,

49–70.

Yao, Z. and Rasmussen, K.J.R. (2016). Perforated Cold-Formed Steel Members in Compression. II: Design. *Journal of Structural Engineering*, **143**, 4016227.

Yao, Z., Rasmussen, K.J.R., Ph, D., Rasmussen, K.J.R. and Asce, M. (2016). Perforated Cold-Formed Steel Members in Compression. I: Parametric Studies. *Journal of Structural Engineering*, **143**, 4016226.

Ye, J. and Chen, W. (2012). Elevated temperature material degradation of cold-formed steels under steady-and transient-state conditions. *Journal of Materials in Civil Engineering*, **25**, 947–957.

Young, B. (2008). Experimental and numerical investigation of high strength stainless steel structures. *Journal of Constructional Steel Research*, **64**, 1225–1230.

Young, B. and Lui, W.-M. (2005). Behavior of cold-formed high strength stainless steel sections. *Journal of Structural Engineering*, **131**, 1738–1745.

Yu, C.K. and Tall, L. (1969). Significance and Application of Stub Column Test Results. Bethlehem, Pennsylvania.

Yu and Schafer, B.W. (2007). Effect of longitudinal stress gradients on elastic buckling of thin plates. *Journal of engineering mechanics*, **133**, 452–463.

Yu, W.-W. and Davis, C.S. (1973). Cold-formed steel members with perforated elements. *Journal of the structural division*, **99**, 2061–2077.

Yun, X. and Gardner, L. (2018). The continuous strength method for the design of cold-formed steel non-slender tubular cross-sections. *Engineering Structures*, **175**, 549–564.

Zhang, X.-Z., Liu, S., Zhao, M.-S. and Chiew, S.-P. (2016). Comparative experimental study of hot-formed, hot-finished and cold-formed rectangular hollow sections. *Case Studies in Structural Engineering*, **6**, 115–129.

Zhang, Y.J., Zhu, Y., Zhao, S. and Hu, K.X. (2009). Experimental research on mechanical properties of steel cooled in different modes after high temperature treatment. *Structural Engineers*, **25**, 104–109.

Zhao, O., Afshan, S. and Gardner, L. (2017). Structural response and continuous strength method design of slender stainless steel cross-sections. *Engineering Structures*, **140**, 14–25.

Zhao, O., Rossi, B., Gardner, L. and Young, B. (2015a). Behaviour of structural stainless steel cross-sections under combined loading–Part II: Numerical modelling and design approach. *Engineering Structures*, **89**, 247–259.

Zhao, O., Rossi, B., Gardner, L. and Young, B. (2015b). Experimental and numerical studies of ferritic stainless steel tubular cross sections under combined compression and bending. *Journal of Structural Engineering*, **142**, 4015110.

Zhao, Rossi, B., Gardner, L. and Young, B. (2015c). Behaviour of structural stainless steel cross-sections under combined loading – Part I: Experimental study. *Engineering Structures*, **89**, 236–246.

Zhao, X.-L. (2000). Section capacity of very high strength (VHS) circular tubes under compression. *Thin-Walled Structures*, **37**, 223–240.

Zhao, X.-L., Van Binh, D., Al-Mahaidi, R. and Tao, Z. (2004). Stub column tests of fabricated square and triangular sections utilizing very high strength steel tubes. *Journal of Constructional Steel Research*, **60**, 1637–1661.

Zhao, X., Tootkaboni, M. and Schafer, B.W. (2015d). Development of a Laser-Based Geometric Imperfection Measurement Platform with Application to Cold-Formed Steel Construction. *Experimental Mechanics*, **55**, 1779–1790.

Zhao, X.L. and Packer, J.A. (2009). Tests and design of concrete-filled elliptical hollow section stub columns. *Thin-Walled Structures*, **47**, 617–628.

Zhou, F. and Young, B. (2010). Web crippling of aluminium tubes with perforated webs. *Engineering Structures*, **32**, 1397–1410.

Zhu, A., Zhu, H., Zhang, X. and Lu, Y. (2016). Experimental study and analysis of inner-stiffened cold-formed SHS steel stub columns. *Thin-Walled Structures*, **107**, 28–38.

Zhu, J.-H. and Young, B. (2011). Cold-Formed-Steel Oval Hollow Sections under Axial Compression. *Journal of Structural Engineering*, **137**, 719–727.

Zhu, Y. and Wilkinson, T. (2018). Finite element analysis of structural steel elliptical hollow sections in pure compression. *In Tubular Structures XI*. 179–186.

Zhu and Young, B. (2012). Design of cold-formed steel oval hollow section columns. *Journal of Constructional Steel Research*, **71**, 26–37.

Publications

Journals:

1) **Singh, T. G.**, & Singh, K. D. (2017). Structural performance of YSt-310 cold-formed tubular steel stub columns. ***Thin-Walled Structures***, 121, 25–40.
2) **Singh, T. G.**, & Singh, K. D. (2018). Experimental investigation on performance of perforated cold-formed steel tubular stub columns. ***Thin-Walled Structures***, 131, 107–121.
3) **Singh, T. G.**, & Singh, K. D. (2019). Post-fire mechanical properties of YSt-310 cold-formed tubular steel sections. ***Journal of Constructional Steel Research***, 153, 654–666
4) **Singh, T. G.**, & Singh, K. D. (2019). Mechanical properties of YSt-310 cold-formed steel tubular sections at elevated temperatures, ***Journal Constructional Steel Research***, 158, 53–70.
5) **Singh, T. G**., & Singh, K. D., Numerical modelling and design of perforated coldformed steel tubular stub columns: DSM approach (*Under preparation*)

Conferences:

1) **Singh, T. G.**, & Singh, K. D. (2018).Capacity of cold-formed steel hollow stub columns with central circular perforations. ***Ninth International Conference on Advances in Steel Structures (ICASS18)***. Department of Civil and Environmental Engineering, The Hong Kong Polytechnic University, Hong Kong, China.
2) **Singh, T. G.**, & Singh, K. D. (2019). Design of Perforated Cold-formed Steel

Tubular Stub Columns. ***17th International Symposium on Tubular Structures (ISTS17).*** Department of Civil and Environmental Engineering, National University of Singapore, Singapore (Full paper submitted).

Appendix A

ESTIMATION OF COLUMN CAPACITY BASED ON DESIGN EQUATIONS FOR UNPERFORATED STUB COLUMNS

Problem: To estimate the nominal Stub column capacity of a RHS having member dimension as 300 × 200 × 10.0 *L*800

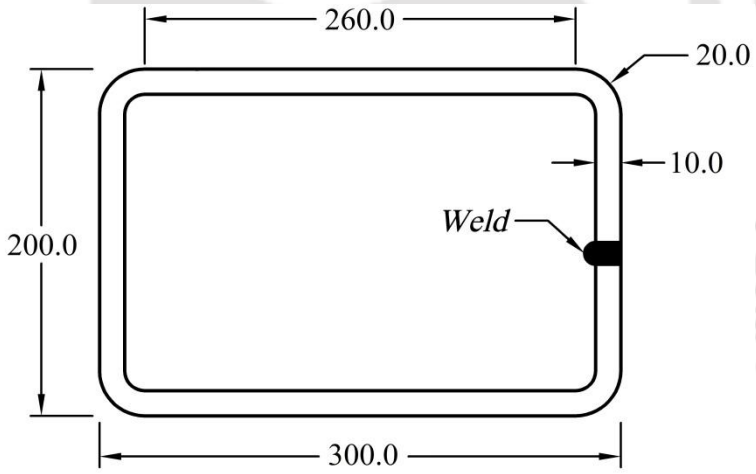

Figure B-1: Cross-sectional dimensions of RHS

Geometric and mechanical properties are detailed below:

i) Geometric properties:

Gross area, $A_g = 9342.48$ mm^2

Minimum $I_g = I_{gx} = 61443000.95$ mm^4

Minimum $r_x = 81.10$ mm

ii) Column capacity based on finite element (FE) results:

$P_{FE} = 4379.40$ kN

Displacement corresponding to ultimate load, δ_u = 4.75

iii) Mechanical properties

E =190653.0 MPa; f_y = 440.26 MPa

(Based on 66.0 × 33.0 × 2.6 cross-sectional material properties)

Cross-section elastic buckling stress, $\sigma_{cr,cs}$ = 1080.31 (from Abaqus (2010)

A.1 Design as per EC3-1-1 (2005):

A.1.1 Calculation of equivalent flat element width, $b_{eq,\,flat}$ considering the effect of element interaction:

A.1.1.1 For more slender element of width, B of RHS:

$$b_{eq,cl} = \sqrt{\frac{k\pi^2 Et^2}{12(1-\nu^2)} \times \frac{1}{\sigma_{cr,cs}}} = \sqrt{\frac{4\pi^2 \times 190653 \times 10^2}{12 \times (1-0.3^2)} \times \frac{1}{1080.31}} = 252.59 \text{ mm} \quad \text{(A.1-1)}$$

$$b_{flat} = 300.0 - 2\times10.0 - 2\times10.0 = 260.0 \text{ mm} \quad \text{(A.1-2)}$$

$$b_{cl} = 300.0 - 10.0 = 290.0 \text{ mm} \quad \text{(A.1-3)}$$

$$\therefore\ b_{eq,\,flat} = c = b_{eq,cl} \times \frac{b_{flat}}{b_{cl}} = 252.59 \times \frac{260.0}{290.0} = 226.46 \text{ mm} \quad \text{(A.1-4)}$$

A.1.1.1 For less slender element of width, D of RHS:

$$b_{flat} = 200.0 - 2\times10.0 - 2\times10.0 = 160.0 \text{ mm} \quad \text{(A.1-5)}$$

$$\therefore\ b_{eq,\,flat} = c = b_{flat} = 160.0 \text{ mm} \quad \text{(A.1-6)}$$

A.1.2 Cross-section classification:

In EC3 (2005), cross-sections are classified based on the parameter, $c/t\varepsilon$ of the most slender plate element:

if $c/t\varepsilon \le 42.0$, then the cross-section belongs to Class–3 sections

if $c/t\varepsilon > 42.0$, then the cross-section belongs to Class–4 sections (A.1-7)

$$\text{where, } \varepsilon = \left(\frac{235}{f_y} \times \frac{190653}{210000}\right)^2 = 0.70$$

For the member considered, the parameter, $c/t\varepsilon$ is calculated as:

$$c/t\varepsilon = \frac{226.46}{10.0*0.7} = 32.35 \leq 42.0$$

Hence, the cross-section belongs to Class–3 Section.

A.1.3 Calculation of stub column capacity, P_{EN}

Since the cross-section belongs to Class–3 Section, the cross-sectional area is fully effective. The stub column capacity (based on EC3-1-1, 2005) is estimated as

$$P_{EN} = A_g f_y = 9342.48*440.26 = \mathbf{4113.12\ kN} \quad \text{(A.1-8)}$$

A.2 Design as per Continuous Strength Method (CSM):

The axial strength of the stub column based on CSM can be estimated using Equation A.2-1:

$$P_{csm} = \begin{cases} f_{CSM} A & \text{for } \bar{\lambda}_p \leq 0.68 \\ \frac{\varepsilon_{csm}}{\varepsilon_y} A f_y & \text{for } \bar{\lambda}_p > 0.68 \end{cases} \quad \text{(A.2-1)}$$

The cross-sectional slenderness, $\bar{\lambda}_p$ is calculated using Equation A.2-2:

$$\bar{\lambda}_p = \sqrt{f_y/\sigma_{cr,cs}} = \sqrt{440.26/1080.31} = 0.64 \leq 0.68 \quad \text{(A.2-2)}$$

Since $\bar{\lambda}_p \leq 0.68$, the deformation capacity $\left(\varepsilon_{csm}/\varepsilon_y\right)$ of the cross-section is calculated using Equation A.2-3, using the base curve base curves (detailed in Afshan and Gardner, 2013; Zhao *et al.*, 2017) for both non-slender sections and slender sections:

$$\frac{\varepsilon_{CSM}}{\varepsilon_y} = \frac{0.25}{\bar{\lambda}_p^{3.6}} = 1.2579 \text{ but } \frac{\varepsilon_{csm}}{\varepsilon_y} \le \min\left(15, \frac{C_1 \times \varepsilon_u}{\varepsilon_y} = \frac{0.4 \times 0.0751}{2.309 \times 10^{-3}} = 13.0\right) \quad \text{(A.2-3)}$$

where,

$$\varepsilon_u = C_3\left(1 - \frac{f_u}{f_y}\right) + C_4 = 0.6\left(1 - \frac{503.29}{440.26}\right) + 0.0 = 0.0751 \quad \text{(A.2-4)}$$

$$\varepsilon_y = \frac{f_y}{E} = \frac{440.26}{190653} = 2.309 \times 10^{-3} \quad \text{(A.2-5)}$$

The CSM design stress is calculated using Equation A.2-6:

$$f_{csm} = f_y + E_{sh}\varepsilon_y\left(\frac{\varepsilon_{csm}}{\varepsilon_y} - 1\right) \quad \text{(A.2-6)}$$

in which, the strain hardening slope is calculated using Equation A.2-7:

$$E_{sh} = \frac{f_u - f_y}{C_2\varepsilon_u - \varepsilon_y} = \frac{503.29 - 440.26}{0.45 \times 0.0751 - 2.0309 \times 10^{-3}} = 2000.66 \text{ MPa} \quad \text{(A.2-7)}$$

$$\therefore \quad f_{csm} = 440.26 + 2000.66 \times 2.30 \times 10^{-3}(1.2579 - 1) = 441.45 \text{ MPa} \quad \text{(A.2-8)}$$

Hence, the axial capacity of stub column based on CSM design approach is estimated by using Equation A.2-1:

P_{CSM} = 441.45×9342.478 = **4124.25 kN**

A.3 Design as per Direct Strength Method (DSM):

A.3.1 Determination of yielding and global buckling:

Nominal column strength as per Section E of AISI S100 – 16 (2016) is the minimum of (P_{ne}, P_{nl}, P_{nd}). Please note that P_{nd} is not considered since the cross-section considered is a closed/ tubular section.

$$P_{DSM} = \min\left(P_{ne}, P_{nl}\right) \tag{A.3-1}$$

The nominal axial capacity (P_{ne}) for yielding and global buckling is estimated based on Section E2 of AISI S100-16 (2016), given by Equation A.3-2:

$$P_{ne} = A_g F_n \tag{A.3-2}$$

in which,

$$F_n = \begin{cases} \left(0.658^{\lambda_c^2}\right) f_y & \text{for } \lambda_c \le 1.5 \\ \left(\dfrac{0.877}{\lambda_c^2}\right) f_y & \text{for } \lambda_c > 1.5 \end{cases} \tag{A.3-3}$$

$$\lambda_c = \sqrt{f_y / F_{cre}} \tag{A.3-4}$$

where,

$$F_{cre} = \frac{\pi^2 E}{(KL/r_x)^2} = \frac{\pi^2 \times 190653}{(1\times 800/81.10)^2} = 19337.71 \text{ MPa} \tag{A.3-5}$$

Slenderness factor, λ_c is calculated using Equation A.3-6:

$$\lambda_c = \sqrt{f_y / F_{cre}} = \sqrt{440.26/19337.71} = 0.151 \tag{A.3-6}$$

Since, $\lambda_c \le 1.5; F_n = \left(0.658^{\lambda_c^2}\right) f_y = \left(0.658^{0.151^2}\right) \times 440.26 =$ **436.08 MPa** (A.3-7)

$P_{ne} = A_g F_n$ = 9342.48× 436.08 = **4074.11 kN** (A.3-8)

Note: P_{ne} = ~ P_y for short columns.

The nominal axial strength for local buckling based on DSM ($P_{nl\text{-}DSM}$) detailed in E3.2.1 of AISI S100-16 (2016) and is calculated using Equation A.3-9:

$$P_{nl-DSM} = \begin{cases} P_{ne} & \text{for } \lambda_l \le 0.776 \\ \left[1 - 0.15\left(\dfrac{P_{crl}}{P_{ne}}\right)^{0.4}\right]\left(\dfrac{P_{crl}}{P_{ne}}\right)^{0.4} P_{ne} & \text{for } \lambda_l > 0.776 \end{cases} \tag{A.3-9}$$

in which

$$\lambda_l = \sqrt{P_{ne} / P_{crl}} \tag{A.3-10}$$

AISI S100-16 (2016) presents the guidelines for determining the critical elastic local buckling force, P_{crl} in Appendix 2, Section 2.3.1.2. Based on this section, P_{crl} shall be based on the lowest buckling stress among all the elements in the cross-section.

$$P_{crl} = A_g f_{crl} \tag{A.3-11}$$

in which,

$$f_{crl} = k \frac{\pi^2 E}{12(1-\upsilon^2)} \left(\frac{t}{w} \right)^2 \tag{A.3-12}$$

where,

k = 4.0

υ = 0.3

w = 300.0 – 2×10.0 – 2×10.0 = 260.0 mm

$\therefore f_{crl}$ = 1019.61 MPa

The critical elastic local buckling force is calculated using Equation A-24:

P_{crl} = 9342.48×1019.61 = **9525.68 kN** (A.3-13)

$$\therefore \lambda_l = \sqrt{\frac{4074.11}{9525.68}} = 0.65 \tag{A.3-14}$$

Since λ_l < 0.776, the nominal axial strength for local buckling, $P_{nl\text{-}DSM}$ is estimated using Equation A3-9:

$P_{nl\text{-}DSM} = P_{ne}$ = **4074.11 kN** (A.3-15)

A.4 Design as per Rossi and Rasmussen (2013):

The nominal axial strength for local buckling based the design curve proposed by Rossi and Rasmussen (2013) is given by Equations A.4-1:

$$\frac{P_{nl-RR}}{P_y} = \begin{cases} 1+\left(1-2.11\lambda_l\right)\left(\dfrac{\sigma_u}{\sigma_{0.2}}-1\right) & \text{for } \lambda_l \le 0.474 \\ \dfrac{0.95}{\lambda_l^{0.8}} - \dfrac{0.22}{\lambda_l^{1.6}} & \text{for } \lambda_l > 0.474 \end{cases} \quad \text{(A.4-1)}$$

where, $P_y = A_g f_y = 9342.48 \times 440.26 = 4113.12$ kN

The procedure to determine the slenderness factor, λ_l is same as those presented in Equations A.3-2 to A.3-14.

$$\therefore \lambda_l = \sqrt{\frac{4074.11}{9525.68}} = 0.65 \quad \text{(A.4-2)}$$

Since $\lambda_l > 0.474$, the nominal axial strength for local buckling, $P_{nl\text{-}RR}$ is estimated using Equation A-30:

$$P_{nl-RR} = \left(\frac{0.95}{0.65^{0.8}} - \frac{0.22}{0.65^{1.6}}\right)4113.12 = \mathbf{3712.50\ kN} \quad \text{(A.4-3)}$$

A.5 Design as per Arrayago *et al.* (2017):

The nominal axial strength for local buckling based the design curve proposed by Arrayago *et al.* (2017) is given by Equations A.5-1:

$$\frac{P_{nl-ARR}}{P_y} = \begin{cases} 1+(1-1.29\lambda_l)\left(\dfrac{\sigma_u}{\sigma_{0.2}}-1\right) & \text{for } \lambda_l \le 0.776 \\ \dfrac{1}{\lambda_l^{0.8}} - \dfrac{0.15}{\lambda_l^{1.6}} & \text{for } \lambda_l > 0.776 \end{cases} \quad \text{(A.5-1)}$$

where, $P_y = A_g f_y$ = 9342.48*440.26 = 4113.12 kN

The procedure to determine the slenderness factor, λ_l is same as those presented in Equations A.3-2 to A.3-14.

$$\therefore \lambda_l = \sqrt{\frac{4074.11}{9525.68}} = 0.65 \quad \text{(A.5-2)}$$

Since λ_l > 0.474, the nominal axial strength for local buckling, $P_{nl\text{-}ARR}$ is estimated using Equation A.5-1:

$$P_{nl-ARR} = \left[1+(1-1.29\times 0.65)\left(\frac{503.29}{440.26}-1\right)\right]4113.12 = \mathbf{4208.22\ kN} \quad \text{(A.5-3)}$$

A.6 Design as per Proposed DSM*:

The nominal axial strength for local buckling based the design curve proposed in this chapter is given by Equations A.6-1:

$$\frac{P^*_{DSM}}{P_{ne}} = \begin{cases} \dfrac{0.9516}{\lambda_l^{0.2016}} & \text{for } \lambda_l \le 0.776 \\ \dfrac{0.776}{\lambda_l^{0.8}} + \dfrac{0.03}{\lambda_l^{1.6}} & \text{for } \lambda_l > 0.776 \end{cases} \quad \text{(A.6-1)}$$

The procedure to determine the nominal axial capacity (P_{ne}) for yielding and global buckling, based on Section E2 of AISI S100-16 (2016), is same as those given in Equation A.3-2 to A.3-8:

$$\therefore\ P_{ne} = A_g F_n = 9342.48^{*}\ 439.57 = \mathbf{4074.11\ kN} \qquad \text{(A.6-2)}$$

Again, the procedure to determine the slenderness factor, λ_l is same as those presented in Equations A.3-10 to A.3-14.

$$\therefore \lambda_l = \sqrt{\frac{4074.11}{9525.68}} = 0.65 \qquad \text{(A.6-3)}$$

Since $\lambda_l > 0.776$, the nominal axial strength for local buckling based on the design curve proposed in this chapter, P^{*}_{DSM} is estimated using Equation A.6-1:

$$P^{*}_{DSM} = \left(\frac{0.9516}{0.65^{0.2016}}\right) 4074.11 = \mathbf{4228.67\ kN}$$

This page is intentionally left blank.

Appendix B

ESTIMATION OF COLUMN CAPACITY BASED ON DESIGN EQUATIONS FOR PERFORATED STUB COLUMNS

Problem: To estimate the nominal Stub column capacity of a RHS having member dimension as 300 × 200 × 10.0 *d*/*w*0.9*L*800

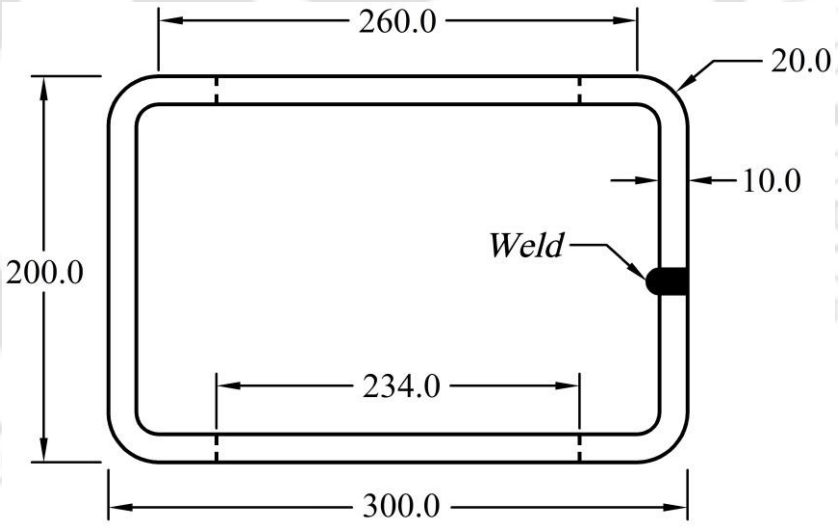

Figure B-1: Cross-sectional dimensions of perforated RHS

i) Geometric properties:

$A_g = 9342.48\,\text{mm}^2$

$A_{net} = 4662.48\,\text{mm}^2$

A_{net}/A_g = 4662.48/9342.48 = 0.5

Minimum $I_g = I_{gx}$ = 61443000.95 mm^4

Minimum $I_{net} = I_{gx,net}$ = 19167000.95 mm^4

ii) Column capacity based on FE

P_{FE-P} = 2491.54 kN

iii) Mechanical properties

E =204082MPa; f_y = 444.55 MPa

(Based on 60 × 60 × 2.9 cross-sectional material properties)

$\therefore P_{ynet}$ = 4662.48*444.55 = 2072.70 kN

B.1 Design based on Shanmugam *et al.* (1999):

The ultimate column capacity considering the equation proposed by Shanmugam *et al.* (1999), P_{STT} is given by the following Equation B.1-1:

$$\frac{P_{STT}}{P_{sq}} = k_1\left[\frac{A_0}{A_s}\right] + k_2\left[\frac{A_0}{A_s}\right]^{1/2} + k_3 \qquad \text{(B.1-1)}$$

The above equation is utilised to predict the ultimate capacity of perforated and unperforated plate. However, the corner area is considered to be fully effective. The axial strength from the corner part, P_{STT-C} is calculated area:

$\therefore$ Total corner area = π*(2*10.0*10.0 + 10.0^2) = 942.48 mm^2

$$P_{STT-C} = 942.48*444.55 = \mathbf{418.98\ kN} \qquad \text{(B.1-2)}$$

B.1.1 Calculation of axial capacity for plate without perforation:

$w = 200 - 2*10 - 2*10 = 160.0$ mm

w/t = 160.0/10.0 = 16.0

m = $(w/t)/100$ = 0.16

A_0 = 0.0 mm^2

A_s = 160.0*800.0 = 128000 mm^2

Since the plate being considered does not have perforation, the coefficient k_1, k_2 and k_3 are considered for perforation size ratio, $0.0 < d/w < 0.4$. The following equations are employed to determine the coefficients:

$$k_1 = -4m^2 + 1.58m - 0.1286 = 0.0218$$
$$k_2 = 3m^2 - 1.52m - 0.8674 = -1.0338 \quad \text{(B.1-3)}$$
$$k_3 = -m^2 + 0.49m + 0.9585 = 1.0113$$

The squash load, P_{sq} is calculated using Equation B.1-4, detailed below:

$$P_{sq} = A_g f_y = 160.0 * 10 * 444.55 = 711.28 \text{ kN} \quad \text{(B.1-4)}$$

The ultimate axial capacity of the unperforated plate, P_{STT-UP} is estimated using Equation B.1-5:

$$P_{STT-UP} = P_{sq}\left(k_1\left[\frac{A_0}{A_s}\right] + k_2\left[\frac{A_0}{A_s}\right]^{1/2} + k_3 \right) = \mathbf{719.32\ kN}$$

B.1.2 Calculation of axial capacity for plate with perforation:

$w = 300.0 - 2*10.0 - 2*10.0 = 260.0$ mm

w/t = 260.0/10.0 = 26.0

m = $(w/t)/100$ = 0.26

$A_0 = \pi d^2/4 = 43005.26$ mm^2

A_s = 260.0*800.0 = 208000.0 mm^2

A_0/A_s = 0.21

$\sqrt{A_0/A_s} = 0.45$

Since the perforation size ratio d/w = 0.9, the coefficient k_1, k_2 and k_3 are considered for perforation size ratio, $0.4 < d/w < 0.7$. The following equations are employed to determine the coefficients:

$$k_1 = 0.0 \quad \text{(B.1-6)}$$

$k_2 = -0.96$
$k_3 = 0.973$

The squash load, P_{sq} is calculated using Equation B.1-7, detailed below:

$$P_{sq} = A_g f_y = 260.0*10.0*444.55 = 1155.83 \text{ kN} \quad \text{(B.1-7)}$$

The ultimate axial capacity of the unperforated plate, P_{STT-P} is estimated using Equation B.1-8:

$$P_{STT-P} = P_{sq}\left(k_1\left[\frac{A_0}{A_s}\right] + k_2\left[\frac{A_0}{A_s}\right]^{1/2} + k_3 \right) = \mathbf{625.30\ kN} \quad \text{(B.1-8)}$$

The axial capacity of the perforated member shall be the sum of individual axial capacity of the all the elements and is calculated using Equations B.1-2, B.1-5 and B.1-8.

$\therefore P_{STT} = P_{STT-C} + 2* P_{STT-UP} + 2* P_{STT-P} = \mathbf{3108.22\ kN}$

B.2 Design based on Dhanalakshmi and Shanmugam (2001):

The ultimate column capacity considering the equation developed by Dhanalakshmi and Shanmugam (2001), P_{DS} is given by the following Equation B.2-1:

$$\frac{P_{DS}}{P_{sq}} = k_1\left[\frac{A_0}{A_s}\right] + k_2\left[\frac{A_0}{A_s}\right]^{1/2} + k_3 \quad \text{(B.2-1)}$$

The parameters are estimated based on the stub column geometric properties, detailed below:

Unperforated plate width, $w = 200 - 2*10 - 2*10 = 160.0\,\text{mm}$ (B.2-2)

Unperforated plate width, $w_0 = 300 - 2*10 - 2*10 = 260.0\,\text{mm}$ (B.2-3)

∴ Slenderness of the stub column, w/t = 260.0/10.0 = 26.0

$m = (w/t)/100 = 0.26$ (B.2-4)

$A_0 = 2*\pi d^2/4 = 86010.52$ mm^2

$A_s = 2*w_0L + 2*wL + 2\pi(t + r_i) = 672125.66$ mm^2

$A_0/A_s = 0.13$

$\sqrt{A_0/A_s} = 0.36$ (B.2-5)

The following Equation (B.2-6) is employed to determine the coefficient k_1, k_2 and k_3:

$$\begin{aligned} k_1 &= -4.5579m^2 + 4.4862m - 1.3724 = -0.5141 \\ k_2 &= -0.8107m^2 + 1.0577m - 0.3354 = -0.1152 \\ k_3 &= 2.5357m^2 - 2.8364m + 1.0908 = 0.5247 \end{aligned} \quad \text{(B.2-6)}$$

The squash load, P_{sq} is calculated using Equation B.2-7, detailed below:

$$P_{sq} = A_g f_y = 9342.48*444.55 = \mathbf{4153.20\ kN} \quad \text{(B.2-7)}$$

The ultimate axial capacity of the perforated column based on the proposal made by Dhanalakshmi and Shanmugam (2001), P_{DS} is estimated by using Equation B.2-1:

$$P_{DS} = P_{sq}\left(k_1\left[\frac{A_0}{A_s}\right] + k_2\left[\frac{A_0}{A_s}\right]^{1/2} + k_3\right) = \mathbf{1729.37\ kN}$$

B.3 Design based on Shanmugam and Dhanalakshmi (2001):

The ultimate column capacity considering the equation developed by Shanmugam and Dhanalakshmi (2001), P_{SD} is given by the following Equation B.3-1:

$$\frac{P_{SD}}{P_{sq}} = k_1\left[\frac{A_0}{A_s}\right] + k_2\left[\frac{A_0}{A_s}\right]^{1/2} + k_3 \quad \text{(B.3-1)}$$

The steps to estimate the parameters are same with those provided in Equations B.2-2 – B.2-5. However, the coefficients k_1, k_2 and k_3 are determined using Equation B.3.2:

$$\begin{aligned} k_1 &= 1.185m^3 - 3.8487m^2 + 3.7321m - 1.2336 = -0.50 \\ k_2 &= 0.1111m^2 + 0.0932m - 0.7763 = -0.74 \\ k_3 &= 0.1100m^2 - 0.5681m + 1.1412 = 1.00 \end{aligned} \quad \text{(B.3-2)}$$

The squash load, P_{sq} is calculated using Equation B.3-3, detailed below:

$$P_{sq} = A_g f_y = 9342.48 * 444.55 = \mathbf{4153.20\ kN} \quad \text{(B.3-3)}$$

The axial capacity of the perforated column based on the proposal made by Shanmugam and Dhanalakshmi (2001), P_{SD} is estimated by using Equation B.3-1:

$$P_{SD} = P_{sq}\left(k_1\left[\frac{A_0}{A_s}\right] + k_2\left[\frac{A_0}{A_s}\right]^{1/2} + k_3 \right) = \mathbf{2776.83\ kN}$$

B.4 Design as per AISI S100-16 (2016):

Nominal column strength as per Section E of AISI S100-16 (2016) is the minimum of (P_{ne}, P_{nl}, P_{nd}). Please note that P_{nd} is not considered in the present study.

The nominal axial capacity (P_{ne}) for yielding and global buckling is estimated based on Section E2 of AISI S100-16 (2016) as follows:

$$I_{avg} = \frac{I_g L_g + I_{net} L_{net}}{L} = 49077270.95\ \text{mm}^4$$

K = Effective length factor = 1.0 (See Chapter C of AISI S100–16, 2016)

I_g = 61443000.95 mm^4

I_{net} = 19167000.95 mm^4

L_g = Segment length without hole = 566.00 mm

L_{net} = Segment length without hole = 234.00 mm

The nominal strength for flexural buckling (P_{ne}) is calculated using Equation B.4-1 – B.4-4 discussed below:

F_{cre} = Elastic global buckling stress estimated based on Section 2.3.2.1.1, Appendix 2 of AISI S100-16 (2016), provided in Equation B.4-1:

$$F_{cre} = \frac{\pi^2 EI_{avg}}{A_g (KL)^2} = \frac{\pi^2 * 204082 * 49077270.95}{614430000.95 * (1*800)^2} = \mathbf{16532.66\ MPa} \quad \text{(B.4-1)}$$

Slenderness factor, λ_c is calculated using Equation B.4-2:

$$\lambda_c = \sqrt{f_y / F_{cre}} = 0.164 \quad \text{(B.4-2)}$$

$$\text{Since, } \lambda_c \leq 1.5; F_n = \left(0.658^{\lambda_c^2}\right) f_y = \left(0.658^{0.164^2}\right) * 444.55 = \mathbf{439.57\ MPa} \quad \text{(B.4-3)}$$

$$P_{ne} = A_g F_n = 9342.48 * 439.57 = \mathbf{4106.72\ kN} \quad \text{(B.4-4)}$$

AISI S100-16 (2016) provides the guidelines for determining the nominal axial strength (P_{nl}) for local buckling interacting with yielding and global buckling either through *Effective Width Method* (EWM) of Section E3.1 or the *Direct Strength Method* (DSM), detailed below:

B.4.1 Effective Width Method (EWM):

The nominal axial strength for local buckling based on *Effective Width Method* ($P_{nl\text{-}EWM}$) in AISI S100-16 (2016) is calculated using Equation B.4-5:

$$P_{nl\text{-}EWM} = A_e F_n \leq P_{ne} \quad \text{(B.4-5)}$$

where A_e is the effective area calculated in accordance with E3.1.2 of AISI S100-16 (2016). A_e is estimated using Equations B.4-6–B.4-8 given below.

$$A_e = \sum_{i=1}^{4} b_i w + \text{Total corner area} \quad \text{(B.4-6)}$$

where *b* is the effective width of all four flat elements of the rectangular cross-section. The effective width *b* is calculated in accordance with Appendix 1.1.1(a) and Appendix 1.1(a) of AISI S100-16 (2016) for uniformly compressed stiffened elements with and without circular perforation respectively.

B.4.1.1 Effective width for flat elements without perforation:

$$w = 200 - 2*10 - 2*10 = 160.0 \text{ mm} \quad \text{(B.4-7)}$$

$$f_{crl} = 4* \frac{\pi^2 E}{12(1-0.3^2)} \left(\frac{10}{160.0} \right)^2 = \mathbf{2882.05\ MPa} \quad \text{(B.4-8)}$$

$$\lambda = \sqrt{\frac{F_n}{f_{crl}}} = \sqrt{\frac{439.57}{2882.05}} = 0.39 \quad \text{(B.4-9)}$$

The local reduction factor, ρ is calculated using the Equation B.4-10, given below:

$$\rho = \begin{cases} 1 & \text{for } \lambda \leq 0.673 \\ (1\text{-}0.22/\lambda)/\lambda & \text{for } \lambda > 0.673 \end{cases} \quad \text{(B.4-10)}$$

Since, $\lambda < 0.673$ $\rho = 1$ (B.4-11)

The effective width, *b* is calculated using the Equation B.4-12, given below:

$\therefore$ $b = \rho w = 1.0*160.0 =$ **160.0 mm** (B.4-12)

B.4.1.2 Effective width for flat elements with perforation:

$$w = 300 - 2*10 - 2*10 = 260.0 \text{ mm}$$

$$f_{crl} = 4* \frac{\pi^2 E}{12(1-0.3^2)} \left(\frac{10}{260.0} \right)^2 = 1091.43 \text{ MPa}$$

$$\lambda = \sqrt{\frac{F_n}{F_{crl}}} = \sqrt{\frac{439.57}{1091.43}} = 0.63$$

The effective width, *b* is calculated using the Equation B.4-13, given below:

$$b = \begin{cases} w - d & \text{for } \lambda \le 0.673 \\ \dfrac{w\left[1 - \dfrac{0.22}{\lambda} - \dfrac{0.8d}{w} + \dfrac{0.085d}{w\lambda}\right]}{\lambda} & \text{for } \lambda > 0.673 \end{cases} \quad \text{(B.4-13)}$$

Since, $\lambda < 0.673$, $b = w - d = 260.0 - 234.0 = \mathbf{26.0\ mm}$ (B.4-14)

$\therefore A_e = 2*160*10 + 2*26*10 + \pi*(2*10*10+10^2) = 4662.48\ mm^2$ (B.4-15)

The nominal axial strength is calculated using Equation B.4-5

$P_{nl\text{-}EWM} = 4662.48*439.57/1000 = \mathbf{2049.49\ kN} \le P_{ne}$

B.4.2 Direct Strength Method (DSM):

The nominal axial strength for local buckling based on *Direct Strength Method* ($P_{nl\text{-}EWM}$) detailed in E3.2.2 of AISI S100-16 (2016) and is calculated using Equation B.4-16:

$$P_{nl-DSM} = \begin{cases} P_{ne} \le P_{ynet} & \text{for } \lambda_l \le 0.776 \\ \left[1 - 0.15\left(\dfrac{P_{crl}}{P_{ne}}\right)^{0.4}\right]\left(\dfrac{P_{crl}}{P_{ne}}\right)^{0.4} P_{ne} \le P_{ynet} & \text{for } \lambda_l > 0.776 \end{cases} \quad \text{(B.4-16)}$$

in which

$P_{ynet} = A_{net}*f_y$

AISI S100-16 (2016) presents the guidelines for determining the critical elastic local buckling force, P_{crl} in Appendix 2, Section 2.3.1.2. Based on this section, P_{crl} shall be based on the lowest buckling stress among all the elements in the cross-section.

$P_{crl} = A_g f_{crl}$ (B.4-17)

In addition, AISI S100-16 (2016) also provides guidelines to estimate the critical elastic local buckling load for member with perforation in Section 2.3.2.2 of Appendix 2. Based on this section, the critical elastic local buckling stress, f_{crl} shall be calculated as both unstiffened elements at the perforation location as well as a separate element where the perforation is not located. To account of the effect of net section, while estimating the critical elastic local buckling stress for unstiffened element at perforation location, the value shall be multiplied with the ratio A_{net}/A_g.

B.4.2.1 For element without perforation

$$w = 200 - 2*10 - 2*10 = 160.0\,\text{mm}$$

$$f_{crl} = 4*\frac{\pi^2 * 204082}{12(1-0.3^2)}\left(\frac{10}{160}\right)^2 = \mathbf{2882.05\ MPa} \quad \text{(B.4-18)}$$

B.4.2.2 For element with perforation:

$$w = 300 - 2*10 - 2*10 = 260.0\,\text{mm} \quad \text{(B.4-19)}$$

Not the perforation location:

$$f_{crl} = 0.43*\frac{\pi^2 * 204082}{12(1-0.3^2)}\left(\frac{10}{260.0}\right)^2 = \mathbf{117.33\ MPa}$$

At the perforation location:

$$f_{crl} = 0.43*\frac{\pi^2 * 204082}{12(1-0.3^2)}\left(\frac{10}{260.0}\right)^2 * 0.5 = \mathbf{58.66\ MPa} \quad \text{(B.4-20)}$$

The critical elastic local buckling stress of the member shall be the minimum of the three values detailed in Equations B.4-18–B.4-20.

$\therefore$ f_{crl} = **58.66 MPa**

The critical elastic local buckling force, P_{crl} is calculated using Equation B.4-17.

P_{crl} = 58.66*9342.478 = **548.07 kN**

The slenderness factor of local buckling for column is estimated based on Equation B.4-21:

$$\lambda_l = \sqrt{4106.71/548.07} = \mathbf{2.74} \quad \text{(B.4-21)}$$

Since, λ_l > 0.776, the nominal axial strength for local buckling is estimated using Equation B.4-16:

$$P_{nl-DSM} = \left[1-0.15\left(\frac{548.07}{4106.72}\right)^{0.4}\right]\left(\frac{548.07}{4106.72}\right)^{0.4} 4106.72 = \mathbf{1710.80\ kN}$$

But, $P_{nl\text{-}DSM} \leq 2072.70$ kN (P_{ynet})

$\therefore$ $P_{nl\text{-}DSM}$ = **1710.80 kN**

B.4.3 Determination of local buckling stress based on the critical buckling stress developed by Moen and Schafer (2009):

B.4.3.1 For element without perforation

$$w = 200-2*10-2*10 = 160.0\,\text{mm}$$

$$f_{crl} = 4*\frac{\pi^2*204082}{12(1-0.3^2)}\left(\frac{10}{160.0}\right)^2 = \mathbf{2882.05\ MPa} \quad \text{(B.4-22)}$$

B.4.3.2 For element with perforation:

$$w = 300-2*10-2*10 = 260.0\,\text{mm} \quad \text{(B.4-23)}$$

Based on Moen and Schafer (2009), the critical elastic buckling for thin plate with perforations is given by Equation (B.4-24):

$$f_{crl} = \min\left(f_{cr}, f_{crh}\right) \quad \text{(B.4-24)}$$

The critical elastic buckling of perforated plate without the influence of perforation, f_{cr} can be evaluated using Equation B.4-25:

$$f_{cr} = 4 * \frac{\pi^2 * 204082}{12(1-0.3^2)} \left(\frac{10}{260.0} \right)^2 = \mathbf{1091.43\ MPa} \qquad \text{(B.4-25)}$$

The critical elastic buckling of perforated plate considering the influence of perforation, f_{crh} can be evaluated using Equation B.4-26:

$$f_{crh} = k_h \frac{\pi^2 E}{12(1-\upsilon^2)} \left(\frac{t}{w_h} \right)^2 \qquad \text{(B.4-26)}$$

The equivalent unstiffened plate element width, w_h on either side of the perforation (at the perforation location) is calculated using Equation (B.4-27)

$$w_h = w/2 - \pi d/8 = 260/2 - \pi * 234.0/2 = 38.11 \text{ mm} \qquad \text{(B.4-27)}$$

The plate buckling coefficient, k_h of unstiffened plate estimated based on the expressions approximated by Yu and Schafer (2007), given by Equation (B.4-28):

For $d/w_h \geq 1$, $\quad k_h = 0.425 + \dfrac{0.2}{(d/w_h)^{0.95} - 0.6}$, (B.4-28)

For $d/w_h < 1$, $\quad k_h = 0.925$.

Since, d/w_h =234.0/8.11 = 6.14 > 1

$$k_h = 0.425 + \frac{0.2}{(6.14)^{0.95} - 0.6} = 0.465$$

The critical elastic buckling of plate with perforation is calculated using Equation (B.4-26):

$$f_{crh} = 0.465 * \frac{\pi^2 204082}{12(1-0.3^2)}\left(\frac{10}{38.11}\right)^2 = \mathbf{5905.50\ MPa}$$

Therefore, considering Moen and Schafer (2009) recommendation, the critical elastic buckling for thin plate with perforations is calculated using Equation B.4-24:

f_{crl} = min (1091.43, 5905.50) = **1091.43 MPa** (B.4-29)

The critical elastic local buckling stress of the member shall be the minimum of the values detailed in Equations B.4-22 and B.4-29.

$\therefore f_{crl}$ = 1091.43 MPa

The critical elastic local buckling force, P_{crl} is calculated using Equation (B.4-17).

P_{crl} = 1091.43*9342.48 = **10196.66 kN** (B.4-30)

The slenderness factor of local buckling for column is estimated based on Equation (B.4-21):

$$\lambda_l = \sqrt{4106.71/10196.66} = 0.635 \quad \text{(B.4-31)}$$

Since, λ_l < 0.776, the nominal axial strength for local buckling considering the critical buckling stress developed by Moen and Schafer (2009) is estimated using Equation B.4-16:

$P_{nl-MS} = P_{ne}$ = **4106.72MPa**

But, $P_{nl\text{-}DSM} \leq$ 2072.70 kN (P_{ynet})

$\therefore P_{nl\text{-}MS}$ = **2072.70 kN**

B.5 Design as per Proposed DSM*:

The steps to estimate the nominal strength for flexural buckling (P_{ne}) is same with those detailed in B.4 of this Appendix using Equation B.4-1–B.4-4:

$\therefore P_{ne}$ = **4106.72 kN**

The critical elastic buckling stress is calculated following the recommendation made by Moen and Schafer (2009). The steps for estimating the critical elastic local buckling stress are same as those presented in Equations B.4-22–B.4-30

$\therefore P_{crl}$ = **10196.66 kN**

In the present study, the proposed equation to estimate the nominal axial strength for local buckling is given by Equation B.5-1:

$$P^*_{DSM} = \begin{cases} P_{ne}\left\{\dfrac{K_1}{\lambda_l^{K_2}}\right\} & \text{for } \lambda_l \le 0.776 \\ P_{ne}\left\{\dfrac{K_3}{\lambda_l^{0.8}} + \dfrac{K_4}{\lambda_l^{1.6}}\right\} & \text{for } \lambda_l > 0.776 \end{cases} \quad \text{(B.5-1)}$$

Since d/w = 0.9; K_1, K_2, K_3 and K_4 are 0.4459, 0.4542, 0.7091 and – 0.2456 respectively. The slenderness factor of local buckling for column is estimated based on Equation (B.4-21):

$$\lambda_l = \sqrt{4106.71/10196.66} = 0.635$$

Since, λ_l < 0.776, the nominal axial strength for local buckling considering the critical buckling stress developed by Moen and Schafer (2009) is estimated using Equation B.4-32:

$$P^*_{DSM} = 4106.72\left\{\frac{0.4459}{0.635^{0.4542}}\right\} = \textbf{2250.67 kN}$$

B.6 Design as per Miller and Peköz (1994):

Miller and Peköz (1994) proposed a simplified equation to estimate the column capacity having perforations. Based on the proposed equation, the effective width is calculated using Equation B.6-1:

$$\begin{aligned} b &= b_{DW} \quad \text{for } (w - b_{DW}) > W_p, \\ b &= w - W_p \quad \text{for } (w - b_{DW}) \le W_p, \end{aligned} \tag{B.6-1}$$

Note: Width of perforation, W_p = diameter of perforation, d.

B.6.1 Calculation of effective design width based on European, American and Australian standards:

The effective design width, b_{DW} is calculated using Equation (B.6-2), given below:

$$b_{DW} = \rho w \tag{B.6-2}$$

The local reduction factor, ρ is calculated using the Equation B.4-10, given below:

$$\begin{aligned} &\text{For } \bar{\lambda}_p \le 0.673; \quad \rho = 1, \\ &\text{For } \bar{\lambda}_p > 0.673; \quad \rho = \left(1 - 0.22/\bar{\lambda}_p\right)/\bar{\lambda}_p \le 1, \end{aligned} \tag{B.6-3}$$

$$\text{where } \bar{\lambda}_p = 0.526 * \left(\frac{w}{t}\right)\sqrt{\frac{f_y}{E}} \tag{B.6-4}$$

B.6.1.1 Calculation of design width for member without perforation:

$$w = 200 - 2*10 - 2*10 = 160.0 \text{ mm}$$

$$\bar{\lambda}_p = 0.526\left(\frac{160}{10}\right)\sqrt{\frac{444.55}{204082}} = 0.39 < 0.673$$

$$\therefore\ b = 1.0*160.0 = 160.0 \text{ mm} \tag{B.6-5}$$

B.6.1.2 Calculation of design width for member with perforation:

$$w = 300 - 2*10 - 2*10 = 260.0 \text{ mm}$$

$$\bar{\lambda}_p = 0.526\left(\frac{260}{10}\right)\sqrt{\frac{444.55}{204082}} = 0.64 < 0.673$$

$\therefore \rho = 1$

The effective design width, b_{DW} is calculated using Equation (B.6-1), given below:

$$b_{DW} = \rho w = 1*260 = 260.0 \text{ mm} \quad \text{(B.6-6)}$$

Since, $w - b_{DW} = 260.0 - 260.0 = 0.0 < 234.0$

$\therefore b = 260.0 - 234.0 = 26.0$ mm

Using the effective widths calculated above in Equations (B.6-6) and (B.6-6), the effective area can be calculated using the Equation (B.4-6)

$\therefore A_e = [(2*160*10) + (2*26.0*10) + \{\pi(2*10*10+10^2)\}] = 4662.48 \text{ mm}^2$

The nominal axial capacity of perforated column based on Miller and Peköz (1994) considering the effective design width based on EC3-1-5 (2006), AISI S100-16 (2016) and AS/NZS 4600 (2005) is estimated as:

$P_{MP\text{-}EC3} = A_e * f_y = 4662.48*444.55 =$ **2072.70 kN**

B.6.2 Calculation of effective design width based on British Standard:

The British standard, BS 5950-5 (1998) provides guidelines to estimate effective design width, b_{DW} as follows:

For $f_y / f_{cr} \le 0.123$, $\quad b_{DW} = w,$

For $f_y / f_{cr} > 0.123$, $\quad b_{DW} = w\left[1+14\left\{\left(\frac{f_y}{f_{cr}}\right)^{1/2} - 0.35\right\}^4\right]^{-0.2}$ (B.6-6)

where $f_{cr} = 4*\frac{\pi^2 E}{12(1-0.3^2)}\left(\frac{t}{w}\right)^2$

B.6.1.1 Calculation of design width for member without perforation:

$w = 200 - 2*10 - 2*10 = 160.0$ mm

$$f_{cr} = 4 * \frac{\pi^2 * 204082}{12(1-0.3^2)} \left(\frac{10}{160.0} \right)^2 = \mathbf{2882.05\ MPa}$$

Since, $f_y / f_{cr} = 444.55 / 2882.05 = 0.154 > 0.123$

$$b_{DW} = 160.0 \left[1 + 14 \left\{ 0.154^{1/2} - 0.35 \right\}^4 \right]^{-0.2} = 159.998 \text{ mm} \quad \text{(B.6-7)}$$

b = 159.998 mm (B.6-8)

B.6.1.2 Calculation of design width for member with perforation:

$$w = 300 - 2*10 - 2*10 = 260.0 \text{ mm}$$

$$f_{cr} = 4 * \frac{\pi^2 * 204082}{12(1-0.3^2)} \left(\frac{10}{260.0} \right)^2 = 1091.43 \text{ MPa}$$

Since, $f_y / f_{cr} = 444.55 / 1091.43 = 0.407 > 0.123$

$$b_{DW} = 260.0 \left[1 + 14 \left\{ 0.407^{1/2} - 0.35 \right\}^4 \right]^{-0.2} = 255.26 \text{ mm}$$

Again, $w - b_{DW}$ = 260.0 – 255.26 = 4.74 < 234.0

$\therefore$ b = 260.0 – 234.0 = 26.0 mm (B.6-9)

Using the effective widths calculated above in Equations (B.6-8) and (B.6-9), the effective area can be calculated using the Equation (B.4-6)

$\therefore A_e$ = [(2*160*10) + (2*26.0*10) + {π(2*10*10+10^2)}] = **4662.48 mm^2**

The nominal axial capacity of perforated column based on Miller and Peköz (1994) considering the effective design width based on BS 5950-5 (1998) is estimated as:

$P_{MP\text{-}BS}$ = $A_e * f_y$ = 4662.48*444.55 = **2072.70 kN**

This page is intentionally left blank.